UNIVERSITY OF BUCHAREST
VIRTUTE ET SAPIENTIA

DOCTORAL THESIS

Advanced Computational Methods for Quantum Information Processing

Author:
Amanda Teodora PREDA

Supervisor:
Prof. Univ. Dr. George Alexandru NEMNEȘ

A thesis submitted in fulfillment of the requirements
for the degree of Doctor of Philosophy

in the

FACULTY OF PHYSICS

“We can only see a short distance ahead, but we can see plenty there that needs to be done”

Alan Turing

UNIVERSITY OF BUCHAREST

Abstract

Faculty of Physics

Doctor of Philosophy

Advanced Computational Methods for Quantum Information Processing

by Amanda Teodora PREDA

Device modeling based on material simulations and transport models are indispensable in order to carry out low-cost exploration and open new pathways into the experimental investigation of low-dimensional nano-electronic devices. The research presented in this doctoral thesis aims to employ state of the art computational methods of quantum transport combined with innovative models based on machine learning techniques to provide a versatile device modeling approach. We explored a range of low-dimensional systems with potential applications in information technology by employing several methods, from *ab initio* calculations based on density functional theory, to tight binding based models, exact diagonalization and the R-matrix formalism.

Acknowledgements

First of all, I would like to thank my supervisor, prof. Alexandru Nemnes, who guided me for almost four years and helped tremendously at each phase of my post-graduate studies. The research presented in this thesis could not have been carried out without his constant support and feedback. Also, I highly appreciate the advice and insights given by prof. Lucian Ion, prof. Iulia Ghiu and prof. Virgil Baran, who have guided me not only through my doctoral degree, but also throughout my master's studies. I am indeed grateful to have had a doctoral committee and supervisor that were involved in the research process, made time to read and give feedback for my thesis and were always available to guide me. Moreover, I am grateful to all our collaborators and all the co-authors that worked on the papers cited in this thesis. Most of all, I would like to mention our collaboration with Brandenburg University of Technology , through prof. Ulrich Wulf and also our collaboration with Reykjavik University and prof. Andrei Manolescu. Last but not least, I want to thank my colleagues Mihaela Cosinschi, Nicolae Filipoiu and Calin Pantis, without whom none of the papers mentioned throughout this work could have been written.

Contents

Dedicated to my parents

Part I

Theoretical Overview

1

Introduction

> "The underlying physical laws necessary for the mathematical theory of a large part of physics and the whole of chemistry are thus completely known, and the difficulty is only that the exact application of these laws leads to equations much too complicated to be soluble. It therefore becomes desirable that approximate practical methods of applying quantum mechanics should be developed, which can lead to an explanation of the main features of complex atomic systems without too much computation."
>
> *Paul Dirac (1929)*

1.1 Motivation and scope of the thesis

The field of condensed matter physics (CMP) holds tremendous importance in both theoretical science and industry-oriented technology. Considering the amount of progress made in this area, it is astonishing to realize that condensed matter physics is a relatively new area of physics. In the 1950s, only a couple of laboratories conducted research programs in condensed matter [1] and university courses on solid state physics were recent additions to the curriculum. Over the course of the next 70 years, condensed matter physics evolved at the highest pace, due to a couple of factors: novel experimental discoveries and more efficient experimental techniques for materials characterization, new theoretical concepts, models and methods that advanced the reach of condensed matter and, last but not least, multiple numerically-based approaches that lead to the programming of highly effective simulation programs.

Condensed matter physics already overlaps with various other branches of the physical sciences, such as statistical and theoretical physics, chemistry, materials science, magnetism and spintronics and, over the last decades, high performance computing. The computational side of CMP has become a fundamental area of research on its own, aiming to open novel pathways into the future of technological progress. The established numerical methods of condensed matter play an essential role not only in the description of systems with thousands of atoms, that cannot be solved otherwise, but also in the design of low dimensional devices that perform at a quantum scale and require precise control of the quantum states. On top of this, with the

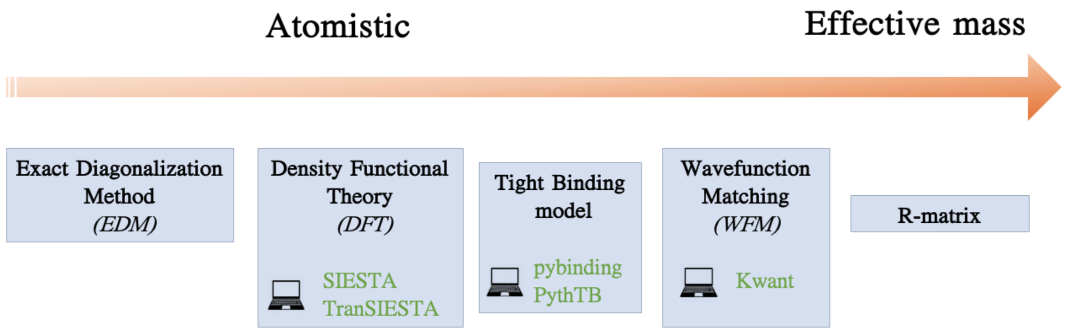

FIGURE 1.1: The simulation methods and programs employed throughout the thesis, ranging from techniques that focus on accurately describing systems of only a couple of particles to tight binding and effective mass formalisms that model solids at mesoscopic scales.

rapid advancements in artificial intelligence and machine learning (ML) techniques, there is a growing interest in employing ML schemes to resolve CMP problems [2].

This thesis is focused on a set of well-established computational methods used in conjunction with machine learning techniques for the purpose of simulating quantum-scale two-dimensional devices with applications in information technology. Since this is the era of swift development of quantum technologies, one needs to acquire a wide and encompassing view of the numerical approaches employed in quantum transport and use them to simulate and guide the design of novel low-dimensional devices. In Figure 1.1, we highlighted the main computational simulation programs that we utilized, covering the spectrum that lies between atomistic approaches and effective mass formalisms. Our goal is to model and simulate low dimensional single and multi-particle systems, providing the building blocks for a new era of quantum-engineered devices that meet the requirements of energy efficiency and scalability. For example, the exact description and control of quantum states is critical to the design of quantum computing architectures. In novel nano-transistor prototypes, quantum transport takes precedence over the classical drift-diffusion models, due to the continuous down-scaling imposed by the prompt technological advances. We explore these avenues of device modeling in the second part of the thesis and the devices that we simulated are presented in Figure 1.2. Also, computational accuracy and time effectiveness must be both accounted for, and to this end we also propose the use of ML techniques in order to aid the device modeling process.

1.2 Chapter summaries

In the second chapter, we introduce the theoretical fundamentals of quantum transport, starting from the well-known Landauer-Buttiker formalism. Along with the down-scaling of solid-state devices, there has been a great effort dedicated to a detailed understanding of the transport phenomena in nano-structures like quantum dots, quantum rings or wires. To this end, the Landauer-Buttiker formalism remains the most popular, by providing a simple, yet elegant description of transport that links the conductance of the mesoscopic device to the transmission function. In turn, the transmission is computed with the aid of the scattering matrix (S-matrix), one of the most relevant mathematical tools employed to describe the transport properties in nanostructures. Moving to a more formal and rigorous approach, we introduce Green's functions and briefly discuss their wide reach in theoretical physics. We

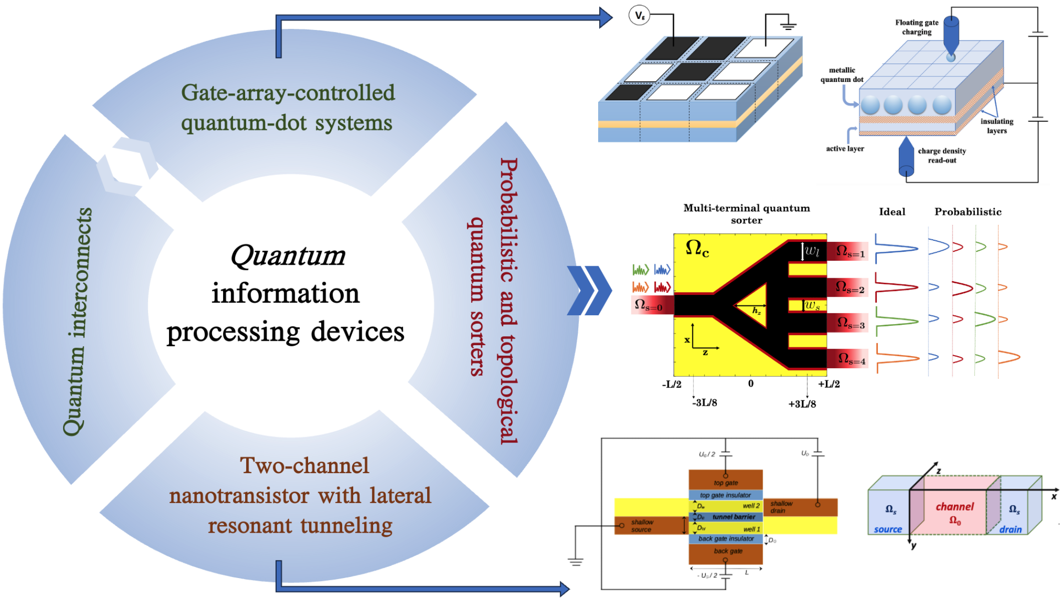

FIGURE 1.2: Low dimensional devices proposed and studied in the thesis, described in detail throughout the final chapters that present the main results.

end this introductory chapter with a section on topological insulators, where we introduce the BHZ model, one of the most popular models that aims to describe the properties of this new class of materials with exotic transport properties.

In Chapter 3, we present a theoretical overview of the computational methods employed in quantum transport. We begin with an introduction into the density functional theory (DFT), which is built onto the work of Hohenberg and Kohn and, subsequently, Kohn and Sham. Due to the accuracy and efficiency of the functionals used to solve the Kohn-Sham auxiliary system, DFT became the standard method in computational materials science. DFT can also be extended to non-equilibrium transport, by means of the non-equilibrium Green's functions formalism, which we introduce in the second section of the chapter. From atomistic simulations, we move on to describe effective-mass approximation models, starting with the R-matrix formalism, an efficient numerical approach that is described in detail in this thesis. We also present the tight binding model and the wavefunction matching method, which are intrinsically connected to the Kwant simulation package, employed extensively in this thesis.

In Chapter 4, we pivot towards a new paradigm in computational condensed matter, namely the use of machine learning (ML) techniques in order to improve and add to the well-established simulation tools. We discuss in this chapter the theory behind some of the most popular ML algorithms: feed forward neural networks, convolutional neural networks, generative adversarial networks and conditional generative adversarial networks.

Chapters 5, 6 and 7 are dedicated to the presentation of the most important original results. In Chapter 5, we introduce an extension of the R-matrix formalism to bi-particle scattering problems, which was previously presented in detail in [3]. Chapter 6 focuses on the modeling and simulation of various low-dimensional devices with potential applications in information technology. We begin by thoroughly describing a two-dimensional bi-particle system where the confining potential of the electrons is controlled by a top gate potential. Employing simulation techniques described in the previous chapters, along with machine learning models, we are able to determine the energy spectra with a high degree of accuracy. Subsequently, we advance to the modeling of periodic systems, focusing on Lieb lattices as a prototype. The next step is to move towards a reconfigurable device, with potential applications in the field of neuromorphic computing. The last section of Chapter 6 is dedicated to the in depth study of a two-channel nanotransistor, where we employed both R-matrix and tight binding based simulations in order to compute the transmission functions and I-V characteristics of a novel prototype of a nanotransistor. Its working principle relies on lateral resonant tunneling and paves the way to low-energy applications.

In Chapter 7 we discuss two 2D multi-terminal devices that work as probabilistic quantum sorters. We explore the possibility of tuning the scattering potential in a low dimensional device such that one can separate the outgoing states by both their transversal mode and spin, providing a way to determine the state of a quantum system by simply measuring the current in an output port. We also explore the possibility of creating such a device with topological insulators and exploiting their unique transport properties in order to increase the accuracy of the quantum sorter. The final chapter presents the summary and conclusions. It is followed by a series of Appendixes that aim to further explain concepts that were not fully detailed in the main part of the thesis and to list some of the codes used in the quantum transport simulations.

2

Fundamentals of quantum transport

2.1 Mesoscopic systems and the Landauer-Büttiker formalism

Historically, quantum transport was built upon a field that appeared around four decades ago, in the 1980s, known as *mesoscopic physics*. The name emphasized an exploration of phenomena that lied between the microscopic and macroscopic realms, using methods from both semi-classical transport and quantum mechanics. The mesoscopic regime became recognized as the bridge between quantum and classical, being materialized into electronic devices along with the down-scaling of all technologies that stand at the core of information processing. Dimensionality itself is not enough to label a system and assign a transport regime, so there are other length scales to be considered: the coherence length ℓ_ϕ, the energy relaxation length, ℓ_{in} , the elastic mean free path, ℓ_0, the Fermi wave length of the electron, λ_F [4, 5]. If the size $\mathcal{L}$ of the sample is much smaller than the energy relaxation length, ℓ_{in} and the phase breaking length, ℓ_ϕ, we reside in the mesoscopic regime and the transport is coherent. Now the question that arises is what formalism we employ to describe such a situation. We discuss in this section the Landauer-Büttiker approach to coherent transport in mesoscopic structures and use it as a building block to introduce fundamental mathematical tools for quantum transport. Then, we shall shift slightly to a new direction of condensed matter, namely topological phenomena and familiarize ourselves with some of the most popular theoretical model that describes topological insulators.

Mesoscopic systems	Conventional systems
Ballistic $\mathcal{L} \leq \ell_e$	Diffusive $\mathcal{L} \gg \ell_e$
Phase coherent $\mathcal{L} \leq \ell_\phi$	Incoherent $\mathcal{L} \gg \ell_\phi$
Quantum confinement effect $\mathcal{L} \leq \lambda_F$	No quantum confinement effect $\mathcal{L} \gg \lambda_F$

TABLE 2.1: Characteristic quantities of mesoscopic and conventional transport, in terms of the system size $\mathcal{L}$

2.1.1 The Landauer formula

Consider a 1D wire connected to two reservoirs (represented as leads) to its left and right, with fixed chemical potentials denoted by $\mu_L \equiv \mu_1$ and $\mu_R \equiv \mu_2$. We assume that there is a net current flowing from left to right, so that $\mu_1 > \mu_2$. If we consider a cross sectional surface denoted as Ω (see Figure 2.1) near the right lead, the current can be expressed as:

$$I = -e \int dEg(E)v(E) \left[\mathcal{T}(E) f\left(E-\mu_1\right) + \mathcal{R}'(E) f\left(E-\mu_2\right) - f\left(E-\mu_2\right)\right], \tag{2.1}$$

where $g(E)$ is the density of states in the leads, $v(E)$ is the velocity, and $f\left(E-\mu_{1,2}\right)$ are the Fermi distributions in the left and right leads respectively. Also, $\mathcal{T}(E)$ is the transmission probability for the electrons from the left leads to end up in right reservoir; $R'(E)$ is the reflection probability of the electrons from the right reservoir to return into the same reservoir. If we consider R to be the reflection probability of the left electrons to return, then, in this simple two terminal case, we consider that $\mathcal{R}'(E) = \mathcal{R}(E)$. Also, since the total probability must be equal to unity, we use the fact that $\mathcal{R}(E) + \mathcal{T}(E) = 1$, hence equation 2.1 becomes:

$$I_\Omega = -e \int dEg(E)v(E)\mathcal{T}(E) \left[f\left(E-\mu_1\right) - f\left(E-\mu_2\right)\right]. \tag{2.2}$$

If the applied voltage difference V_{12} is small, $\mu_1 - \mu_2 = |e| V_{12} \ll k_\mathrm{B} T$, we are in the linear response regime, we can use the expansion:

$$f\left(E-\mu_2\right) = f\left(E-\mu_1\right) + f'\left(E-\mu_1\right)\left(\mu_1-\mu_2\right) + \ldots \tag{2.3}$$

Therefore,

$$f_1(E) - f_2(E) = \frac{\partial f_1(E)}{\partial E}\left(\mu_1-\mu_2\right) = -\frac{\partial f_1(E)}{\partial E}|e|V_{12}.$$

Using the formula for the density of states in the 1D case ($g(\varepsilon) = 1/hv(\varepsilon)$), we obtain the result

$$\begin{aligned} I &= e\left(\mu_\mathrm{R}-\mu_\mathrm{L}\right) \int dEg(E)v(E) \left(-\frac{\partial f}{\partial \varepsilon}\right) \mathcal{T}(E) \\ &= \frac{e}{h}\left(\mu_2-\mu_1\right) \int dE \left(-\frac{\partial f}{\partial E}\right) \mathcal{T}(E). \end{aligned} \tag{2.4}$$

At low temperatures, we can assume that $T \to 0$, which allows us to replace the derivative of the Fermi distribution with $\partial f/\partial E \to -\delta\left(E-E_\mathrm{F}\right)$, where $\delta\left(x-x_0\right)$ is the Dirac delta function. Hence, the current is rewritten as:

$$I = \frac{e}{h}\left(\mu_\mathrm{R}-\mu_\mathrm{L}\right)\mathcal{T}\left(E_\mathrm{F}\right). \tag{2.5}$$

If we take note of the fact that the conductance in the system is $G = dI/dV$, we easily obtain the well-known Landauer formula:

$$\begin{aligned} G &= \frac{e^2}{h}\mathcal{T}\left(E_\mathrm{F}\right) \quad \text{(per spin channel)} \\ G &= \frac{2e^2}{h}\mathcal{T}\left(E_\mathrm{F}\right) \quad \text{(spin degeneracy included)} \end{aligned} \tag{2.6}$$

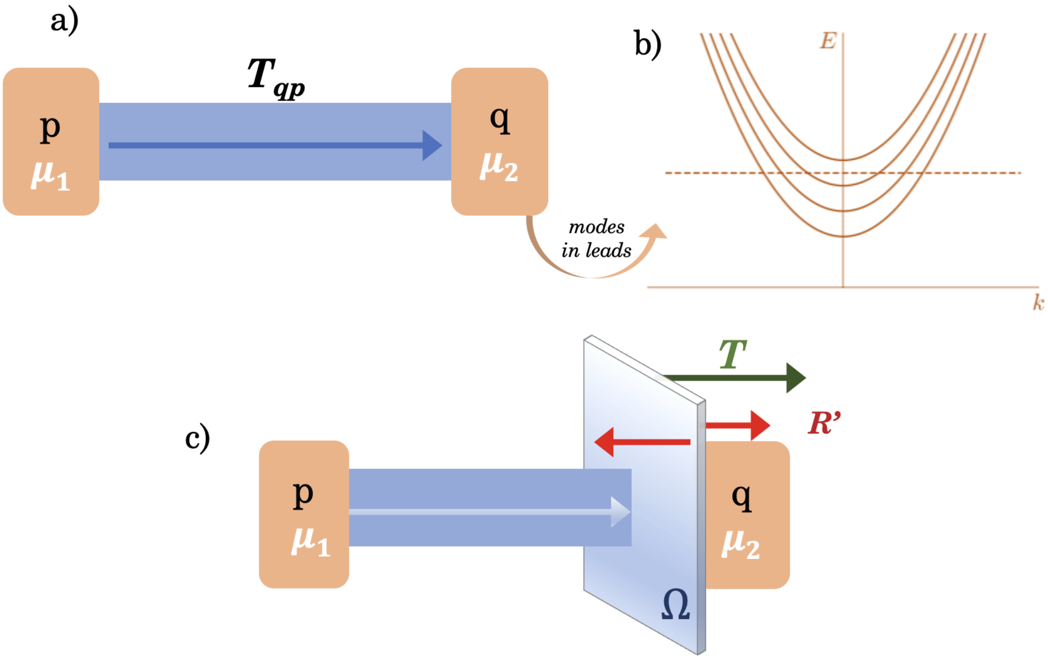

FIGURE 2.1: (a) A schematic representation of an ideal two-terminal system, with leads indexed by p and q, where $T_{p\to q} = T_{qp}$ is the transmission probability of an electron injected into terminal p to reach q. (b) Transverse modes into one of the ideal leads, considered to be translationally invariant along the transport direction and supplied with particles from the reservoirs.

For a case when we have N perfectly conducting channels:

$$G_0 = g_\mathrm{s} \frac{e^2}{h} N, \tag{2.7}$$

where g_s accounts for the spin degeneracy.

Before we move on to the next section, there is one important observation to make about the formalism derived above. The Landauer formula is highly intuitive from a quantum mechanical perspective, since it directly relates the transmission probability to the conductance of the sample. It is to be expected that if the transmission through the quantum system is null, then the conductance should be zero as well. An interesting question arises in the opposite case, when the transmission is equal to unity and $G = e^2/h$, which is, of course, a finite value. The same reasoning applied before would lead us to believe that a wire with no scattering would have infinite conductance, which is clearly not the case. The solution to this is to associate the resistance h/e^2 with the contact resistance, due to the coupling between the ideal wire and the leads. Therefore,

$$G^{-1}_{total} = G^{-1}_\mathrm{wire} + \frac{h}{e^2}. \tag{2.8}$$

Conductance quantization

The first experimental proof of conductance quantization in two-dimensional (2D) systems came in the form of two seminal papers published independently in 1988, by van Wees *et al.* [6] and Wharam *et al.* [7]. In these papers, the authors presented

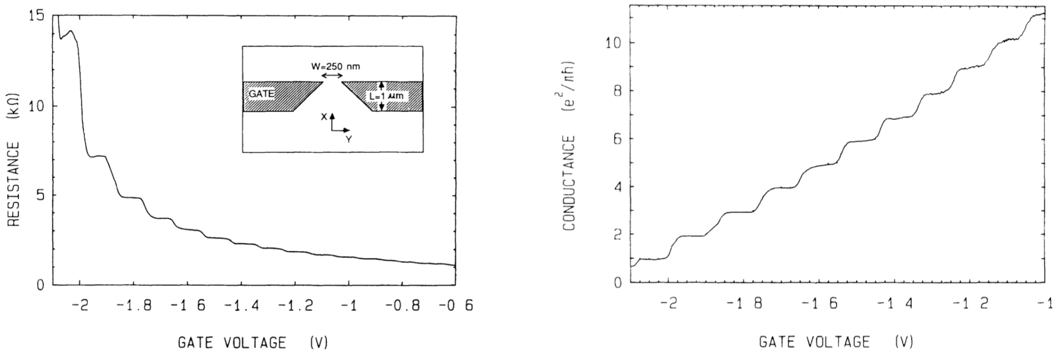

FIGURE 2.2: (a) Resistance of the quantum point contact as a function of the gate voltage. In the inset, the authors represented a schematic top view of the split gate structure. (b) Conductance of the same quantum point contact as a function of gate voltage after subtracting the contact conductance G_C. Reprinted with permission from *Physical Review Letters* [6]

their surprising results on the low temperature conductance of quantum point contacts. They reported the first experimental results on the resistance quantization of point contacts created within the two-dimensional electron gas (2DEG) of GaAs-AlGaAs heterostructures. The quantum point contact behaviour is obtained with the aid of a split gate structure that is used to deplete the electronic gas underneath it (see the inset in Figure 2.2). In this manner, one can recreate experimentally narrow constrictions in the 2DEG, with widths around $W \approx 250$ nm, comparable to the Fermi wavelength $\lambda_F \approx 40$ nm and much shorter than the mean free path $l_0 \approx 10\,\mu$m [8]. This method allows for the control of the width of the point contact, a property which, in contrast, cannot be modified easily in the case of metal point contacts.

After a detailed investigation of the structure, both research groups have noticed that the resistance of the 2DEG has well-defined quantized plateaus. In order to separate the resistance of the 2DEG from the resistance of the whole system, one needs to substract the contact resistance, discussed previously, which is gate voltage independent and has a value of approximately 25.8 kΩ. The conductance plateaus were observed for:

$$G = \frac{2e^2}{h} N, \tag{2.9}$$

where N is an integer number. Therefore, the conductance is quantized in units of the conductance quantum:

$$G_0 = \frac{e^2}{h} = 3.8740459 \times 10^{-5} \Omega^{-1}. \tag{2.10}$$

The potential applied to the gate electrodes repels the electrons, which resembles a quantum barrier. A narrow constriction is formed in the 2DEG. Increasingly negative voltages create greater repulsion, and make the constriction narrower. In turn, the number of open channels through the constriction is determined by its width. A new channel opens up when the energy of the electrostatically induced barrier surpasses the Fermi energy. Therefore, one can write

$$E_n \equiv n^2 \frac{\hbar^2}{2m} \left(\frac{\pi}{W}\right)^2 = E_F = \frac{\hbar^2 k_F^2}{2m}, \tag{2.11}$$

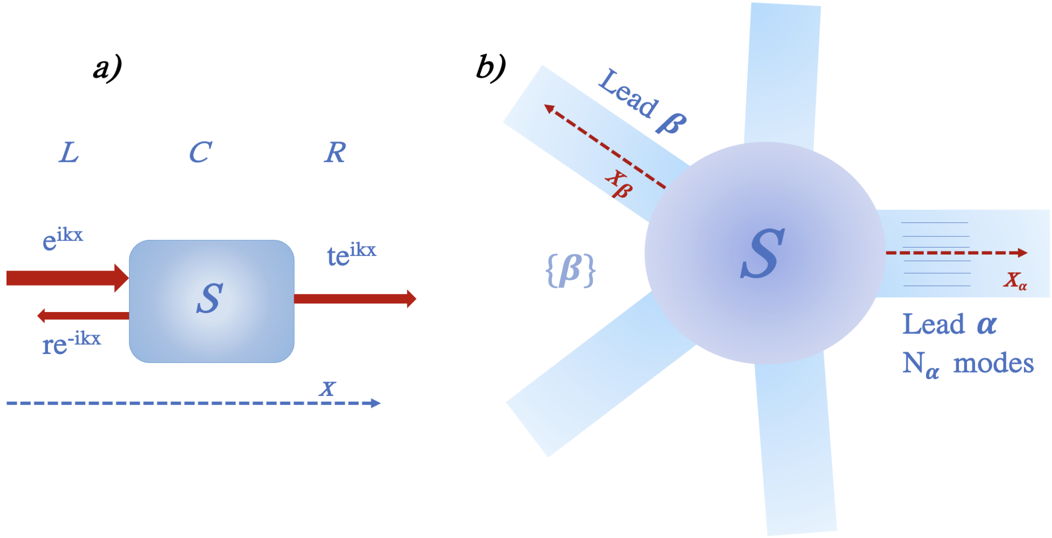

FIGURE 2.3: (a) Representation of a two-terminal system, where we can use one coordinate system for the L+C+R device. (b) Generalization to a multi-terminal system, where we consider that each lead has its own coordinate system and x_α perpendicular on the cross-section of the lead, pointing away from the scattering region.

where W is the width of the constriction, n is the number of channels, E_F is the Fermi energy and k_F is the Fermi wavelength. The number of open channels is then:

$$N_{\text{open}} = \left[\frac{\mathrm{k_F} W}{\pi}\right], \tag{2.12}$$

where the brackets stand for integer part. When this experiment was performed, the result of conductance quantization was not expected in a system that is so far from the ideal waveguide.

2.1.2 The S-matrix

The Landauer-Buttiker formalism links the conductance of a mesoscopic system to the transmission, therefore the next step is to look into the theoretical tools we use to calculate the transmission. We shall consider a simple system composed of three regions: the right and the left leads, and a central scattering region. The leads are considered to be reflectionless, perfect straight contacts with hard walls in which we assume asymptotic solutions for the wavefunctions. The electrons are injected into the leads through macroscopic conductors that are considered reservoirs, where one can define thermodynamic quantities like the chemical potential and the temperature. The leads connected to this reservoirs are modeled as semi-infite, to preserve translational invariance along the transport direction, but they have a lateral confinement potential that induces the transverse modes of propagation.

The Hamiltonian of a lead α is:

$$H_\alpha = \frac{1}{2m^*} p_{x_\alpha}^2 + \frac{1}{2m^*} p_y^2 + V(y), \quad y \in [0, W], \tag{2.13}$$

where W is the width of the leads and $V(y)$ is the confinement potential. The eigenstates of $\mathcal{H}_{L,R}$ are a product between a plane wave and a transverse wavefunction.

In order to express the scattering states in a manner that is also suitable for a multi-terminal system, we define a local coordinate x_α in each lead α and consider that x_α is positive in the direction pointing away from the scattering region (see Figure 2.3). Hence, incoming plane waves will be of the type $e^{-ik_n x_\alpha}$ and outgoing plane waves will pe $e^{ik_n x_\alpha}$, where n denotes a particular transverse mode in lead α.

Therefore, the eigenfunctions can be written as:

$$\phi^{\pm}_{\alpha n}(x,y) = e^{\mp ik_n x_\alpha}\chi_{\alpha,n}(y), \quad (x,y) \in \alpha, \tag{2.14}$$

where the ± superscript stands for incoming/outgoing states and

$$\chi_{\alpha,n}(y) = \sqrt{\frac{2}{W}}\sin\left(n\frac{\pi y}{W}\right), \quad \text{n=1,2,} \ldots, N_\alpha\,, \tag{2.15}$$

are the transverse functions. Also, N_α is the total number of channels in lead α.

The total energy is:

$$E = \frac{\hbar^2}{2m^*}k_n^2 + \varepsilon_n, \quad \varepsilon_n = \frac{\hbar^2}{2m^*}\left(\frac{\pi n}{W}\right)^2, \tag{2.16}$$

The wavefunctions in the leads are a linear combination of the incoming and outgoing states, while in the scattering center region the form of the wavefunction is unknown at this point. In the following, we restrict our discussion to the simpler two-terminal case, where $\alpha = L, R$ and we denote by $a_{L,R}$ the amplitudes of the incoming waves and by $b_{L,R}$ the amplitued of the outgoing ones. We can therefore write the system wavefunction as:

$$\begin{aligned}
\psi(x,y) &= \begin{cases} \sum_m a^L_m \phi^+_{Lm}(x,y) + \sum_m b^L_m \phi^-_{Lm}(x,y), & (x,y) \in L \\ \sum_n a^R_n \phi^+_{Rn}(x,y) + \sum_n b^R_n \phi^-_{Rn}(x,y), & (x,y) \in R \\ \psi_{C,E}(x,y), & (x,y) \in C \end{cases} \\
\Rightarrow \psi(x,y) &= \begin{cases} \sum_m a^L_m e^{-ik_m x_L}\chi_m(y) + \sum_m b^L_m e^{ik_m x_L}\chi_m(y), & (x,y) \in L \\ \sum_n a^R_n e^{-ik_n x_R}\chi_n(y) + \sum_n b^R_n e^{ik_n x_R}\chi_n(y), & (x,y) \in R \\ \psi_{C,E}(x,y), & (x,y) \in C \end{cases}
\end{aligned} \tag{2.17}$$

In the framework of the scattering matrix formalism we are looking for a mathematical object that links the coefficients of the incoming and outgoing states. These coefficients are represented in column vector form as:

$$\mathbf{c_{in}} = \begin{pmatrix} a^L_1 \\ a^R_1 \\ \cdot \\ \cdot \\ \cdot \\ a^L_n \\ a^R_n \end{pmatrix} \quad \text{and} \quad \mathbf{c_{out}} = \begin{pmatrix} b^L_1 \\ b^R_1 \\ \cdot \\ \cdot \\ \cdot \\ b^L_n \\ b^R_n \end{pmatrix} \tag{2.18}$$

The notations L, R, C stand for the left/right leads and the central region and we denote $\mathcal{D}$ to be the dimension of the central region along the x direction. The fundamental principles of quantum mechanics impose that the wavefunction and its first derivative must be continuous. Keeping this in mind, we obtain a linear system of equations that determine the coefficients a, b:

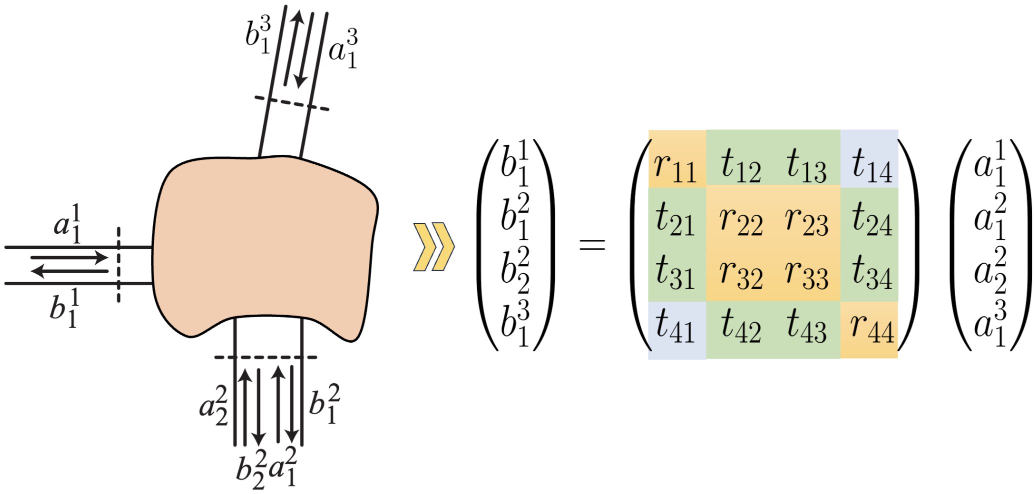

FIGURE 2.4: Block structure of the S matrix for a three terminal system. The wavefunction coefficients are denoted by a, b, where the superscript stands for the leads and the subscript indexes the mode.

$$\begin{aligned} \left(a_m^L + b_m^L\right) &= \int dy \chi_m(y) \psi_{C,E}(0, y) \\ \left(b_n^R e^{ik_n \mathcal{D}} + a_n^R e^{-ik_n \mathcal{D}}\right) &= \int dy \chi_n(y) \psi_{C,E}(\mathcal{D}, y) \\ ik_m \left(b_m^L - a_m^L\right) &= \int dy \chi_m(y) \left(\partial_x \psi_C(x, y)\right)_{x=0} \\ ik_n \left(b_n^R e^{ik_n(E)\mathcal{D}} - a_n^R e^{-ik_n(E)\mathcal{D}}\right) &= \int dy \chi_n(y) \left(\partial_x \psi_{C,E}(x, y)\right)_{x=\mathcal{D}} \end{aligned} \tag{2.19}$$

For now, we are not concerned with the explicit form of the wavefunction in the central region, $\psi_{C,E}(x, y)$. However, we notice that we can define a matrix that directly relate the outgoing amplitudes to the incoming ones:

$$b_{\alpha m} = \sum_{\beta n} s_{\alpha m, \beta n} a_{\beta n}, \tag{2.20}$$

where m, n stand for the number of modes in leads α, β. This is known as the S-matrix (scattering matrix) and it will become a fundamental quantity in quantum transport.

Matrix formulation In matrix form, the equation above looks in the following manner:

$$\mathbf{c}_{\text{out}} \equiv \begin{pmatrix} \mathbf{b}^L \\ \mathbf{b}^R \end{pmatrix} = \begin{pmatrix} \mathbf{r} & \mathbf{t}' \\ \mathbf{t} & \mathbf{r}' \end{pmatrix} \begin{pmatrix} \mathbf{a}^L \\ \mathbf{a}^R \end{pmatrix} \equiv \mathbf{S} \begin{pmatrix} \mathbf{a}^L \\ \mathbf{a}^R \end{pmatrix} \equiv \mathbf{S}\mathbf{c}_{\text{in}} \tag{2.21}$$

$$\Rightarrow \mathbf{S} = \begin{pmatrix} \mathbf{r} & \mathbf{t}' \\ \mathbf{t} & \mathbf{r}' \end{pmatrix} \tag{2.22}$$

For a case with multiple modes in each lead:

$$\begin{aligned}\boldsymbol{c}_{\text{in}} &= \left(a_1^L, \dots, a_{N_L}^L, a_1^R, \dots, a_{N_R}^R\right)^T \\ \boldsymbol{c}_{\text{out}} &= \left(b_1^L, \dots, b_{N_L}^L, b_1^R, \dots, b_{N_R}^R\right)^T\end{aligned} \tag{2.23}$$

with $N_{L,R} = N_{L,R}(E)$ being the number of modes in the leads. The scattering matrix has the following block form:

$$S = \begin{pmatrix} \boldsymbol{r}_{N_L \times N_L} & \boldsymbol{t}'_{N_L \times N_R}, \\ \boldsymbol{t}_{N_R \times N_L} & \boldsymbol{r}'_{N_R \times N_R}, \end{pmatrix} \tag{2.24}$$

For a 2-terminal system with one open channel at a given energy, the spin-generalized S-matrix becomes a 4 × 4 matrix:

$$\mathbf{S} = \begin{bmatrix} \begin{pmatrix} r_{\uparrow\uparrow} & r_{\uparrow\downarrow} \\ r_{\downarrow\uparrow} & r_{\downarrow\downarrow} \end{pmatrix} & \begin{pmatrix} t'_{\uparrow\uparrow} & t'_{\uparrow\downarrow} \\ t'_{\downarrow\uparrow} & t'_{\downarrow\downarrow} \end{pmatrix} \\ \begin{pmatrix} t_{\uparrow\uparrow} & t_{\uparrow\downarrow} \\ t_{\downarrow\uparrow} & t_{\downarrow\downarrow} \end{pmatrix} & \begin{pmatrix} r'_{\uparrow\uparrow} & r'_{\uparrow\downarrow} \\ r'_{\downarrow\uparrow} & r'_{\downarrow\downarrow} \end{pmatrix} \end{bmatrix} \tag{2.25}$$

Unitarity of the S-matrix

We determined that the S-matrix relates the outgoing wavefunctions amplitudes to the incoming amplitudes. There is, however, one additional physical constraint that we have to account for, namely current conservation. Hence, we are looking for a scattering matrix that is also unitary. The condition we impose is that the probability current, which is proportional to particle flux, remains constant. Using the well-known form of the probability current operator:

$$\mathbf{j} = \frac{\hbar}{m^*} \operatorname{Im}\left(\psi^* \nabla \psi\right) = \frac{\hbar}{2m^* i}\left(\Psi^* \nabla \Psi - \Psi \nabla \Psi^*\right) \tag{2.26}$$

we prove that, for the scattering wavefunction of the type $\psi(x,y) = \sum_m a_m^L e^{-ik_m x_L} \chi_m(y)$, the probability current is proportional to the squared amplitude:

$$j = \sum_m^{N_L+N_R} c^*_{\text{out},m} c_{\text{out},m} \frac{\hbar k_m}{m^*} = \sum_m c^*_{\text{out},m} c_{\text{out},m} v_m, \tag{2.27}$$

where v_m is the velocity. The incoming/outgoing particle flux must be conserved, therefore:

$$j_{out} = \sum_m c^*_{out,m} c_{out,m} \frac{\hbar k_m}{m^*} = \sum_{m,n} s^*_{mn} c^*_{in,n} s_{mn} c_{in,n} \frac{\hbar k_m}{m^*} = \sum_{m,n} s^*_{mn} |c_{in,n}|^2 s_{mn} \frac{\hbar k_m}{m^*} \tag{2.28}$$

$$j_{in} = \sum_n c^*_{in,n} c_{in,n} \frac{\hbar k_n}{m^*} = \sum_n |c_{in,n}|^2 \frac{\hbar k_n}{m^*} \tag{2.29}$$

Current conservation implies that $\mathbf{j}_{\text{out}} = \mathbf{j}_{\text{in}}$, therefore:

$$\begin{aligned}
&\sum_{m,n} |s_{mn}|^2 \frac{\hbar k_m}{m^*} = \sum_n \frac{\hbar k_n}{m^*} \\
&\Rightarrow \sum_m |s_{mn}|^2 \frac{k_m}{k_n} = 1, \\
&\Rightarrow \tilde{s}_{mn} = s_{mn}\sqrt{\frac{k_m}{k_n}},
\end{aligned} \tag{2.30}$$

where $\tilde{\mathbf{S}}$ is the unitary S matrix.
In matrix form, the relation above is:

$$\begin{aligned}
&\Rightarrow \left(\mathbf{k}^{1/2}\mathbf{S}\mathbf{k}^{-1/2}\right)^\dagger \left(\mathbf{k}^{1/2}\mathbf{S}\mathbf{k}^{-1/2}\right) = \mathbf{1}, \\
&\Rightarrow \widetilde{\mathbf{S}} = \mathbf{k}^{1/2}\mathbf{S}\mathbf{k}^{-1/2}.
\end{aligned} \tag{2.31}$$

The unitarity of the S-matrix ensures current conservation. The transmission and reflection matrices uphold the following relations if the scattering matrix is unitary:

$$\begin{aligned}
\boldsymbol{r}\boldsymbol{r}^\dagger + \boldsymbol{t}'\boldsymbol{t}'^\dagger &= \boldsymbol{r}^\dagger\boldsymbol{r} + \boldsymbol{t}^\dagger\boldsymbol{t} = \mathbf{1}_{N_L} \\
\boldsymbol{r}'\boldsymbol{r}'^\dagger + \boldsymbol{t}\boldsymbol{t}^\dagger &= \boldsymbol{t}'^\dagger\boldsymbol{t}' + \boldsymbol{r}'^\dagger\boldsymbol{r}' = \mathbf{1}_{N_R} \\
\boldsymbol{r}\boldsymbol{t}^\dagger + \boldsymbol{t}'\boldsymbol{r}'^\dagger &= \boldsymbol{r}^\dagger\boldsymbol{t}' + \boldsymbol{t}^\dagger\boldsymbol{r}' = \mathbf{0}_{N_L\times N_R}
\end{aligned}$$

Time Reversal Symmetry

We shall now discuss briefly the influence of a magnetic field, which breaks time reversal invariance, onto the S-matrix of a quantum system. Consider the Hamiltonian for a charged particle in a magnetic field:

$$\hat{H}_B = \frac{1}{2m}(\mathbf{p} - q\mathbf{A})^2 + V(\boldsymbol{r}) = \frac{1}{2m}[\hat{\boldsymbol{p}} + |e|\boldsymbol{A}(\boldsymbol{r})]^2 + V(\boldsymbol{r}), \tag{2.32}$$

where the relation between the magnetic induction and the vector potential is $\mathbf{B} = \nabla \times \mathbf{A}$.

The scattering states satisfy the Schrödinger equation:

$$\hat{H}_B \psi(\boldsymbol{r}) = E\psi(\boldsymbol{r}),$$

with the incoming ($\boldsymbol{a}$) and the outgoing ($\boldsymbol{b}$) amplitudes related by the scattering matrix

$$\mathbf{b} = \mathbf{S_B a}.$$

Under time reversal, the Hamiltonian is transformed as $\hat{\mathcal{T}}^{-1}\hat{H}_B\hat{\mathcal{T}} \equiv \hat{H}_{-B}$ and its eigentstaes are $\psi^*(\boldsymbol{r}) = \hat{\mathcal{T}}\psi(\boldsymbol{r})$, where $\mathcal{T}$ is the time-reversal operator. In short, if $\Psi_{\mathbf{B}}(\mathbf{r})$ is a solution so is $\Psi^*_{-\mathbf{B}}(\mathbf{r})$. Therefore, we can construct new eigenstates by complex conjugation followed by the reversal of the magnetic field. Time reversal changes the direction of propagation, so the incoming and the outgoing amplitudes of ψ^* are given by $\boldsymbol{b}^*$ and $\boldsymbol{a}^*$, respectively, with

$$\boldsymbol{a}^* = \boldsymbol{S}_{-B}\boldsymbol{b}^*,$$

$$\boldsymbol{a}^* = \mathbf{S}_{-\mathrm{B}}\boldsymbol{b}^* \Rightarrow \boldsymbol{a}^* = \mathbf{S}_{-\mathrm{B}}\mathbf{S}^*_{\mathrm{B}}\boldsymbol{a}^*. \tag{2.33}$$

This shows that:

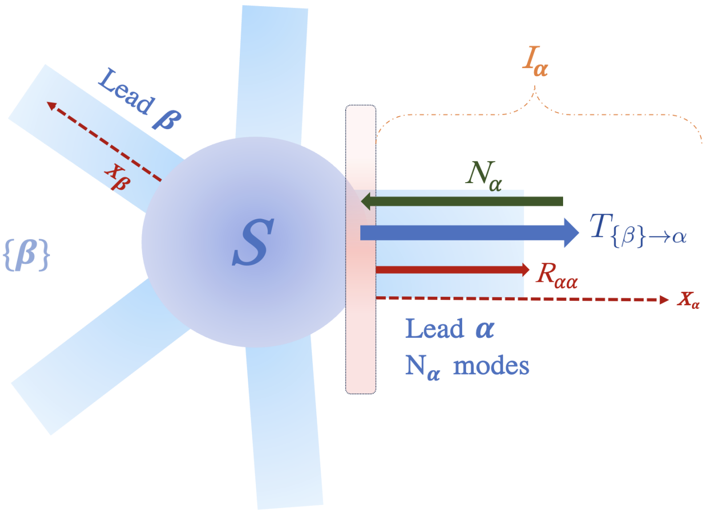

FIGURE 2.5: Representation of a multi-terminal system, where α, β denote the leads, N_α represents the total number of channels in lead α, $T_{\{\beta\}\to\alpha}$ is the transmission probability from all leads $\{\beta\}$ to lead α and $R_{\alpha\alpha}$ represent the reflections back into lead α. Each lead has its own coordinate system and x_α is perpendicular to the cross section of the lead and points away from the scattering region.

$$\mathbf{S}_{-\mathbf{B}}\mathbf{S}^*_{\mathbf{B}} = \mathbf{1} \quad \Rightarrow \quad \mathbf{S}^*_{-\mathbf{B}} = \mathbf{S}^\dagger_{\mathbf{B}} \quad \Rightarrow \quad \mathbf{S}_{\mathbf{B}} = \mathbf{S}^T_{-\mathbf{B}}. \tag{2.34}$$

For $\boldsymbol{B} = 0$ the system is invariant under time reversal (in commutator language this translates to $\left[\hat{H}_{\mathbf{B}=0}, \hat{\mathcal{T}}\right] = 0$), and the S-matrix is symmetric:

$$\mathbf{S}_{\mathbf{B}=0} = \mathbf{S}^T_{\mathbf{B}=0}.$$

Generalization to multi-terminal systems

Many applications of coherent transport rely on multi-terminal devices, so in this section we outline the generalization of formula 2.4 to a case where there are multiple leads connected to the scattering region. Consider that an electron is injected in the system through lead α, mode m and the total number of modes in this particular lead is denoted by N_α. By making use of the S-matrix defined in the previous section, the scattering state in lead α can be written as [9]:

$$\begin{aligned}\psi^{(\alpha)}_{\alpha m} &= \phi^+_{\alpha m, k_m}(x_\alpha, y) + \sum_n^{N_\alpha} s_{\alpha n, \alpha m}\phi^-_{\alpha m, k_m}(x_\alpha, y) \\ &= \sum_n^{N_\alpha} \delta_{mn}\phi^+_{\alpha m, k_m}(x_\alpha, y) + \sum_n^{N_\alpha} s_{\alpha n, \alpha m}\phi^-_{\alpha m, k_m}(x_\alpha, y),\end{aligned} \tag{2.35}$$

where $s_{\alpha n, \alpha m}$ is the reflection amplitude of mode m of lead α into mode n in the same lead. In lead, β, the wavefunction is:

$$\begin{aligned}\psi^{(\alpha)}_{\alpha m} &= \sum_n^{N_\beta} s_{\alpha m, \beta n}\phi^-_{\beta n, k_n}(x_\beta, y) \\ &= \sum_n^{N_\beta} s_{\beta n, \alpha m} e^{ik_n x_\beta}\chi_{\beta, n}(y), \quad (x, y) \in \beta, \quad \beta \neq \alpha\end{aligned} \tag{2.36}$$

where $s_{\beta n,\alpha m}$ represents the transmission amplitude from mode m in lead α to mode n in lead β.

In order to compute the current in this multi-terminal case, we employ the same approach encountered in section 2.1.1. Consider that α is the lead of interest and the current is flowing through a cross section in this lead α, from the scattering region into the lead (see Figure 2.5). Hence, the current is written as:

$$\begin{aligned} I_\alpha &= -e\int dEg(E)v(E)\left[\sum_{\beta\neq\alpha,m,n}|s_{\alpha m,\beta n}|^2 f_\beta(E) + \sum_{m,n}|s_{\alpha n,\alpha m}|^2 f_\alpha(E) - \sum_{m}^{N_\alpha}\delta_{mn}f_\alpha(E)\right] \\ &= -e\int dEg(E)v(E)\left[\sum_{\beta,m,n}|s_{\alpha m,\beta n}|^2 f_\beta(E) - \sum_{\beta,m,n}\delta_{mn}\delta_{\alpha\beta}f_\beta(E)\right], \end{aligned} \tag{2.37}$$

where N_α is the total number of transverse modes in lead α.

In 1D, the density of states is:

$$g(E) = \frac{2}{hv(E)} = \frac{1}{\pi\hbar}\sqrt{\frac{2m}{E}}. \tag{2.38}$$

Therefore,

$$I_\alpha = g_s\frac{|e|}{h}\int_0^\infty \mathrm{d}E\sum_{\beta mn}\left\{\delta_{\alpha\beta}\delta_{mn} - \left|s_{\alpha n,\beta m}\right|^2\right\}f_\beta(E), \tag{2.39}$$

where g_s stanss for spin degeneracy. One can rewrite the equation above in a more physically transparent form, by separating the transmission and reflection coefficients:

$$\begin{aligned} \mathcal{R}_\alpha(E) &= \sum_{\substack{n,m \\ n,m\in\alpha}}\frac{k_n^\alpha(E)}{k_m^\alpha(E)}\left|r_{nm}^\alpha(E)\right|^2, \\ \mathcal{T}_{\alpha\beta}(E) &= \sum_{\substack{n \\ n\in\alpha}}\sum_{m}\frac{k_n^\alpha(E)}{k_m^\beta(E)}\left|t_{nm}^{\alpha\beta}(E)\right|^2, \end{aligned} \tag{2.40}$$

$$I_\alpha = g_s\frac{|e|}{h}\int dE\{[N_\alpha(E) - \mathcal{R}_\alpha(E)]\,f_\alpha(E) - \sum_{\substack{\beta \\ \beta\neq\alpha}}\mathcal{T}_{\alpha\beta}(E)f_\beta(E)\}. \tag{2.41}$$

Notice that the reflection and transmission coefficients satisfy the following condition:

$$N_\alpha(E) = \mathcal{R}_\alpha(E) + \sum_\beta \mathcal{T}_{\alpha\beta}(E), \tag{2.42}$$

which is the generalization of $R + T = 1$ for a system of two single mode leads.

In the linear response approximation, equation 2.41 can be expressed as:

$$\begin{aligned} I_\alpha &= g_s \cdot \frac{|e|}{h} \sum_\beta \int dE \mathcal{T}_{\alpha\beta}(E) \left(\frac{\partial f_\alpha(E)}{\partial E} \right) (\mu_\beta - \mu_\alpha) \\ &= \sum_\beta G_{\alpha\beta} \cdot \left(\frac{\mu_\alpha}{-|e|} - \frac{\mu_\beta}{-|e|} \right) \\ \Rightarrow I_\alpha &= \sum_{\substack{\beta \\ \beta\neq\alpha}} G_{\alpha\beta} \cdot (V_\beta - V_\alpha) \,, \end{aligned} \tag{2.43}$$

where $G_{\alpha\beta}$ are the conductance matix elements, identified as:

$$G_{\alpha\beta} = g_s \frac{e^2}{h} \int dE \mathcal{T}_{\alpha\beta}(E) \left(\frac{-\partial f_\alpha(E)}{\partial E} \right). \tag{2.44}$$

2.2 Green's functions

2.2.1 Formal definition

A Green's function is the solution of a linear differential equation with a Dirac delta source with homogeneous boundary conditions [10]:

$$\mathcal{L} G\left(x, x'\right) = \delta\left(x - x'\right), \tag{2.45}$$

where $\mathcal{L}$ is a general linear operator and $\delta(x)$ is the well-known delta Dirac distribution:

$$\delta\left(x - x'\right) = \begin{cases} \infty, & \text{at } x = x' \\ 0, & \text{otherwise} \end{cases} \tag{2.46}$$

Let us take a brief look at one simple example from electromagnetism, namely the Poisson equation:

$$\nabla^2 \phi(\boldsymbol{x}) = -\frac{\rho(\boldsymbol{x})}{\epsilon_0}, \tag{2.47}$$

which for a point charge of magnitude unity, located at $\boldsymbol{x}'$, reads:

$$\epsilon_0 \nabla^2 \phi(\boldsymbol{x}) = -\delta(\boldsymbol{x} - \boldsymbol{x}').$$

The potential ϕ that solves this equation is:

$$\phi(\boldsymbol{x}) = \frac{1}{4\pi\epsilon_0 |\boldsymbol{x} - \boldsymbol{x}'|}, \tag{2.48}$$

therefore

$$\nabla^2 \left[\frac{1}{4\pi |\boldsymbol{x} - \boldsymbol{x}'|} \right] = -\delta(\boldsymbol{x} - \boldsymbol{x}'), \tag{2.49}$$

and the Green's function is:

$$G(\boldsymbol{x}, \boldsymbol{x}') = -\frac{1}{4\pi |\boldsymbol{x} - \boldsymbol{x}'|}. \tag{2.50}$$

Green's functions can be employed in an important class of problems, known as Sturm–Liouville problems, which are second-order linear differential equations that define an eigenvalue problem that reads:

$$\mathcal{L}\varphi = \lambda\varphi. \tag{2.51}$$

The study of the eigenvalues and eigenfunctions of this type of equation became of great importance in the realm of quantum mechanics also, and Green's functions allowed for the conversion of a differential problem to an integral form. From the set of eigenvalues, the Green's functions could now be built as a spectral expansion [10].

2.2.2 Green's functions as propagators

Let us consider the fundamental cases of time dependent and independent Schrodinger equations and follow the basic theory of Green's functions applied to quantum mechanical systems.

We begin with the single-particle Hamiltonian:

$$\mathcal{H} = \underbrace{-\frac{\hbar^2}{2m}\nabla^2}_{\mathcal{H}_0} + \underbrace{V(\mathbf{r})}_{\hat{V}}. \tag{2.52}$$

We can write the time dependent Schrodinger equations for the interacting system and for the non-interacting system as well:

$$\begin{aligned} \mathrm{i}\hbar\frac{\partial|\Psi(t)\rangle}{\partial t} &= \hat{H}|\Psi(t)\rangle = \left(\hat{H}_0 + \hat{V}\right)|\Psi(t)\rangle, \\ \mathrm{i}\hbar\frac{\partial\,|\Psi_0(t)\rangle}{\partial t} &= \hat{H}_0\,|\Psi_0(t)\rangle\,. \end{aligned} \tag{2.53}$$

Notice that the equations above have the general form:

$$\hat{\mathcal{L}}\psi(t) = f(t), \tag{2.54}$$

where

$$\begin{aligned} \hat{\mathcal{L}} &= \mathrm{i}\hbar\frac{\partial}{\partial t} - \hat{H}, \\ \hat{\mathcal{L}} &= \mathrm{i}\hbar\frac{\partial}{\partial t} - \hat{H}_0. \end{aligned} \tag{2.55}$$

From the fundamental theory of Green's functions discussed above, we know that $\hat{G}(t)$ satisfy the following equation:

$$\hat{\mathcal{L}}\hat{G}(t) = \mathbf{1}\delta(t). \tag{2.56}$$

For the Schrodinger equations in 2.53, there are two types of Green's functions that encompass a full description of the state vector:

$$\left(\mathrm{i}\hbar\frac{\partial}{\partial t} - \hat{H}\right)\hat{G}^{a,r}(t) = \hat{1}\delta(t), \tag{2.57}$$

where

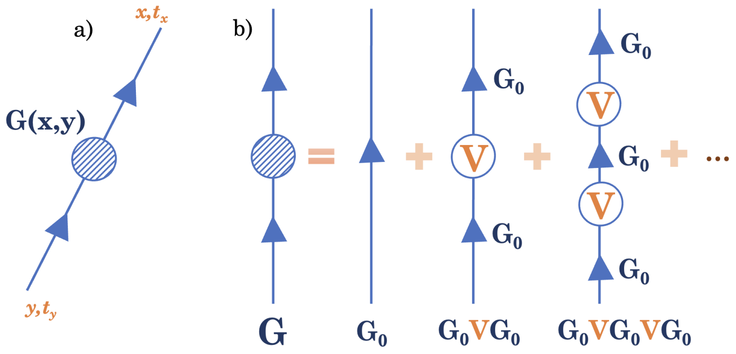

FIGURE 2.6: (a) Pictorial representation of the full propagator. Propagators can be considered the building blocks of Feynman diagrams. (b) The full propagator as a sum of all the scattering processes ((adapted from [11]))

$$\begin{cases} \hat{G}^r(t) = 0 & t > 0, \quad \text{retarded,} \\ \hat{G}^a(t) = 0 & t < 0, \quad \text{advanced.} \end{cases} \tag{2.58}$$

A good solution is:

$$\hat{G}^r(t) = \begin{cases} -\frac{\mathrm{i}}{\hbar} e^{-\mathrm{i}\hat{H}t/\hbar} & t > 0, \\ 0 & t < 0, \end{cases} \tag{2.59}$$

Therefore, in the case of a time independent Hamiltonian, the retarded Green's function is actually proportional to the time evolution operator and it directly relates the state vector $|\Psi(t_0)\rangle$ to $|\Psi(t)\rangle$ at a time $t > t_0$:

$$|\Psi(t)\rangle = \mathrm{i}\hbar\hat{G}^r(t - t_0)\,|\Psi(t_0)\rangle\,, \tag{2.60}$$

and for this reason, the retarded Green's function is also known as a propagator. Moving further with the calculations, we obtain:

$$\begin{gathered} \left(\mathrm{i}\hbar\frac{\partial}{\partial t} - \hat{H}_0\right)\hat{G}_0^{a,r}(t) = \hat{1}\delta(t), \\ \Rightarrow \left(\mathrm{i}\hbar\frac{\partial}{\partial t} - \hat{H}_0\right) = \hat{1}\delta(t)\left[\hat{G}_0^{a,r}(t)\right]^{-1}. \end{gathered} \tag{2.61}$$

Similarly,

$$\left(\mathrm{i}\hbar\frac{\partial}{\partial t} - \hat{H}_0 - \hat{V}\right)\hat{G}^{a,r}(t) = \hat{1}\delta(t), \tag{2.62}$$

therefore:

$$\hat{1}\delta(t)\left[\hat{G}_0^{a,r}(t)\right]^{-1}\hat{G}^{a,r}(t) - \hat{V}\hat{G}^{a,r}(t) = \hat{1}\delta(t). \tag{2.63}$$

Now we multiply to the left with $\hat{G}_0^{a,r}$:

$$\hat{1}\delta(t)\hat{G}^{a,r}(t) = \hat{1}\delta(t)\hat{G}_0^{a,r}(t) + \hat{G}_0^{a,r}(t)\hat{V}\hat{G}^{a,r}(t). \tag{2.64}$$

By integrating the equation above from t_0 to t we obtain the Lippmann-Schwinger equation for the retarded Green's function:

$$\hat{G}^r(t - t_0) = \hat{G}_0^r(t - t_0) + \int_{t_0}^{t} dt'\hat{G}_0^r(t - t')\,\hat{V}\hat{G}^r(t' - t_0)\,. \tag{2.65}$$

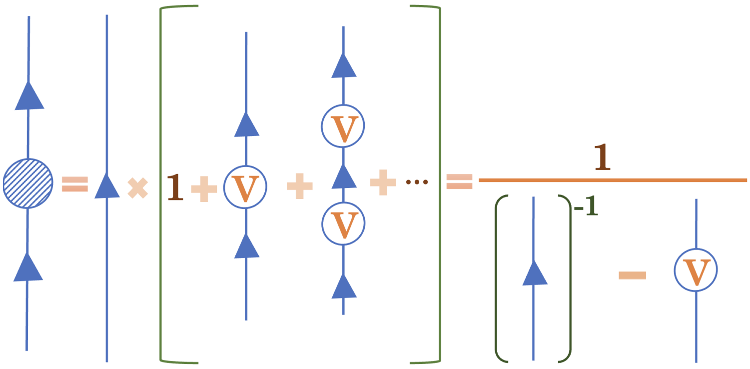

FIGURE 2.7: Dyson's equation in graphical form (adapted from [11]).

We can rewrite equation 2.65 in a manner that encapsulates the essence of perturbation theory and the diagrammatic approach of quantum field theory. We can replace the retarded Green's function in the integral with the formula we obtained from the Lippman-Schwinger equation and do that recursively to obtain an expansion for the full Green's function.

$$\hat{G}^r\left(t-t_0\right) = \hat{G}_0^r\left(t-t_0\right) + \int_{t_0}^{t} dt' \hat{G}_0^r\left(t-t'\right) \hat{V} \underbrace{\hat{G}^r\left(t'-t_0\right)}_{=\hat{G}_0^r(t-t_0)+\dots} \tag{2.66}$$

$$\begin{aligned} \Rightarrow \hat{G}^r\left(t-t_0\right) =& \hat{G}_0^r\left(t-t_0\right) + \int_{t_0}^{t} dt' \hat{G}_0^r\left(t-t'\right) \hat{V} \hat{G}_0^r\left(t'-t_0\right) \\ &+ \int_{t_0}^{t} dt' \int_{t_0}^{t'} dt'' \hat{G}_0^r\left(t-t'\right) \hat{V} \hat{G}_0^r\left(t'-t''\right) \hat{V} \hat{G}_0^r\left(t''-t_0\right) + \cdots \end{aligned} \tag{2.67}$$

This is also known as *Dyson's equation* (see Figure 2.6). If the series converges, we can consider the interaction side as only one term, known as self energy:

$$\begin{aligned} \hat{G}^r\left(t-t_0\right) =& G_0^r\left(t-t_0\right) \\ &+ \int_{t_0}^{t} dt' \int_{t_0}^{t'} dt'' \hat{G}_0^r\left(t-t'\right) \hat{\Sigma}^r\left(t'-t''\right) \hat{G}^r\left(t''-t_0\right). \end{aligned} \tag{2.68}$$

In order to visualize this in a more intuitive manner, let us represent the Green's function in a symbolic matrix way, directly from 2.57:

$$\hat{G} = \frac{1}{E-\hat{H}}. \tag{2.69}$$

Therefore, the full propagator can be expressed as:

$$\begin{aligned} G =& \frac{1}{E-H_0-V} = \frac{1}{E-H_0} + \frac{1}{E-H_0} V \frac{1}{E-H_0} \\ &+ \frac{1}{E-H_0} V \frac{1}{E-H_0} V \frac{1}{E-H_0} + \dots, \end{aligned} \tag{2.70}$$

where we have used the following matrix identity:

$$\frac{1}{A+B} = \frac{1}{A} - \frac{1}{A}B\frac{1}{A} + \frac{1}{A}B\frac{1}{A}B\frac{1}{A} - \dots.$$

This brings us directly to the Dyson equation in the form:

$$G = G_0 + G_0VG_0 + G_0VG_0VG_0 + \dots \tag{2.71}$$

$$\begin{aligned} G &= G_0\left(1 + VG_0 + VG_0VG_0 + \dots\right) \\ \Rightarrow G &= \frac{G_0}{1 - VG_0} = \frac{1}{G_0^{-1} - V}. \end{aligned} \tag{2.72}$$

Through Dyson's equation, the complex perturbation problem, involving an infinite series of terms, can be turned into an intuitive picture of particle scattering (see Figure 2.7). The perturbation V is thought of as a scattering process that interrupts the free propagation.

2.3 Topological phenomena in condensed matter physics

2.3.1 The Quantum Hall Effect and the birth of topological band theory

The first experiment showcasing the quantum Hall effect was realized in 1980 by Klaus von Klitzing and it lead to him being awarded the Nobel Prize 5 years later [12]. The experiment was conducted on a Si MOSFET at very low temperatures ($T \approx 1$ K, achieved using liquid Helium) and strong magnetic fields of over 10 Tesla. The original results and the device setup are shown in Figure 2.8 and one notices immediately that both the Hall and longitudinal resistivity exhibit a striking behaviour. The Hall resistivity remains on a perfect plateau for a set of values of the magnetic field, where it takes integer values that depend only on fundamental constant:

$$\rho_{xy} = \frac{2\pi\hbar}{e^2}\frac{1}{n}, \quad n \in \mathbf{N}. \tag{2.73}$$

Also, while ρ_{xy} sits on a plateau, the longitudinal resistivity is null and it spikes only when ρ_{xy} jumps to the next plateau [13]. Understanding this unprecedented behaviour requires some fundamental quantum mechanics notions about charged particles in a magnetic field. The Hamiltonian describing such a system is:

$$H = \frac{1}{2m}(\mathbf{p} + e\mathbf{A})^2. \tag{2.74}$$

Let us now assume that electrons are restricted to the 2D plane and the magnetic field is constant and perpendicular to it, such that $\nabla \times \mathbf{A} = B\hat{\mathbf{z}}$. If we work in the Landau gauge, we can choose the vector potential to be $\mathbf{A} = xB\hat{\mathbf{y}}$, hence the Hamiltonian becomes:

$$H = \frac{1}{2m}\left(p_x^2 + \left(p_y + eBx\right)^2\right). \tag{2.75}$$

Notice that the vector potential breaks translational symmetry in the x direction. Taking this into consideration, we employ the following form for the eigenfunctions of the quantum system:

$$\psi_k(x, y) = e^{iky}f_k(x). \tag{2.76}$$

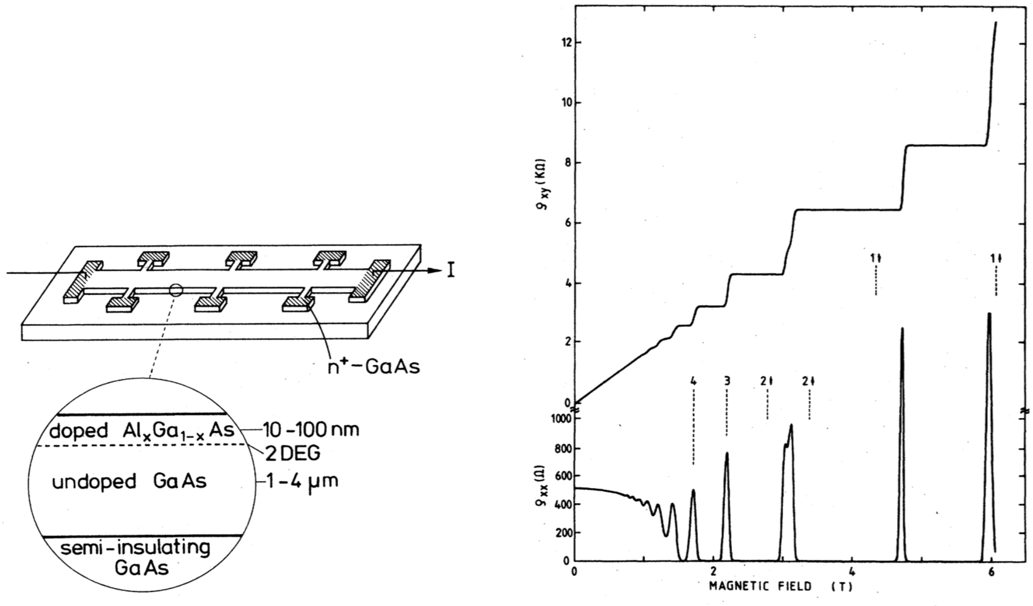

(A) (B)

FIGURE 2.8: (A) Experimental setup for the measurements in the Quantum Hall effect. (B) Experimental curves for the Hall resistance $R_H = \rho_{xy}$ and the resistivity $\rho_{xx} \sim R_x$ as a function of the magnetic field, at $V_g = 0$ V and $T \approx 8$ mK (reproduced with permission from Physical Review B [12]).

After some mathematical gymnastics detailed in [13], we reach the conclusion that the system Hamiltonian is actually the same Hamiltonian that describes harmonic oscillator with a shifted center:

$$H_k = \frac{1}{2m} p_x^2 + \frac{m\omega_B^2}{2} \left(x + k l_B^2\right)^2 \tag{2.77}$$

where $\omega_B = eB/m$ is the cyclotron frequency and $l_B = \sqrt{\frac{\hbar}{eB}}$ is known as magnetic length. The conclusion is that a charged particle confined to a 2D plane in a perpendicular magnetic field will display quantized energy levels known as Landau levels. This gives us a way to understand the behaviour of the quantized Hall conductance in Figure 2.8. If n Landau levels are completely filled at a given chemical potential (Fermi energy), the transverse Hall resistivity is $\rho_{xy} = \frac{2\pi\hbar}{e^2}\frac{1}{n}$. The longitudinal resistivity vanishes because since the transport along the chiral edge states does not allow for dissipation of energy in the bulk.

The QHE can even be described through a classical approach, since, due to the Lorentz force, electrons gain circular trajectories. In the bulk regions, the electrons go full circle, while at the edges they hit the margin repeatedly forming the so called "skipping orbits".

Both the Integer Quantum Hall Effect and its fractional counterpart are compelling examples of how the edges of a mesoscopic system can lead to interesting new states and phases in condensed matter physics. These effects have paved the way for new and intriguing fields, both from a theoretical and experimental perspective, in particular the topological aspects of band theory. As Klaus von Klitzing said:

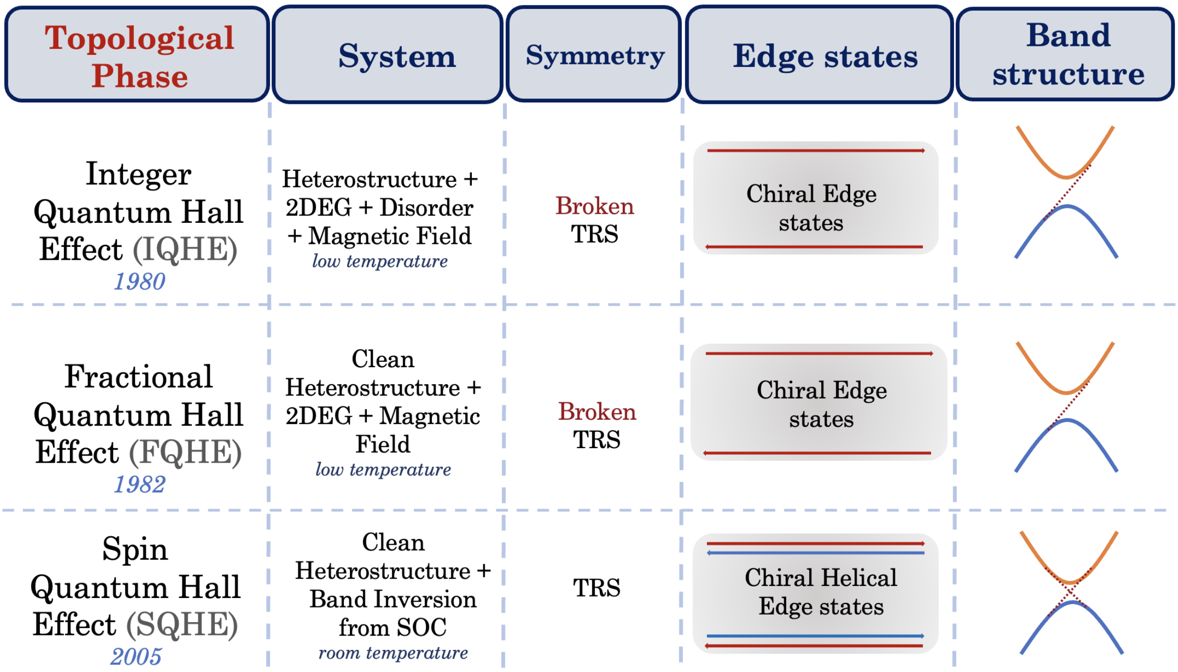

Topological Phase	**System**	**Symmetry**	**Edge states**	**Band structure**
Integer Quantum Hall Effect (IQHE) *1980*	Heterostructure + 2DEG + Disorder + Magnetic Field *low temperature*	Broken TRS	Chiral Edge states	
Fractional Quantum Hall Effect (FQHE) *1982*	Clean Heterostructure + 2DEG + Magnetic Field *low temperature*	Broken TRS	Chiral Edge states	
Spin Quantum Hall Effect (SQHE) *2005*	Clean Heterostructure + Band Inversion from SOC *room temperature*	TRS	Chiral Helical Edge states	

FIGURE 2.9: Overview of the topological phases mentioned in this thesis.

> *"This unexpected direction is an excellent demonstration of how basic research on a practical device can open up a completely new field of research with new theories and unforeseeable applications — a real quantum leap"* (Klaus von Klitzing [14])

2.3.2 Topological phases of matter

Before the discovery of the QHE, phases in condensed matter were described by means of the Landau-Ginzburg theory of phase transitions. Symmetry was already recognized as a fundamental tenet of theoretical physics and a particular phase of the system was characterized by a local order parameter, such as magnetization. The QHE was the first instance of a quantum phase emerging without the breaking of a local symmetry, but rather a global symmetry of the system. Global symmetry is not dependent on the geometry of the system and is also robust to perturbations, as opposed to local symmetry. In the particular case of the QHE, the edge states are a consequence of the breaking of time reversal symmetry (TRS) due to the perpendicular magnetic field applied to the 2D device. This experiment and the fundamental theoretical implications it brought along have prompted further research into this novel field of condensed matter – topological band theory. Multiple other topological phases were discovered subsequently, some of them being exemplified in Figure 2.9.

In mathematics, topology is an area which deals with abstract spaces and studies mathematical structures that are insensitive to smooth deformations. Take the example illustrated in Figure 2.10, with a pie (disk shaped) and a doughnut (shaped like a torus). The disk cannot be smoothly deformed into the surface of a doughnut and they are actually distinguished by an integer called the genus, g. The genus is basically the number of holes in the surface. Surfaces with different genus cannot be deformed into one another, and are considered to be topologically distinct [15].

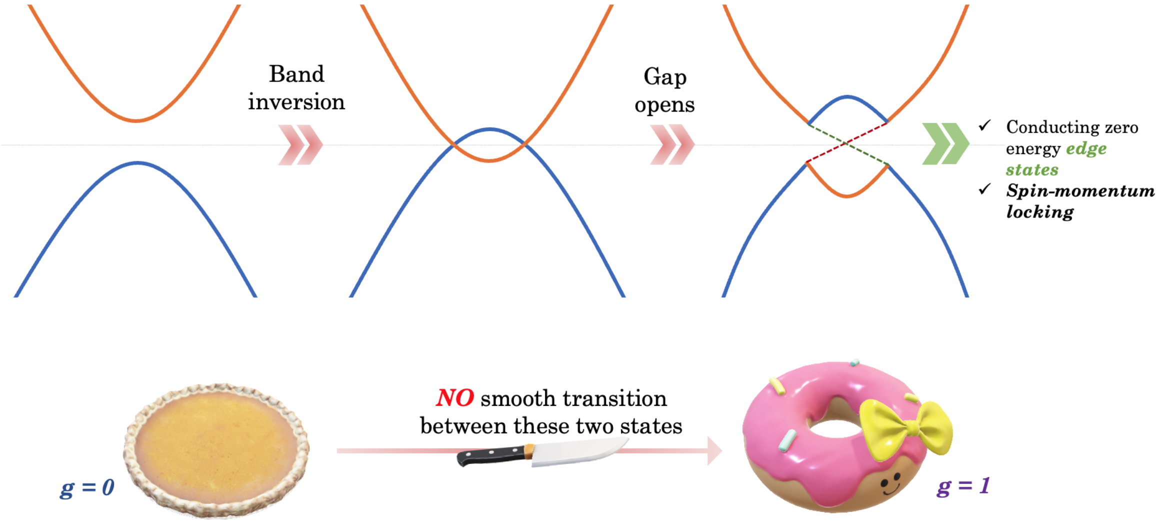

FIGURE 2.10: (a) Schematic representation of the band inversion mechanism in topological insulators (b) Pictorial representation of two topologically distinct surfaces, that cannot be deformed into one another, just as two topological phases are distinct through the values of their topological invariant.

Meanwhile, a doughnut and a coffee cup are equivalent and could not be distinguished from a topological perspective. The rigorous term for topological equivalence is *homeomorphism*. Also, a property of the topological spaces that are conserved under a homeomorphism is called a **topologial invariant**. In the simple example we gave, the topological invariant is the genus of the geometrical shapes.

For a more extensive review of the topological phases, which do not enter the scope of this thesis, we recommend referring to [16].

2.3.3 Quantum Spin Hall effect and the BHZ model

The first experimentally discovered two-dimensional topological insulator was the CdTe/HdTe/CdTe quantum well. CdTe has the band structure of a normal semiconductor, with the valence band (Γ_8, originating from p-type bands) is separated by an energy gap from the conduction band Γ_6 (originating from $s-$ type bands). However, bulk HgTe displays an inverted bandstructure, with the Γ_8 bands above the Γ_6 bands. Basically, an electron like band becomes a hole-like band.

The fundamental source of the band inversion mechanism in HgTe has been known for decades and attributed to high spin-orbit splitting in Te and relativistic corrections to the energy levels in Hg [17]. Usually, this mechanism may occur in narrow band-gap semiconductors, with strong SOC and heavy atoms. Since materials suitable for topological insulators (TIs) are of great interest recently, more comprehensive research was done on this subject, employing both new experimental techniques (angle-resolved photoelectron spectroscopy, ARPES) and density functional theory DFT based calculations [18]. When the middle layer of HgTe is below a critical thickness d_c, the energy bands are normally ordered, like the ones of CdTe. However, above d_c, the bands are expected to align in the inverted regime. The transition between these two phases occurs at $d_c \approx 6.3\,nm$, so the experimental process is essential in the fabrication of this type of TIs [19].

Bernevig, Hughes and Zhang introduced an effective 4-band model that describes the CdTe/HdTe/CdTe quantum well near the Γ point [19]. Firstly, the Hamiltonian for the 2D TI model has to preserve time reversal symmetry intact. Before diving into the other structural details of the BHZ Hamiltonian, we can check that the simplest manner to define a time reversal invariant model is to double the Hilbert space and work with a Hamiltonian of the form:

$$\mathcal{H}(\mathbf{k}) = \begin{bmatrix} H(\mathbf{k}) & 0 \\ 0 & H^*(-\mathbf{k}) \end{bmatrix} = \frac{1+\sigma_z}{2} H(\mathbf{k}) + \frac{1-\sigma_z}{2} H^*(-\mathbf{k}) \tag{2.78}$$

We can easily check that the Hamiltonian defined above preserves time reversal invariance:

$$\begin{aligned} (i\sigma_y K)\, \mathcal{H}(\mathbf{k})\, (i\sigma_y K)^{-1} &= \begin{bmatrix} 0 & 1 \\ -1 & 0 \end{bmatrix} \cdot \begin{bmatrix} H^*(-\mathbf{k}) & 0 \\ 0 & H(\mathbf{k}) \end{bmatrix} \cdot \begin{bmatrix} 0 & -1 \\ 1 & 0 \end{bmatrix} \\ &= \begin{bmatrix} 0 & H(\mathbf{k}) \\ -H^*(-\mathbf{k}) & 0 \end{bmatrix} \cdot \begin{bmatrix} 0 & -1 \\ 1 & 0 \end{bmatrix} = H_2(\mathbf{k}) \end{aligned} \tag{2.79}$$

The main symmetry considerations are the following [20]:

- In the presence of time reversal symmetry, each state must be doubly degenerate according to Kramers theorem. We can order the subbands as $|E_1, j_z = +\frac{1}{2}\rangle$, $|H_1, j_z = +\frac{3}{2}\rangle$, $|E_1, j_z = -\frac{1}{2}\rangle$, $|H_1, j_z = -\frac{3}{2}\rangle$, where $|E\pm\rangle$ and $|H\pm\rangle$ are Kramers partners. The states labeled with $+$ are usually referred to as the spin-up, since they have positive total angular momentum projection, while the $-$ states are reffered to as spin-down.
- $|E_1\pm\rangle$ and $|H_1\pm\rangle$ have different parity, since they originate from s-like and p-like bands. Therefore, the states are connected by matrix elements that are odd under the parity transformation.

The BHZ Hamiltonian has the following form in the basis $|E_1, j_z = +\frac{1}{2}\rangle$, $|H_1, j_z = +\frac{3}{2}\rangle$, $|E_1, j_z = -\frac{1}{2}\rangle$, $|H_1, j_z = -\frac{3}{2}\rangle$:

$$\mathcal{H}_{BHZ} = \begin{pmatrix} \epsilon_{\mathbf{k}} + M_{\mathbf{k}} & Ak_+ & 0 & 0 \\ Ak_- & \epsilon_{\mathbf{k}} - M_{\mathbf{k}} & 0 & 0 \\ 0 & 0 & \epsilon_{\mathbf{k}} + M_{\mathbf{k}} & -Ak_- \\ 0 & 0 & -Ak_+ & \epsilon_{\mathbf{k}} - M_{\mathbf{k}} \end{pmatrix}, \tag{2.80}$$

where we have defined the following quantities:

$$\begin{cases} \epsilon_{\mathbf{k}} = C - D\left(k_x^2 + k_y^2\right) \\ M_{\mathbf{k}} = M - B\left(k_x^2 + k_y^2\right) \\ k_{x,y} = -i\partial_{x,y} \\ k_\pm = k_x \pm ik_y \end{cases} \tag{2.81}$$

The quantities A, B, C, D and M are model parameters. When $sgn(M) = sgn(B)$ the system is in a non-trivial topological phase. The exact solutions of the BHZ Hamiltonian were derived by Zhou *et al.* [21]. In the calculations, they considered a semi-infinite plane with open boundary conditions at $y = 0$ and translationa invariance along the x direction. This assumption implies that k_x is a good quantum

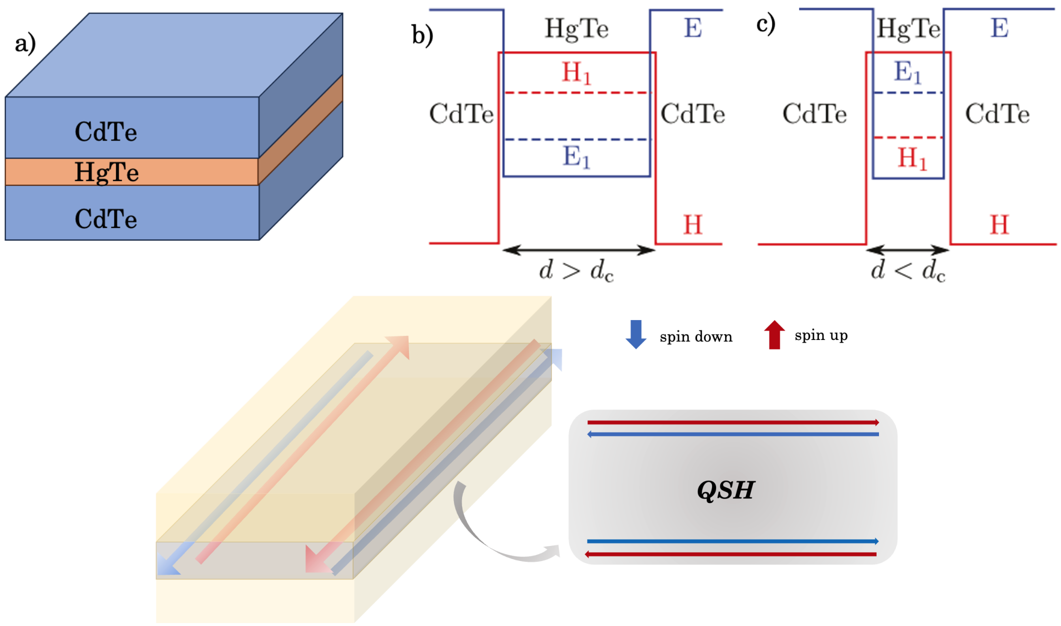

FIGURE 2.11: (a) Schematic representation of the design of a HgTe TI (b) Band arrangement when d is larger than the critical d_c and (c) the band inversion that brings the material in a non-trivial topological phase (d) Pictorial representation of the spin Quantum Hall helical edge states.

number for the system, while for k_y we make the substituion $k_y \Rightarrow -i\partial_y$. Since The BHZ Hamiltonian has a block diagonal form imposed by its underlying symmetries

$$\mathcal{H}\left(k_x, -i\partial y\right) = \begin{pmatrix} h(k) & 0 \\ 0 & h^*(-k) \end{pmatrix},$$

it is possible to solve the eigenvalue problem for one block $h(k) \equiv h(k)^{\uparrow}$ and obtain the other spinor by applying a time reversal symmetry operation. The trial wavefunction employed to solve the eigenvalue problem has the form:

$$\Psi_{\uparrow}(k_x, y) = \begin{pmatrix} \Phi^1_{\uparrow} \\ \Phi^2_{\uparrow} \end{pmatrix} e^{k_x x} e^{\lambda y}.$$

If λ is real and positive, the wavefunction decays to zero as one moves further from the boundary of the system. This condition is achieved in the topological phase, when $M/B > 0$. Since B is usually a negative material parameter, if $M < 0$ the system will display helical edge states. The edge states are known as helical because one of their defining feature is that they are orthogonal eigenstates of the helicity operator [22]. For this reason, the edge states that emerge in a QSHE system present spin-momentum locking.

Reminder 1: Symmetry operators

Time reversal symmetry operator:

$$\Theta = -i\left(\sigma_y \otimes \sigma_0\right)\mathcal{K}, \tag{2.82}$$

where $\mathcal{K}$ represents complex conjugation.
Inversion operator:

$$\mathcal{I}_{2D} = \sigma_z \otimes \sigma_0 \tag{2.83}$$

In order to account for spin-orbit interaction in a topological insulator, one may add a linear Rashba term that breaks inversion symmetry and couples the $|E_1, j_z = \pm\frac{1}{2}\rangle$ has the following form [23]:

$$\mathcal{H}_R = \begin{pmatrix} 0 & 0 & -i\alpha_R k_- & 0 \\ 0 & 0 & 0 & 0 \\ i\alpha_R k_+ & 0 & 0 & 0 \\ 0 & 0 & 0 & 0 \end{pmatrix}. \tag{2.84}$$

Notice that $\mathcal{H}_R(k) \neq \mathcal{I}_{2D}\mathcal{H}_R(-k)\mathcal{I}_{2D}$. Also, the bulk inversion asymmetry (BIA) term can be introduced as [24]:

$$\mathcal{H}_{\text{BIA}} = \begin{pmatrix} 0 & 0 & 0 & -\Delta \\ 0 & 0 & \Delta & 0 \\ 0 & \Delta & 0 & 0 \\ -\Delta & 0 & 0 & 0 \end{pmatrix}, \tag{2.85}$$

where Δ is a material parameter. The BIA term couples the two spin channels and breaks S_z symmetry. Rashba SOI is also a source of axial spin symmetry breaking.

Zeeman coupling can be added to a BHZ model through the Hamiltonian [25] (supplementary material):

$$\mathcal{H}_Z = \mu_B \begin{pmatrix} g_1^{\perp} B_Z & 0 & g_1^{\parallel}\left(B_X - iB_Y\right) & 0 \\ 0 & g_2^{\perp} B_Z & 0 & g_2^{\parallel}\left(B_X + iB_Y\right) \\ g_1^{\parallel}\left(B_X + iB_Y\right) & 0 & -g_1^{\perp} B_Z & 0 \\ 0 & g_2^{\parallel}\left(B_X - iB_Y\right) & 0 & -g_2^{\perp} B_Z \end{pmatrix} \tag{2.86}$$

where $g_{1,2}^{\perp,\parallel}$ are longitudinal and transverse effective g-factors that depend on material characteristics.

To model ferromagnetic leads, one can add a Zeeman term to the Hamiltonian [23]:

$$\hat{V}_Z = H_0 \begin{pmatrix} 0 & 0 & e^{-i\theta} & 0 \\ 0 & 0 & 0 & 0 \\ e^{i\theta} & 0 & 0 & 0 \\ 0 & 0 & 0 & 0 \end{pmatrix}, \tag{2.87}$$

where H_0 is the strength of the magnetic field and θ is the in-plane magnetization angle between the leads.

3

Methodologies for quantum transport

3.1 Overview of density functional theory

Most of the physical and chemical properties of materials depend on an accurate calculation of the band structure of solids. However, the problem of determining the quantum states of a system with N electrons is extremely complex because it involves $3N$ Cartesian coordinates in the many-body wavefunction, $\Psi\left(\mathbf{r}_1, \mathbf{r}_2, \cdots, \mathbf{r}_N\right)$. Density functional theory (DFT) replaces the complicated interacting multi-electronic problem with a single particle problem of an electron in an effective potential. It has been successfully applied to determine electronic structures, binding energies, phonon spectra or forces for molecular dynamics simulations [26, 27]. As we shall discuss in this chapter, the essence of DFT is that you don't need to know the detailed form of the many-body wavefunction, since the electronic density is enough to determine all the relevant ground state properties. However, the downside is that the theory cannot tell specifically how ground state energy depends on the electronic density and one needs a set of approximations to express the system Hamiltonian as a functional of $n(\mathbf{r})$.

Density functional theory emerged in 1964 when Hohenberg and Kohn published their seminal paper [28], in which they introduced the theorems that remain, to this day, the pillars of all DFT-based approaches. The two theorems are presented in Theorem Box 3.1. While they may seem simple at first, the Hohenberg-Kohn theorems lead to an outstanding insight into the physics of a many-body system. We know from the fundamentals of quantum mechanics that the total energy E of a quantum system is:

$$E = \langle\Psi|\hat{H}|\Psi\rangle = \int d\mathbf{r}_1 \ldots d\mathbf{r}_N \Psi^*\left(\mathbf{r}_1, \ldots, \mathbf{r}_N\right) \hat{H} \Psi\left(\mathbf{r}_1, \ldots, \mathbf{r}_N\right) \tag{3.1}$$

The Hamiltonian in the expression above is a sum of all the kinetic energy terms and the interaction potentials involved in a multi-electronic system:

$$\hat{H}\left(\mathbf{r}_1, \mathbf{r}_2, \cdots, \mathbf{r}_N\right) = -\sum_i \frac{1}{2}\nabla_i^2 + \sum_i V_{\text{ext}}\left(\mathbf{r}_i\right) + \frac{1}{2}\sum_{i \neq j} \frac{1}{\left|\mathbf{r}_i - \mathbf{r}_j\right|}, \tag{3.2}$$

where V_{ext} is an external potential. It is obvious that any change in E must be associated with changes in the many-body wavefunction $\Rightarrow$ E is a functional of Ψ:

$$E = \mathcal{F}[\Psi] \tag{3.3}$$

Theorem 1: Hohenberg and Kohn theorems

Theorem I:
For any system of interacting particles in an external potential $V_{\text{ext}}(\mathbf{r})$, the potential $V_{\text{ext}}(\mathbf{r})$ is determined uniquely, except for a constant, by the ground state particle density $n_0(\mathbf{r})$.
Theorem II:
A universal functional for the energy $E[n]$ in terms of the density $n(\mathbf{r})$ can be defined, valid for any external potential $V_{\text{ext}}(\mathbf{r})$. For any particular $V_{\text{ext}}(\mathbf{r})$, the exact ground state energy of the system is the global minimum value of this functional, and the density $n(\mathbf{r})$ that minimizes the functional is the exact ground state density $n_0(\mathbf{r})$.

The first of the HK theorems goes even further and proves that if E is the lowest possible energy of the system (the energy of the ground state), then E is a *functional* of the electron density *only*:

$$E = \mathcal{F}[n(\mathbf{r})]$$

In the ground state, the electronic density uniquely determines the external potential of the nuclei V_{ext} ($n \rightarrow V_{\text{ext}}$). In any quantum state the external potential, V_{ext}, determines uniquely the many-electron wavefunction ($V_{\text{ext}} \rightarrow \Psi$) and total energy, E, is a functional of the many-body wavefunction ($\Psi \rightarrow E$). This result is highly relevant from a computational perspective, since is drastically reduces the dimension of the problem at hand.

$\Rightarrow$ *The energy of any quantum state is generally a functional of the entire wavefunction,* $\Psi(\mathbf{r}_1, \mathbf{r}_2, \cdots, \mathbf{r}_N)$*, which contains* $3N$ *variables, but the ground-state energy depends only on* $n(\mathbf{r})$*, which is a function of three variables only.*

3.1.1 The Kohn-Sham auxiliary system

The Hohenberg-Kohn theorems have guided condensed matter physicists in the right direction, but solving the many-body problem directly was still a futile endeavor. The solution was developed by Kohn and his post-doctoral student Sham [29]. The stroke of brilliance in their insight started with how they partitioned the energy terms and replaced the many-body system with an auxiliary single-electron system.

To explain this thoroughly, let's begin with the total energy of an interacting n-electron system in the Hartree-Fock approach:

$$E = E_{\text{kin}} + E_{\text{ext}} + E_{\text{H}} + E_{\text{x}} \tag{3.4}$$

In order to map the N-electron problem onto a simpler system of N non-interacting electrons, we need to find an equivalent description of the interacting terms of the Hamiltonian:

$$E_{kin} = E_{\text{kin}}^{\text{non}} + E_{\text{kin}}^{\text{int}}$$
$$E_{\text{H}} + E_{\text{x}} \rightarrow E_{\text{H}} + E_{\text{x}} + E_{\text{c}}^{\text{int}}$$

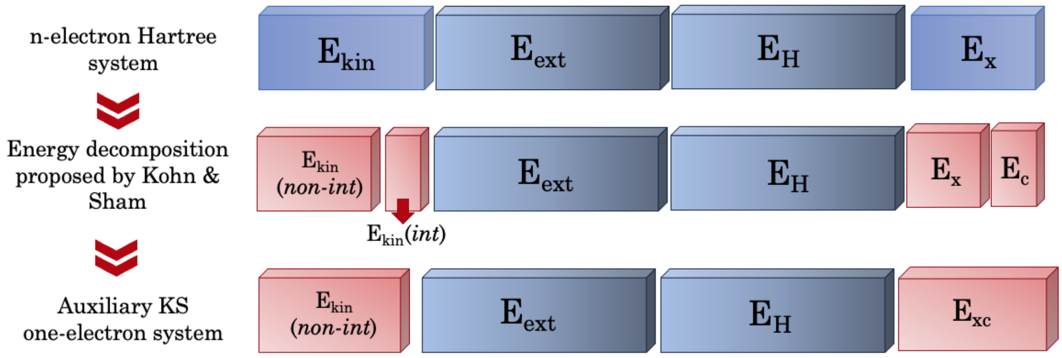

FIGURE 3.1: Energy partition scheme in the Kohn-Sham approach

Note that there is an energy term, called correlation energy (E_c^{int}) that is accounted for in this approach, but was neglected in the HF method. If we group all the interacting terms together as

$$E_{\text{xc}} = E_{\text{x}} + E_c^{int} + E_{kin}^{int} = E_{\text{x}} + E_{\text{c}}, \tag{3.5}$$

then we are left to only deal with a ubiquitous term called *exchange-correlation energy*. The terms E_{kin}^{int} and E_c^{int} are put together, since they both account for correlation effects [30] . The final expression of the Kohn-Sham Hamiltonian is therefore the following:

$$E = E_{kin}^{\text{non}} + E_{\text{ext}} + E_H + E_{xc} \tag{3.6}$$

Before we move on, let us discuss briefly the energy terms in the equations above.

Kinetic energy

In the interacting many body system, the kinetic energy term is formally expressed as:

$$E_{kin} = T = -\frac{1}{2}\int \Psi_i^*(\boldsymbol{r})\nabla_i^2\Psi_i(r)dr \tag{3.7}$$

In the non-interacting KS system, however, the kinetic energy can be expressed as a sum, in terms of the single-particle KS orbitals ϕ_i :

$$E_{\text{kin}}^{non} = -\frac{1}{2}\sum_{i=1}^{N}\phi_i^*(r)\nabla_i{}^2\phi_i(r)$$

This non-interacting kinetic energy accounts for most of the total kinetic energy, and the neglected parts are included in the exchange-correlation term, E_{xc}.

Coulomb interaction and the Hartree energy

Standing at the core of the well-known mean field approximation, the Hartree potential represents the electrostatic interaction between an electron at position r and the electron density at r':

$$U_H(\boldsymbol{r}) = \int \frac{\rho(\boldsymbol{r}')}{|\boldsymbol{r}-\boldsymbol{r}'|}d\boldsymbol{r}'$$

This potential can be easily determined in terms of the electron density, through the Poisson equation:

$$\nabla^2 U_H(r) = -4\pi\rho(r) \tag{3.8}$$

The Hartree energy can also be expressed as an expectation value, leading to the familiar (and very much classical) Coulombian electrostatic interaction:

$$E_H[\rho(r)] = \int U_H(\boldsymbol{r})\rho(\boldsymbol{r})d\boldsymbol{r} = \frac{1}{2}\iint \frac{\rho(\boldsymbol{r})\rho(\boldsymbol{r'})}{|\boldsymbol{r}-\boldsymbol{r'}|}d\boldsymbol{r}d\boldsymbol{r'}$$

The issue with this approach is that it describes an electron embedded in the electrostatic field of all electrons, including the reference electron itself. This causes the emergence of a self interaction which is erronous from a physical perspective. Fortunately, this self-interaction will be corrected by the exchange energy term, which we briefly discuss below.

Exchange and correlation energy

The exchange-correlation energy term accounts for all the many-body effects in the system.

E_x is the exchange energy between electrons with the same spin and it stems from the Pauli exclusion principle, which in turn implies that the wavefunction is antisymmetric. The formal mathematical definition of this term is:

$$E_x = \frac{1}{2}\sum_{ij}^{N} \underbrace{\iint \frac{\phi_{i,\sigma}(\boldsymbol{r})^{*}\phi^{*}_{j,\sigma}(\boldsymbol{r'})\,\phi_{i,\sigma}(\boldsymbol{r'})\,\phi_{j,\sigma}(\boldsymbol{r})}{|\boldsymbol{r}-\boldsymbol{r'}|}d\boldsymbol{r}d\boldsymbol{r'}}_{J_{\mathrm{ij}}} \tag{3.9}$$

It can be proven that the exchange integral J_{ij} is always positive [31]. This leads to less overlapping of the electronic wavefunctions and less repulsive interactions, hence the net effect is attractive (suggested by the negative sign in equation 3.9).

Now if we look at the case of two electrons of different spins, they are allowed to occupy the same orbital. However, they also repel each other because they both have negative charge. This effect is known as correlation, and it also results in less overlapping of electron densities, generating a small attractive energy. This correlation effect was neglected in the Hartree-Fock method [30].

Now that all the terms implicated in the KS formulation are clear, let us return to the expression for the energy functional. From the H-K theorems, we know that the total energy of the system in its ground state is a functional of the density:

$$\begin{aligned} E[n] &= \langle\Psi_0|\,\mathcal{H}\,|\Psi_0\rangle = \langle\Psi_0|\,\mathbf{T}+\mathbf{W}\,|\Psi_0\rangle + \langle\Psi_0|\,\hat{\mathbf{V}}_{ext}\,|\Psi_0\rangle \\ &\equiv \mathcal{F}[n] + \int d\mathbf{r}V_{ext}(\mathbf{r})n(\mathbf{r}) \\ &\text{with} \\ &\mathbf{T} = -\sum_i \frac{1}{2}\nabla_i^2, \quad \text{and} \quad \mathbf{W} = \frac{1}{2}\sum_{i\neq j}\frac{1}{|\mathbf{r}_i-\mathbf{r}_j|} \end{aligned} \tag{3.10}$$

where $\mathbf{T}$ is the kinetic energy operator, $\mathbf{W}$ is the electron-electron interaction operator, $\mathbf{V}_{\text{ext}}$ describes a local time-independent external potential (like the electron-ion potential), $|\Psi_0\rangle$ is a ground-state many-body wave-function, and $n(\mathbf{r})$ is the corresponding density.

However, the functional $F[n]$ is universal, and if we take into account the energy partition proposed by Kohn and Sham, we can rewrite the total energy as:

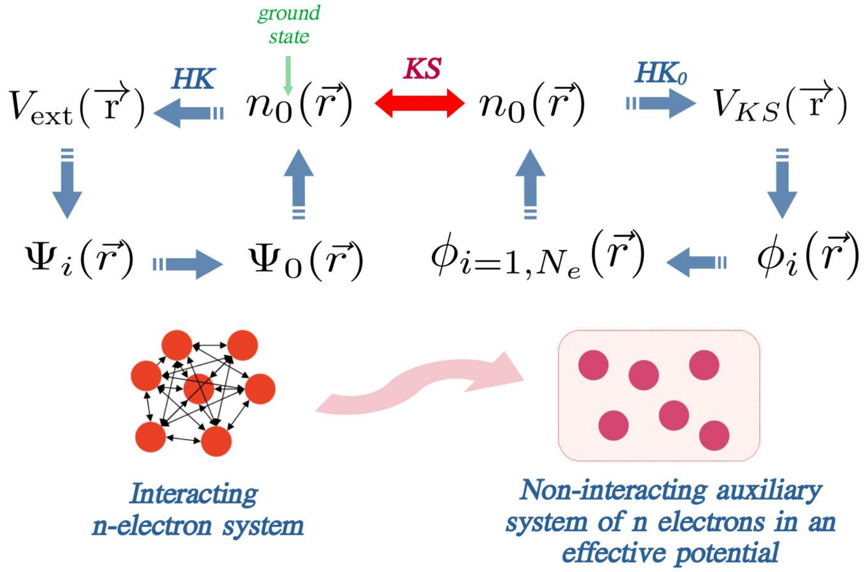

FIGURE 3.2: Schematic representation of the Kohn-Sham ansatz and its use of the Hohenberg-Kohn theorems. The notation $\Phi_0(\mathbf{r})$ stands for the ground state many body wavefunction, n_0 represents the ground state density, while HK_0 implies that Hohenberg-Kohn theorems were used for the non-interacting problem. The wavefunctions denoted by $\phi_i(\mathbf{r})$ stand for the fictitious single-particle states (Kohn-Sham orbitals). The KS double arrow indicates a connection between the many-body system and the auxiliary independent particle system proposed by Kohn and Sham (adapted from [32]).

$$E = \mathcal{F}[n((r))] + E_{ext}$$

$$= \overbrace{\underbrace{-\sum_i \int d\mathbf{r}\phi_i^*(\mathbf{r})\frac{\nabla^2}{2}\phi_i(\mathbf{r})}_{\text{Kinetic energy (non-int)}} + \underbrace{\frac{1}{2}\iint d\mathbf{r}d\mathbf{r}'\frac{n(\mathbf{r})n(\mathbf{r}')}{|\mathbf{r}-\mathbf{r}'|}}_{\text{Hartree energy}} + \underbrace{E_{xc}[n]}_{\text{XC energy}}}^{\text{Universal functional}} + \underbrace{\int d\mathbf{r}n(\mathbf{r})V_{\text{ext}}(\mathbf{r})}_{\text{System dependent } E_{ext}} \tag{3.11}$$

Now what is left is to find the equations that ϕ_i satisfy and determine the total energy of the system, E. Since the ground-state density, n_0, is precisely the function that minimizes the total energy, $E = \mathcal{F}[n]$ (Hohenberg-Kohn variational principle), we can write that:

$$\left.\frac{\delta\mathcal{F}[n(\mathbf{r})]}{\delta n}\right|_{n_0} = 0 \tag{3.12}$$

Applying the variational principle along with the constraint that the fictional single particle states (a.k.a Kohn-Sham orbitals) are normalized, we arrive at a set of equations called **Kohn–Sham equations** :

$$\begin{gathered}\left[-\frac{1}{2}\nabla^2 + V_{\text{ext}}(\mathbf{r}) + V_{\text{H}}(\mathbf{r}) + V_{xc}(\mathbf{r})\right]\phi_i(\mathbf{r}) = \varepsilon_i\phi_i(\mathbf{r}), \\ \text{where} \quad V_{xc}(\mathbf{r}) = \left.\frac{\delta E_{xc}[n]}{\delta n}\right|_{n(\mathbf{r})}\end{gathered} \tag{3.13}$$

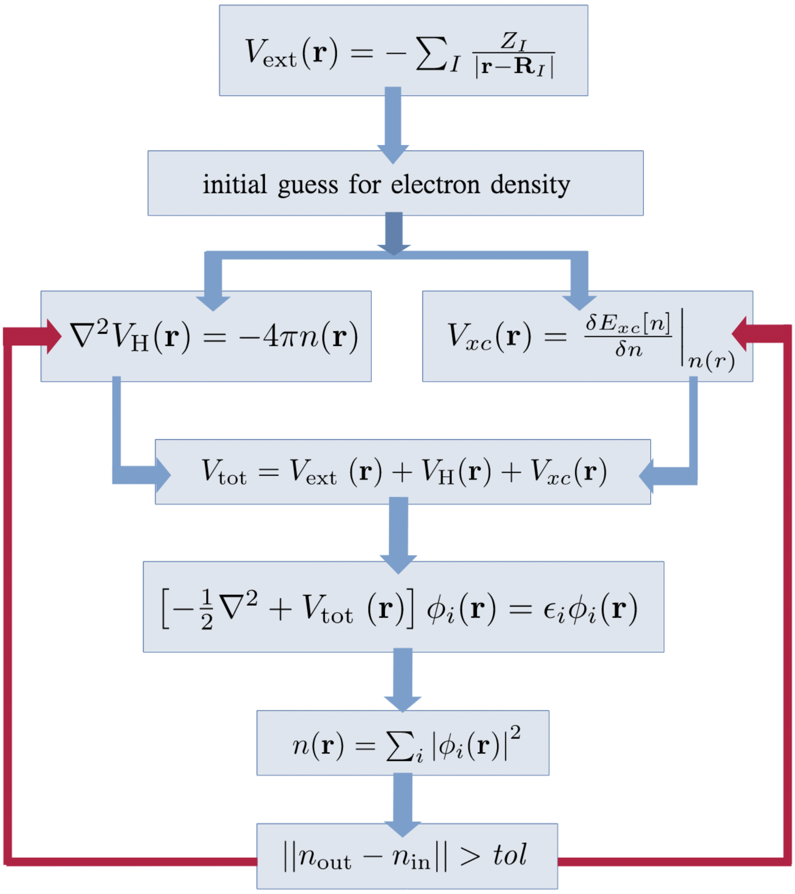

FIGURE 3.3: Self-consistent cycle of numerical DFT calculations.

and you can find the detailed derivation in A.

Furthermore, now that we concluded rigorously that there must be a functional $E_{xc}[n]$ which gives the exact ground-state energy and density, the problem remains to construct useful approximations of $E_{xc}[n]$. The priority of DFT is, therefore, is to construct accurate exchange and correlation functionals. Two of the most famous approximations for the functionals are:

- **Local Density Approximation** ⇒ The exchange–correlation energy is an integral over all space with the exchange–correlation energy density at each point assumed to be the same as in a homogeneous electron gas with that density (its generalization is known as LSDA ⇒ local density spin approximation)

- **Generalized-gradient approximations** ⇒ The LDA fails in situations where the density undergoes rapid changes. GGA improves this by considering the gradient of the electron density.

At the end of this discussion, we can also grasp the relevance density functional theory has in computational condensed matter. The method can be implemented as a self-consistent cycle and the better the approximations for the exchange-correlations functionals are, the more accurate the solution is for the ground state problem. Following the equations presented in this section, we can summarize the steps of the cycle as follows (check also Figure 3.3):

1. Specify the nuclear coordinates to calculate V_{ext}

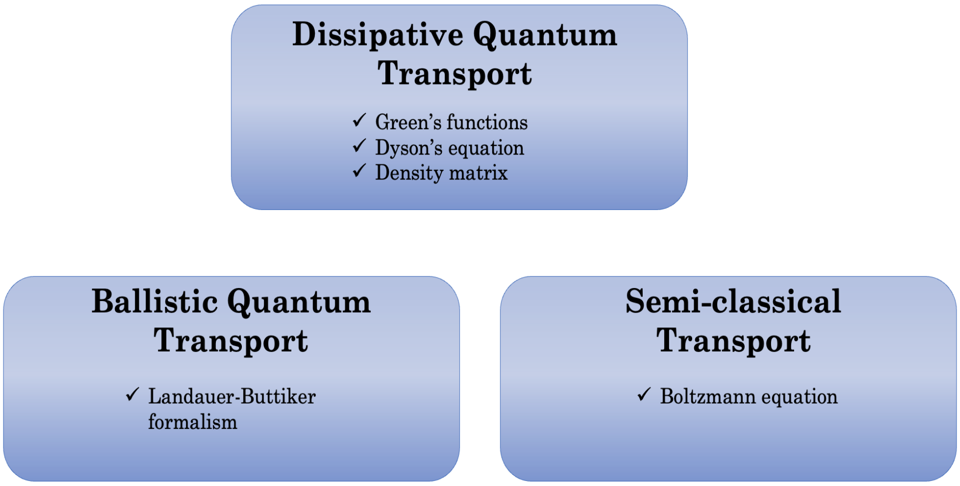

FIGURE 3.4: Brief hierarchy of transport models.

2. "Guess" a possible electron density
3. Obtain initial estimates for V_H and V_{xc}
4. Numerical solution of the Kohn–Sham equations
5. Repeat until the new density matches the old density within a desired tolerance

In order to perform effective electronic structure calculations and ab initio molecular dynamics simulations the framework of DFT, we work with the SIESTA (*Spanish Initiative for Electronic Simulations with Thousands of Atoms*) package [33, 34]. It uses the KS-DFT method, employing the LDA and GGA approximations and also uses norm-conserving pseudopotentials. The basis set is defined by atomic orbitals, instead of the more commonly used plane waves basis.

3.2 Non-equilibrium Green's Functions method for Quantum Transport

3.2.1 Key ideas of NEGF

To understand the fundamentals of nonequilibrium transport in nanoscale systems, we will outline the approach of Datta [35] , one of the founders of the method. We begin by studying a simpler system composed of three separated regions: the channel region, the source and the drain regions. For this isolated device components, the Schrodinger equations can be written as:

$$\begin{cases} (E - H_\ell + i\eta)\,\Phi_\ell = S_\ell & \text{for the left isolated source} \quad (3.14a) \\ (E - H)\psi = 0 & \text{for the central isolated channel} \quad (3.14b) \\ (E - H_r + i\eta)\,\Phi_r = S_r & \text{for the right isolated drain} \quad (3.14c) \end{cases}$$

In the system above, $i\eta\Phi_{l,r}$ represents the extraction of electrons from the source (left) and drain (right), while the terms $S_{l,r}$ stand for the reinjection of electrons from external sources. It is also essential to take note of how the term $i\eta$ transforms the Hamiltonian into a non-Hermitian operator (η is an infinitesimal term, so our reservoir Hamiltonians are only "slightly" non-Hermitian). This is directly related to a term we call self-energy, which provides, in the context of many body physics, an elegant manner to account for more complicated interactions in the quantum system. We will also point out soon how this is also related to the broadening of the energy levels in the channel, which in turn gives a finite lifetime for the electrons injected into it.

When the source and drain are coupled to the central region, one needs to also account for the coupling (this time Hermitian) Hamiltonian between the contacts and the central region (which will be denoted by $V_{l,r}$) and the scattered waves into the leads (which we denote by $\chi_{l,r}$).

$$\begin{cases} (E - H_\ell + i\eta)\left(\Phi_\ell + \chi_\ell\right) - V_\ell^\dagger \psi = S_\ell & (3.15a) \\ -V_{ell}\left(\Phi_\ell + \chi_\ell\right) + (E - H)\psi - V_r\left(\Phi_r + \chi_r\right) = 0 & (3.15b) \\ (E - H_r + i\eta)\left(\Phi_r + \chi_r\right) - V_r^\dagger \psi = S_r & (3.15c) \end{cases}$$

From equations 3.15a and 3.14a:

$$\underbrace{(E - H_\ell + i\eta)\,\Phi_\ell}_{=S_\ell} + (E - H_\ell + i\eta)\,\chi_\ell - V_\ell^\dagger \psi = S_\ell, \tag{3.16}$$

therefore:

$$\chi_\ell = (E - H_\ell + i\eta)^{-1} V_\ell^\dagger \psi \equiv G_\ell V_\ell^\dagger \psi. \tag{3.17}$$

We identify

$$G_\ell(E) = (E - H_\ell + i\eta)^{-1} \tag{3.18}$$

as the Green's function of the left source. Similarly,

$$\begin{aligned} &\chi_r = (E - H_r + i\eta)^{-1} V_r^\dagger \psi \equiv G_r V_r^\dagger \psi \quad \text{with} \\ &G_r(E) = (E - H_r + i\eta)^{-1}. \end{aligned} \tag{3.19}$$

Also, from equation 3.15b, we obtain:

$$(E - H)\psi - V_\ell \chi_\ell - V_r \chi_r = V_\ell \Phi_\ell + V_r \Phi_r. \tag{3.20}$$

If we substitute 3.17 and 3.19 into 3.20:

$$(E - H - \Sigma(E))\psi = S, \tag{3.21}$$

where we have defined the contact self energy:

$$\begin{aligned} \Sigma(E) &= \Sigma_\ell(E) + \Sigma_r(E) \\ &= V_\ell G_\ell(E) V_\ell^\dagger + V_r G_r(E) V_r^\dagger. \end{aligned} \tag{3.22}$$

The self energy is not Hermitian, and while the real part of the self energy gives an energy shift in the eigenvalues of the central region, its imaginary part accounts for a finite lifetime of the eigenstates. We can therefore define another relevant quantity in the NEGF formalism:

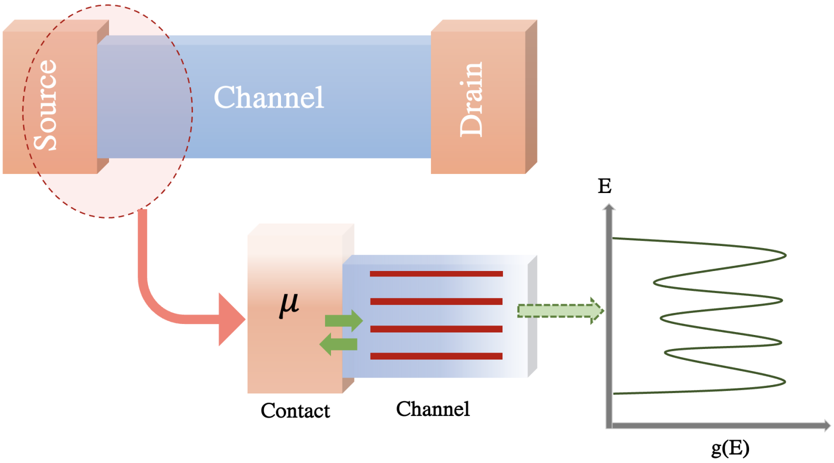

FIGURE 3.5: The partitioning of a simple prototype of quantum system for transport calculations into three regions: left reservoir, channel, right reservoir. In the lower half of the figure, there is a schematic representation of the coupling between the reservoir and the channel, and the broadening of the discrete energy levels into a continous density of states $g(E)$.

$$\Gamma_{l,r} = i\left(\Sigma_{l,r} - \Sigma^{\dagger}_{l,r}\right), \tag{3.23}$$

known as broadening matrix (also referred to as level-width function or scattering function). The self energy can include all phase-breaking mechanisms, both the ones coming from interactions and scattering inside the central region and also from the coupling between the channel and the environment.

The generalization of the density of states for a D-dimensional system can also be expressed in terms of the Green's functions, as follows:

$$g_D(E) = \frac{1}{\pi L^D}\mathrm{Tr}[A(E)], \tag{3.24}$$

where $A(E)$ is the spectral function defined as:

$$A(E) = i\left(G(E) - G^{\dagger}(E)\right). \tag{3.25}$$

In conclusion, the transport problem is partitioned into two components, as illustrated in Figure 3.5. The scattering region (channel) is defined by the Hamiltonian matrix **H**, while the contacts (source and drain) are included through the self energy matrices Σ_L/Σ_R. The channel is regarded as a mesoscopic system, with discrete energy levels and the contacts work as semi-infinite reservoirs, relatively large compared to the central region. Due to the coupling between the middle region and the electrodes, the system is regarded as an open and non-equilibrium system.

If we express the equations presented above in matrix form, the Hamiltonian looks as follows:

$$H = H_0 + V = \begin{pmatrix} H_L & 0 & 0 \\ 0 & H_C & 0 \\ 0 & 0 & H_R \end{pmatrix} + \begin{pmatrix} 0 & V_{LC} & 0 \\ V_{CL} & 0 & V_{CR} \\ 0 & V_{RC} & 0 \end{pmatrix}, \tag{3.26}$$

where the notations L, C, R stand for the right reservoir, the central region and the left reservoir respectively. The system Green's functions can also be expressed in matrix form

$$G = \begin{pmatrix} G_L & G_{LC} & G_{LR} \\ G_{CL} & G_C & G_{CR} \\ G_{RL} & G_{RC} & G_R \end{pmatrix}, \tag{3.27}$$

hence we can write:

$$\begin{pmatrix} E - H_L & -V_{LC} & 0 \\ -V_{CL} & E - H_C & -V_{CR} \\ 0 & -V_{RC} & E - H_R \end{pmatrix} \begin{pmatrix} G_L & G_{LC} & G_{LR} \\ G_{CL} & G_C & G_{CR} \\ G_{RL} & G_{RC} & G_R \end{pmatrix} = \begin{pmatrix} 1 & 0 & 0 \\ 0 & 1 & 0 \\ 0 & 0 & 1 \end{pmatrix}. \tag{3.28}$$

Also note that the interaction potentials accounting for the channel-reservoir coupling obey the relations

$$\boldsymbol{V}_{CL} = \boldsymbol{V}^{\dagger}_{LC}, \quad \boldsymbol{V}_{CR} = \boldsymbol{V}^{\dagger}_{RC}. \tag{3.29}$$

Since there is no coupling between the right and left reservoir, the Green's functions G_{RL} and G_{LR} are null. Therefore, we can rewrite equations 3.28 :

$$\begin{pmatrix} \boldsymbol{E} - \boldsymbol{H}_L & -\boldsymbol{V}_{LC} & 0 \\ -\boldsymbol{V}^{\dagger}_{LC} & \boldsymbol{E} - \boldsymbol{H}_C & -\boldsymbol{V}^{\dagger}_{RC} \\ 0 & -\boldsymbol{V}_{RC} & \boldsymbol{E} - \boldsymbol{H}_R \end{pmatrix} \begin{pmatrix} \boldsymbol{G}_L & \boldsymbol{G}_{LC} & 0 \\ \boldsymbol{G}_{CL} & \boldsymbol{G}_C & \boldsymbol{G}_{CR} \\ 0 & \boldsymbol{G}_{RC} & \boldsymbol{G}_R \end{pmatrix} = \boldsymbol{I}, \tag{3.30}$$

Explicitly, we have the following system to solve:

$$\begin{aligned} (\boldsymbol{E} - \boldsymbol{H}_L)\,\boldsymbol{G}_{LC} - \boldsymbol{V}_{LC}\boldsymbol{G}_C &= 0 \\ -\boldsymbol{V}^{\dagger}_{LC}\boldsymbol{G}_{LC} + (\boldsymbol{E} - \boldsymbol{H}_C)\,\boldsymbol{G}_C - \boldsymbol{V}^{\dagger}_{RC}\boldsymbol{G}_{RC} &= \boldsymbol{I} \\ -\boldsymbol{V}_{RC}\boldsymbol{G}_C + (\boldsymbol{E} - \boldsymbol{H}_R)\,\boldsymbol{G}_{RC} &= 0 \end{aligned} \tag{3.31}$$

From first and last equations in 3.31

$$\begin{aligned} G_{LC} &= g_L V_{LC} G_C \\ G_{RC} &= g_R V_{RC} G_C, \end{aligned}$$

where we denote $g_{L,R} = [E - H_{L,R}]^{-1}$ as the Green's functions of the isolated leads. Combining these results with the second equation in 3.31, we obtain

$$G_C = [E - H_C - \Sigma_L - \Sigma_R]^{-1},$$

where

$$\Sigma_L = V_{CL} g_L V_{LC} \quad \text{and} \quad \Sigma_R = V_{CR} g_R V_{RC}$$

are the lead self energies. Again, keep in mind that, in terms of the Green's functions, one can define the spectral function:

$$A(E) = i\left(G(E) - G^{\dagger}(E)\right) = 2\pi \sum_n |\Psi_n(E)\rangle \langle \Psi_n(E)|,$$

where $\{|\Psi_n(E)\rangle\}$ is the complete set of system eigenfunctions. Also, recall the coupling matrices:

$$\Gamma_L = i\left(\Sigma_L - \Sigma_L^\dagger\right) \quad \text{and} \quad \Gamma_R = i\left(\Sigma_R - \Sigma_R^\dagger\right).$$

Scattering states

Let us now calculate the current and transmission through such a system. The Schrodinger equation in matrix form for the system is [36]:

$$\begin{pmatrix} \boldsymbol{H}_L^0 & \boldsymbol{V}_{LS} & 0 \\ \boldsymbol{V}_{LC}^\dagger & \boldsymbol{H}_C^0 & \boldsymbol{V}_{RC}^\dagger \\ 0 & \boldsymbol{V}_{RC} & \boldsymbol{H}_R^0 \end{pmatrix} \begin{pmatrix} \boldsymbol{\Psi}_L^{(l)} \\ \boldsymbol{\Psi}_C^{(l)} \\ \boldsymbol{\Psi}_R^{(l)} \end{pmatrix} = E \begin{pmatrix} \boldsymbol{\Psi}_L^{(l)} \\ \boldsymbol{\Psi}_C^{(l)} \\ \boldsymbol{\Psi}_R^{(l)} \end{pmatrix}, \tag{3.32}$$

The wavefunctions in vector form for the left, central and right leads are $\boldsymbol{\Psi}_L$, $\boldsymbol{\Psi}_C$ and $\boldsymbol{\Psi}_R$.

To compute the scattering states from one lead, we consider the orthogonal eigenstates of the isolated chosen lead and then treat the interaction between the lead and the device as a perturbation. Consider $|\Psi_0^{(l)}\rangle$ to be an orthogonal eigenstate of the (isolated) left lead, characterized by Hamiltonian $\boldsymbol{H}_L^0$. The propagated state in the device region is:

$$|\Psi^{(l)}\rangle = GV\,|\Psi_0^{(l)}\rangle + |\Psi_0^{(l)}\rangle \tag{3.33}$$

The superscript (l) indicated that the scattering state originates from the left lead. Also,

$$|\boldsymbol{\Psi}_{\boldsymbol{0}}^{(l)}\rangle = \begin{pmatrix} \Psi_0^{(l)} \\ 0 \\ 0 \end{pmatrix}, \quad |\Psi\rangle = \begin{pmatrix} |\psi_L^{(l)}\rangle \\ |\psi_C^{(l)}\rangle \\ |\psi_R^{(l)}\rangle \end{pmatrix} \tag{3.34}$$

By substituting the matrix form of the Green's function and the potential, we obtain:

$$\begin{aligned} \boldsymbol{GV} &= \begin{pmatrix} G_L & G_{LC} & 0 \\ G_{CL} & G_C & G_{CR} \\ 0 & G_{RC} & G_R \end{pmatrix} \begin{pmatrix} 0 & V_{LC} & 0 \\ V_{CL} & 0 & V_{CR} \\ 0 & V_{RC} & 0 \end{pmatrix} \\ &= \begin{pmatrix} G_{LC}V_{CL} & G_L V_{LC} & G_{LC}V_{CR} \\ G_C V_{CL} & G_{CL}V_{LC} + G_{CR}V_{RC} & G_C V_{CR} \\ G_{RC}V_{CL} & G_R V_{RC} & G_{RC}V_{CR} \end{pmatrix} \end{aligned} \tag{3.35}$$

Hence, the scattering states vector is:

$$\begin{pmatrix} |\psi_L^{(l)}\rangle \\ |\psi_C^{(l)}\rangle \\ |\psi_R^{(l)}\rangle \end{pmatrix} = \begin{pmatrix} G_{LC}V_{CL} & G_L V_{LC} & G_{LC}V_{CR} \\ G_C V_{CL} & G_{CL}V_{LC} + G_{CR}V_{RC} & G_C V_{CR} \\ G_{RC}V_{CL} & G_R V_{RC} & G_{RC}V_{CR} \end{pmatrix} \begin{pmatrix} \Psi_0^{(l)} \\ 0 \\ 0 \end{pmatrix}. \tag{3.36}$$

Finally, by using the Green's functions, we have arrived at a result that relates the scattering states in the L,R, C regions to the unperturbed state origibating in the left lead:

Quantity	Definition	Relations
Correlation function	$G^n = \psi\psi^\dagger$	$G^n = Af$
Self energy	$\Sigma = VGV^\dagger$	$\Gamma = i\left(\Sigma - \Sigma^\dagger\right)$
Retarded GF	$G = (E - H - \Sigma + i\eta)^{-1}$	-
Advanced GF	$G = (E - H - \Sigma - i\eta)^{-1}$	
Spectral function	$A = i\left(G - G^\dagger\right)$	-
Broadening function	$\Gamma = i\left(\Sigma - \Sigma^\dagger\right)$	
Density of states	$g(E) = 2\sum_k \delta\left(E - E_k\right)$	$g(E) = \frac{1}{\pi}\,\mathrm{Tr}\,A(E)$
Current	$I = e\frac{dG^n}{dt}$	$\frac{2e}{h}\int_{-\infty}^{\infty} \mathrm{Tr}\left(\Gamma_R G_C \Gamma_L G_C^\dagger\right)$

TABLE 3.1: Fundamental quantities in NEGF

$$\begin{aligned}
|\psi_C^{(l)}\rangle &= G_C V_{CL}\,|\Psi_0^{(l)}\rangle\,, \\
|\psi_L^{(l)}\rangle &= \left(1 + g_L V_{LC} G_C V_{CL}\right)|\Psi_0^{(l)}\rangle \\
&= |\psi_0^{(l)}\rangle + g_L V_{LC}\,|\psi_C^{(L)}\rangle\,, \\
|\psi_R^{(l)}\rangle &= g_R V_{RC} G_C V_{CL}\,|\Psi_0^{(l)}\rangle \\
&= g_R V_{RC}\,|\psi_C^{(L)}\rangle\,.
\end{aligned} \tag{3.37}$$

Charge density matrix

Our goal now is to compute the current in the device in the framework of the NEGF formalism and compare it to the previously obtained result, calculated by means of the Landauer-Büttiker formalism. One can also define the spectral function in the following manner:

$$\begin{aligned}
A = 2\pi \int \mathrm{d}k\delta\left(E - E_k\right)|k\rangle\langle k| = \\
= 2\pi g(E)|k(E)\rangle\langle k(E)|,
\end{aligned} \tag{3.38}$$

where $g(E)$ is the density of states.

The charge density matrix is defined as:

$$\rho = \sum_n f(n, \mu)\,|\psi_n\rangle\,\langle\psi_n|\,, \tag{3.39}$$

where

$$f\left(n, \mu_L\right) = \frac{1}{1 + e^{(E_n - \mu_L)/k_B T}}, \tag{3.40}$$

is the Fermi-Dirac distribution function. The charge density matrix will prove to be an important quantity in the self consistent cycle of numerical NEGF calculations.

$$
\begin{aligned}
\rho_{C\leftarrow L} &= \int_{-\infty}^{\infty} \mathrm{d}E g(E) f\left(E,\mu_L\right) \left|\Psi_C\right\rangle \left\langle \Psi_C\right| \\
&= \int_{-\infty}^{\infty} \mathrm{d}E f\left(E,\mu_L\right) \sum_k g(E) G_C V_{CL}^{\dagger} \left|\psi_0^{(l)}\right\rangle \left\langle \psi_0^{(l)}\right| V_{CL} G_C^{\dagger} \\
&= \int_{-\infty}^{\infty} \mathrm{d}E f\left(E,\mu_L\right) G_C V_{CL}^{\dagger} \left(\sum_c g(E) \left|\psi_0^{(l)}\right\rangle \left\langle \psi_0^{(l)}\right| \right) V_{CL} G_C^{\dagger} = \\
&= \int_{-\infty}^{\infty} \mathrm{d}E f\left(E,\mu_L\right) G_C V_{CL}^{\dagger} \frac{a^{(l)}}{2\pi} V_{CL} G_C^{\dagger}.
\end{aligned}
\tag{3.41}
$$

We now use the formula for the spectral density of states in the left lead ($a^{(l)}$) and the equation for the level-width function

$$
\begin{aligned}
\Gamma_L = i(\Sigma_L - \Sigma_L^{\dagger}) = i(V_{CL} g_L V_{LC} - V_{CL}^{\dagger} g_L^{\dagger} V_{LC}^{\dagger}) = i V_{LC}^{\dagger} (g_L - g_L^{\dagger}) V_{LC} \\
V_{LC}^{\dagger} a^{(l)} V_{LC} = i V_{LC}^{\dagger} (g_L - g_L^{\dagger}) V_{LC},
\end{aligned}
\tag{3.42}
$$

such that:

$$
\rho_{C\leftarrow L} = \frac{1}{2\pi} \int_{E=-\infty}^{\infty} \mathrm{d}E f\left(E,\mu_L\right) G_C \Gamma_L G_C^{\dagger}. \tag{3.43}
$$

Therefore, the total density matrix in the non-equilibrium case is a sum over all the contacts:

$$
\rho = 2 \times \frac{1}{2\pi} \int_{E=-\infty}^{\infty} \mathrm{d}E \sum_s f\left(E,\mu_s\right) G_C \Gamma_i G_C^{\dagger}. \tag{3.44}
$$

For a two-lead case, it has the form:

$$
\rho = 2 \times \frac{1}{2\pi} \int_{E=-\infty}^{\infty} \mathrm{d}E \left[f\left(E,\mu_L\right) G_C \Gamma_L G_C^{\dagger} + f\left(E,\mu_R\right) G_C \Gamma_R G_C^{\dagger} \right] \tag{3.45}
$$

The spectral function is defined by the sum of contributions arising from all the leads. Therefore, we can compute the device spectral function from states originating from the left/right reservoir:

$$
\begin{aligned}
A_C^{(L,R)} &= 2\pi \sum_l \left|\psi_{C,l}^{(L)}\right\rangle \left\langle \psi_{C,l}^{(L)}\right| \\
&= 2\pi \sum_l G_C V_{CL} \left|\psi_0^{(l)}\right\rangle \left\langle \psi_0^{(l)}\right| V_{LC} G_C^{\dagger} \\
&= G_C V_{CL} a_L V_{LC} G_C^{\dagger} \\
&= G_C \Gamma_{L,R} G_C^{\dagger}
\end{aligned}
\tag{3.46}
$$

Hence, the non-equilibrium density matrix can also be expressed as:

$$
\rho = 2 \times \frac{1}{2\pi} \int_{-\infty}^{\infty} \mathrm{d}E \left[f_L(E) A_C^{(L)}(E) + f_R(E) A_C^{(R)}(E) \right]. \tag{3.47}
$$

From equation 3.47, the electron density can be computed:

$$
n(\mathbf{r}) = \langle \mathbf{r} | \rho | \mathbf{r} \rangle \quad \Rightarrow \text{diagonal elements of } \rho \tag{3.48}
$$

Along with density functional theory, a self-consistent procedure for determining the transport properties of a device at finite bias can be formulated [37].

Current and transmission

For this case, we will compute the current following the approach in [38] , using the continuity equation applied to our two terminal system. When the system reaches equilibrium, the total probability is conserved, therefore:

$$\begin{aligned}
0 &= \frac{\partial}{\partial t}\left(\sum_c |\Psi_c|^2\right) = \frac{\partial}{\partial t}\left(\sum_c \langle\Psi|\Psi\rangle\right) = \sum_c \frac{\partial}{\partial t}\langle\Psi|c\rangle\langle c|\Psi\rangle \\
&= \sum_c \left(\frac{\partial\langle\Psi \mid c\rangle}{\partial t}\langle c \mid \Psi\rangle + \langle\Psi \mid c\rangle\frac{\partial\langle c \mid \Psi\rangle}{\partial t}\right) \\
&= \frac{i}{\hbar}\sum_c(\langle\Psi|H|c\rangle\langle c \mid \Psi\rangle - \langle\Psi \mid c\rangle\langle c|H|\Psi\rangle) \\
&= \frac{i}{\hbar}\left(\langle\Psi|\, H \,|\Psi_C\rangle - \langle\Psi_C|H|\Psi\rangle\right) \\
&= \frac{i}{\hbar}\left(\langle\Psi\,|H_C + V_{LC} + V_{RC}|\,\Psi_C\rangle - \left\langle\Psi_C\left|H_C + V_{LC}^{\dagger} + V_{RC}^{\dagger}\right|\Psi\right\rangle\right) = \\
&= \frac{i}{\hbar}\left(\underbrace{\left[\langle\Psi_L\,|V_{LC}|\,\Psi_C\rangle - \left\langle\Psi_C\left|V_{LC}^{\dagger}\right|\Psi_L\right\rangle\right]}_{\mathcal{P}_{L\to C}} + \underbrace{\left[\langle\Psi_R\,|V_{RC}|\,\Psi_C\rangle - \left\langle\Psi_C\left|V_{RC}^{\dagger}\right|\Psi_R\right\rangle\right]}_{\mathcal{P}_{R\to C}}\right).
\end{aligned} \tag{3.49}$$

The first square bracket ($\mathcal{P}_{L\to C}$) is the probability current from the left contact to the device and the second bracket ($\mathcal{P}_{R\to C}$) is the probability current from the right contact. Also, note that the sum $\sum_c$ runs over all the states in the central device region. We can generalize equation 3.49 to any contact s and determine the current by multiplying with the charge $-e$:

$$I_s = -\frac{ie}{\hbar}\left[\langle\Psi_s\,|V_{sC}|\,\Psi_C\rangle - \left\langle\Psi_C\left|V_{sC}^{\dagger}\right|\Psi_s\right\rangle\right]. \tag{3.50}$$

Therefore,

$$\begin{aligned}
i_{R\leftarrow L} &= -\frac{ie}{\hbar}\left[\langle\Psi_R\,|V_{RC}|\,\Psi_C\rangle - \left\langle\Psi_C\left|V_{RC}^{\dagger}\right|\Psi_R\right\rangle\right] \\
&= -\frac{ie}{\hbar}\left[g_R^{\dagger}V_{RC}^{\dagger}G_C^{\dagger}V_{CL}^{\dagger}\,\langle\Psi_0^{(l)}|\,V_{RC}G_CV_{CL}\,|\Psi_0^{(l)}\rangle - G_C^{\dagger}V_{CL}^{\dagger}\,\langle\Psi_0^{(l)}|\,V_{RC}^{\dagger}g_RV_{RC}G_CV_{CL}\,|\Psi_0^{(l)}\rangle\right] \\
&= -\frac{ie}{\hbar}\left[\langle\Psi_0^{(l)}|\,V_{CL}^{\dagger}G_C^{\dagger}V_{RC}^{\dagger}g_R^{\dagger}V_{RC}G_CV_{CL}\,|\Psi_0^{(l)}\rangle - \langle\Psi_0^{(l)}|\,V_{CL}^{\dagger}G_C^{\dagger}V_{RC}^{\dagger}g_RV_{RC}G_CV_{CL}\,|\Psi_0^{(l)}\rangle\right] \\
&= -\frac{ie}{\hbar}\left[\langle\Psi_0^{(l)}|\,V_{CL}^{\dagger}G_C^{\dagger}V_{RC}^{\dagger}\left(g_R^{\dagger} - g_R\right)V_{RC}G_CV_{CL}\,|\Psi_0^{(l)}\rangle\right] \\
&= \frac{e}{\hbar}\left[\langle\Psi_0^{(l)}|\,V_{CL}^{\dagger}G_C^{\dagger}\Gamma_RG_CV_{CL}\,|\Psi_0^{(l)}\rangle\right].
\end{aligned} \tag{3.51}$$

If we sum over all the modes, integrate over energy and note that the levels are filled from the left reservoir with a probability (the Fermi-Dirac distribution), we can write the current as:

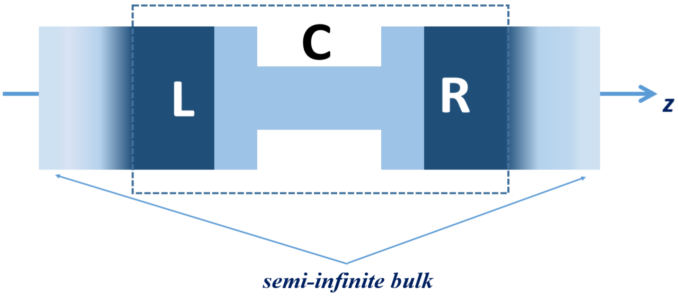

FIGURE 3.6: Consider the model of a device above. The contact region (C) is coupled to two semi-infinite electrodes (L,R). In the TranSIESTA package, only a finite section of the system is considered, since the semi-infinite electrodes would involve infinite Green's function matrices. Also, the influence of the semi-infinite leads onto the central region is accounted for through the self-energies.

$$\begin{aligned} I_{R\leftarrow L} &= 2 \times \frac{e}{\hbar} \int_{-\infty}^{\infty} \mathrm{d}E f\left(E, \mu_L\right) \sum_n g(E) \left\langle \psi_0^{(l)} \middle| V_{LC} G_C^{\dagger} \Gamma_R G_C V_{LC}^{\dagger} \middle| \psi_0^{(l)} \right\rangle \\ &= \frac{2e}{\hbar} \int_{-\infty}^{\infty} \mathrm{d}E f\left(E, \mu_L\right) \sum_{m,n} g(E) \left\langle \psi_0^{(l)} \right| V_{LC} \left| m \right\rangle \left\langle m \right| G_C^{\dagger} \Gamma_R G_C V_{LC}^{\dagger} \left| \psi_0^{(l)} \right\rangle , \end{aligned} \tag{3.52}$$

where we just inserted the identity operator $\sum_m |m\rangle \langle m|$. In the following, we will use the identities $\langle \phi | A | \psi \rangle^{\dagger} = \langle \psi | A^{\dagger} | \phi \rangle$ and $\langle \phi | A^{\dagger} B^{\dagger} | \psi \rangle^{\dagger} = \langle \psi | B A | \phi \rangle$ to arrive at the final result:

$$\begin{aligned} I_{R\leftarrow L} &= \frac{2e}{\hbar} \int_{-\infty}^{\infty} dE f\left(E, \mu_L\right) \sum_m \left\langle m \middle| G_C^{\dagger} \Gamma_R G_C V_{LC}^{\dagger} \left(\sum_n g(E) \left| \psi_0^{(l)} \right\rangle \left\langle \psi_0^{(l)} \right| \right) V_{LC} \middle| m \right\rangle \\ &= \frac{2e}{\hbar} \int_{-\infty}^{\infty} dE f\left(E, \mu_L\right) \sum_m \left\langle m \middle| G_C^{\dagger} \Gamma_R G_C V_{LC}^{\dagger} \frac{a_1}{2\pi} V_{LC} \middle| m \right\rangle = \\ &= \frac{2e}{h} \int_{-\infty}^{\infty} dE f\left(E, \mu_L\right) \mathrm{Tr} \left(G_C^{\dagger} \Gamma_R G_C \Gamma_L \right) \\ &= \frac{2e}{h} \int_{-\infty}^{\infty} dE f\left(E, \mu_L\right) \mathrm{Tr} \left(\Gamma_R G_C \Gamma_L G_C^{\dagger} \right) . \end{aligned} \tag{3.53}$$

Hence, the total current in the two-terminal device is:

$$I = \frac{2e}{h} \int_{E=-\infty}^{\infty} \mathrm{d}E \left(f\left(E, \mu_L\right) - f\left(E, \mu_R\right) \right) \mathrm{Tr} \left(G_C^{\dagger} \Gamma_R G_C \Gamma_L \right) . \tag{3.54}$$

This also gives us a new and convenient relation for the transmission (at $T = 0K$) [36]:

$$T(E) = \mathrm{Tr} \left(\boldsymbol{t} \boldsymbol{t}^{\dagger} \right) = \mathrm{Tr} \left(\Gamma_R G_C \Gamma_L G_C^{\dagger} \right) . \tag{3.55}$$

3.2.2 Transport simulations with NEGF + DFT

The SIESTA code was extended to out-of-equilibrium systems by combining DFT with the NEGF formalism [37], in the form of the TranSIESTA package. Through

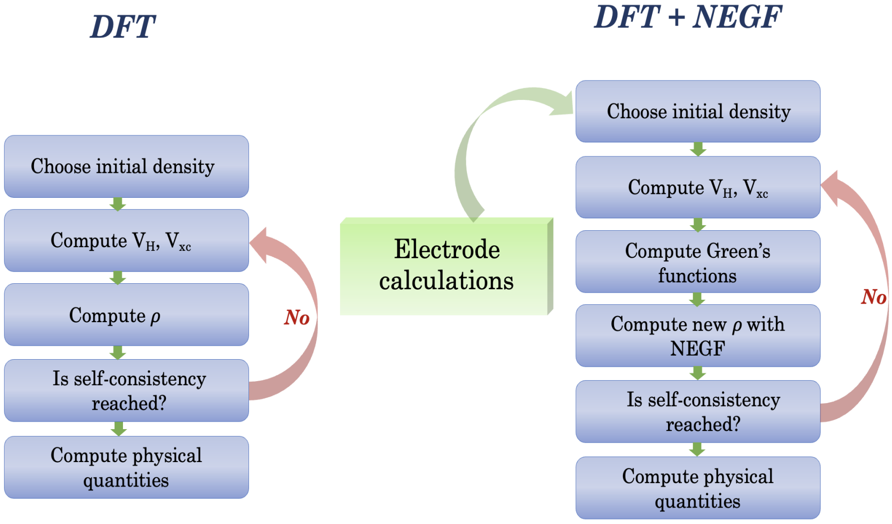

FIGURE 3.7: Comparison between DFT andf DFT+NEGF self-consistency cycles.

this approach, the density matrix is computed with the aid of the Green's functions formalism, as indicated in Equations 3.45 and 3.47.

To compute the transport properies of the system partitioned as sugested in figure 3.6, we are only interested in the finite Hamiltonian for the $L - C - R$ part:

$$\mathbf{H} = \begin{pmatrix} \mathbf{H}_L + \mathbf{\Sigma}_L & \mathbf{V}_L & 0 \\ \mathbf{V}_L^{\dagger} & \mathbf{H}_C & \mathbf{V}_R \\ 0 & \mathbf{V}_R^{\dagger} & \mathbf{H}_R + \Sigma_R \end{pmatrix} \tag{3.56}$$

As we discussed in the previous section, the Hamiltonians in the L, R and C regions are $\mathbf{H}_L$, $\mathbf{H}_R$ and $\mathbf{H}_C$. The interaction between the $L - C$ and $R - C$ regions are described by $\mathbf{V}_L$ and $\mathbf{V}_R$ respectively and the self energies $\mathbf{\Sigma}_L$ and $\mathbf{\Sigma}_R$ account for the interaction between the L and R regions to the remaining parts of the semi-infinite electrodes. Since the electrodes are modeled as semi-infinite bulk, the matrix of the system Hamiltonian is theoretically infinite. However, we are only interested in the finite matrix defined in 3.56 and its inverse. The matrix inversion algorithm is crucial, since the simulation involves large matrices that may induce numerical issues. The $(\mathbf{H}_{L/R} + \Sigma_{L/R})$ blocks of the Hamiltonian are computed in a separate calculation, based on conventional DFT calculations for periodic bulk systems.

In the TranSIESTA module run, the transmission function is computed under finite bias conditions. The fundamental idea is to calculate the density from the Green's function formalism during the self-consistency cycle of a DFT calculation. The full SIESTA + TranSIESTA run starts from an initial guess for the density in the scattering region. Subsquently, the Kohn-Sham Hamiltonian in the central region is built and a density matrix that corresponds to it is determined by means of NEGF. If the initial and final density matrices differ only by a small margin of error, that is imposed *a priori*, the calculation has converged. Otherwise, the procedure is repeated until a satisfying result is achieved.The iterative loop can be summarized as follows:

$$\underbrace{\text{initial}\, n(x) \Rightarrow \text{SIESTA} \Rightarrow \phi_{\text{KS}}(x) \Rightarrow \text{NEGF} \Rightarrow \text{ new } n(x)}_{\textit{TRANSIESTA} \quad \textit{package}}$$

A comparison between the DFT and DFT+NEGF approaches is represented in Figure 3.7.

3.3 Quantum transport with TranSIESTA in 2D systems

The main results presented in this section were published in [39]

We can illustrate the utility of DFT+NEGF calculations by presenting the results in [39], where we investigated the properties of phosphorene nanoribbons and the influence of the substrate onto the transport properties. The motivation of this study was to build on top of current research that focused on the difficulty of band gap modulation in freestanding phosphorene nanoribbons, where high in plane electric field are needed to close the gap. We employed DFT and NEGF with the aid of the TranSIESTA package, along with some Python librarier that allowed for efficient and instructive data processing.

In figure 3.8a, we represented the materials of interest: zig-zag phosphorene nanoribbons (zPNR), hexagonal boron nitride (hBN) nanoribbons and graphene-hBN-graphene (G-hBN-G) double junction. The heterojuctions have two types of support layers - either simple hBN nanoribbons or a G-hBN-G double junction. The goal of stacking phosphorene on top of these two types of substrates is to enhance its tunability properties. External electric fields can also be applied, either in-plane $(\mathcal{E}_x)$ or perpendicular to the zPNR $(\mathcal{E}_y)$ (see 3.8a).

The first step of the analysis consists of DFT calculations on pristine 2D phosphorene and freestanding zPNRs. In this manner, we check the previously obtained results. The electronic properties of phisphorene are illustrated in Figure 3.8b. In Figure 3.8b(a), the band structure for bulk 2D phosphorene is represented along a chosen k-path following the high symmetry points. Notice the direct band gap of ~ 0.82eV, found at the Γ point (while the bandgap is underestimated compared to its experimentally determined value, this is expected within the LDA approximation). The corresponding density of the states associated to the pristine 2D phosphorene is displayed in 3.8b (b).

In the next parts of the study, we investigated the influence of the support layers on the electronic and transport properties of zPNRs. We consider the zPNR@hBN system and analyze the ideal transmission for a series of values for the electric field and subsequently compare it with the transmission of the freestanding PNR. In Figure 3.8b, one can see the reduction of the band gap for both systems, as the in-plane electric field $\mathcal{E}_x$ is increased. The main observation is that in the zPNR@hBN configuration, the band gap is closed at a significantly smaller $\mathcal{E}_x$, in the range of $0.2 - 0.3$ V/Å. Consequently, there is a sharp increase in the conductance of the heterostructure for electric fields below 0.3 V/Å. This is relevant from an experimental point of view, since the maximum values of the electric fields for which the system experiences bandgap closure are brought into a feasible range.

In order to gain a better understanding of nanoscale transport in such a 2D structure, we visualize the atomic currents and bond currents in the system. For this purpose, we employed a Python package called SISL [40], optimized for the post-processing of the data obtained through *ab-initio* calculations. The library was developed a in order to manipulate and analyze input and output files from the SIESTA and TRANSIESTA codes. Local currents are highly useful to look into possible correlations between a particular molecular or atomistic property and its role for the

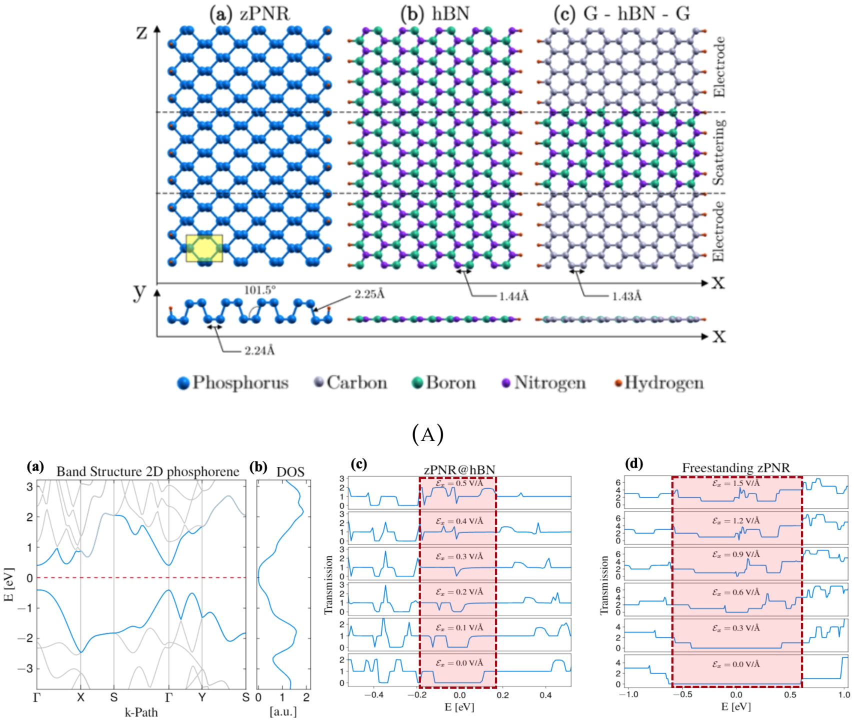

(A)

(B)

FIGURE 3.8: (A)(a) zig-zag phosphorene nanoribbon (zPNR); (b) hexagonal boron nitride (hBN) nanoribbon; (c) graphene-hBN-graphene (G-hBN-G) double junction. (B) (a) Band structure of 2D phosphorene along $\Gamma - X - S - \Gamma - Y - S$. (b) Density of states (DOS) of the 2D structure. (c), (d) Transmission functions for various in-plane electric fields, denoted by $\mathcal{E}_x$. Notice that the energy gap of the freestanding zPNR is reduced due to the interaction with the support layer in the ZPNR@hBN structure.

charge transport within the mesoscopic system. For this reason, bond currents are also referred to as "transmission pathways" [41].

In TBtrans, the orbiltal currents are defined in terms of the spectral density matrix and they are implemented following the equation:

$$J_{\alpha\beta} = i\left[\mathbf{H}_{\beta\alpha}\mathbf{A}_{\alpha\beta} - \mathbf{H}_{\alpha\beta}\mathbf{A}_{\beta\alpha}\right], \tag{3.57}$$

where the factor $e/\hbar$ was left out. In order to obtain the bond currents, one simply sums over all the orbital indices. As a consequence of the continuity equation, a sum of the bond currents that cross a definite surface separating the originating electrode from the rest of the device will be equal to the total current [42, 43].

$$J_{\nu\mu} = \sum_{\alpha\in\nu}\sum_{\beta\in\mu} J_{\alpha\beta} \tag{3.58}$$

The total bond current acting on an individual atom can be represented in vectorial form:

$$\vec{J}_\nu = \sum_{\nu\neq\mu} J_{\nu\mu}\vec{v}_{\nu\mu}$$

In Figures 3.9 we plot the atomic currents in the freestanding zPNR (Figure 3.9a) and in the active region of the *zPNR@hBN* and zPNR@G-hBN-G heterostructures

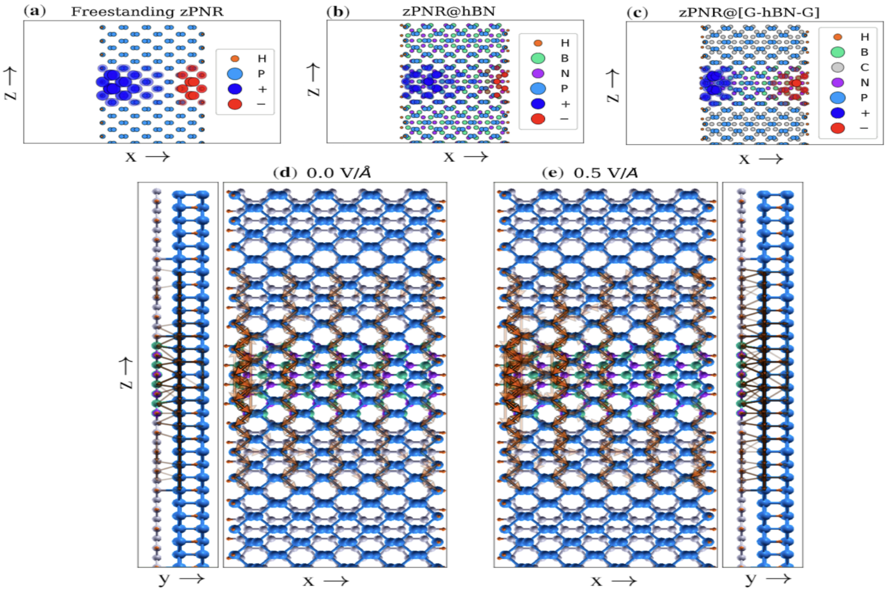

FIGURE 3.9: (a), (b), (c) The distribution of atomic currents in free-standing zPNR, zPNR@hBN and zPNR@G−hBN-G heterostructures. The value of the electric field is $\mathcal{E}_x = 0.5$ V/Å. (d), (e) The bond current distribution for the zPNR@G- hBN-G heterostructure, integrated over the $[0, 1.5]$eV interval, for the following values of the electric field: $\mathcal{E}_x = 0$ and $\mathcal{E}_x = 0.5$ V/Å.

(figures 3.9 b,c). The atomic currents in the case of zero electric field are plotted as reference, and the dark blue and red markers denote the current difference once an in plane electric field $\mathcal{E}_y = 0.5$ V/Å is applied along the x-axis. It is worth noting that the in-plane electric field displaces the charge towards the edges of the structure, and also enhances the coupling between the two layers. Since hBN is highly insulating, in the active region most of the current flows through the zPNRs segments. Due to the electric field, the atomic currents become visible on the underlying layer of hBN. Bond currents illustrate the flow patterns in the zPNR@G-hBN-G structure more accurately, as one can see in Figures 3.9d),e).

$$\underbrace{DFT}_{SIESTA} \Rightarrow \underbrace{DFT + NEGF}_{TranSIESTA} \Rightarrow \underbrace{\text{Post-processing}}_{sisl} \Rightarrow \text{Physical insights}$$

3.4 The tight binding formalism

The tight binding model is built upon the assumption that the electron is strongly bound to the nucleus, such that its wavefunction is localized to a region of small dimensions (relative to the inter-nuclear distances). Formally, this implies that the electronic wavefunction can be expressed as a *linear combination of atomic orbitals*(LCAO).

In order to outline the theoretical side of the TB formalism, let us begin with the assumption that, around each lattice site, the Hamiltonian can be approximated by the Hamiltonian of the localized atom. We call this the atomic Schrodinger equation [44]:

$$\mathcal{H}_{at}\varphi_j(\mathbf{r}) = \varepsilon_j\varphi_j(\mathbf{r}), \tag{3.59}$$

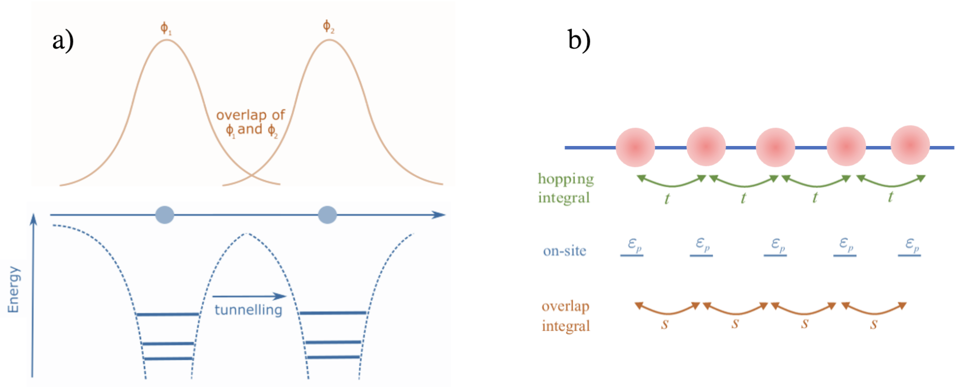

FIGURE 3.10: (a) Two sites in a chain one-dimensional atomic chain. The overlap of the wavefunctions allows for tunnelling between the two potential wells. (b) An ideal 1D chain with a one atom basis in the tight binding model and intuitive illustrations of the main quantities involved: the hopping energy (t), the on-site energy (ε_p) and the overlap matrix (s)

where ε_j are the energy eigenvalues and $\varphi_j(\mathbf{r})$ are the wavefunctions describing the well-localized bound levels of the atomic Hamiltonian $\mathcal{H}_{at}$. The atomic wavefunctions in equation 3.59 are considered to be of negligible amplitude when $\mathbf{r}$ is larger than the lattice constant. To this atomic Hamiltonian, we will add an additional term that accounts for the periodic potential of the crystal:

$$\mathcal{H} = \mathcal{H}_{at} + \Delta U(\mathbf{r}), \tag{3.60}$$

such that the crystal Schrodinger equation is:

$$\mathcal{H}\Psi_{(\mathbf{r})} = (\mathcal{H}_{at} + \Delta U(\mathbf{r}))\Psi(\mathbf{r}) = E_n\Psi(\mathbf{r}). \tag{3.61}$$

Since we are dealing with (ideal) crystalline solids, the electrons are described by a Bloch function, such that translational symmetry is conserved:

$$T_{\mathbf{R}}\Psi_{\mathbf{k}}(\mathbf{r}) = \Psi_{\mathbf{k}}(\mathbf{r} + \mathbf{R}) = e^{i\mathbf{k}\cdot\mathbf{R}}\Psi_{\mathbf{k}}(\mathbf{r}) \tag{3.62}$$

where $T_{\mathbf{R}}$ is the translation operator along the Bravais lattice vector $\mathbf{R}$ and $\Psi_{\mathbf{k}}(\mathbf{r}, \mathbf{k})$ is the wavefunction for the electron in the crystal.

All this suggests that the solution of the crystal Hamiltonian in equation 3.61 has the form:

$$\psi(\mathbf{r}) = \sum_{\mathbf{R}} e^{i\mathbf{k}\cdot\mathbf{R}}\tilde{\phi}(\mathbf{r} - \mathbf{R}) \tag{3.63}$$

where the function $\tilde{\phi}(\mathbf{r})$ is not the exact atomic wavefunction $\phi(\mathbf{r})$, but it can be expanded in a linear combination of atomic wavefunctions:

$$\tilde{\phi}(\mathbf{r}) = \sum_n C_n\phi_n(\mathbf{r}) \tag{3.64}$$

Now we have arrived at the core premise of the TB model, which is that the crystal Bloch wavefunction can be written as a linear combination of the atomic orbitals [45]:

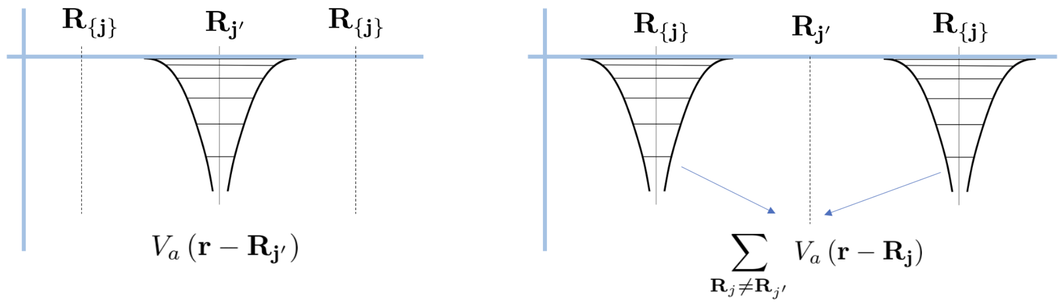

FIGURE 3.11: Pictorial display of the splitting of the crystal potential into the on-site atomic potential and the rest of the periodic potential

$$\begin{aligned}\Psi_{\mathbf{k}}(\mathbf{r}) &= \frac{1}{\sqrt{N}}\sum_{\mathbf{R}} e^{i\mathbf{k}\cdot\mathbf{R}}\sum_{n} C_n\phi_n(\mathbf{r}-\mathbf{R}) \\ &= \sum_{n} C_n \frac{1}{\sqrt{N}}\sum_{\mathbf{R}} e^{i\mathbf{k}\cdot\mathbf{R}}\phi_n(\mathbf{r}-\mathbf{R}),\end{aligned} \tag{3.65}$$

where n indexes the atomic wavefunctions in the unit cell, N is the number of unit cells and C_n are the complex expansions coefficients.

With the general form of the crystal wavefunction, we focus on solving the following eigenvalue problem:

$$\mathcal{H}\Psi_{n\mathbf{k}}(\mathbf{r}) = E_n(\mathbf{k})\Psi_{n\mathbf{k}} \tag{3.66}$$

to determine the bandstructure.

Again, as in equation 3.60, the single particle Hamiltonian of the periodic lattice structure is expressed as:

$$\mathcal{H} = \frac{\hat{p}^2}{2m} + \sum_{R_j} V_a\left(\boldsymbol{r}-\boldsymbol{R}_j\right) = \mathcal{H}_{\text{at}}\left(\boldsymbol{R}_j\right) + \sum_{R_{j'}\neq R_j} V_a\left(\boldsymbol{r}-\boldsymbol{R}_{j'}\right)$$

where we singled out the arbitrarily chosen potential on R_j. The eigenvalue problem is:

$$\begin{aligned}&\left(\mathcal{H}_{\text{at}}\left(\boldsymbol{R}_j\right) + \sum_{R_{j'}\neq R_j} V_a\left(\boldsymbol{r}-\boldsymbol{R}_{j'}\right)\right)\sum_{n} C_n\frac{1}{\sqrt{N}}\sum_{\mathbf{R}_\mathrm{j}} e^{i\mathbf{k}\cdot\mathbf{R}_\mathrm{j}}\phi_n(\mathbf{r}-\mathbf{R}_\mathrm{j}) \\ &\qquad = E_n(\mathbf{k})\sum_{n} C_n\frac{1}{\sqrt{N}}\sum_{\mathbf{R}_\mathrm{j}} e^{i\mathbf{k}\cdot\mathbf{R}_\mathrm{j}}\phi_n(\mathbf{r}-\mathbf{R}_\mathrm{j})\end{aligned} \tag{3.67}$$

$$\Rightarrow \sum_{n} C_n\left(\mathcal{H}_{\text{at}}\left(\boldsymbol{R}_j\right) + \sum_{R_{j'}\neq R_j} V_a\left(\boldsymbol{r}-\boldsymbol{R}_{j'}\right) - E_n(\mathbf{k})\right)\sum_{\mathbf{R}_\mathrm{j}} e^{i\mathbf{k}\cdot\mathbf{R}_\mathrm{j}}\phi_n(\mathbf{r}-\mathbf{R}_\mathrm{j}) = 0$$

To solve this we multiply to the left with $e^{-ik\mathbf{R}'_\mathrm{j}}\phi^*_m(\mathbf{r}-\mathbf{R}'_\mathrm{j})$ and integrate over the crystal volume. The term

$$\sum_{R_j,R_{j'}}\int d^3r e^{-ik\mathbf{R}'_\mathrm{j}}\phi^*_m(\mathbf{r}-\mathbf{R}'_\mathrm{j})E_n(\mathbf{k})e^{i\mathbf{k}\cdot\mathbf{R}_\mathrm{j}}\phi_n(\mathbf{r}-\mathbf{R}_\mathrm{j}), \tag{3.68}$$

leads us to the the overlap matrix element:

$$\begin{aligned}\mathcal{S}_{mn}(\boldsymbol{k}) &= \sum_{\boldsymbol{R}_j,\boldsymbol{R}_{j'}} \int d^3r e^{i\boldsymbol{k}\cdot\left(\boldsymbol{R}_j-\boldsymbol{R}_{j'}\right)} \phi_m^*\left(\boldsymbol{r}-\boldsymbol{R}_j'\right)\phi_n\left(\boldsymbol{r}-\boldsymbol{R}_j\right) \\ &= \sum_{\boldsymbol{R}_j'} \int d^3r e^{-i\boldsymbol{k}\cdot\boldsymbol{R}_j'} \phi_m^*\left(\boldsymbol{r}-\boldsymbol{R}_j'\right)\phi_n(\boldsymbol{r}) \\ &= \delta_{mn} + \sum_{\boldsymbol{R}_j'\neq 0} e^{-i\boldsymbol{k}\cdot\boldsymbol{R}_j'} \alpha_{mn}\left(\boldsymbol{R}_j'\right),\end{aligned} \tag{3.69}$$

where we set $R_j = 0$ due to translational invariance. The term α_{mn} is considered negligible if the overlap between the wavefunctions of neighboring orbitals is not taken into account.

The Hamiltonian matrix element is (we chose a reference orbital described by the Bravais vector R_j):

$$\begin{aligned}\mathcal{H}_{mn}(\boldsymbol{k}) &= \sum_{\boldsymbol{R}_j,\boldsymbol{R}_{j'}} \int d^3r e^{i\boldsymbol{k}\cdot\left(\boldsymbol{R}-\boldsymbol{R}_{j'}\right)} \phi_m^*\left(\boldsymbol{r}-\boldsymbol{R}_{j'}\right)\left\{H_{\mathrm{at}}\left(\boldsymbol{R}_j\right) + V_{\boldsymbol{R}_j\neq\boldsymbol{R}_j'}\left(\boldsymbol{r}-\boldsymbol{R}_{j'}\right)\right\}\phi_n\left(\boldsymbol{r}-\boldsymbol{R}\right) \\ &= E_n^{\mathrm{at}}\mathcal{S}_{mn}(\boldsymbol{k}) + \sum_{\boldsymbol{R}_j,\boldsymbol{R}_{j'}} \int d^3r e^{i\boldsymbol{k}\cdot\left(\boldsymbol{R}_j-\boldsymbol{R}_{j'}\right)} \phi_m^*\left(\boldsymbol{r}-\boldsymbol{R}_{j'}\right) V_{\boldsymbol{R}_{j'}\neq\boldsymbol{R}_j'}\left(\boldsymbol{r}-\boldsymbol{R}_{j'}\right)\phi_n\left(\boldsymbol{r}-\boldsymbol{R}_j\right).\end{aligned} \tag{3.70}$$

Again, we set $\boldsymbol{R}_j = 0$ and get:

$$\begin{aligned}\mathcal{H}_{mn}(\boldsymbol{k}) &= E_m^{\mathrm{at}}\mathcal{S}_{mn}(\boldsymbol{k}) + \sum_{\boldsymbol{R}_{j'}} \int d^3r e^{-i\boldsymbol{k}\boldsymbol{R}_{j'}} \phi_m^*\left(\boldsymbol{r}-\boldsymbol{R}_{j'}\right) V_{R_{j'}\neq 0}\left(\boldsymbol{r}-\boldsymbol{R}_{j'}\right)\phi_n\left(\boldsymbol{r}\right) \\ &= E_m^{\mathrm{at}}\mathcal{S}_{mn}(\boldsymbol{k}) + \underbrace{\int d^3r\phi_m^*\left(\boldsymbol{r}\right) V_{R_{j'}\neq 0}\left(\boldsymbol{r}-\mathbf{R}_{\mathbf{j}'}\right)\phi_n\left(\boldsymbol{r}\right)}_{\mathcal{C}_{mn}} \\ &\quad + \sum_{\boldsymbol{R}_{j'}\neq 0} e^{-i\boldsymbol{k}\boldsymbol{R}_{j'}} \underbrace{\int d^3r\phi_m^*\left(\boldsymbol{r}-\boldsymbol{R}_{j'}\right) V_{R_{j'}\neq 0}\left(\boldsymbol{r}-\boldsymbol{R}_{j'}\right)\phi_n\left(\boldsymbol{r}\right)}_{t_{\mathrm{mn}}},\end{aligned} \tag{3.71}$$

where

$$t_{mn}\left(\boldsymbol{R}_j\right) = \int d^3r\phi_m^*\left(\boldsymbol{r}-\boldsymbol{R}_{j'}\right) V_{R_{j'}\neq 0}\left(\boldsymbol{r}-\boldsymbol{R}_{j'}\right)\phi_n\left(\boldsymbol{r}\right) \tag{3.72}$$

is the hopping (transfer) integral. This term suggests that, through the interaction with a nucleus $R_{j'}$ (where $R_{j'}$ does not point to the same unit cell where orbital $\phi_n\left(\boldsymbol{r}\right)$ is localized), then an electron from orbital $\phi_n\left(\boldsymbol{r}\right)$ could be transferred to a neighboring orbital site.

We will mention here the terminology used to classify the Hamiltonian matrix elements [46, 47, 44]:

- on-site ⇒ the atomic wavefunctions and the potential are all centred on the same site
- two-centre ⇒ where a wavefunction and the potential are on the same site and the other wavefunction is on a different site

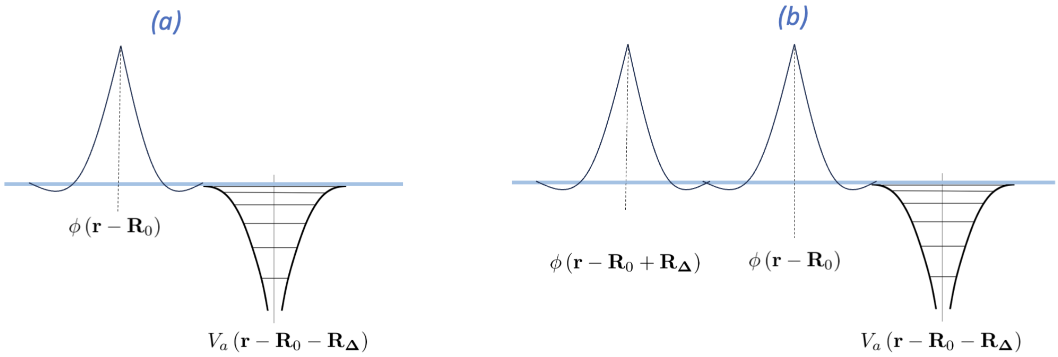

FIGURE 3.12: Representation of two-centre integrals (a) and three centre integrals in the TB model (Δ is the distantce to a nearest neighbor, while R_0 is the atomic site chosen as reference).

- Three-centre ⇒ the atomic wavefunctions and the potential are all on different sites. Therefore, the integral of the form of $\int d\mathbf{r}\phi_n{}^*\left(\mathbf{r}-\mathbf{R}_i\right)\mathcal{H}\phi_m\left(\mathbf{r}-\mathbf{R}_j\right)$ involves a product of an atomic wavefunction $\boldsymbol{\phi}_n{}^*\left(\mathbf{r}-\mathbf{R}_i\right)$ located on the atom at position $\mathbf{R}_i$, another atomic wavefunction $\phi_m\left(\mathbf{r}-\mathbf{R}_j\right)$ on the atom at $\mathbf{R}_j$, and a spherical potential function located on a third atom.

The Secular Equation

The eigenvalue problem in equation 3.66 can be rewritten in the form:

$$\det\left[\mathcal{H}_{mn}(\boldsymbol{k})-E_{\boldsymbol{k}}\mathcal{S}_{mn}(\boldsymbol{k})\right]=0, \tag{3.73}$$

where $\mathcal{H}_{mn}$ and $\mathcal{S}_{mn}$ are matrix elements of the Hamiltonian and of the overlap integrals:

$$\begin{aligned}\mathcal{H}_{mn}&=\frac{1}{N}\sum_{\mathbf{R},\mathbf{R}'}e^{i\mathbf{k}\cdot(\mathbf{R}'-\mathbf{R})}t^{mn}_{\mathbf{R},\mathbf{R}'} &\quad t^{mn}_{\mathbf{R},\mathbf{R}'}&=\langle\varphi_m(\mathbf{r}-\mathbf{R})|\,\mathcal{H}\,|\varphi_n\left(\mathbf{r}-\mathbf{R}'\right)\rangle\\ \mathcal{S}_{mn}&=\frac{1}{N}\sum_{\mathbf{R},\mathbf{R}'}e^{i\mathbf{k}\cdot(\mathbf{R}'-\mathbf{R})}s^{mn}_{\mathbf{R},\mathbf{R}'} &\quad s^{mn}_{\mathbf{R},\mathbf{R}'}&=\left\langle\varphi_m(\mathbf{r}-\mathbf{R})\mid\varphi_n\left(\mathbf{r}-\mathbf{R}'\right)\right\rangle,\end{aligned} \tag{3.74}$$

This is known as the *secular equation*. To solve the secular equation in Equation 3.73, one needs to evaluate the matrix elements of the Hamiltonian. Basically, the methods used to obtain these matrix elements and the level of approximation of the calculation will distinguish between various tight binding approaches. An example of the TB model applied to a lattice with multiple atoms in the unit cell (the Lieb lattice) is presented in C.

Application to the 1D chain

Let us write the TB Hamiltonian in a more intuitive form for a simple 1D chain lattice (one atom per uni cell) with only NN hopping and s-type orbitals only. Indices m and n are used to denote orbital sites (see figure 3.13). Hence, the hopping integral is:

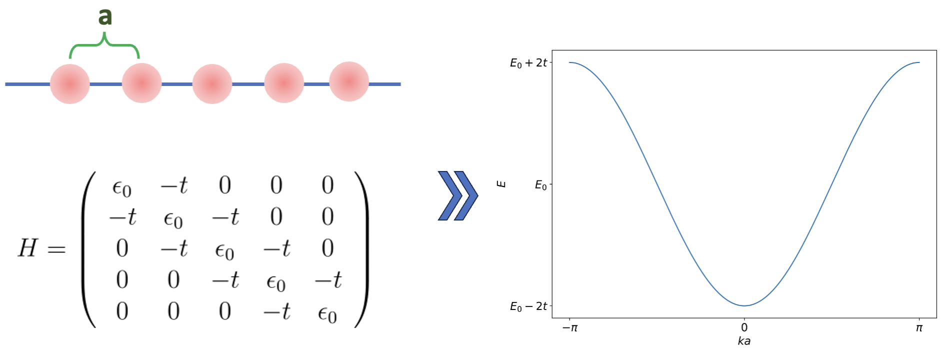

$$H = \begin{pmatrix} \epsilon_0 & -t & 0 & 0 & 0 \\ -t & \epsilon_0 & -t & 0 & 0 \\ 0 & -t & \epsilon_0 & -t & 0 \\ 0 & 0 & -t & \epsilon_0 & -t \\ 0 & 0 & 0 & -t & \epsilon_0 \end{pmatrix}$$

FIGURE 3.13: The TB Hamiltonian for an ideal 1D lattice with a one-atom basis and the corresponding dispersion relation.

$$t\left(\boldsymbol{R}_n - \boldsymbol{R}_m\right) = \begin{cases} \varepsilon_s & n = m \\ -t & n = m \pm 1 \\ 0 & \text{otherwise} \end{cases} \tag{3.75}$$

With the matrix elements defined in the section above, we obtain:

$$\begin{aligned} H_{n,m} = \epsilon_0 \delta_{n,m} - t\left(\delta_{n+1,m} + \delta_{n-1,m}\right), \\ \text{with} \quad \epsilon_0 = \epsilon_{at} + \varepsilon_s. \end{aligned} \tag{3.76}$$

$$H_{n,m} = \langle n|\, H\, |m\rangle = \epsilon_0 \delta_{n,m} - t\left(\delta_{n+1,m} + \delta_{n-1,m}\right) \tag{3.77}$$

If we apply the completeness relations $\sum_n |n\rangle \langle n| = I$, we get:

$$\begin{aligned} H &= \sum_{n,m} |n\rangle \langle n|\, H\, |m\rangle \langle m| \\ &= \sum_{n,m} \underbrace{\langle n|\, H\, |m\rangle}_{\epsilon_0} |n\rangle \langle m|\, \delta_{n,m} - \underbrace{\langle n|\, H\, |m\rangle}_{t} \left(\delta_{n+1,m} + \delta_{n-1,m}\right) |n\rangle \langle m| \\ &= \sum_n \epsilon_0 |n\rangle \langle n| - t \sum_n \left(|n+1\rangle \langle n| + |n\rangle \langle n+1|\right) \end{aligned} \tag{3.78}$$

We will encounter this simple 1D Hamiltonian in section 3.8, where we introduce a simulation tool based on the tight binding model.

Second quantization formulation

In the second quantization, the Hamiltonian is described in terms of creation and annihilation operators. Due to Pauli's exclusion principle, in the case of fermions, the creation and annihilation operators satisfy the anticommutation rule:

$$\left\{\hat{c}_s, \hat{c}_s^\dagger\right\} = \hat{c}_s \hat{c}_s^\dagger + \hat{c}_s^\dagger \hat{c}_s = 1 \tag{3.79}$$

If we neglect electron-electron interaction (two-body operators), the Hamiltonian in the language of the occupation number representation is written as:

$$\hat{\mathcal{H}} = \sum_{ij} \langle i|\mathcal{H}|j\rangle \hat{c}_i^\dagger \hat{c}_j \tag{3.80}$$

Since the term $\langle i|\mathcal{H}|j\rangle$ is associated to the hopping parameter t_{ij}, the TB Hamiltonian is:

$$\hat{\mathcal{H}} = \sum_{ij} t_{ij}\hat{c}_i^{\dagger}\hat{c}_j \tag{3.81}$$

A tight binding Hamiltonian that includes the nearest neighbors (NN) as well as the next-nearest neighbors (NNN) is:

$$\hat{\mathcal{H}} = \sum_{i} \epsilon_0\hat{c}_i^{\dagger}\hat{c}_i + \sum_{\langle ij\rangle} t_{ij}\hat{c}_i^{\dagger}\hat{c}_j + \sum_{\langle\langle ij\rangle\rangle} t'_{ij}\hat{c}_i^{\dagger}\hat{c}_j \tag{3.82}$$

3.5 The R-matrix method

3.5.1 Introduction to the R-matrix formalism

The R-matrix formalism was initially introduced in the context of nuclear reactions in the years 1946 and 1947 by Wigner and Eisenbud. In the 1960s, it became apparent that the method could be applied to a wider variety of atomic, molecular and optical systems, particularly in resonant processes [48]. The core idea of the R matrix formalism is to divide the entire space into multiple subspaces separated by a boundary, that are generally known as external and internal regions. In each region, the wavefunction is represented in different manners. While the external region is considered infinite and the wavefunction is described by asymptotic conditions, the hamiltonian of the internal region must describe the scattering processes or interaction potentials that encompass the defining features of the physical systems. In this manner, the formalism gained traction in the field of condensed matter also, since we can partition a nanostructure into the internal interaction (scattering) region and the leads with translational symmetry along the transport direction. Through the R matrix method, the scattering matrix on the system can be expressed in terms of the eigenfunctions of the Hamiltonian that describes the internal region, as long as the appropriate boundary conditions are chosen [49].

3.5.2 Theoretical overview and extensions of the formalism

The wavefuntion that describes a state of energy E is a solution of the Schrodinger equation:

$$\left[\frac{1}{2m^*}\mathbf{P}^2 + V_{(\mathbf{r})}\right]\Psi(E,\mathbf{r}) = E\Psi(E,\mathbf{r}), \tag{3.83}$$

where $\mathbf{P} = -i\hbar\nabla$ is the momentum operator, $V(\mathbf{r})$ is the effective potential and m^* is the effective mass. Consider the system in Figure 3.14 . The potential energy has a perpendicular component, which we assume to be independent of the z coordinate. Therefore, we can write the effective potential as:

$$V(\mathbf{r}) = V(z) + V_{\perp}(\mathbf{r}_{\perp}). \tag{3.84}$$

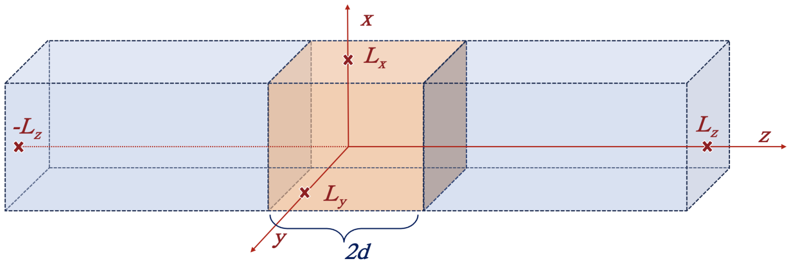

FIGURE 3.14: Scattering region with size $2d$ sandwiched between two leads (note that $d \ll L_z$)

Since the potential is separable, the solution to the Schrodinger equation can be written as a product of two wavefunctions:

$$\Psi_\nu^{(s)}(\mathbf{r};E) = \phi_\nu\left(\mathbf{r}_\perp\right)\psi^{(s)}(z;\epsilon), \tag{3.85}$$

where $E = E_\nu^\perp + \epsilon$, ν is an index for the energy levels $E_\perp$ and s is the index for the leads. The functions ϕ_ν and the energies $E_\perp$ are solutions of:

$$\left[\frac{1}{2m^*}\mathbf{P}_\perp^2 + V_\perp\left(\mathbf{r}_\perp\right)\right]\phi_\nu\left(\mathbf{r}_\perp\right) = E_\nu^\perp\phi_\nu\left(\mathbf{r}_\perp\right) \tag{3.86}$$

Also, the orthogonality and completeness relations are fulfilled:

$$\begin{gathered}\int d\mathbf{r}_\perp \phi_\nu^*\left(\mathbf{r}_\perp\right)\phi_{\nu'}\left(\mathbf{r}_\perp\right) = \delta_{\nu\nu'} \\ \sum_\nu \phi_\nu^*\left(\mathbf{r}_\perp\right)\phi_\nu\left(\mathbf{r}'_\perp\right) = \delta\left(\mathbf{r}_\perp - \mathbf{r}'_\perp\right)\end{gathered} \tag{3.87}$$

Now we will focus on the one dimensional problem (Figure 3.15):

$$\left[\frac{1}{2m^*}P_z^2 + V(z) - \epsilon\right]\psi^{(s)}(z,\epsilon) = 0. \tag{3.88}$$

The wavefunctions are a superposition of the incident waves and the scattered waves:

$$\psi(z,\epsilon) = \begin{cases} A\exp\left[ik_1(z+d)\right] + B\exp\left[-ik_1(z+d)\right], & z \leq -d \\ C\exp\left[-ik_2(z-d)\right] + D\exp\left[ik_2(z-d)\right], & z \geq d \end{cases} \tag{3.89}$$

where A, B, C and D are complex coefficients.

$$\begin{aligned} A &= \psi^{in}(\epsilon,-d); \\ B &= \psi^{\text{out}}(\epsilon,-d); \\ C &= \psi^{in}(\epsilon,d); \\ D &= \psi^{\text{out}}(\epsilon,d). \end{aligned} \tag{3.90}$$

The coefficients corresponding to the outgoing and incoming waves are related by means of the S matrix (scattering matrix) in the following manner:

$$\begin{pmatrix} \psi^{\text{out}}(\epsilon,-d) \\ \psi^{\text{out}}(\epsilon,+d) \end{pmatrix} = \mathbf{S}(\epsilon)\begin{pmatrix} \psi^{\text{in}}(\epsilon,-d) \\ \psi^{\text{in}}(\epsilon,+d) \end{pmatrix}, \tag{3.91}$$

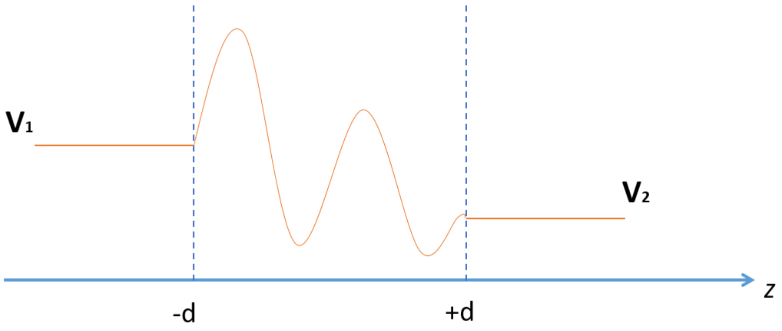

FIGURE 3.15: Schematic representation of a 1D scattering potential, showing the leads with constant potentials $V_{1,2}$ and the central region ranging from $(-d, d)$.

where

$$\mathbf{S}(\epsilon) = \begin{pmatrix} r & t \\ t & r \end{pmatrix}. \tag{3.92}$$

We can write

$$\begin{bmatrix} \psi^{\text{out}}(\epsilon, -d) \\ \psi^{\text{out}}(\epsilon, +d) \end{bmatrix} = \begin{bmatrix} S(\epsilon; -d, -d) & S(\epsilon; -d, +d) \\ S(\epsilon; +d, -d) & S(\epsilon; +d, +d) \end{bmatrix} \begin{bmatrix} \psi^{in}(\epsilon, -d) \\ \psi^{in}(\epsilon, +d) \end{bmatrix}, \tag{3.93}$$

where

$$\begin{bmatrix} S(\epsilon; -d, -d) & S(\epsilon; -d, +d) \\ S(\epsilon; +d, -d) & S(\epsilon; +d, +d) \end{bmatrix} = \begin{bmatrix} S_{11} & S_{12} \\ S_{21} & S_{22} \end{bmatrix} \tag{3.94}$$

Therefore, the scattering functions are:

$$\begin{aligned} \psi^{(1)}(\epsilon, z) &= \frac{\theta(\epsilon - V_1)}{\sqrt{2\pi}} \begin{cases} \exp[ik_1(z+d)] + S_{11}(\epsilon)\exp[-ik_1(z+d)], & z \leq -d \\ S_{21}(\epsilon)\exp[ik_2(z-d)], & z \geq d \end{cases} \\ \psi^{(2)}(\epsilon, z) &= \frac{\theta(\epsilon - V_2)}{\sqrt{2\pi}} \begin{cases} S_{12}(\epsilon)\exp[-ik_1(z+d)], & z \leq -d \\ \exp[-ik_2(z-d)] + S_{22}(\epsilon)\exp[ik_2(z-d)], & z \geq d \end{cases} \end{aligned} \tag{3.95}$$

where the step function is defined in the usual way:

$$\theta(\epsilon - V_s) = \begin{cases} 1, & \epsilon \geq V_s \\ 0, & \epsilon < V_s \end{cases}, \quad s = 1, 2 \tag{3.96}$$

Hence, if we have a particle coming from $z = -\infty$, the scattering states are described by

$$\psi^{(1)}(\epsilon, z) = \frac{1}{\sqrt{2\pi}} \begin{cases} \exp[ik_1(z+d)] + S_{11}(\epsilon)\exp[-ik_1(z+d)], & z \leq -d \\ S_{21}(\epsilon)\exp[ik_2(z-d)], & z \geq d \end{cases} \tag{3.97}$$

and if the particle is incident from $z = +\infty$, we have:

$$\psi^{(2)}(\epsilon, z) = \frac{1}{\sqrt{2\pi}} \begin{cases} S_{12}(\epsilon)\exp[-ik_1(z+d)], & z \leq -d \\ \exp[-ik_2(z-d)] + S_{22}(\epsilon)\exp[ik_2(z-d)], & z \geq d \end{cases} \tag{3.98}$$

The transmission and reflection coefficients are:

$$\begin{aligned} r^{(1)}(\epsilon) &= S_{11}(\epsilon), \\ t^{(1)}(\epsilon) &= S_{21}(\epsilon), \\ r^{(2)}(\epsilon) &= S_{22}(\epsilon), \\ t^{(2)}(\epsilon) &= S_{12}(\epsilon). \end{aligned} \tag{3.99}$$

Also, we can rewrite the equations above in matrix form:

$$\begin{bmatrix} \psi^{(1)}(\epsilon; -d) & \psi^{(1)}(\epsilon; +d) \\ \psi^{(2)}(\epsilon; -d) & \psi^{(2)}(\epsilon; +d) \end{bmatrix} = \frac{1}{\sqrt{2\pi}} \left[\ \mathbf{1} + \mathbf{S}^t(\epsilon)\ \right] \tag{3.100}$$

where $\mathbf{1}$ is the unit matrix and $\mathbf{S}^t$ is the transpose of the scattering matrix.

Also, we can write the matrix of the derivatives at the interface

$$\begin{bmatrix} \frac{d}{dz}\psi^{(1)}(\epsilon, z)\Big|_{z=-d} & \frac{d}{dz}\psi^{(1)}(\epsilon, z)\Big|_{z=+d} \\ \frac{d}{dz}\psi^{(2)}(\epsilon, z)\Big|_{z=-d} & \frac{d}{dz}\psi^{(2)}(\epsilon, z)\Big|_{z=+d} \end{bmatrix} = -\frac{i}{\sqrt{2\pi}} \frac{2\pi}{d} \mathbf{K}(\epsilon) \left[\ \mathbf{1} - \mathbf{S}^t(\epsilon)\ \right] \tag{3.101}$$

where

$$\mathbf{K}(\epsilon) = \begin{pmatrix} \frac{k_1}{\pi/2d} & 0 \\ 0 & \frac{k_2}{\pi/2d} \end{pmatrix} \tag{3.102}$$

or

$$K_{ss'} = \frac{2d}{\pi} k_s \delta_{ss'}$$

The main idea of the R-matrix formalism is that for an arbitrary potential in the scattering region, the functions $\psi^{(s)}(z, \epsilon)$ have to be expanded into a basis of eigenfunctions of a problem that can be solved. We write the Schrodinger equation in the interaction region

$$\left[-\frac{\hbar^2}{2m^*} \frac{d^2}{dz^2} + V(z) - \epsilon_l \right] \chi_l(z) = 0 \tag{3.103}$$

and impose the following boundary conditions:

$$\frac{d\chi_l}{dz}\bigg|_{z=\pm d} = 0. \tag{3.104}$$

$\chi_l(z)$ are known as the Wigner-Eisenbud functions, they are defined only in the interval $z \in [-d, d]$ and verify the orthogonality and completeness conditions:

$$\begin{aligned} \int_{-d}^{d} dz \chi_l(z) \chi_{l'}(z) &= \delta_{ll'}, \\ \sum_l \chi_l(z) \chi_l\left(z'\right) &= \delta\left(z - z'\right), \end{aligned} \tag{3.105}$$

The wavefunctions in the scattering region are expanded in terms of the Wigner-Eisenbud functions:

$$\psi^{(s)}(\epsilon, z) = \sum_l a_l^{(s)}(\epsilon) \chi_l(z), \tag{3.106}$$

with the expansion coefficients

$$a_l^{(s)}(\epsilon) = \int_{-d}^{d} dz \chi_l(z) \psi^{(s)}(\epsilon, z). \tag{3.107}$$

In order to compute the expansion coefficients we multiply equation 3.88 by $\chi_l^*(z)$ and equation 3.103 by $\psi^{(s)}(\epsilon, z)$ and then integrate the difference between the two over the interval $[-d, d]$. We integrate by parts, taking the boundary conditions into account, and obtain:

$$a_l^{(s)}(\epsilon) = -\frac{\hbar^2}{2m^*}\frac{1}{\epsilon - \epsilon_l}\left[\chi_l(d)\frac{d\psi^{(s)}}{dz}\bigg|_{z=+d} - \chi_l(-d)\frac{d\psi^{(s)}}{dz}\bigg|_{z=-d}\right]. \tag{3.108}$$

We define now the R-function:

$$R(\epsilon; z, z') = \frac{\hbar^2}{2m^*}\frac{\pi}{2d}\sum_l \frac{\chi_l(z)\chi_l(z')}{\epsilon - \epsilon_l}, \tag{3.109}$$

and the R-matrix:

$$R(\epsilon) = \begin{pmatrix} R(\epsilon; -d, -d) & R(\epsilon; d, -d) \\ R(\epsilon; -d, d) & R(\epsilon; d, d) \end{pmatrix} \tag{3.110}$$

If we insert equation 3.108 into equation 3.106, we obtain the expression for the scattering functions in the region $z \in [-d, d]$:

$$\psi^{(s)}(\epsilon, z) = \frac{2d}{\pi}\left[R(\epsilon; -d, z)\frac{\partial\psi^{(s)}}{\partial z}\bigg|_{z=-d} - R(\epsilon; d, z)\frac{\partial\psi^{(s)}}{\partial z}\bigg|_{z=d}\right]. \tag{3.111}$$

Together with 3.101, we obtain the scattering functions in terms of the R and S matrices:

$$\begin{aligned} \psi^{(1)}(\epsilon, z) &= \frac{\theta(\epsilon - V_1)}{\sqrt{2\pi}}\frac{2d}{\pi}\left\{ik_1\left[1 - \mathbf{S}_{11}(\epsilon)\right]R(\epsilon; -d, z) - ik_2\mathbf{S}_{21}(\epsilon)R(\epsilon; d, z)\right\}, \\ \psi^{(2)}(\epsilon, z) &= \frac{\theta(\epsilon - V_2)}{\sqrt{2\pi}}\frac{2d}{\pi}\left\{-ik_1\mathbf{S}_{12}(\epsilon)R(\epsilon; -d, z) + ik_2\left[1 - \mathbf{S}_{22}(\epsilon)\right]R(\epsilon; d, z)\right\} \end{aligned}. \tag{3.112}$$

3.5.3 The two-dimensional R-matrix method

The Schrödinger equation that describes the whole system is:

$$\left(-\frac{\hbar}{2m^*}\Delta + V(\mathbf{r})\right)\cdot\Psi(\mathbf{r}; E) = E\cdot\Psi(\mathbf{r}; E) \tag{3.113}$$

As we discussed in the previous section, the potential in the leads is separable and can be written as a sum of a longitudinal and transversal part:

$$V_s(\mathbf{r}) = V_\perp\left(\mathbf{r}_{\perp,s}\right) \tag{3.114}$$

In the leads, the solution of the Schrodinger equation is a superposition of the incident and reflected wavefunction:

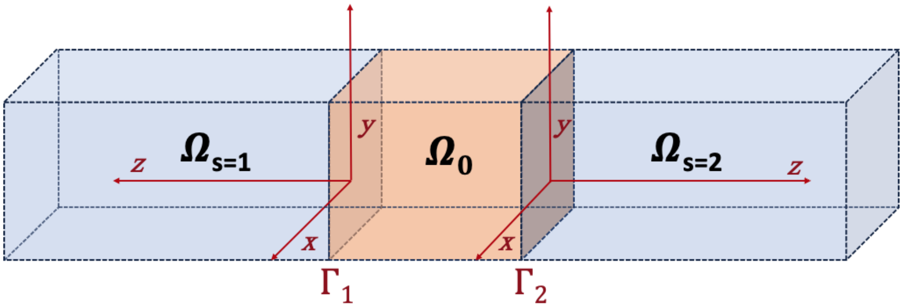

FIGURE 3.16: The scheme of the device. The surfaces Γ_1 and Γ_2 separate the interaction region Ω_0 from the leads 1 and 2.

$$\Psi_s\left(\mathbf{r}\in\Omega_s;E\right)=\sum_i \Psi_\nu^{\text{in}}\cdot e^{-ik_\nu z_s}\cdot\Phi_\nu\left(\mathbf{r}_{\perp,s}\right)+\sum_i \Psi_\nu^{\text{out}}\cdot e^{ik_\nu z_s}\cdot\Phi_\nu\left(\mathbf{r}_{\perp,s}\right), \tag{3.115}$$

where the longitudinal wave vector is:

$$k_\nu=\frac{\sqrt{2m^*\left(E-E_\nu^\perp\right)}}{\hbar}. \tag{3.116}$$

The transverse modes are solutions to the following Schrodinger equation:

$$\left(-\frac{\hbar}{2m^*}\Delta+V_{\perp,s}\left(\mathbf{r}_{\perp,s}\right)\right)\cdot\Phi_\nu\left(\mathbf{r}_{\perp,s}\right)=E_\nu^\perp\cdot\Phi_\nu\left(\mathbf{r}_{\perp,s}\right) \tag{3.117}$$

In the scattering region, we solve the Wigner-Eisenbud problem

$$\left(-\frac{\hbar}{2m^*}\Delta+V(\mathbf{r})\right)\cdot\chi_l(\mathbf{r})=\epsilon_l\cdot\chi_l(\mathbf{r}), \tag{3.118}$$

with the same boundary conditions proposed in the first chaper:

$$\left.\frac{\partial\chi_l}{\partial z_s}\right|_{\Gamma_s}=0 \tag{3.119}$$

We multiply equation 3.113 by $\chi_l^*(z)$ and equation 3.118 by $\Psi(\mathbf{r})$, then we substract them and integrate over the scattering region, to obtain:

$$-\frac{\hbar}{2m^*}\iiint_{\Omega_0}\left(\triangle\Psi(\mathbf{r})\cdot\chi_l^*(\mathbf{r})-\triangle\chi_l^*(\mathbf{r})\cdot\Psi(\mathbf{r})\right)d^3\mathbf{r}=(E-\epsilon_l)\iiint_{\Omega_0}\Psi(\mathbf{r})\cdot\chi_l^*(\mathbf{r})d^3\mathbf{r} \tag{3.120}$$

We expand the wavefunction in the basis of the Wigner-Eisenbud functions:

$$\Psi(\mathbf{r})=\sum_l a_l\cdot\chi_l(\mathbf{r}) \tag{3.121}$$

Also, we use Green's identity

$$\int_D(f\Delta g-g\Delta f)dV=\int_{\partial D}(f\nabla g-g\nabla f)\cdot\mathbf{n}\cdot dS \tag{3.122}$$

and from equation 3.120 it follows that:

$$\begin{aligned}
a_l\left(E-\epsilon_l\right) &= -\frac{\hbar^2}{2m^*}\int_{\Gamma=\sum_s \Gamma_s} \mathbf{n}_\Gamma\cdot\left(\chi_l^*\nabla\Psi-\Psi\nabla\chi_l^*\right)d\Gamma \\
&= -\frac{\hbar^2}{2m^*}\int_\Gamma \left(\chi_l^*\cdot\mathbf{n}_\Gamma\cdot\nabla\Psi-\Psi\cdot\mathbf{n}_\Gamma\cdot\nabla\chi_l^*\right)d\Gamma \\
&= -\frac{\hbar^2}{2m^*}\sum_s\int_{\Gamma_s}\left(\chi_l^*|_{\Gamma_s}\left.\frac{\partial\Psi}{\partial z_s}\right|_{\Gamma_s}-\Psi|_{\Gamma_s}\left.\frac{\partial\chi_l^*}{\partial z_s}\right|_{\Gamma_s}\right)d\Gamma_s
\end{aligned} \tag{3.123}$$

where $\mathbf{n}_\Gamma$ is the normal to the cross-section of the leads.Hence, the expansion coefficients are:

$$a_l\left(E-\epsilon_l\right) = -\frac{\hbar^2}{2m^*}\sum_s\int_{\Gamma_s}\left(\chi_l^*|_{\Gamma_s}\left.\frac{\partial\Psi}{\partial z_s}\right|_{\Gamma_s}\right)d\Gamma_s \tag{3.124}$$

Now we impose the continuity condition of the wavefunction at the boundaries:

$$\Psi(\mathbf{r})|_{\Gamma_s} = \Psi_s(\mathbf{r})|_{\Gamma_s} \tag{3.125}$$

We apply now $\int_{\Gamma_s}\phi_i\left(\vec{r}_{\perp,s}\right)d\Gamma_s$ on 3.125. For the left side of the equation we obtain

$$\int_{\Gamma_s}\phi_i\left(\mathbf{r}_{\perp,s}\right)\cdot\Psi(\mathbf{r})\Big|_{\Gamma_s}d\Gamma_s = \int_{\Gamma_s}\phi_i\left(\mathbf{r}_{\perp,s}\right)\cdot\sum_l a_l\cdot\chi_l(\mathbf{r})\Big|_{\Gamma_s}d\Gamma_s \tag{3.126}$$

and using the expression for the expansion coefficients 3.124, we have the following result:

$$\begin{aligned}
\int_{\Gamma_s}\phi_i\left(\mathbf{r}_{\perp,s}\right)\cdot\Psi(\mathbf{r})\Big|_{\Gamma_s}d\Gamma_s = -\frac{\hbar^2}{2m^*}\sum_l\frac{1}{E-\epsilon_l}\sum_{s'}\int_{\Gamma_s}\phi_i\left(\mathbf{r}_{\perp,s}\right)\cdot\chi_l(\mathbf{r})\Big|_{\Gamma_s}d\Gamma_s \\
\times\int_{\Gamma_{s'}}\left(\chi_l^*\cdot\frac{\partial\Psi}{\partial z_{s'}}\right)\Big|_{\Gamma_{s'}}d\Gamma_{s'}
\end{aligned} \tag{3.127}$$

For the right hand side of the equation, we have:

$$\int_{\Gamma_s}\phi_i\left(\mathbf{r}_{\perp,s}\right)\cdot\Psi_s(\mathbf{r})\Big|_{\Gamma_s}d\Gamma_s = \int_{\Gamma_s}\phi_i\left(\mathbf{r}_{\perp,s}\right)\sum_{i'}\left(\Psi_\nu^{\text{in}}\cdot\phi_{i'}\left(\mathbf{r}_{\perp,s}\right)+\Psi_\nu^{\text{out}}\cdot\phi_{i'}\left(\mathbf{r}_{\perp,s}\right)\right)d\Gamma_s \tag{3.128}$$

$$\Rightarrow \int_{\Gamma_s}\phi_i\left(\mathbf{r}_{\perp,s}\right)\cdot\Psi_s(\mathbf{r})\Big|_{\Gamma_s}d\Gamma_s = \Psi_\nu^{\text{in}}+\Psi_\nu^{\text{out}} \tag{3.129}$$

Now we impose the continuity condition for the derivatives

$$\frac{1}{m^*}\cdot\left.\frac{\partial\Psi}{\partial z_s}\right|_{\Gamma_s} = \frac{1}{m^*}\cdot\left.\frac{\partial\Psi_s}{\partial z_s}\right|_{\Gamma_s} = \frac{1}{m^*}\left(-i\sum_{i'}k_{\nu'}\left(\Psi_{\nu'}^{\text{in}}-\Psi_{\nu'}^{\text{out}}\right)\phi_{i'}\left(\mathbf{r}_{\perp,s}\right)\right) \tag{3.130}$$

and define the R function as we did in 3.109 :

$$R\left(\mathbf{r},\mathbf{r}';E\right) = -\frac{\hbar^2}{2m^*}\sum_l\frac{\chi_l(\mathbf{r})\cdot\chi_l^*\left(\mathbf{r}'\right)}{E-\epsilon_l} \tag{3.131}$$

and the R-matrix:

$$R_{\nu\nu'} = \int_{\Gamma_s} \int_{\Gamma_{s'}} \phi_i \left(\mathbf{r}_{\perp,s}\right) \cdot \phi_{i'} \left(\mathbf{r}_{\perp,s'}\right) \cdot R\left(\mathbf{r} \in \Gamma_s, \mathbf{r}' \in \Gamma_{s'}; E\right) d\Gamma_{s'} d\Gamma_s \tag{3.132}$$

We insert equation 3.131 into 3.132 and obtain:

$$R_{\nu\nu'} = -\frac{\hbar^2}{2m^*} \sum_l \frac{1}{E-\epsilon_l} \int_{\Gamma_s} \phi_i \left(\mathbf{r}_{\perp,s}\right) \cdot \chi_l \left(\mathbf{r} \in \Gamma_s\right) d\Gamma_s \cdot \int_{\Gamma_{s'}} \phi_{i'} \left(\mathbf{r}_{\perp,s}\right) \cdot \chi_l^* \left(\mathbf{r}' \in \Gamma_{s'}\right) d\Gamma_{s'} \tag{3.133}$$

If we define

$$\int_{\Gamma_s} \phi_i \left(\mathbf{r}_{\perp,s}\right) \cdot \chi_l \left(\mathbf{r} \in \Gamma_s\right) d\Gamma_s = \left(\chi_l\right)_\nu$$

and

$$\int_{\Gamma_{s'}} \phi_{i'} \left(\mathbf{r}_{\perp,s}\right) \cdot \chi_l^* \left(\mathbf{r}' \in \Gamma_{s'}\right) d\Gamma_{s'} = \left(\chi_l\right)_{\nu'}^*,$$

the R-matrix is:

$$R_{\nu\nu'} = -\frac{\hbar^2}{2m^*} \sum_l \frac{\left(\chi_l\right)_\nu \cdot \left(\chi_l\right)_{\nu'}^*}{E-\epsilon_l}. \tag{3.134}$$

From the continuity conditions, we get

$$\Psi_\nu^{\text{in}} + \Psi_\nu^{\text{out}} = -i \sum_{\nu'} R_{\nu\nu'} \cdot k_{\nu'} \left(\Psi_{\nu'}^{\text{in}} - \Psi_{\nu'}^{\text{out}}\right), \tag{3.135}$$

and we can rewrite the relation above as:

$$\begin{aligned} \sum_{\nu'} \Psi_\nu^{\text{in}} \delta_{\nu\nu'} + \sum_{\nu'} \Psi_\nu^{out} \delta_{\nu\nu'} &= -\sum_{\nu'} i R_{\nu\nu'} k_{\nu'} \cdot \Psi_{\nu'}^{\text{in}} + \sum_{\nu'} i R_{\nu\nu'} k_{\nu'} \cdot \Psi_{\nu'}^{\text{out}} \\ \rightarrow \sum_{\nu'} \left(\delta_{\nu\nu'} - i R_{\nu\nu'} k_{\nu'}\right) \cdot \Psi_{\nu'}^{\text{out}} &= -\sum_{\nu'} \left(\delta_{\nu\nu'} + i R_{\nu\nu'} k_{\nu'}\right) \cdot \Psi_{\nu'}^{\text{in}} \end{aligned} \tag{3.136}$$

Therefore, we obtain a relation between the S and R matrices:

$$S_{\nu\nu'} = -\left(\delta_{\nu\nu'} - i R_{\nu\nu'} k_{\nu'}\right)^{-1} \cdot \left(\delta_{\nu\nu'} + i R_{\nu\nu'} k_{\nu'}\right) \tag{3.137}$$

Now we can work with the current scattering matrix:

$$\tilde{\mathbf{S}}(E) = \mathbf{K}^{1/2}(E) S(E) \mathbf{K}^{-1/2}(E), \tag{3.138}$$

which is unitary:

$$\tilde{\mathbf{S}}(E) \tilde{\mathbf{S}}^\dagger(E) = \tilde{\mathbf{S}}^\dagger(E) \tilde{\mathbf{S}}(\epsilon) = \hat{\mathbf{1}}. \tag{3.139}$$

The transmission is expressed in terms of $\tilde{\mathbf{S}}$:

$$T_{\nu\nu'}(E) = \left|\tilde{S}_{\nu\nu'}(E)\right|^2 \tag{3.140}$$

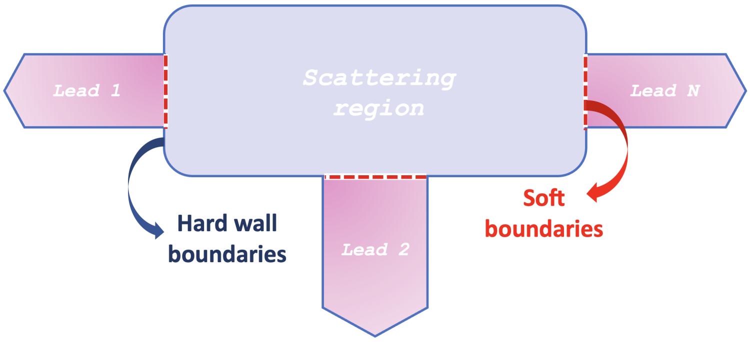

FIGURE 3.17: Schematic representation of a two-dimensional device for transport calculations. The mathematical surfaces that separate the interior region (scattering region) from the N leads do not necessarily correspond to physical interfaces (adapted from [51]).

3.5.4 The R-matrix method for spin dependent transport

The total state is constructed from direct product:

$$|\Psi\rangle = \int d^3x \,(\Psi_+(\mathbf{x})|\mathbf{x}\rangle \otimes |\uparrow\rangle + \Psi_-(\mathbf{x})|\mathbf{x}\rangle \otimes |\downarrow\rangle) \equiv \begin{pmatrix} |\Psi_+\rangle \\ |\Psi_-\rangle \end{pmatrix}$$

To simply the notations, we will write the spinor as:

$$|\Psi\rangle = \sum_\sigma \Psi_\sigma(x,y)|\sigma\rangle = \Psi_\uparrow|\uparrow\rangle + \Psi_\downarrow|\downarrow\rangle \tag{3.141}$$

To be or not to be Hermitian

Let us focus briefly on the 1D case, where the interaction region is in the finite interval $[a,b]$. The Schrödinger equation in the whole space is:

$$H\Psi(x) = E\Psi(x), \quad \text{where} \quad H = -\frac{\hbar^2}{2m}\frac{d^2}{dx^2} + V(x) \quad -\infty < x < \infty.$$

However, note that H is not Hermitian in the $[a,b]$ interval, since:

$$\begin{aligned} &\int dx\,[\Psi_1(x)H\Psi_2(x) - \Psi_2(x)H\Psi_1(x)]] \\ &= -\frac{\hbar^2}{2m}\left[\Psi_1(x)\Psi_2'(x) - \Psi_1'(x)\Psi_2(x)\right]_a^b \end{aligned} \tag{3.142}$$

To avoid the problems arising from the non-Hermiticity of Hamiltonian operator in the scattering finite region, we will add a *boundary surface Bloch operator* defined generally as [50]:

$$\mathcal{L}_\mathcal{B} = \frac{\hbar^2}{2m}\left[\delta(x-a)\left(\frac{d}{dx} - \lambda_a\right) - \delta(x-b)\left(\frac{d}{dx} - \lambda_b\right)\right], \tag{3.143}$$

where λ depends on the chosen boundary condition for the Wigner-Eisenbud functions: $\frac{\partial \chi_1}{\partial z_s}\Big|_{\mathbf{r}_s} = \lambda_s \cdot \chi_1\big|_s$.

In this case,

$$\begin{aligned}
&\int_a^b dx \left[\Psi_1(x)\left(H+\mathcal{L}_\mathcal{B}\right)\Psi_2(x) - \Psi_2(x)\left(H+\mathcal{L}_\mathcal{B}\right)\Psi_1(x)\right]] \\
&= -\frac{\hbar^2}{2m}\int_a^b dx \left[\Psi_1(x)\left(\frac{d^2}{dx^2}+\mathcal{L}_\mathcal{B}\right)\Psi_2 - \Psi_1(x)\left(\frac{d^2}{dx^2}+\mathcal{L}_\mathcal{B}\right)\Psi_2(x)\right] \\
&= -\frac{\hbar^2}{2m}\int_a^b dx \left[\Psi_1(x)\left(\frac{d^2}{dx^2}\right)\Psi_2 - \Psi_1(x)\left(\frac{d^2}{dx^2}\right)\Psi_2(x)\right] \\
&- \frac{\hbar^2}{2m}\int_a^b dx \left[\Psi_1(x)\left(\delta(x-a)\left(\frac{d}{dx}-\lambda_a\right) - \delta(x-b)\left(\frac{d}{dx}-\lambda_b\right)\right)\Psi_2\right] \\
&- \frac{\hbar^2}{2m}\int_a^b dx \left[\Psi_2(x)\left(\delta(x-a)\left(\frac{d}{dx}-\lambda_a\right) - \delta(x-b)\left(\frac{d}{dx}-\lambda_b\right)\right)\Psi_1\right] \\
&= -\frac{\hbar^2}{2m}\left[\Psi_1(x)\frac{d}{dx}\Psi_2(x) - \Psi_2(x)\frac{d}{dx}\Psi_1(x)\right]_a^b \\
&- \frac{\hbar^2}{2m}\left[\Psi_1(x)\delta(x-a)\left(\frac{d}{dx}+1\right)\Psi_2(x) - \Psi_2(x)\delta(x-b)\left(\frac{d}{dx}-1\right)\Psi_1(x)\right]_a^b \\
&= -\frac{\hbar^2}{2m}\left[\left[\left(\Psi_1(x)\frac{d}{dx}\Psi_2(x) + \Psi_2(x)\frac{d}{dx}\Psi_1(x)\right)\right]_{x=b} - \left[\left(\Psi_2(x)\frac{d}{dx}\Psi_1(x) + \Psi_1(x)\frac{d}{dx}\Psi_2(x)\right)\right]_{x=a}\right] \\
&= 0,
\end{aligned} \tag{3.144}$$

where we used the well-known property of the delta Dirac distribution:

$$\lim_{\epsilon\to 0+}\int^{a_0+\epsilon} f(r)\delta\left(r-a_0\right)\mathrm{d}r = f\left(a_0\right), \tag{3.145}$$

We will see in the following how this procedure is equivalent to rewriting the Hamiltonian as $\tilde{H}_{mn} = \left(H_{mn}+H^*_{nm}\right)/2$.

Bloch operators

A multi-terminal system, that can be solved with the R-matrix method is displayed schematically in Figure 3.17. The leads and the scattering region meet at a set of boundary surfaces that are known as "soft boundaries" (see Figure 3.17), where we consider Dirichlet or von-Neumann conditions for the WE functions. On the other hand, the boundaries between the coloured shaded areas and the unshaded regions are treated as as “hard walls” (infinite potential outside the boundary), so the electron wave functions are nonzero only in the shaded regions [51]. Note that these boundaries are mathematical, and they do not necessarily correspond to the physical setup of the of the multi-terminal system.

The time independent Schrodinger equation for the scattering region is:

$$\mathcal{H}\Psi = \left(\mathbf{T}+\mathbf{V}+\mathbf{H}_{\mathrm{SO}}\right)\Psi = E\Psi \tag{3.146}$$

where T is the kinetic energy operator, V stands for the potential and H_{SO} accounts for the spin orbit-coupling Hamiltonian. We have discussed how, in a finite region (e.g. the scattering region), the Hamiltonian is not Hermitian and in order to produce a Hermitian operator we add to $\mathcal{H}$ the Bloch operator $\mathcal{L}_\mathcal{B}$ [52, 48].

First, let us take a closer look at our system Hamiltonian expressed in matrix form. The kinetic energy term can be written as:

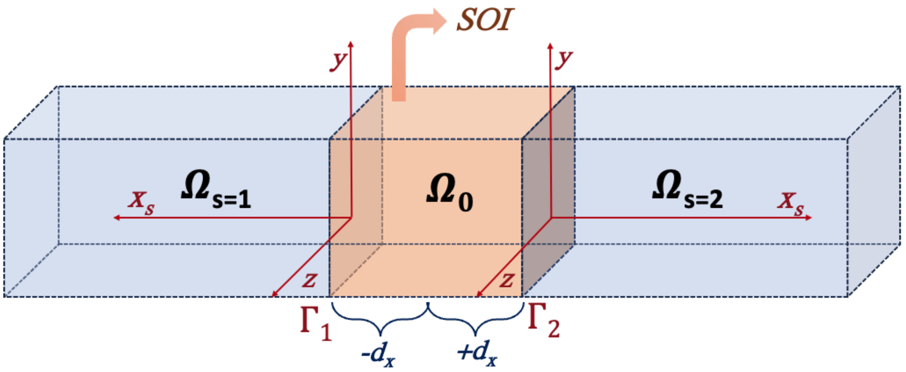

FIGURE 3.18: The scheme of the device. The surfaces Γ_1 and Γ_2 separate the interaction region Ω_0 from the leads 1 and 2.

$$\mathbf{T} = -\frac{\hbar^2}{2m} \cdot \left[\frac{\partial^2}{\partial x^2} + \frac{\partial^2}{\partial y^2}\right] \cdot \mathbf{I}_\sigma \tag{3.147}$$

where I_σ is the identity matrix. For the spin orbit coupling part, we will first consider a typical Rashba SOI interaction, usually expressed as:

$$\begin{aligned}\mathbf{H}_{SO} &= \frac{\alpha}{\hbar}\left(p_y\sigma_x - p_x\sigma_y\right) = \frac{\alpha}{\hbar}\left(-i\hbar\frac{\partial}{\partial y}\sigma_x + i\hbar\frac{\partial}{\partial x}\sigma_y\right) \\ &= i\alpha\left(\frac{\partial}{\partial x}\sigma_y - \frac{\partial}{\partial y}\sigma_x\right)\end{aligned} \tag{3.148}$$

where α is the Rashba coefficient, a material dependent parameter that can also be controlled by an external electric field. We can also write the Hamiltonian directly in matrix form, as follows:

$$\mathcal{H} = \begin{pmatrix} -\frac{\hbar^2}{2m}\Delta + V & \frac{\alpha}{\hbar}\left(ip_x + p_y\right) \\ \frac{\alpha}{\hbar}\left(-ip_x + p_y\right) & -\frac{\hbar^2}{2m}\Delta + V \end{pmatrix} = \begin{pmatrix} -\frac{\hbar^2}{2m}\Delta + V & \alpha\left(\frac{\partial}{\partial x} - i\frac{\partial}{\partial y}\right) \\ \alpha\left(-\frac{\partial}{\partial x} - i\frac{\partial}{\partial y}\right) & -\frac{\hbar^2}{2m}\Delta + V \end{pmatrix} \tag{3.149}$$

Adding the Bloch operators, the Schrodinger equation for the system is:

$$\left(\mathbf{T} + \mathcal{L}_T + \mathbf{V} + \mathbf{H}_{SO} + \mathcal{L}_{SO}\right)\Psi = E\Psi + \mathcal{L}_T\Psi + \mathcal{L}_{SO}\Psi \tag{3.150}$$

The Wigner-Eisenbud equation, written in the scattering region takes the form:

$$\left(\mathbf{T} + \mathcal{L}_T + \mathbf{V} + \mathbf{H}_{SO} + \mathcal{L}_{SO}\right)\chi_l = \epsilon_l\chi_l, \tag{3.151}$$

with the boundary conditions:

$$\left.\frac{\partial\chi_l}{\partial x_s}\right|_{\Gamma_s} = \lambda_{\Gamma_s}\cdot\chi_l|_{\Gamma_s} \tag{3.152}$$

The Bloch operators $\mathcal{L}_T$ and $\mathcal{L}_{SO}$ in 2D Hilbert space are defined as:

$$\begin{aligned}\mathcal{L}_T &= \frac{\hbar^2}{2m}\sum_s \delta_{x,x_s}\left(\frac{\partial}{\partial z_s} - \lambda_{\Gamma_s}\right)\cdot I_\sigma, \\ \mathcal{L}_{SO} &= -i\frac{\alpha}{2}\sum_s \eta_s\delta_{x,x_s}\cdot\sigma_y = -i\frac{\alpha}{2}\sum_s \eta_s\delta_{x,x_s}\cdot\begin{pmatrix} 0 & -i \\ i & 0 \end{pmatrix},\end{aligned} \tag{3.153}$$

where $\eta_s = \langle \widehat{x_s}, \widehat{x} \rangle$ is a vector perpendicular to the cross-section of the lead (Γ_s) and I_σ is the identity matrix. In our two-terminal 2D example, the two boundaries are situated at (see Figure 3.18):

$$\begin{aligned} x_1 &= -d_x = a, \\ x_2 &= +d_x = b, \end{aligned}$$

and therefore $\eta_1 = -1$ and $\eta_2 = +1$. Hence, the Bloch operator corresponding to the kinetic energy term is:

$$\mathcal{L}_{\mathcal{T}} = +\frac{\hbar^2}{2m}\left[(+1)\cdot\delta(x-a)\left(-\frac{\partial}{\partial x}-(-\lambda_a)\right)+(+1)\cdot\delta(x-b)\left(-\frac{\partial}{\partial x}-(\lambda_b)\right)\right] \cdot \begin{pmatrix} 1 & 0 \\ 0 & 1 \end{pmatrix}. \tag{3.154}$$

The Bloch operator for spin orbit coupling can also be expressed in a different manner, which will become useful in the future calculations:

$$\begin{aligned} \mathcal{L}_{\mathrm{SO}} &= -i\frac{\alpha}{2}\sum_s \eta_s\delta(z-z_s)\sigma_y = -i\frac{\alpha}{2}\sum_s \eta_s\delta(x-x_s)\cdot\begin{pmatrix} 0 & -i \\ i & 0 \end{pmatrix} \\ \mathcal{L}_{\mathrm{SO}} &= -\frac{\alpha}{2}\left[(-1)\cdot\delta(x-a)+(+1)\delta(x-b)\right]\cdot\begin{pmatrix} 0 & 1 \\ -1 & 0 \end{pmatrix} \\ \Rightarrow \mathcal{L}_{\mathrm{SO}} &= -i\frac{\alpha}{2}\sum_s \eta_s\delta(x-x_s)i\cdot\left(|\downarrow\rangle\,|\uparrow\rangle - |\uparrow\rangle\,\langle\downarrow|\right) \\ &= \frac{\alpha}{2}\sum_s \eta_s\delta(x-x_s)\left(|\downarrow\rangle\,|\uparrow\rangle - |\uparrow\rangle\,\langle\downarrow|\right) \end{aligned} \tag{3.155}$$

where $s = 1,2$ and $\eta_1 = -1$, $\eta_2 = +1$.

We know that:

$$\begin{cases} T + \mathcal{L}_T & = T^\dagger + \mathcal{L}_T^\dagger \\ V & = V^\dagger \\ H_{SO} + \mathcal{L}_{SO} & = H_{SO}^\dagger + \mathcal{L}_{SO}{}^\dagger \end{cases} \tag{3.156}$$

From equations 3.150 and 3.151, we obtain the following relation:

$$0 = (E-\epsilon_l)\underbrace{\langle\chi_l|\psi\rangle}_{a_l} + \langle\chi_l|L_T\Psi\rangle + \langle\chi_l|L_{SO}\psi\rangle \tag{3.157}$$

$$\Rightarrow a_l(E-\epsilon_l) = -\langle\chi_l|L_T\psi\rangle - \langle\chi_l|L_{SO}\psi\rangle \tag{3.158}$$

Let us now compute the terms on the r.h.s of equation 3.158. First, keep in mind that the wavefunctions also account for the spin degreee of freedom:

$$\begin{aligned} |\chi_l\rangle &= \sum_\sigma \chi_{l,\sigma}(x,y)\cdot|\sigma\rangle \\ |\Psi\rangle &= \sum_\sigma \Psi_\sigma(x,y)\cdot|\sigma\rangle \end{aligned} \tag{3.159}$$

Hence, the terms we are interested in are:

$$
\begin{aligned}
-\langle\chi_l|\mathcal{L}_{\mathcal{T}}\psi\rangle &= -\frac{\hbar^2}{2m}\sum_{\sigma'\sigma}\sum_s\int_{\Gamma_s} d\Gamma_s\cdot\left[\chi^*_{l,s}\big|_{\Gamma_s}\frac{\partial\psi_{\sigma'}}{\partial z_s}\right]\langle\sigma|\sigma'\rangle \\
&= -\frac{\hbar^2}{2m}\sum_{\sigma}\sum_s\int_{\Gamma_s} d\Gamma_s\cdot\left[\chi^*_{l,s}\big|_{\Gamma_s}\frac{\partial\psi_{\sigma}}{\partial z_s}\right]
\end{aligned}
\tag{3.160}
$$

$$
-\langle\chi_l|\mathcal{L}_{\mathcal{SO}}\psi\rangle = -\frac{\alpha}{2}\sum_s\sum_\sigma\int_{\Gamma_s} d\Gamma\eta_s\sigma\,\chi^*_{l,-\sigma}\big|_{\Gamma_s}\,\psi_\sigma\big|_{\Gamma_s},
\tag{3.161}
$$

where we used the following relations:

$$
\begin{aligned}
\mathcal{L}_{\mathcal{SO}}\left|\psi\right\rangle &= \mathcal{L}_{\mathcal{SO}}\left(\sum_\sigma\psi_\sigma\left|\sigma\right\rangle\right)\sim -i\sigma_y\left(\sum_\sigma\psi_\sigma\left|\sigma\right\rangle\right) \\
&= \psi_\uparrow\left|\downarrow\right\rangle - \psi_\downarrow\left|\uparrow\right\rangle \\
\langle\chi_l|\mathcal{L}_{\mathcal{SO}}\Psi\rangle &\sim \langle\chi_{l,\uparrow}\left|\uparrow\right\rangle - \chi_{l,\downarrow}\left|\downarrow\right\rangle|\Psi_\uparrow\left|\downarrow\right\rangle - \Psi_\downarrow\left|\uparrow\right\rangle\rangle \\
&= -\chi^*_{l,\uparrow}\Psi_\downarrow + \chi^*_{l,\downarrow}\Psi_\uparrow \\
&= \sum_\sigma\sigma\cdot\chi^*_{l,-\sigma}\Psi_\sigma
\end{aligned}
\tag{3.162}
$$

where $\sigma = \pm 1$, corresponding to $\left|\uparrow\right\rangle, \left|\downarrow\right\rangle$. For a detailed derivation of these relations in the particular cases of Rashba and Dresselhaus SOCs, check Appendix E.

Now we turn our attention to the scattering states, adapted to the spinful case:

$$
\Psi_s\left(\mathbf{r}\in\Omega_s;E\right) = \sum_{i,\sigma}\Psi^{\text{in}}_\nu\cdot e^{-ik_\nu z_s}\cdot\Phi_\nu\left(\mathbf{r}_{\perp,s}\right)\cdot\left|\sigma\right\rangle + \sum_{i,\sigma}\Psi^{\text{out}}_\nu\cdot e^{ik_\nu z_s}\cdot\Phi_\nu\left(\mathbf{r}_{\perp,s}\right)\cdot\left|\sigma\right\rangle
\tag{3.163}
$$

At the boundary of the interaction region ($z_s = 0$), the lead wavefunction is:

$$
\Psi_s\left(\mathbf{r}\in\Omega_s;E\right)\Bigg|_{\Gamma_s} = \sum_{i,\sigma}\Psi^{\text{in}}_\nu\cdot\Phi_\nu\left(\mathbf{r}_{\perp,s}\right)\cdot\left|\sigma\right\rangle + \sum_{i}\Psi^{\text{out}}_\nu\cdot\Phi_\nu\left(\mathbf{r}_{\perp,s}\right)\cdot\left|\sigma\right\rangle
\tag{3.164}
$$

and it has to be equal to the wavefunction in the scattering region, expressed as a linear combination of Wigner-Eisenbud functions:

$$
\Psi\left(\mathbf{r}\in\Omega_s;E\right)\Bigg|_{\Gamma_s} = \sum_{l,\sigma}a_l\cdot\chi_{l,\sigma}(\mathbf{r})\Bigg|_{\Gamma_s}\cdot\left|\sigma\right\rangle
\tag{3.165}
$$

Now we multiply to the left with $\Phi(\mathbf{r}_\perp, s)$ and project the equations in spin space:

$$
\langle\sigma'|\left\langle\Phi(\mathbf{r}_\perp,s)\right|\Psi_s(\mathbf{r})\Bigg|_s = \langle\sigma'|\left\langle\Phi(\mathbf{r}_\perp,s)\right|\Psi(\mathbf{r})\Bigg|_s
\tag{3.166}
$$

From this, we obtain:

$$
\begin{aligned}
\Psi^{in}_\nu + \Psi^{out}_\nu &= \int_{\Gamma_s} d\Gamma_s\cdot\Phi_i(\mathbf{r}_{\perp,s})\cdot\sum_{l,\sigma}a_l\cdot\chi_{l,\sigma}(\mathbf{r})\cdot\langle\sigma'|\sigma\rangle \\
&= \sum_l\int_{\Gamma_s} d\Gamma_s\cdot\Phi_i(\mathbf{r}_{\perp,s})\cdot\chi_{l,\sigma}(\mathbf{r})\cdot a_l,
\end{aligned}
\tag{3.167}
$$

similarly to the approach presented in 3.5.3. Insert the expression for the WE coefficients derived in equation 3.158 to obtain:

$$\begin{gathered}\Psi_\nu^{in} + \Psi_\nu^{out} = \int_{\Gamma_s} d\Gamma_s \cdot \boldsymbol{\Phi}_i(\mathbf{r}_\perp, s) \cdot \sum_{l,\sigma} \chi_{l,\sigma}(\mathbf{r}) \cdot \frac{1}{E - \epsilon_l} \\ \cdot \left[-\frac{\hbar^2}{2m} \sum_{s,\sigma} \int_{\Gamma_s'} d\Gamma_s' \cdot \left(\chi_{l,s'}^* \frac{\partial \Psi_{\sigma'}}{\partial z_s'} \right) \Bigg|_{\Gamma_s'} - \frac{\alpha(x)}{2} \sum_{s',\sigma'} \int_{\Gamma_{s'}} d\Gamma_{s'} \eta_{s'} \sigma \cdot (\chi_{l,-\sigma'}^* \Psi_{\sigma'}) \Bigg|_{\Gamma_s'} \right]\end{gathered} \tag{3.168}$$

The partial derivative and the scattering function at the boundary Γ_s are:

$$\begin{aligned} \frac{\partial \Psi_{\sigma'}}{\partial z_s} \Bigg|_{\Gamma_s} &= -i \sum_{i'} k_{\nu'} \left[\Psi_{\nu'}^{in} - \Psi_{\nu'}^{out} \right] \cdot \boldsymbol{\Phi}_{i'} \\ \psi_{\sigma'} \Bigg|_{\Gamma_s} &= \sum_{i'} \left[\Psi_{\nu'}^{in} + \Psi_{\nu'}^{out} \right] \cdot \boldsymbol{\Phi}_{i'} \end{aligned} \tag{3.169}$$

Replacing 3.169 into 3.168, we get:

$$\begin{gathered} \Psi_\nu^{in} + \Psi_\nu^{out} = \sum_l \frac{1}{E - \epsilon_l} \int_{\Gamma_s} d\Gamma_s \cdot \boldsymbol{\Phi}_i(\mathbf{r}_{\perp,s}) \cdot \chi_{l,\sigma} \Bigg|_{\Gamma_s} \cdot \\ \left[-\frac{\hbar^2}{2m} \sum_{s',i',\sigma'} \int_{\Gamma_{s'}} d\Gamma_{s'} \cdot \chi_{l,\sigma'}^* \Bigg|_{\Gamma_{s'}} \boldsymbol{\Phi}_{i',\sigma'}(-ik_{\nu'}) \left[\Psi_{\nu'}^{in} - \Psi_{\nu'}^{out} \right] - \right. \\ \left. \frac{\alpha(x)}{2} \sum_{s',i',\sigma'} \int_{\Gamma_{s'}} d\Gamma_{s'} \eta_{s'} \sigma' \chi_{l,-\sigma'} \Bigg|_{\Gamma_{s'}} \cdot \boldsymbol{\Phi}_{i',\sigma'} \cdot \left[\Psi_{\nu'}^{in} + \Psi_{\nu'}^{out} \right] \right] \end{gathered} \tag{3.170}$$

Finally, we can write that:

$$\Psi_\nu^{in} + \Psi_\nu^{out} = -i \sum_{\nu'} R_{\nu\nu'} k_{\nu'} \left[\Psi_{\nu'}^{in} - \Psi_{\nu'}^{out} \right] + \sum_{\nu'} \left[\Psi_{\nu'}^{in} + \Psi_{\nu'}^{out} \right] Q_{\nu\nu'}, \tag{3.171}$$

where

$$\begin{aligned} R_{\nu\nu'} &= -\frac{\hbar^2}{2m} \sum_l \frac{\int_{\Gamma_s} d\Gamma_s \boldsymbol{\Phi}_{i,\sigma} \chi_{l,\sigma} \Big|_{\Gamma_s} \cdot \int_{\Gamma_{s'}} d\Gamma_{s'} \boldsymbol{\Phi}_{i',\sigma'} \chi_{l,\sigma'}^* \Big|_{\Gamma_{s'}}}{E - \epsilon_l} \\ Q_{\nu\nu'} &= -\frac{\alpha(x)}{2} \sum_l \frac{\int_{\Gamma_s} d\Gamma_s \boldsymbol{\Phi}_{i,\sigma} \chi_{l,\sigma} \Big|_{\Gamma_s} \cdot \int_{\Gamma_{s'}} d\Gamma_{s'} \eta_{s'} \sigma' \cdot \boldsymbol{\Phi}_{i',\sigma'} \chi_{l,-\sigma'}^* \Big|_{\Gamma_{s'}}}{E - \epsilon_l} \end{aligned} \tag{3.172}$$

with $\nu = (s, i, \sigma)$. Therefore, equation 3.171 can be written as:

$$\sum_{\nu'} \left[\delta_{\nu\nu'} - ik_{\nu'} R_{\nu\nu'} - Q_{\nu\nu'} \right] \Psi_{\nu'}^{out} = -\sum_{\nu'} \left[\delta_{\nu\nu'} + ik_{\nu'} R_{\nu\nu'} - Q_{\nu\nu'} \right], \tag{3.173}$$

arriving at the formula for the scattering matrix:

$$S = -\frac{1 - Q + iR\kappa}{1 - Q - iR\kappa} = -\left[1 - Q - iR\kappa\right]^{-1} \cdot \left[1 - Q + iR\kappa\right] \tag{3.174}$$

If the SOI is restricted to the scattering region, then $Q = 0$, so the S-matrix defined above becomes:

$$S = -\frac{1 + iR\kappa}{1 - iR\kappa} = -\left[1 - iR\kappa\right]^{-1} \cdot \left[1 + iR\kappa\right] \tag{3.175}$$

$$\tilde{S} = \kappa^{1/2} S \kappa^{-1/2} \tag{3.176}$$

Application of Bloch operators to Rashba and Dresselhaus SOI

Let us now apply the method of Bloch operators for two SOI Hamiltonians that are prevalent in quantum transport applications: the Rashba and Dressealhaus spin-orbit coupling.

The Rashba spin orbit interaction is defined as:

$$\begin{aligned} H_R &= \frac{\alpha}{\hbar}\left(p_y\sigma_x - p_x\sigma_y\right) = \frac{\alpha}{\hbar}\left(-i\hbar\frac{\partial}{\partial y}\sigma_x + i\hbar\frac{\partial}{\partial x}\sigma_y\right) \\ &= i\alpha\left(\frac{\partial}{\partial x}\sigma_y - \frac{\partial}{\partial y}\sigma_x\right), \end{aligned} \tag{3.177}$$

and in matrix form:

$$H_R = \begin{pmatrix} 0 & \frac{\partial}{\partial x} - i\frac{\partial}{\partial y} \\ -\frac{\partial}{\partial x} - i\frac{\partial}{\partial y} & 0 \end{pmatrix} \tag{3.178}$$

The Dresselhaus spin-orbit interaction is:

$$\begin{aligned} H_D &= \frac{\beta}{\hbar}\left(p_x\sigma_x - p_y\sigma_y\right) = \frac{\beta}{\hbar}\left(-i\hbar\frac{\partial}{\partial x}\sigma_x + i\hbar\frac{\partial}{\partial y}\sigma_y\right) \\ &= i\beta\left(-\frac{\partial}{\partial x}\sigma_x + \frac{\partial}{\partial y}\sigma_y\right) \end{aligned} \tag{3.179}$$

In matrix form, the Hamiltonian is written as:

$$H_D = \begin{pmatrix} 0 & -i\frac{\partial}{\partial x} + \frac{\partial}{\partial y} \\ -i\frac{\partial}{\partial x} - \frac{\partial}{\partial y} & 0 \end{pmatrix} \tag{3.180}$$

The Bloch operator is:

$$\mathcal{L}_R = \frac{1}{2}\frac{\partial\alpha(x)}{\partial x} i\sigma_y = \frac{1}{2}\frac{\partial\alpha}{\partial x}\begin{pmatrix} 0 & 1 \\ -1 & 0 \end{pmatrix} \tag{3.181}$$

and if we consider that $\alpha(x)$ is a Heavisided function, with a finite value only inside the scattering region, then:

$$\mathcal{L}_R = \frac{\alpha}{2}\left(\delta(x-a) - \delta(x-b)\right) i\sigma_y = -\frac{\alpha}{2}\sum_s \eta_s \delta(x - x_s) i\sigma_y \tag{3.182}$$

Let us separate the Rashba Hamiltonian matrix into:

$$\mathcal{H}_R = \frac{\alpha}{2}\left[\begin{pmatrix} 0 & \frac{\partial}{\partial x} \\ -\frac{\partial}{\partial x} & 0 \end{pmatrix} + \begin{pmatrix} 0 & -i\frac{\partial}{\partial y} \\ -i\frac{\partial}{\partial y} & 0 \end{pmatrix}\right] = \frac{\alpha}{2}\left(H_R^x + H_R^y\right) \tag{3.183}$$

Let us focus first on H_R^x and prove that is is not Hermitian:

Reminder 2: Adjoint of a linear operator

The linear operator $H^\dagger$ associated with H is, in general, defined as:

$$\langle v|H^\dagger|u\rangle = \langle u|Hv\rangle \tag{3.184}$$

More explicitly:

$$\langle v|H^\dagger|u\rangle = \langle u|H^\dagger|v\rangle^*, \qquad \forall u, v. \tag{3.185}$$

$$\begin{aligned}
\langle\phi_i|\, H_R^x - H_R^{x\dagger}\, |\phi_j\rangle &= \langle\phi_i|\frac{\partial}{\partial x}|\phi_j\rangle - \overline{\langle\phi_j| - \frac{\partial}{\partial x}|\phi_i\rangle} \\
&= \int_a^b dx\phi_i^* \frac{\partial}{\partial x}\phi_j - \int_a^b dx\overline{\phi_j^* \left(-\frac{\partial}{\partial x}\right)\phi_i} \\
&= \int_a^b dx\phi_i^* \frac{\partial}{\partial x}\phi_j - \int_a^b dx\phi_j^* \left(-\frac{\partial}{\partial x}\phi_i^*\right) \\
&= \int_a^b dx\left[\frac{\partial}{\partial x}\left(\phi_i^*\phi_j\right) - \frac{\partial}{\partial x}\phi_i^* \cdot \phi_j\right] + \int_a^b dx\phi_j\frac{\partial}{\partial x}\phi_i^* \\
&= \phi_i^*\phi_j\Big|_a^b
\end{aligned} \tag{3.186}$$

From Equation 3.182:

$$\begin{aligned}
\langle\phi_i|\, \mathcal{L}_R - \mathcal{L}_R^\dagger\, |\phi_j\rangle &= \langle\phi_i|\mathcal{L}_R|\phi_j\rangle - \overline{\langle\phi_j| - \mathcal{L}_R|\phi_i\rangle} \\
&= \frac{\alpha}{2}\left[\phi_i^*\phi_j\Big|_a - \phi_i^*\phi_j\Big|_b + \phi_j\phi_i^*\Big|_a - \phi_j\phi_i^*\Big|_b\right] \quad = -\alpha\phi_i^*\phi_j\Big|_a^b
\end{aligned} \tag{3.187}$$

Notice that:

$$\mathcal{H}_R - \mathcal{H}_R^\dagger + \mathcal{L}_R - \mathcal{L}_R^\dagger = 0 \tag{3.188}$$

We follow the same procedure for the Dresselhaus SOI, focusing on the non-Hermitian part of the Hamiltonian:

$$H_D^x = \begin{pmatrix} 0 & -i\frac{\partial}{\partial x} \\ -i\frac{\partial}{\partial x} & 0 \end{pmatrix} \tag{3.189}$$

In a similar manner, we show that:

$$\begin{aligned}
\langle\phi_i|\, H_D^x - H_D^{x\dagger}\, |\phi_j\rangle &= \langle\phi_i| - i\frac{\partial}{\partial x}|\phi_j\rangle - \overline{\langle\phi_j| + i\frac{\partial}{\partial x}|\phi_i\rangle} \\
&= -i\int_a^b dx\phi_i^*\frac{\partial}{\partial x}\phi_j - i\int_a^b dx\phi_j\left(\frac{\partial}{\partial x}\phi_i^*\right) \\
&= -i\phi_i^*\phi_j\Big|_a^b
\end{aligned} \tag{3.190}$$

The Bloch operator for the Dresselhaus SOC is defined in the same way:

$$\mathcal{L}_D = -\frac{\beta}{2}\left(\delta(x-a) - \delta(x-b)\right) i\sigma_x = \frac{\beta}{2}\sum_s \eta_s \delta(x - x_s) i\sigma_x, \tag{3.191}$$

and we can prove that:

$$\begin{aligned} \langle\phi_i|\, \mathcal{L}_D - \mathcal{L}_D^\dagger \,|\phi_i\rangle &= \langle\phi_i|\mathcal{L}_D|\phi_j\rangle - \overline{\langle\phi_j|\mathcal{L}_D|\phi_i\rangle} \\ &= -i\frac{\beta}{2}\left[\phi_i^*\phi_j\Big|_a^b - \phi_i^*\phi_j\Big|_b + \phi_i\phi_j^*\Big|_a - \phi_i\phi_j^*\Big|_b\right] \\ &= +i\beta\phi_i^*\phi_j\Big|_a^b \end{aligned} \tag{3.192}$$

Similarly, we proved that:

$$\mathcal{H}_D - \mathcal{H}_D^\dagger + \mathcal{L}_D - \mathcal{L}_D^\dagger = 0 \tag{3.193}$$

To summarize, we proved that:

$$\mathcal{L}_R - \mathcal{L}_R^\dagger = \begin{pmatrix} 0 & L \\ -L & 0 \end{pmatrix} - \begin{pmatrix} 0 & -L \\ L & 0 \end{pmatrix} = 2\begin{pmatrix} 0 & L \\ -L & 0 \end{pmatrix} = 2\mathcal{L}_R \tag{3.194}$$

and

$$\mathcal{L}_D - \mathcal{L}_D^\dagger = \begin{pmatrix} 0 & iL \\ iL & 0 \end{pmatrix} - \begin{pmatrix} 0 & -iL \\ -iL & 0 \end{pmatrix} = 2\begin{pmatrix} 0 & iL \\ iL & 0 \end{pmatrix} = 2\mathcal{L}_D,$$

where $L = \langle\phi_1|\, \mathcal{L}_{D,R} \,|\phi_2\rangle$.

Also,

$$\begin{aligned} \mathcal{H} - \mathcal{H}^\dagger + \mathcal{L} - \mathcal{L}^\dagger &= 0 \\ \Rightarrow \mathcal{H} + \mathcal{L} &= \frac{\mathcal{H} + \mathcal{H}^\dagger}{2} \end{aligned} \tag{3.195}$$

Observation 1: Hermitian operator

Adding a Bloch operator to a non-Hermitian Hamiltonian is equivalent to:

$$\mathcal{H} - \mathcal{H}^\dagger + \mathcal{L} - \mathcal{L}^\dagger = 0 \Rightarrow \mathcal{H} + \mathcal{L} = \frac{\mathcal{H} + \mathcal{H}^\dagger}{2}, \tag{3.196}$$

which automatically creates a Hermitian operator.

3.5.5 Implementation and numerical simulations

Following the overview of the R-matrix formalism, it became clear that computing the R-matrix requires first solving the Wigner-Eisenbud problem. Numerically, this involves solving the eigenvalue problem:

$$H\chi_l = \epsilon_l \chi_l, \tag{3.197}$$

with the appropriate boundary conditions:

$$\frac{\partial \chi_l}{\partial z_s}\Big|_{\Gamma_s} = 0$$

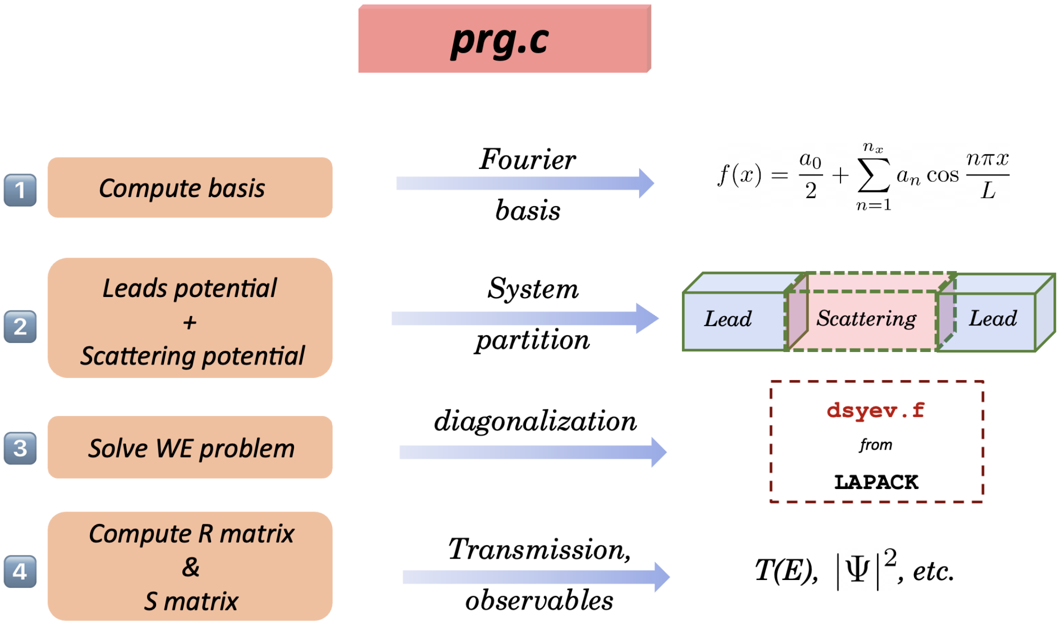

FIGURE 3.19: Brief workflow of how the R matrix code is built

Basically, we need to diagonalize the Hamiltonian matrix and to do that first we have to write the Wigner-Eisenbud functions χ_l in a basis that obeys the costraints imposed by the specified boundary conditions. The systems discussed in this thesis are two-dimensional, so we will exemplify the choice of basis functions for a 2D case.

Assuming we choose the coordinates x and y to represent the 2D scattering region, we then associate with it a 2D grid indexed by integers (i, j). The potential is separable, therefore our basis functions can be expressed as a product between their x and y components:

$$u_m(x, y) = u_x^i(x) \cdot u_y^j(y), \quad \text{with} \quad m \equiv (i, j), \tag{3.198}$$

where

$$\begin{aligned} u_x^i(x) &= \begin{cases} \frac{1}{\sqrt{2d_x}} & , i = 0 \\ \frac{1}{\sqrt{d_x}} \cos\left(i \cdot \frac{\pi}{2d_x}\,(x + d_x)\right) & , 1 \leq i \leq N_{b_x} - 1 \end{cases} \\ u_y^j(y) &= \frac{1}{\sqrt{d_y}} \sin\left((j+1)\frac{\pi}{2d_y}\,(y + d_y)\right), 0 \leq j \leq N_{b_y} - 1. \end{aligned} \tag{3.199}$$

The number of basis elements is determined by N_{b_x} and N_{b_y}. Equation 3.199 is a Fourier basis written in discretized form. This is an orthonormal basis and it also satisfies the boundary conditions which impose that the derivative must be zero at the boundary between the scattering region and the leads.

The Hamiltonian matrix elements are :

$$H_{mm'} = \langle u_m | \, H \, | u_{m'} \rangle \tag{3.200}$$

If we account for the spin, the Hilbert space is doubled and we express the Hamiltonian in a block matrix form, as we have also evidenced in the previous section:

$$H = \begin{pmatrix} \langle \uparrow |H| \uparrow \rangle & \langle \uparrow |H| \downarrow \rangle \\ \langle \downarrow |H| \uparrow \rangle & \langle \downarrow |H| \downarrow \rangle \end{pmatrix} \tag{3.201}$$

In order to implement the diagonalization procedure, we employed the LAPACK library [53]. Three diagonalization subroutines can be used:

- DSYEV computes all eigenvalues and, optionally, eigenvectors of a real symmetric matrix A.
- ZHEEV computes all eigenvalues and, optionally, eigenvectors of a complex Hermitian matrix A.

We chose the *ZHEEV* subroutine, since we are dealing with complet but Hermitian matrices.

3.6 The exact diagonalization method

The non-interacting one-body Hamiltonian for an electron in a two-dimensional confinement potential $V(\mathbf{r})$ is:

$$H_0 = -\frac{\hbar^2}{2m^*}\left(\frac{\partial^2}{\partial x^2} + \frac{\partial^2}{\partial y^2}\right) + V\left(r\right), \tag{3.202}$$

where m^* is the effective mass and $\mathbf{r} \equiv (x, y)$ is the position vector in two-dimensions.

The N-particle Hamiltonian is written as a sum of the single particle operators and the two-body operator, which describes the Coulomb interaction:

$$\mathcal{H} = \sum_{i=1}^{N} H_i + \frac{1}{2}\sum_i \sum_j V_{ij}, \tag{3.203}$$

where

$$\begin{aligned} H_i &= H_0\left(\mathbf{r}_i\right), \\ V_{ij} &= V_C\left(\mathbf{r}_i, \mathbf{r}_j\right) = \frac{e^2}{4\pi\epsilon_0\epsilon_r}\frac{1}{\left|\mathbf{r}_i - \mathbf{r}_j\right|}. \end{aligned} \tag{3.204}$$

The Hamiltonian in the second quantization becomes:

$$\mathcal{H} = \mathcal{H}_0 + \mathcal{H}_{\text{int}} = \sum_a \epsilon_a c_a^\dagger c_a + \frac{1}{2}\sum_{abcd} V_{abcd} c_a^\dagger c_b^\dagger c_d c_c \tag{3.205}$$

The matrix elements of the Coulomb potential are calculated in terms of the single-particle eigenfunctions

$$V_{abcd} = \left\langle \phi_a(\mathbf{r})\phi_b\left(\mathbf{r}'\right) \left| V_C\left(\mathbf{r} - \mathbf{r}'\right) \right| \phi_c(\mathbf{r})\phi_d\left(\mathbf{r}'\right) \right\rangle, \tag{3.206}$$

which can be explicitly written as:

$$\begin{aligned} V_{abcd} = &\int d\mathbf{r} \int d\mathbf{r}' \sum_{\sigma_z, \sigma_z'} \phi^*_{a,\sigma_z}(\mathbf{r})\phi^*_{b,\sigma_z'}\left(\mathbf{r}'\right) \\ &\times \frac{e^2}{4\pi\epsilon_0\epsilon_r}\frac{1}{\left|\mathbf{r} - \mathbf{r}'\right|}\phi_{c,\sigma_z}(\mathbf{r})\phi_{d,\sigma_z'}\left(\mathbf{r}'\right). \end{aligned} \tag{3.207}$$

Having determined the matrix elements V_{abcd}, one may proceed with the diagonalization of the N-particle Hamiltonian [54]:

$$\mathcal{H}\Psi_n = E_n\Psi_n, \tag{3.208}$$

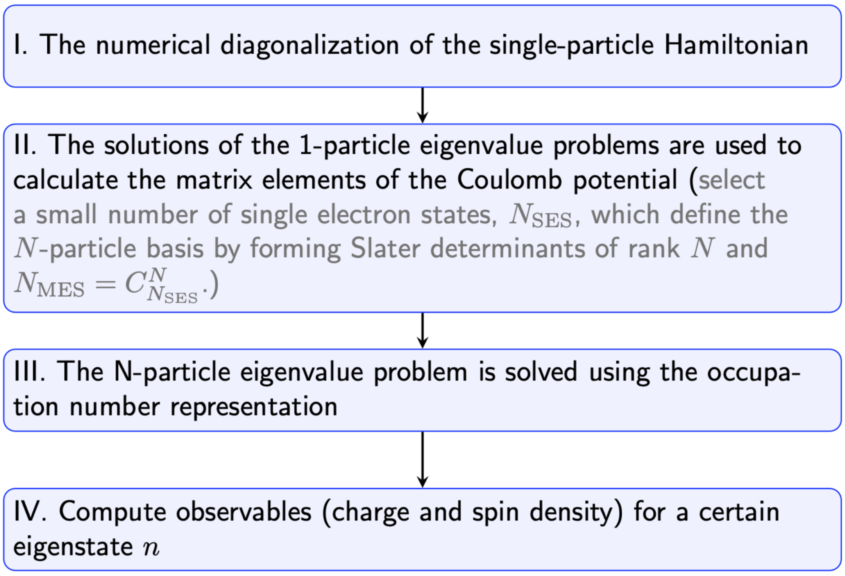

I. The numerical diagonalization of the single-particle Hamiltonian

II. The solutions of the 1-particle eigenvalue problems are used to calculate the matrix elements of the Coulomb potential (select a small number of single electron states, N_{SES}, which define the N-particle basis by forming Slater determinants of rank N and $N_{\mathrm{MES}} = C^N_{N_{\mathrm{SES}}}$.)

III. The N-particle eigenvalue problem is solved using the occupation number representation

IV. Compute observables (charge and spin density) for a certain eigenstate n

FIGURE 3.20: Workflow of the exact diagonalization numerical implementation

where E_n and $\Psi_n \equiv \Psi_n\left(\mathbf{r}_1, \sigma_{z1}, \ldots, \mathbf{r}_{\mathrm{N}}, \sigma_{z\mathrm{N}}\right)$ are the eigenvalues and eigenfunctions of the many-body system.

3.6.1 Numerical implementation

The exact diagonalization method relies on the fact that if we define a finite basis of many-particle states of dimension $D = N_{MES}$, then we can compute the matrix elements of the Hamiltonian of the system $H_{ij} = \langle\psi_i|\, H\, |\psi_j\rangle$.

The first step is the diagonlization of the single particle Hamiltonian $\mathcal{H}_0$, so for a finite system we define a two-dimensional basis which also accounts for the spin:

$$\begin{aligned} |\phi_k\rangle &= \sum_{\sigma_z} \sum_{k}^{N_b^2} |\mathcal{U}_k^{xy}\rangle \otimes |\sigma_z\rangle\,, \\ \mathcal{U}_k^{(xy)} &= u_i(x) \times u_j(y), \end{aligned} \tag{3.209}$$

where $u_i(x) = \sqrt{\frac{2}{L}} \sin\left(i\frac{\pi}{L}\left(x + \frac{L}{2}\right)\right)$ and $k = (i, j)$. The number of basis elements along the two spatial directions is $N_b = N_{bx} = N_{by}$ and the total basis size is $2 \times N_b^2$. The single particle eigenvalue problem to solve is

$$\mathcal{H}_0 \Phi_a(x, y) = \epsilon_a \Phi_a(x, y) \tag{3.210}$$

and to this end we evaluate the matrix elements $\left\langle \varphi_{k\sigma_z} \left|\mathcal{H}_0\right| \varphi_{k'\sigma_z'} \right\rangle$ on a real space grid with $N_x \times N_y$ points. The eigenfunctions are used to calculate the matrix elements of the Coulomb potential V_{abcd}, which is one of the most computationally demanding part. For this reason, we select a small number of single electron states N_{SES} which in turn define the dimension of the N-particle basis $N_{\mathrm{MES}} = C^N_{N_{\mathrm{SES}}}$.

After the single-particle Hamiltonian is diagonalized and we have the pairs of eigenvalues end eigefunctions $\{\epsilon_a; \Phi_a\}$, then we consider that the many-body Hilbert space is spanned by the Fock states built from the previously selected single-particle states. In the occupation number representation, any Fock state can be formally written as a sequence of particle numbers occupying a certain state:

$$|\psi_k\rangle = |n_1^{(k)} n_2^{(k)} ... n_s^{(k)} ...\rangle \tag{3.211}$$

3.7 Wavefunction matching

Wave function matching (WFM) is an intuitive and transparent technique in transport, that can be explained with fundamental quantum mechanical concepts. It was introduced by Ando in 1991 [55], in order to perform efficient numerical transport calculations in ballistic mesoscopic strictures. The WFM method aids directly with the calculation of transmission and reflection coefficients for any nano-system that can be represented through an appropriate tight binding Hamiltonian. As the name directly suggests, this method is based on the matching of the wave function in the scattering region with the wave functions in the leads, also known as Bloch modes [56, 57]. This is rooted in a fundamental tenet of quantum mechanics, namely the continuity of the wavefunctions and their first order derivatives at the potential boundary.

In this section, we will briefly explain the WFM method for the simple case of a 1D wire with a scattering region and two terminals, following the reasoning presented in [57, 58]. Through this approach, we also highlight the relation between the WFM method and the tight binding and NEGF formalisms discusses in the previous sections.

The first step is to discretize the Schrodinger equation by approximating the second derivative with a finite difference expression:

$$f''(x) \approx \frac{\frac{f(x+h)-f(x)}{h} - \frac{f(x)-f(x-h)}{h}}{h} = \frac{f(x+h) - 2f(x) + f(x-h)}{h^2}. \tag{3.212}$$

The physical meaning behind this well known mathematical approximation shall become more transparent in the next section. Using the formula above, one can express the eigenvalue problem in the following manner:

$$-\frac{\hbar^2}{2m}\left\{\frac{(\psi_{i+1} - 2\psi_i + \psi_{i-1})}{(\delta x)^2}\right\} + V_i\psi_i = E\psi_i, \tag{3.213}$$

where $\delta x = x_{i+1} - x_i$ (the distance between the equidistant points on the grid).

Due to the translational invariance along the transport direction, the solutions in the leads are plane waves indexed by the wavevectors k_L and k_R:

$$k_L = \frac{\sqrt{2m\,(E - V_L)}}{\hbar}; k_R = \frac{\sqrt{2m\,(E - V_R)}}{\hbar}. \tag{3.214}$$

At point $i = 0$, the discretized Schrodinger equation is:

$$E\psi_0 + \frac{\hbar^2}{2m(\delta x)^2}\{\psi_1 - 2\psi_0 + \psi_{-1}\} - V_0\psi_0 = 0 \tag{3.215}$$

The general form of the wave function is:

$$\psi(x) = Ae^{ik_L x} + Be^{-ik_L x}, \tag{3.216}$$

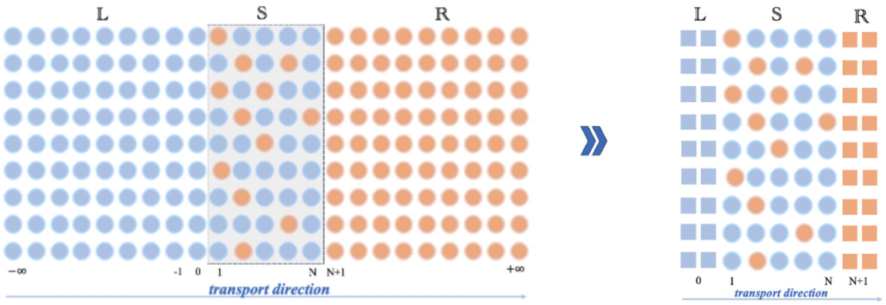

FIGURE 3.21: Pictorial representation of a two terminal 2D system., partitioned into a scattering region (S) centered between left and right leads. The semi-infinite leads are modeled with an effective finite Hamiltonian, by adding self-energy terms in the right and left terminals (*adapted from* [57]).

capturing the suerposition between the incoming states in the left lead and the reflected ones. Again, we highlight the form of the wavefunction at $x = 0$:

$$\psi(0) = \psi_0 = A + B \tag{3.217}$$

Also, we require the wavefunction at point $i = -1$:

$$\begin{aligned} \psi_{-1} &= Ae^{-ik_L\delta x} + Be^{ik_L\delta x} \\ &= Ae^{-ik_L\delta x} + (\psi_0 - A)\, e^{ik_L\delta x}, \end{aligned} \tag{3.218}$$

where we used equation 3.217 to replace coefficient B. Therefore, we can rewrite the Schrodinger equation 3.215 as:

$$\begin{aligned} &E\psi_0 + \frac{\hbar^2}{2m(\delta x)^2}\left\{\psi_1 - 2\psi_0 + Ae^{-ik_L\delta x} + (\psi_0 - A)\, e^{ik_L\delta x}\right\} - V_0\psi_0 = 0 \\ \Rightarrow &E\psi_0 + \frac{\hbar^2}{2m(\delta x)^2}\left\{\psi_1 - 2\psi_0 + e^{ik_L\delta x}\psi_0\right\} - V_0\psi_0 = \underbrace{\frac{\hbar^2}{2m(\delta x)^2} A\left\{e^{ik_L\delta x} - e^{-ik_L\delta x}\right\}}_{\text{source term}}, \end{aligned} \tag{3.219}$$

We employ a similar approach for the right interface between the scattering region and the semi-infinite lead:

$$E\psi_{N+1} + \frac{\hbar^2}{2m(\delta x)^2}\left\{\psi_{N+2} - 2\psi_{N+1} + \psi_N\right\} - V_{N+1}\psi_{N+1} = 0 \tag{3.220}$$

We assume that in the right lead there is no incoming wave, so we only account for the transmitted wave (see Figure 3.22):

$$\psi_{N+2} = Ce^{ik_R(N+2)\delta x} = \psi_{N+1}e^{ik_R\delta x} \tag{3.221}$$

For the right boundary, we obtain

$$E\psi_{N+1} + \frac{\hbar^2}{2m(\delta x)^2}\left\{\psi_{N+1}e^{ik_R\delta x} - 2\psi_{N+1} + \psi_N\right\} - V_{N+1}\psi_{N+1} = 0 \tag{3.222}$$

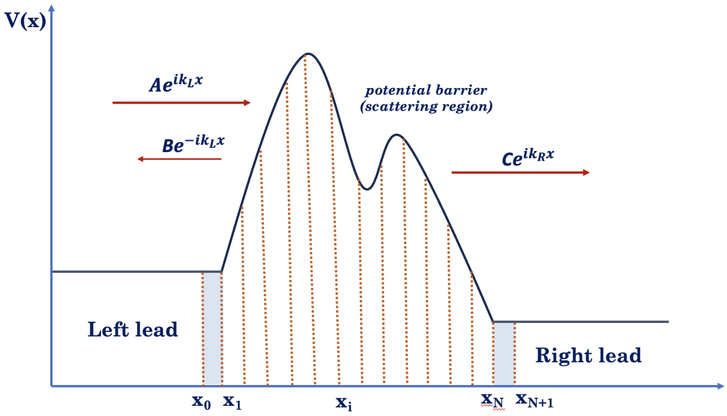

FIGURE 3.22: Discretization of a 1D potential barrier, where the shaded regions represent the boundaries between the leads and the scattering region.

For the grid points indexed with $i = 1, ..., N$, we use equation 3.213. To account for the boundaries, we use equations 3.219 and 3.222. The entire scattering problem can be written in matrix form as:

$$(E\mathbf{I} - \mathbf{H})\,\boldsymbol{\psi} = \mathbf{q}. \tag{3.223}$$

In the matrix equation above, E are the energy eigenvalues of the system, I is the identity matrix, ψ is a column vector with all the coefficients of the wavefunctions and $\mathbf{q}$ is the source vector of dimension $N+2$. The only nonzero element of the source vector is the first one, given in equation 3.219.

$\mathcal{H}$ is the tridiagonal Hamiltonian matrix of dimensions $(N+2) \times (N+2)$. Most of its elements are identical to the ones given by the finite difference Hamiltonian in the discretized Schrodinger equation, with the exception of the first and last diagonal elements:

$$\begin{aligned}
&H_{i,i+1} = H_{i,i-1} = -\frac{\hbar^2}{2m\delta x^2} \quad \text{0<i<N+1} \\
&H_{i,i} = -\frac{\hbar^2}{m\delta x^2} + V_i \\
&H_{0,0} = -\frac{\hbar^2}{m\delta x^2} + V_0 - \frac{\hbar^2}{2m(\delta x)^2}e^{ik_L\delta x}, \\
&H_{N+1,N+1} = -\frac{\hbar^2}{m\Delta^2} + V_{N+1} - \frac{\hbar^2}{2m(\delta x)^2}e^{ik_R\delta x},
\end{aligned} \tag{3.224}$$

The last two terms in the set above are modified from the finite difference version with the following quantities:

$$\begin{aligned}
\Sigma_L(E) &= -\frac{\hbar^2}{2m(\delta x)^2}e^{ik_L\delta x} \\
\Sigma_R(E) &= -\frac{\hbar^2}{2m(\delta x)^2}e^{ik_R\delta x}
\end{aligned} \tag{3.225}$$

These are the self energies of the left/right leads that we introduced in section 3.2.

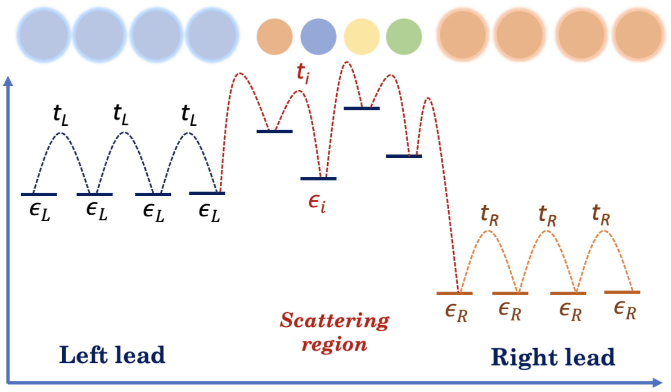

FIGURE 3.23: Representation of a 1D atomic chain and the potential along the structure (adapted from [58, 57]).

The transmission amplitude is given by the wavefunction on the right side of the barrier, normalized to the amplitude of the incoming wave. The wavefunctions are also normalized to the velocities, to obtain a unitary scattering matrix, so the transmission coefficient is:

$$t = \sqrt{\frac{v_R}{v_L}}\frac{\psi_{N+1}}{A}. \tag{3.226}$$

The reflection amplitude is similarly determined from the wavefunction on the left side minus the incoming wave (also normalized to the amplitude of the incoming wave):

$$r = \frac{\psi_0 - A}{A} \tag{3.227}$$

Tight binding formulation

In section 3.4, we introduced the secular equation 3.73 of a tight binding model. Let us focus on a simple 1D chain, schematically represented in 3.23, in order to highlight the relation between the TB approach and WFM method. If we consider only nearest neighbors hopping and assume, for simplicity, that the hopping parameter is real, the Hamiltonian is:

$$\mathcal{H} = \sum_{i=-\infty}^{\infty} \varepsilon_i |i\rangle\langle i| + \sum_{i=-\infty}^{\infty} t_{i,i+1}(|i\rangle\langle i+1| + |i+1\rangle\langle i|), \tag{3.228}$$

Considering that $\{|i\rangle\}$ form a complete basis for the tight binding system, the wave function can be written as:

$$|\Psi\rangle = \sum_i |i\rangle\langle i \mid \Psi\rangle = \sum_i c_i |i\rangle,$$

where $c_i = \langle i \mid \Psi\rangle$. The Schrodinger equation is:

$$\sum_{i=-\infty}^{\infty} (\varepsilon_i - E)c_i|i\rangle + \sum_{i=-\infty}^{\infty} t_{i,i+1}c_{i+1}|i\rangle + \sum_{i=-\infty}^{\infty} t_{i-1,i}c_i|i\rangle = 0 \tag{3.229}$$

Assuming that the atomic wavefunctions are orthogonal, notice that we can rewrite the Schrodinger equation in matrix form and work with the secular equation 3.73, introduced in section 3.4:

$$(E\mathbf{I} - \mathbf{H})\mathbf{\Psi} = \mathbf{0} \tag{3.230}$$

The Hamiltonian operator is:

$$\mathbf{H} = \begin{pmatrix} \ddots & \cdots & 0 & 0 & \\ \vdots & \epsilon_{i-1} & t_{i-1} & 0 & 0 \\ 0 & t_{i-1} & \epsilon_i & t_i & 0 \\ 0 & 0 & t_i & \epsilon_{i+1} & \vdots \\ & 0 & 0 & \cdots & \ddots \end{pmatrix} \tag{3.231}$$

and the secular equation implies solving:

$$\begin{pmatrix} \ddots & \cdots & 0 & 0 & \\ \vdots & E-\epsilon_{i-1} & t_{i-1} & 0 & 0 \\ 0 & t_{i-1} & E-\epsilon_i & t_i & 0 \\ 0 & 0 & t_i & E-\epsilon_{i+1} & \vdots \\ & 0 & 0 & \cdots & \ddots \end{pmatrix} \cdot \begin{pmatrix} \vdots \\ c_{i-1} \\ c_i \\ c_{i+1} \\ \vdots \end{pmatrix} = 0 \tag{3.232}$$

Equation 3.232 can be written explicitly, component by component:

$$-t_{i-1}c_{i-1} + (E - \epsilon_i)\, c_i - t_i c_{i+1} = 0 \tag{3.233}$$

If we compare this with our results for the WFM method in 1D, in Equation 3.224, we can identify the following correspondence between the terms involved:

$$\begin{aligned} c_i &\rightarrow \psi_i && \Rightarrow \quad \textbf{wave function amplitudes} \\ \epsilon_i &\rightarrow -\frac{\hbar^2}{m(\delta x)^2} + V_i && \Rightarrow \quad \textbf{on-site energy} \\ t_i &\rightarrow -\frac{\hbar^2}{2m(\delta x)^2} && \Rightarrow \quad \textbf{hopping energy term} \end{aligned} \tag{3.234}$$

As a consequence of translational invariance, the wavefunctions in consecutive cells of the periodic 1D chain are related by a constant phase factor. Therefore, if $c_{i-1} = c$ then $c_i = \lambda c$ and $c_{i+1} = \lambda^2 c$. Rewriting equation 3.233, we get:

$$\begin{aligned} -t + (E-\varepsilon)\lambda - t\lambda^2 = 0, \\ \Rightarrow \lambda = \frac{E-\varepsilon}{2t} \pm \left[\left(\frac{E-\varepsilon}{2t}\right)^2 - 1\right]^{\frac{1}{2}}. \end{aligned} \tag{3.235}$$

For $\left|\frac{E-\varepsilon}{2t}\right| \leq 1$, we can define a wave number k:

$$\cos(ka) = \frac{E-\varepsilon}{2t}, \tag{3.236}$$

which leads to

$$\begin{aligned} \lambda_{\pm} &= \cos(ka) \pm \left[\cos^2(ka) - 1\right]^{1/2} \\ \Rightarrow \lambda_{\pm} &= e^{\pm ika}, \end{aligned} \tag{3.237}$$

However, there is one more case to be discussed, namely $\left|\frac{E-\varepsilon}{2t}\right| > 1$, when we define κ by

$$\begin{aligned} \cosh(\kappa a) &= \left|\frac{E-h}{2\beta}\right|, \\ \Rightarrow \lambda_{\pm} &= +e^{\mp\kappa a} \qquad \text{if} \quad \frac{E-\varepsilon}{2t} > 1; \\ \lambda_{\pm} &= -e^{\mp\kappa a} \qquad \text{if} \quad \frac{E-\varepsilon}{2t} < -1. \end{aligned} \tag{3.238}$$

These are known as evanescent modes, which describe waves that are decaying away from the scattering region, either to the left or to the right. While these states do not contribute to transport and have no effect on the transmission function, they need to be accounted for in order to form a complete basis and properly match de wavefunctions at the interfaces [59, 57]. Also, note that the WFM method can also be translated into Green's functions formalism [59, 60]. As pointed out in [60], the retarded Green function, that we intoduced in 3.2, consists of propagating waves that move outwards from the source and/or evanescent states that decay away from the source.

3.8 Numerical simulations with KWANT

Kwant is an open source Python library tailored for quantum transport calculations based on the tight binding model and the wavefunction matching method [61]. While the Kwant package is highly versatile, with a user-friendly and transparent syntax, it did not compromise on computational efficiency, competing even with C-based codes written for transport. While this Python package is also suited for performing simulations on finite systems, its main functionality is to compute transport based quantities in device set-ups that we have encountered already in this thesis, namely systems partitioned into three parts – the left and right semi-infinite leads and the central scattering region.

The Hamiltonians that can be implemented in Kwant are varied, ranging from the simplest 1D atomic chains to more exotic topological Hamiltonians [62, 63, 64, 65], superconductors [66, 67] or systems that exhibit Majorana states [68, 69]. While outside of the scope of this thesis, it's worth mentioning that the Kwant developers also implemented its time dependent counterpart, TKwant [70], which expands even further the capabilities of the Python-based package.

In this section, we shall present the basics of the discretization approach of Kwant, along with an explicit example of the discretization of a more exotic Hamiltonian, namely the BHZ Hamiltonian that describes TIs.

3.8.1 General remarks

In order to exemplify the manner in which Kwant approaches the discretization, we shall consider a 2D system which can be described by the Schrodinger equation:

$$H = -\frac{\hbar^2}{2m}\left(\partial_x^2 + \partial_y^2\right) + V(y), \tag{3.239}$$

where $V(x,y)$ is a confining potential. From a physical point of view, the dicretization of the Hamiltonian implies rewriting it in a tight binding form. The chosen quantum system can be modeled by a 2D lattice, where each lattice site is indexed by a set of discrete coordinates (i,j). Hence,

$$\begin{aligned} |x,y\rangle &\rightarrow |x_i,y_j\rangle = |i\cdot a, j\cdot a\rangle \equiv |i,j\rangle\,, \\ V(x,y) &\rightarrow V\left(x_i,y_j\right) = V\left(a\cdot i, a\cdot j\right) \equiv V\left(i,j\right), \end{aligned} \tag{3.240}$$

where i,j stand for the site index (grid points) along directions x,y and a is the lattice constant. Now to proceed with the discretization of the momentum operators, we remember the finite difference formulas for the first and second order derivatives:

$$\begin{aligned} \partial_x f\left(x_n,y_n\right) &\approx \frac{f\left(x_n+d\right)-f\left(x_n-d\right)}{2a} \\ \partial_x^2 f\left(x_n,y_n\right) &\approx \frac{f\left(x_n+d\right)+f\left(x_n-d\right)-2f\left(x_n\right)}{a^2} \end{aligned} \tag{3.241}$$

Expressing the formulas above in terms of the positional states $\langle i,j|$, we obtain:

$$\partial_x \equiv \frac{1}{2a}\sum_{i,j}\left[|i+1,j\rangle\langle i,j| - |i-1,j\rangle\langle i,j|\right]. \tag{3.242}$$

for the first order derivative and

$$\begin{aligned} \partial_x^2 &\equiv \frac{1}{a^2}\sum_{i,j}\left[|i+1,j\rangle\langle i,j| + |i-1,j\rangle\langle i,j| - 2\,|i,j\rangle\langle i,j|\right], \\ &\equiv \frac{1}{a^2}\sum_{i,j}\left[|i+1,j\rangle\langle i,j| + |i,j\rangle\langle i+1,j| - 2\,|i,j\rangle\langle i,j|\right] \end{aligned} \tag{3.243}$$

for the second order derivative. All that is left now is to substitute the expressions above into Equation 3.239:

$$\begin{aligned} H = \sum_{i,j}[(V(ai,aj)+4t)|i,j\rangle\langle i,j| - t(|i+1,j\rangle\langle i,j| + |i,j\rangle\langle i+1,j| \\ +|i,j+1\rangle\langle i,j| + |i,j\rangle\langle i,j+1|)] \end{aligned} \tag{3.244}$$

Taking note of the similarity between the Hamiltonian derived above and the TB Hamltonian introduced in Equation 3.78 (albeit for a 1D case), one can easily identify that

$$t = \frac{\hbar^2}{2ma^2}. \tag{3.245}$$

holds the meaning of a hopping parameter.

3.8.2 Discretization of the BHZ Hamiltonian

The BHZ Hamiltonian was introduced in section 2.3.3 as:

$$\mathcal{H}_{BHZ} = \sigma_0\otimes\sigma_0\epsilon(k) + \sigma_0\otimes\sigma_z M(k) + \sigma_z\otimes\sigma_x Ak_x - \sigma_0\otimes\sigma_y Ak_y, \tag{3.246}$$

where

$$\begin{aligned}\epsilon(k) &= C - D\left(k_x^2 + k_y^2\right), \\ M(k) &= M - B\left(k_x^2 + k_y^2\right).\end{aligned}$$

In order to discretize it, we have to substitute the first and second order derivatives:

$$\begin{aligned}k_i &\to -i\partial_i \\ k_i^2 &\to -\partial_i^2.\end{aligned}$$

The first term in the Hamiltonian is:

$$\begin{aligned}&\sigma_0 \otimes \sigma_0 \epsilon(k) = \sigma_0 \otimes \sigma_0 \left(C - D\left(k_x^2 + k_y^2\right)\right) \\ &= \sigma_0 \otimes \sigma_0 \left(C + D\frac{1}{a^2}\left(|i+1,j\rangle\langle i,j| + |i-1,j\rangle\langle i,j| - 4\,|i,j\rangle\langle i,j| + |i,j+1\rangle\langle i,j| + |i,j-1\rangle\langle i,j|\right)\right) \\ &= \sigma_0 \otimes \sigma_0 \left(C - \frac{4D}{a^2}\right)|i,j\rangle\langle i,j| + \sigma_0 \otimes \sigma_0 \frac{D}{a^2}\left(|i+1,j\rangle\langle i,j| + |i-1,j\rangle\langle i,j|\right) + \\ &+ \sigma_0 \otimes \sigma_0 \frac{D}{a^2}\left(|i,j+1\rangle\langle i,j| + |i,j-1\rangle\langle i,j|\right)\end{aligned} \tag{3.247}$$

Similarly,

$$\begin{aligned}&\sigma_0 \otimes \sigma_z \epsilon(k) = \sigma_0 \otimes \sigma_z \left(M - B\left(k_x^2 + k_y^2\right)\right) \\ &= \sigma_0 \otimes \sigma_z \left(M - \frac{4B}{a^2}\right)|i,j\rangle\langle i,j| + \sigma_0 \otimes \sigma_z \frac{B}{a^2}\left(|i+1,j\rangle\langle i,j| + |i-1,j\rangle\langle i,j|\right) + \\ &+ \sigma_0 \otimes \sigma_z \frac{B}{a^2}\left(|i,j+1\rangle\langle i,j| + |i,j-1\rangle\langle i,j|\right)\end{aligned} \tag{3.248}$$

The last two terms can be rewritten as:

$$\begin{aligned}\sigma_z \otimes \sigma_x A k_x &= -i\sigma_z \otimes \sigma_x A \partial_x \\ &= -i\sigma_z \otimes \sigma_x A \frac{1}{2a}\left(|i+1,j\rangle\langle i,j| - |i-1,j\rangle\langle i,j|\right)\end{aligned} \tag{3.249}$$

and

$$\begin{aligned}\sigma_0 \otimes \sigma_y A k_y &= -i\sigma_0 \otimes \sigma_y A \partial_y \\ &= -i\sigma_0 \otimes \sigma_y A \frac{1}{2a}\left(|i,j+1\rangle\langle i,j| - |i,j-1\rangle\langle i,j|\right).\end{aligned} \tag{3.250}$$

To summarize, we have three types of terms that emerge in the discretized form of the Hamiltonian:

- Onsite terms:

$$\sum_{i,j}\left[\sigma_0 \otimes \sigma_0 \left(C - \frac{4D}{a^2}\right) + \sigma_0 \otimes \sigma_z \left(M - \frac{4B}{a^2}\right)\right]|i,j\rangle\langle i,j| \tag{3.251}$$

- Hopping in the x direction:

$$\sum_{i,j}\left[\sigma_0\otimes\sigma_0\frac{D}{a^2}+\sigma_0\otimes\sigma_z\frac{B}{a^2}-i\sigma_z\otimes\sigma_x\frac{A}{2a}\right]|i+1,j\rangle\langle i,j|+\text{ h.c.} \tag{3.252}$$

- Hopping in the y direction:

$$\sum_{i,j}\left[\sigma_0\otimes\sigma_0\frac{D}{a^2}+\sigma_0\otimes\sigma_z\frac{B}{a^2}+i\sigma_0\otimes\sigma_y\frac{A}{2a}\right]|i,j+1\rangle\langle i,j|+\text{ h.c.} \tag{3.253}$$

In second quantization formalism, the BHZ Hamiltonian can be written as [23]:

$$\mathcal{H}^{TB}_{BHZ}=\sum_{i,j}c^\dagger_{i,j}c_{i,j}\hat{V}+\sum_{i,j}c^\dagger_{i+1,j}c_{i,j}\hat{T}_x+\sum_{i,j}c^\dagger_{i,j+1}c_{i,j}\hat{T}_y+\text{ h.c.} \tag{3.254}$$

where,

$$\begin{aligned}
\hat{V} &= \left(C-\frac{4D}{a^2}\right)\underbrace{\sigma_0\otimes\sigma_0}_{\mathcal{I}_{4\times4}}+\left(M-\frac{4B}{a^2}\right)\sigma_z\otimes\sigma_0 \quad \text{on-site term}\\
\hat{T}_x &= \begin{pmatrix} \frac{D}{a^2}+\frac{B}{a^2} & -\frac{iA}{2a} & 0 & 0\\ -\frac{iA}{2a} & \frac{D}{a^2}-\frac{B}{a^2} & 0 & 0\\ 0 & 0 & \frac{D}{a^2}+\frac{B}{a^2} & \frac{iA}{2a}\\ 0 & 0 & \frac{iA}{2a} & \frac{D}{a^2}-\frac{B}{a^2}\end{pmatrix} \quad \text{hopping in x-direction}\\
\hat{T}_y &= \begin{pmatrix} \frac{D}{a^2}+\frac{B}{a^2} & \frac{A}{2a} & 0 & 0\\ -\frac{A}{2a} & \frac{D}{a^2}-\frac{B}{a^2} & 0 & 0\\ 0 & 0 & \frac{D}{a^2}+\frac{B}{a^2} & \frac{A}{2a}\\ 0 & 0 & -\frac{A}{2a} & \frac{D}{a^2}-\frac{B}{a^2}\end{pmatrix} \quad \text{hopping in y-direction.}
\end{aligned} \tag{3.255}$$

4

Machine Learning methods in condensed matter

4.1 Overview

Machine learning (ML) techniques have garnered impressive popularity in the last years and are finding various applications in areas that range from something as mundane as movie recommendations to cutting edge technologies, finance and healthcare. At their core, machine learning algorithms rely on the gathering of large amounts of data and finding patterns in the datasets in order to learn from past experience and make autonomous predictions. It has also become evident in the last decades that both experimental and theoretical physics have become intrinsically linked to computational methods and simulations programs, relying on the continuous rise in computing power and efficiency. Therefore, it is of no surprise that ML methods have found their way into various areas of science as well, providing innovative approaches to data manipulation and analysis and solving problems that, only a few year ago, were considered overly demanding from a computational perspective. To highlight the relation between ML and physics even more, it is worth mentioning that the Nobel Prize of 2024 was awarded to John Hopfield and Geoffrey Hinton for their contributions to ML. Both of them have taken concepts from theoretical physics and applied them successfully to seminal ML algorithms – the Hopfield network and the Boltzmann machines.

Materials science is an impressive source of large and comprehensive datasets, with multiple parameters and features. It has become apparent to scientists in this field that they have to shift towards a new paradigm of research, in order to handle efficiently the large amount of data gathered from experiments and simulations. Since data manipulation and pattern recognition are the tenets of ML, materials science is a perfect fit for machine learning approaches. The type of data that is available along with the end goal have to be taken into consideration when building a ML model. Depending on these conditions, one may classify ML approaches into three main categories: supervised learning, unsupervised learning and reinforcement learning (see Figure 4.1).

All these classes of algorithms have found a variety of applications in both theoretical and experimental condensed matter physics. For instance, neural networks

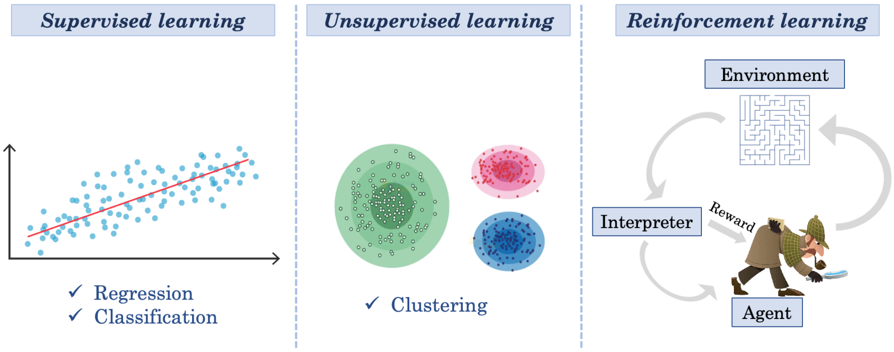

FIGURE 4.1: The three main categories that encompass the majority of ML models. Supervised learning deals with datasets where both the input and output are known and the ML algorithm learns a complex $\mathcal{D}$-dimensional function that links the features to the targets. In unsupervised learning, the program has to identify patterns in the data without any *a priori* knowledge of what meaning they might possess. Reinforcement learning (RL) works with a completely new philosophy – the algorithm is trained only through trial and error. The code has three main components, the environment, the agent and the interpreter and the goal is for the agent to learn how to "move" in the created environment in order to achieve a predefined goal. The interpreter acts like a judge, giving the agent rewards when it makes optimal choices and punishing it when it makes mistakes.

were successfully employed to discriminate between phases of matter and identify phase transitions in classical and quantum systems [71] and also to identify topological order [72, 73]. Multiple types of classification and regression algorithms were applied to predict the chemical composition of materials [74] and even aid in the discovery and design of new materials [75]. Basically, ML is a powerful tool for inverse design applications, where one imposes a desired functionality and trains a model to identify the ideal chemical structure or composition that leads to it [76].

Our research group began exploring ML methods for applications in materials science by exploiting the large datasets we already obtained through intensive DFT-based calculations, as described in Figure 4.2. Our goal was to predict relevant materials properties, such as the band gap, from datasets generated with the SIESTA and TranSIESTA packages [77, 78, 79]. We expanded our expertise gradually, moving towards ML metthods suitable for image processing and generative models, in order to analyze datasets from exact diagonalization procedures, R-matrix simulations and even molecular dynamics. To this end, in this chapter we focus mainly on the ML methods that we employed, starting with the deceivingly simple, but ubiquitously versatile artificial neural networks (ANN). The last sections are dedicated to image processing algorithms, ending with specific applications of all these models to physically relevant systems.

4.2 Artificial Neural Networks

The idea of neural networks was initially inspired by the 1943 model of a biological neuron developed by McCulloch and Pitts [80], the subsequent concept of the perceptron of Rosenblatt [81] and the ideas about the actual learning process expanded by Hebb [82, 83]. The perceptron, as basic learning unit described schematically in Figure 4.3a became the building block of artificial neural networks, but it was soon

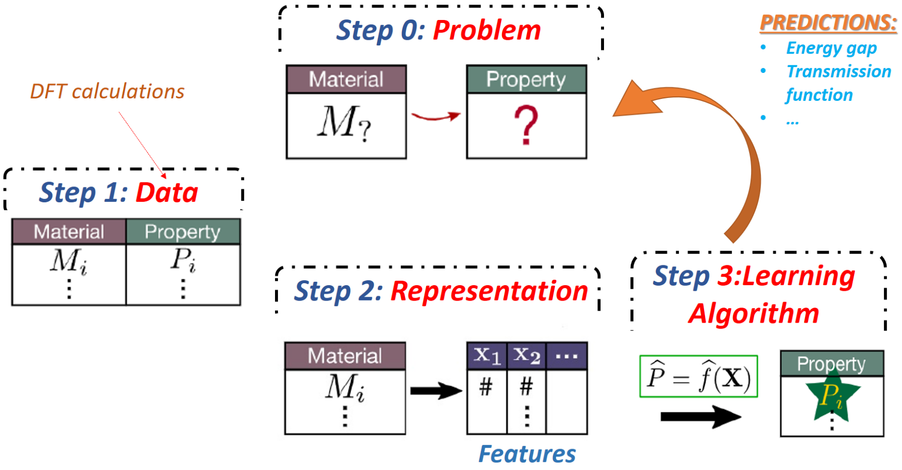

FIGURE 4.2: A workflow for the DFT+ML approach to exploring the properties of materials. Large datasets are initially gathered with the aid of DFT-based simulations tools and a goal for the model is identified. A crucial step is to check the data, eliminate any possible outliers or redundancies and then find an ideal manner to define the relevant features for the system. Then, an appropriate ML model is trained with the input data and the end result is a program that should be able to make accurate predictions almost instantly.

realizes that a simple brain inspired network of linear computing elements was not complex enough to learn complicated patterns. The second breakthrough came in the 1980s, when several groups of researchers created effective ways to train ANNs, by means of what we now call "back-propagation". Therefore, when we talk about neural networks we basically refer to a computational applications that employs variations of the gradient descent method to solve a wide variety of regression and classification problems [84]. In the realm of applied data science, researchers use machine learning methods as tools that allows them to make swift and accurate predictions based on large amounts of data for otherwise complex systems that would require a great deal of computational resources and time.

The basic element of a neural network is known as a neuron, which is a nonlinear function that transforms an input vector to a single output value. The function is parametrized by a set of weights w_{ij} and a bias (or threshold b_j). In order to induce the nonlinearity required to tackle a larger class of realistic problems, an activation function is applied to the linear transformation. There are a number of different activation functions that one can use, but an important condition is that they need to be differentiable. Mathematically, we can represent one layer j of the neural network with m neurons in the following manner:

$$y_j = f\left(\sum_{i=1}^{m} w_{ji} x_i + b_j\right), \tag{4.1}$$

where

$$\begin{cases} x_i \Rightarrow & \text{input} \\ y_j \Rightarrow & \text{output} \\ b_\text{j} \Rightarrow & \text{bias} \\ w_\text{ji} \Rightarrow & \text{synaptic weights} \\ f \Rightarrow & \text{activation function} \end{cases}$$

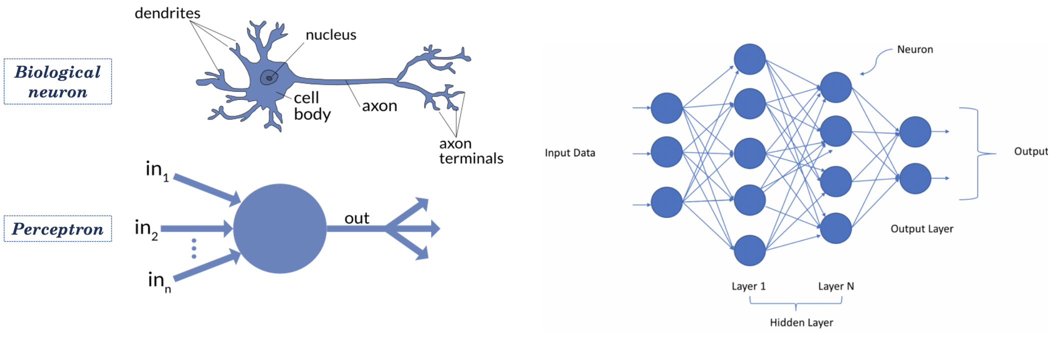

(A) (B)

FIGURE 4.3: (A) In the upper side of the figure, a representation of the biological neuron, that inspired ANNs. The first type of neural network (NN), known as perceptron, is sketched below. (B) The architecture of an artificial neural network, as we use it today, highlighting the input and output layers, connected by multiple hidden layers with various numbers of neurons each.

In matrix form:

$$Y = f\left(W^{\top} X + B\right) \tag{4.2}$$

where

$$\begin{cases} X \Rightarrow & \text{input column vector of size (m x 1)} \\ Y \Rightarrow & \text{output column vector, after activation, of size (n x 1)} \\ B \Rightarrow & \text{bias, column vector of size (n x 1)} \\ W \Rightarrow & \text{weights matrix of size (m x n)} \\ f \Rightarrow & \text{activation function, applied element-wise} \end{cases}$$

The generalization to multiple layers is straightforward:

$$\begin{aligned} Z^l &= W^{l^T} Y^{l-1} + B^l \\ Y^l &= f^l\left(Z^l\right). \end{aligned} \tag{4.3}$$

where l denotes the l^{th} layer of the network.

4.2.1 Activation functions

The activation function of a neural network defines how the weighted sum of the input is transformed into an output from a node (or nodes) in a layer of the network. Without activation functions, no matter how many layers the ANN has, its capacity to represent a dataset would not increase and it would be as powerful as a linear regression model [85]. In other words, any number of linear layers could simply be reduced to one layer and give the same result. Therefore, the non-linearity induced by the activation function is essential to capacity of a neural network and their power of adaptability to high dimensional data spaces. While there is no ultimate set of rules that guides the programmers in choosing the ideal activation functions, there are many studies that explore the impact of activation functions on the performance of the ML model [86, 87, 88]. There is also research into new types of activation functions that can adapt in real time to the learning process of the network [89, 90].

We will enumerate here the most popular activation functions and outline their crucial features:

- Hyperbolic tangent ⇒ The output of the tanh function always ranges between -1 and +1

$$\tanh(z) = \frac{e^z - e^{-z}}{e^z + e^{-z}} \tag{4.4}$$

- Rectified linear unit (ReLU) ⇒ If the input value is 0 or greater than 0, the ReLU function outputs the input as it is. If the input is less than 0, the ReLU function outputs the value 0

$$\mathrm{ReLU}(z) = \begin{cases} 0 & \text{if } z < 0 \\ z & \text{otherwise} \end{cases} = \max(0, z) \tag{4.5}$$

- Sigmoid ⇒ The sigmoid function converts its input into a probability value between 0 and 1. It converts large negative values towards 0 and large positive values towards 1. It must be used in the output layer when we build a binary classifier

$$\sigma(z) = \frac{1}{1 + e^{-z}} \tag{4.6}$$

- Softmax ⇒ It is the multi-class generalization of the sigmoid function:

$$\sigma(\mathbf{z})_i = \frac{e^{z_i}}{\sum_{j=1}^{K} e^{z_j}} \tag{4.7}$$

  The softmax function takes an input vector **z** and generates

$$\sigma(\mathbf{z})_i = \begin{bmatrix} e^{z_1} / \sum_i e^{z_i} \\ \vdots \\ e^{z_k} / \sum_i e^{z_i} \end{bmatrix} \tag{4.8}$$

  which is a probability distribution over K items, where K is the number of classes.

Loss functions

Let us consider a dataset of n values marked $y_1, \dots, y_n$, each associated with a fitted (predicted) value $f_1, \dots, f_n$. In order for the network to learn, the loss should become minimal at the end of the training process. So, given a loss function $\mathcal{L}$(prediction, truth), we must adjust the weights w, w_0 of every layer to minimize

$$\mathrm{O}\left(w, w_0\right) = \sum_i \mathcal{L}\left(\mathrm{NN}\left(x_i; w, b\right), f_i\right),$$

where NN is the output of our single-unit neural net for a given input. Choosing the appropriate loss function depending on the problem at hand is essential, so we will enumerate here some of the most popular loss functions.

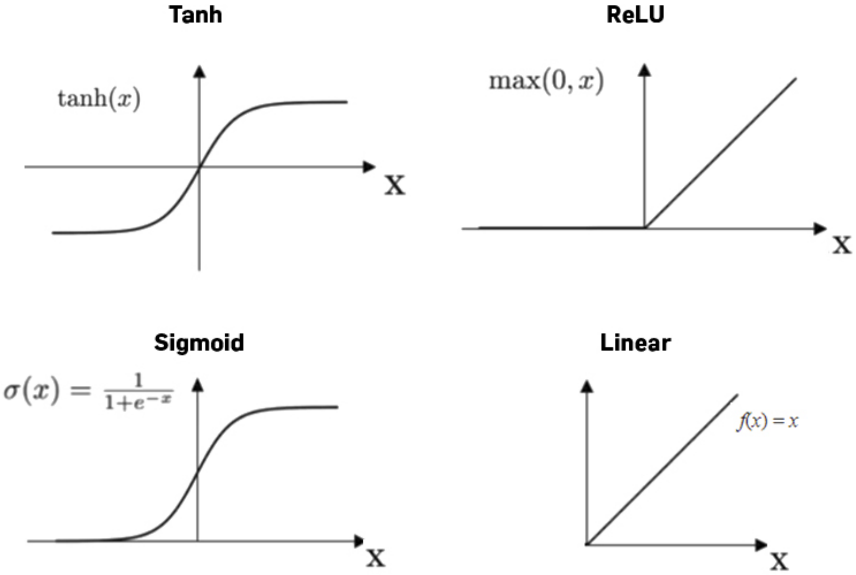

FIGURE 4.4: Examples of activation functions. Note that the sigmoid is suitable for classification problems.

Mean squared error

The mean squared error is defined as:

$$MSE = \frac{1}{N}\sum_{n=1}^{N}\left(t^{(n)} - o^{(n)}\right)^2$$

where N - number of samples, $t_{(i)}$ - ground truth label (target) for i^{th} sample and $o_{(i)}$ - predicted label for i-th sample

Coefficient of determination (R^2)

$$R^2 = 1 - \frac{SS_{\text{res}}}{SS_{\text{tot}}} \tag{4.9}$$

where

$$\begin{cases} SS_{\text{res}} = \sum_i \left(t_i - o_i\right)^2 \text{ residual sum of squares} \\ SS_{\text{tot}} = \sum_i \left(t_i - \bar{t}\right)^2 \text{ total sum of squares} \\ \bar{t} = \frac{1}{n}\sum_{n=1}^{N} t^{(n)} \quad \text{mean of the observed data} \end{cases}$$

Cross-entropy

The idea of cross-entropy has its origin in the field of information theory, where the Shannon entropy was introduced [91]. Similar to statistical physics, entropy measures the degree of disorder in a system. In the context of information theory, entropy gives a measure for the uncertainty of an event. The exact formulation used as a cost function in machine learning algorithms is:

Loss	Activation function (f)	Task
Mean squared error	ReLU	regression
Binary cross entropy	sigmoid	classification
Categorical cross-entroy	softmax	multi-class classification

TABLE 4.1: Common loss functions and activation functions employed in different tasks performed by the ANN.

$$E_{\text{binary}} = -\frac{1}{N}\sum_{n=1}^{N} t^{(n)} \log o^{(n)} + \left(1 - t^{(n)}\right) \log\left(1 - o^{(n)}\right), \tag{4.10}$$

where

$$o^{(n)} = \frac{1}{1 + \exp\left(-z^{(n)}\right)}. \tag{4.11}$$

This loss function penalizes the model more heavily when it assigns a low probability to the true class and it is used in binary classification problems. In the case of a multi-categorical classification, the loss has the following form:

$$E_{\text{multi-class}}\left(\mathrm{o}, \mathrm{t}\right) = -\frac{1}{n}\sum_{i=1}^{n}\sum_{\mathrm{k}=1}^{\mathrm{K}} t_{\mathrm{k}} \cdot \log\left(o_{\mathrm{k}}\right) \tag{4.12}$$

where

$$o(z_i) = \frac{e^{z_i}}{\sum_{j=1}^{K} e^{z_j}}. \tag{4.13}$$

In table 4.1, we mentioned some common loss functions and activation functions employed in different tasks performed by the ANN.

4.2.2 Backpropagation and gradient descent

The backpropagation algorithm is used in feed-forward ANNs. Since they are part of the category of supervised learning, the algorithm is provided with examples of the inputs and outputs. An error is then computed between the output of the network and the real output, with a loss function of our choosing. The goal is to minimize that error through training and adjust the weights of the network such that it reaches an optimal set of hyper-parameters and exhibits the highest performance. The adjusting of the weights is done by a method known as gradient descent.

Let us go through a simple example. Assume that we use the mean squared error to quantify the discrepancy between the output of the neural network and the target variable:

$$E = \frac{1}{2}\sum_{k}\left(o_k - t_k\right)^2, \tag{4.14}$$

where o_k stands for the output of the NN and t_k denotes the target value. The derivative of the error function with respect to the output is:

$$\frac{\partial E}{\partial o_k} = o_k - t_k \tag{4.15}$$

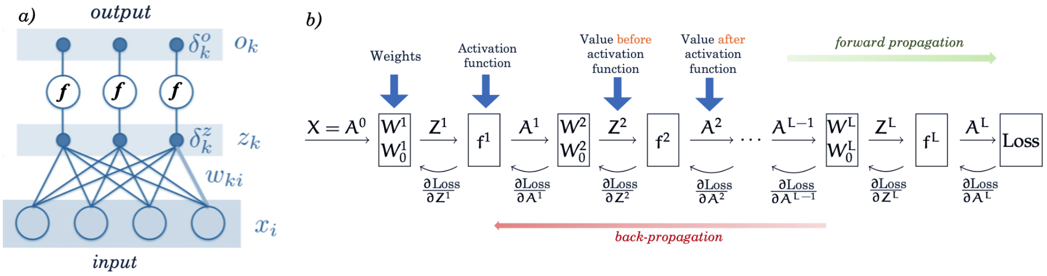

FIGURE 4.5: a) The structure of a single ANN layer, where the input values x_i are linearly transformed into z_k by simple multiplication with the weights matrix w. Subsequently, an activation function f is applied in order to induce non-linearity in the neural network. b) Qualitative scheme of the back-propagation algorithm, which encapsulates the learning process of an ANN (adapted from [84]).

Let us assume we employed the logistic activation function in this ANN architecture:

$$o_k^{(n)} = f\left(z_k^{(n)}\right) = \left(1 + \exp\left(-z_k^{(n)}\right)\right)^{-1}$$
$$\frac{\partial o_k^{(n)}}{\partial z_k^{(n)}} = o_k^{(n)}\left(1 - o_k^{(n)}\right)$$

so the output of the k layer is given by the activation function applied on the input coming from the previous layer. Using the chain rule, we express the gradient of the error function with respect to the weights in the following manner:

$$\frac{\partial E}{\partial w_{ki}} = \sum_{n=1}^{N} \frac{\partial E}{\partial o_k^{(n)}} \frac{\partial o_k^{(n)}}{\partial z_k^{(n)}} \frac{\partial z_k^{(n)}}{\partial w_{ki}} = \sum_{i=1}^{N} \left(o_k^{(n)} - t_k^{(n)}\right) o_k^{(n)} \left(1 - o_k^{(n)}\right) x_i^{(n)} \tag{4.16}$$

Hence, we update the weight accordingly:

$$w_{ki} \leftarrow w_{ki} - \eta \frac{\partial E}{\partial w_{ki}} = w_{ki} - \eta \sum_{n=1}^{N} \left(o_k^{(n)} - t_k^{(n)}\right) o_k^{(n)} \left(1 - o_k^{(n)}\right) x_i^{(n)} \tag{4.17}$$

where η is the learning rate. The learning rate defines the step size with which the algorithm moves towards the minimum at each iteration.

Optimizers

The example presented above is a basic approach that encompasses the philosophy of the backpropagation method. However, in modern deep learning algorithms, gradient descent-based methods became more refined, in order to increase the performance of the model. In a ML code, the algorithm that is responsible for the tuning of the network parameters during training is known as an optimizer. These algorithms are highly specialized, building on top of the simple gradient descent approach and decreasing the probability that the network will remain stuck in a local minimum during the learning process. Some of the best optimizers are: Stochastic Gradient Descent (SGD) [92], RMSprop [93], Adagrad and Adam [94].

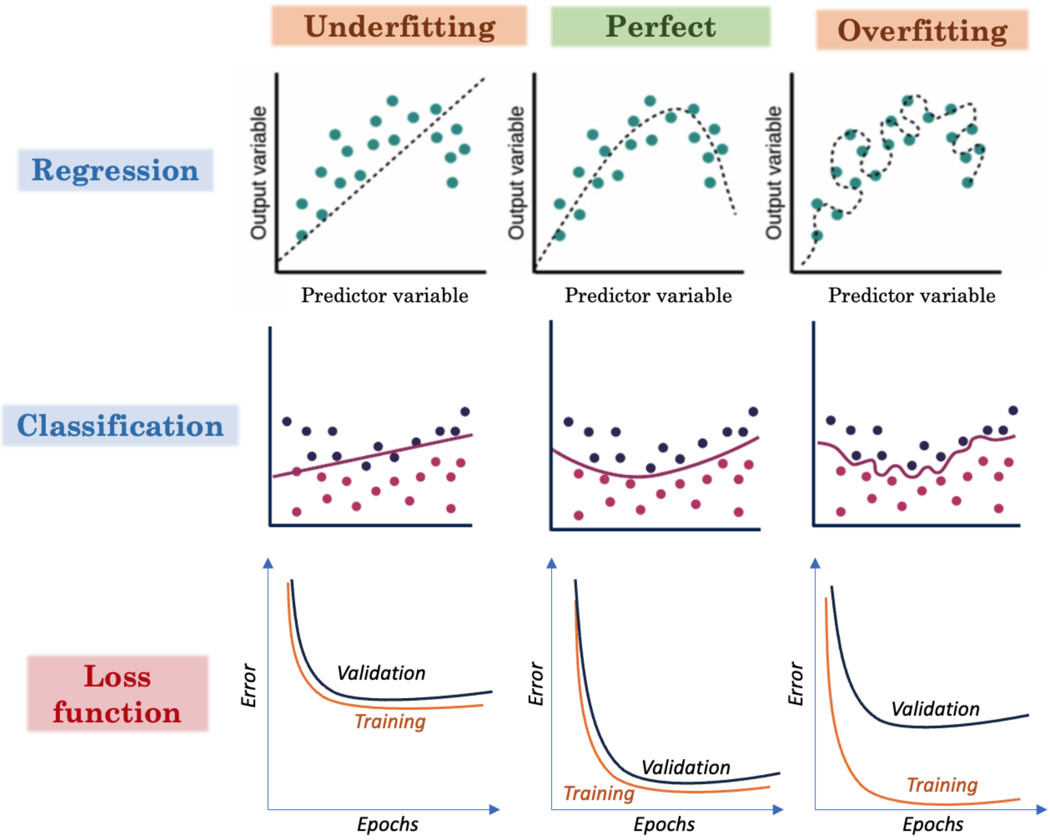

FIGURE 4.6: Qualitative plots depicting what underfitting, overfitting and an ideal model would output for regression and classification problems. In the last row, the loss functions are represented, following the validation and training losses. In the ideal case, both losses should go towards minimal values.

How often are the weights updated?

- After a full sweep through the training data (batch gradient descent)

$$w_{ki} \leftarrow w_{ki} - \eta \frac{\partial E}{\partial w_{ki}}$$

- After each training case (stochastic gradient descent)
- After a mini-batch of training cases

4.2.3 Optimization techniques for the ANN

Programming the optimal ML model is not always an easy task and usually implies that one needs to also go through a process of trial and error to identify the ideal parameters for the architecture of the network. Choosing the best parameters is not straightforward, since there is no definitive set of rules to follow. However, we propose here, as a guideline, some aspects that should be tuned in order to achieve the highest level of prediction accuracy:

- Modifying the number of hidden layers of the NN and the number neurons in each layer ⇒ The number of hidden layers and neurons is directly related to how complex the ANN is. The complexity of the model must be proportional, however, to the complexity of the problem that needs to be solved.

- Using the right activation function ⇒ Choosing the right activation function is highly consequential for the accuracy of the model. For example, a linear activation function implied that the network learns to adapt only to linear changes in the input values. Basically, an ANN with linear activation functions would not be capable of providing better results that a basic linear regression fit. For this reason, non-linear activation functions are the preferred option in most cases, since the end goal is to identify complex patterns in the data, that would be elusive to other statistical data analysis approaches [85].

- Activation function in the output layer ⇒ One needs to pay attention to the type of problem they want to solve when implementing a neural network. To this end, some activation functions are tailored for classification problems, as we discussed in section 4.2.1, and the model would return high errors if this is not accounted for.

- Normalize/scale data ⇒ This is an important aspect of data preprocessing, which explores the given dataset before feeding it the model. For the network, it is ideal to prepare a dataset that is scaled to the difference between the maximum and minimum values of each type of features.

- Improve feature selection ⇒ The importance of feature selection is difficult to understate in the framework of ML. Selecting the appropriate features influences the computation time and improves the prediction performance. Choosing the right features is akin to speaking a language that the ML model understands best, and leads to a better grasp of the data, giving more profound insights into the hidden patterns. A good set of features aims to minimize redundancy and noise and eliminate the outliers or irrelevant data points. Many feature selection methods are already well known [95] and are readily implemented, but one always needs to account for the characteristics of the problem at hand.

- Change the learning rate ⇒ The learning rate gives the step with which the optimizer searches for the minimum of the loss function. The ideal learning rate is a tradeoff between training time and accuracy.

- Training time (number of epochs) ⇒ The training time is crucial when it comes to the final stage of creating the ML model, namely testing it on new data. Choosing the wrong duration of the training process may lead to two extreme scenarios, underfitting and overfitting (see Figure 4.6). The training duration is measured on epochs, and each epoch represents the number times the ML model will go through the entire set of training data.

- Batch size ⇒ The batch size defines the number of samples the network goes through before updating its parameters towards loss minimization. It is advisable to use a batch size that has a value equal to a power of two, since the unit of memory is a bit. The smaller the batch size, the more the training process will take.

- Weight initialization ⇒ The weights of the NN enable the neurons in the various layers to learn different aspects of the multi-dimensional mapping that the model aims to perform. If all the neurons learned in the same manner, the model would perform worse, this is why the weights are automatically assigned randomly. To this end, there is ongoing research that explores the most optimal ways to initialize the weights in a NN [96, 97, 98].

- Dropout ⇒ Dropout refers to the random elimination of some of the nodes of the network from chosen hidden layers. This method helps to avoid overfitting, since it forces the network to adapt to situations when not all of the neurons are useful to the training process. This actually decreases the probability that the neurons become overly specialized, learning the training data too well, while becoming unable to adapt to a new dataset.
- Data augmentation ⇒ Data augmentation is another regularization technique that is especially useful when one deals with smaller datasets. It expands the size of the training dataset by creating artificial samples that usually exploit symmetries in the considered system. For example, when it comes to image recognition models, one can apply rotations, mirroring and random crop to the inputs. This is also a good way to balance a dataset. However, take note of the fact that the newly created data is still artificial and in some cases it might actually hinder the performance of the model by inducing redundancies.
- Early stopping ⇒ The goal of early stopping is to limit the number epochs. The ML models should be trained until the training error reaches a plateau, or one notices that the validation error starts increasing (which indicates overfitting). When these conditions are met, the model should stop training.

4.3 Convolutional Neural Networks

Fully connected feed forward ANNs are highly versatile since they make no assumptions about the type of data they are given. However, if we know some defining characteristics of the data we are working with, then other architectures may prove to be more efficient. This is where convolutional neural networks come into play, a type of NNs that deal with image processing. They have become highly popular lately due to the wide variety of visual data they can help analyze, from simple 2D camera images, to 3D representations. The structure of CNNs takes full advantage of how images are represented as 2D arrays of pixels that can either take one integer value or three integer values to encode the red, green and blue color channels. Images have some important characteristics that are exploited by CNNs, namely spatial locality and translational invariance [84].

A typical structure for convolutional network consists of three main blocks (see figure 4.7). In the beginning, the first layer performs several convolutions in parallel to produce a set of activation maps. In the second block, each linear activation is run through a nonlinear activation function, such as the rectified linear activation function (ReLU). In the third block, we use a pooling function to modify the output of the layer further and the final block is represented by a network of fully connected layers, similar to the ones we work with in NNs.

4.3.1 Convolutional layers

Mathematically, a convolution is an integral that expresses the amount of overlap of one function g as it is shifted over another function f:

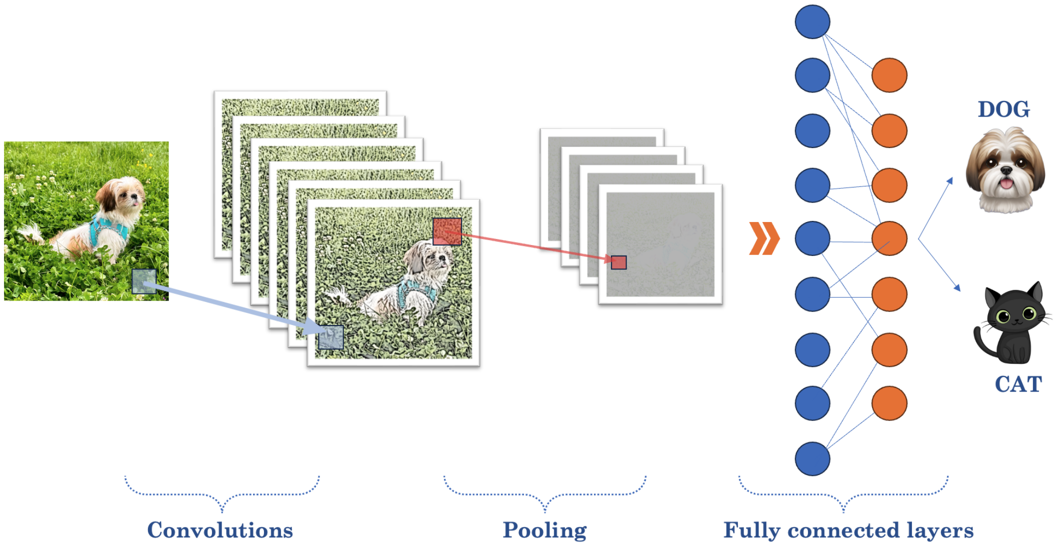

FIGURE 4.7: General structure of a convolutional neural network, comprised of convolutional layers, pooling layers and the final flattened fully connected layers.

$$[f * g](t) \equiv \int_0^t f(\tau)g(t-\tau)d\tau \tag{4.18}$$

where the symbol $*$ denotes the convolution of f and g. The first argument, function f, is known as the input and function g is referred to as the kernel. The result of the convolution is sometimes called a feature map. In the machine learning algorithms discussed here, the input is a multi-dimensional array of data (a tensor), while the kernel (also known as a filter in this context) is a multi-dimensional array of parameters that are optimized through the learning algorithm. For this type of discrete 2D problem, the convolution has the following form [99] :

$$\begin{gathered}(I * K)(i,j) = \sum_m \sum_n I(m,n)K(i-m,j-n) \\ \text{or} \\ (K * I)(i,j) = \sum_m \sum_n I(i-m,j-n)K(m,n).\end{gathered} \tag{4.19}$$

As it is explicitly pointed out in [99], the convolutional layer takes advantage of three important concepts: sparse interactions, parameter sharing and equivariant representations. We have seen that in feed forward neural networks, each input and output interact through the weights matrix and the activation function. However, in image processing, this approach would not only be computationally demanding, but also highly inefficient. This is due to the fact that not all pixels are equally relevant and the algorithm should be tailored to detect and enhance the essential features. The convolutional layer accomplishes this by using a kernel that is smaller than the input image. Parameter sharing refers to how the same filter is applied to every area in the input image, so the same weights that we have already trained can be used again. Equivariance implies that if we change the input, for example by shifting a pixel in one direction, the output image will be altered in the same manner.

The kernel slides across the height and width of the image, producing a two-dimensional representation of the input known as an activation map. The sliding

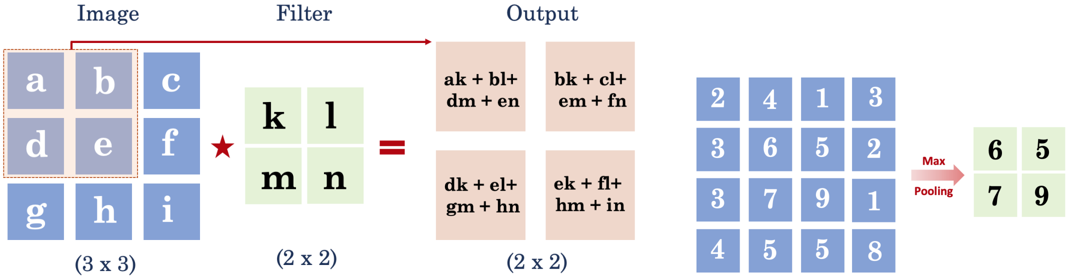

(A) (B)

FIGURE 4.8: (A) An example of a 2D convolution. (B) An example of a max-poolig operation.

step of the kernel across the image is called a stride. If we have an input of size $W \times W \times D$ and N number of kernels with a spatial size of F with stride S and amount of padding P, then the size of the output of the convolution is determined by (see also Figure 4.8):

$$W_{\text{out}} = \frac{W - F + 2P}{S} + 1. \tag{4.20}$$

The activation map will have a size of $W_{\text{out}} \times W_{\text{out}} \times N$.

4.3.2 Pooling layers

A pooling function replaces the output of the network at a certain location with a summary statistic of the nearby outputs [99]. The most popular is the max pooling operation, which return the maximum value within a rectangular neighbourhood (see figure 4.8b). Pooling helps in reducing the size of the representation and it can also help to make the representations more robust to small translations in the input image.

If we have an activation map of size $W \times W \times N$, a pooling kernel of spatial size F, and stride S, then the size of output can be determined by the following formula:

$$W_{\text{out}} = \frac{W - F}{S} + 1. \tag{4.21}$$

This will yield an output volume of size $W_{\text{out}} \times W_{\text{out}} \times D$.

4.4 Autoencoders

Autoencoders were introduced in 1986 [100] with the goal to reconstruct inputs with the highest accuracy. Its objective is to learn a representation of the data that encompasses the essential information and reconstruct the input as well as possible [101]. This representation is called latent feature representation and it has much smaller dimensions than the input. As it is represented in figure 4.9, the two building blocks of the autoencoder are two neural networks known as encoder and decoder.

Some of the main applications of autoencoders are :

- Dimensionality reduction ⇒ An autoencoder can be used to extract the essential features of the input data using the bottleneck architecture for the encoder/decoder networks. Subsequently, one can use the latent feature representation for other tasks, such as classification problems. The main advantage

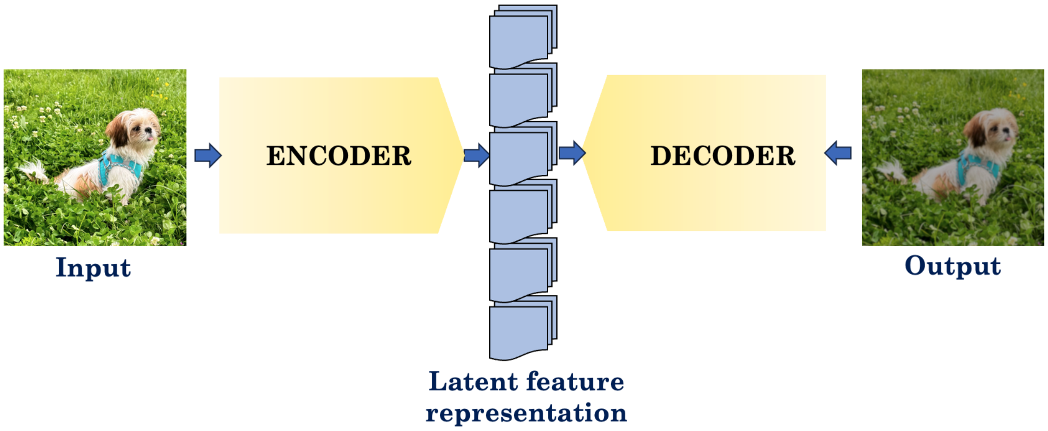

FIGURE 4.9: General structure of an autoencoder

is that autoencoders are able to deal with large amount of data in an efficient manner and it can minimize the computational time while retaining high accuracy.

- Anomaly detection ⇒ Autoencoders can be employed as anomaly detection tools by initially training the algorithm on a representative data set and computing the reconstruction error. If one then adds a different data element as the input, the autoencoder will not be able to recreate it properly, displaying high reconstruction errors for the "anomaly".
- Denoising ⇒ They can also be used to correct errors in the input dataset, if it is trained, for example, with noisy images as input and the original images as output.

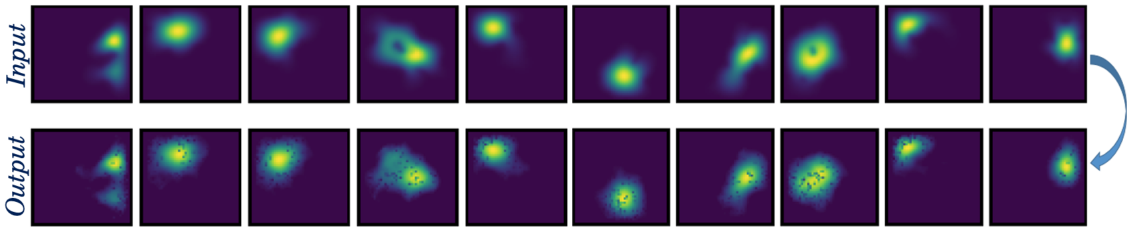

FIGURE 4.10: Results of an autoencoder on a set of charge densities calculated using the ED method.

4.5 Generative Adversarial Networks

"The harder the conflict, the more glorious the triumph"

Thomas Paine

Generative adversarial networks were proposed fairly recently, on 2014, by Ian Goodfellow [102] and they garnered an impressive amount of recognition in the artificial intelligence community. The main idea of GANs is based in a zero-sum game theory scenario, where two players have to constantly compete against each other in order to maximize their own gain. The GAN architecture is built on this philosophy and it consists of two networks, known as the generator and the discriminator.

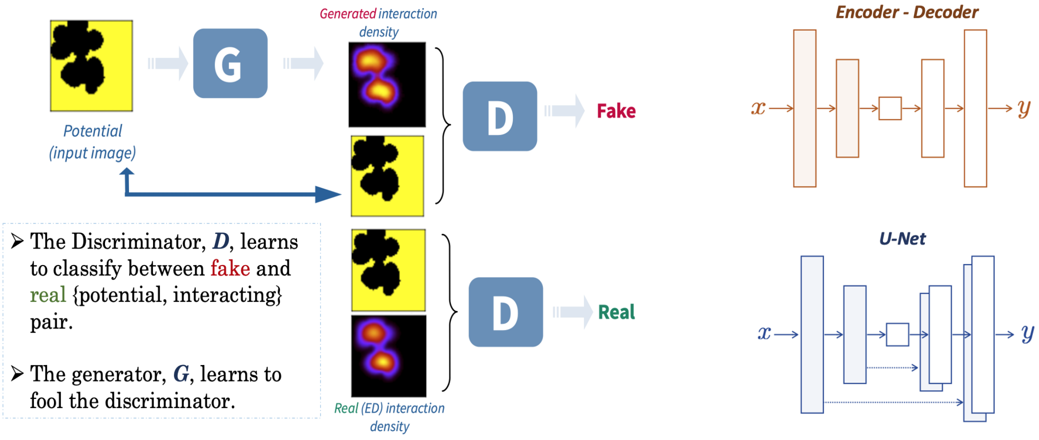

- The Discriminator, ***D***, learns to classify between fake and real {potential, interacting} pair.
- The generator, ***G***, learns to fool the discriminator.

(A) (B)

FIGURE 4.11: (A) Simplified scheme of the cGAN's learning process (B) Different possible architectures for the generator network.

The generator's role is to create fake data that is as close to the real data as possible, while the discriminator's job is to distinguish between what is real and what is a fake (generated by his adversary).

Let us discuss more what this adversarial scenario means in a formal mathematical approach. If the input data given to the discriminator is the real one, then its output should be close to unity. However, if the input data to the discriminator is the data generated by G, there will be two different perspectives to consider. From the viewpoint of the discriminator, it should be able to determine that the data is fake, so its output should be closer to 0. The loss that should be maximized in this case is $\mathcal{L}_{GAN}(G,D) = \mathbb{E}_{x,z}[\log(1-D(G(z)))]$. However, from the generator's perspective, its job is to fool the discriminator, so the loss for the generator is minimized. We can summarize this discussion in a representative manner as follows [103]:

$$
\begin{aligned}
&X = X_{\text{truth}} \Rightarrow D(X) \to 1 \quad \Rightarrow \quad \max_{D} \quad \mathcal{L}_{GAN}(G,D) = \mathbb{E}_{x,z}[\log(D(x))] \\
&\mathrm{X} = \mathrm{G(Z)} \Rightarrow \begin{cases} \mathrm{D(X)} \to 0 & \Rightarrow \quad \max_D \mathcal{L}_{GAN}(G,D) = \mathbb{E}_{x,z}[\log(1-D(G(z)))] \\ \mathrm{D(X)} \to 1 & \Rightarrow \quad \min_G \mathcal{L}_{GAN}(G,D) = \mathbb{E}_{x,z}[\log(D(x))] \end{cases}
\end{aligned}
\tag{4.22}
$$

where $\mathbb{E}_{x,z}$ is the expectation value.
Using the following notations:

$$
\begin{cases} x \Rightarrow \text{input image} \\ y \Rightarrow \text{output image} \\ z \Rightarrow \text{noise vector} \end{cases}
$$

the loss function of the GAN has the following form:

$$
\mathcal{L}_{GAN}(G,D) = \mathbb{E}_y[\log D(y)] + \mathbb{E}_{x,z}[\log(1-D(G(x,z))] \tag{4.23}
$$

The conflict between the generator and the discriminator is a 2-player minmax game, where the objective can be mathematically represented through the loss functions defined above in the following formula:

$$\min_G \max_D \quad \mathcal{L}_{GAN}(G,D) = \mathbb{E}_{x,z}[\log(D(x))] + \mathbb{E}_{x,z}[\log(1 - D(G(x,z)))] \tag{4.24}$$

4.5.1 *Conditional* Generative Adversarial Networks

If the generative adversarial networks are given an extra condition that both the generator and discriminator have to abide, then they are known as conditional GANs (cGANs). They were introduced shortly after the traditional GANs, in 2014 [104]. Usually, this extra information is a label. Therefore, in addition to the random input is fed to the generator along with its label. Now the generator has to produce fake data that is related to this label. Then, both the fake and real pairs of image and label are given to the discriminator, and it must decide what pair is real or fake (see Figure 4.11). In this manner, the generator becomes proficient not only at recreating fakes of the dataset, but also fake representatives of certain labels.

The loss in this case is written as:

$$\begin{aligned} \mathcal{L}_{cGAN}(G,D) &= \mathbb{E}_{x,y}[\log D(x,y)] + \mathbb{E}_{x,z}\left[\log(1 - D(x, G(x,z)))\right], \\ &\Rightarrow G^* = \arg\min_G \max_D \mathcal{L}_{cGAN}(G,D) \end{aligned} \tag{4.25}$$

This approach can be refined even further. For example, one can also add the $\mathcal{L}_1$ or $\mathcal{L}_2$ losses to the objective of the generator, in order to force it to produce images that are as close as possible to the ground truth. This method is also used in a cGAN-based model for image translation, named pix2pix [105], that we employed for charge density predictions:

$$\begin{aligned} \mathcal{L}^{\text{p2p}}_{\text{cGAN}}(G,D) &= \mathbb{E}_{x,y}[\log D(x,y)] + \mathbb{E}_{x,z}\left[\log(1 - D(x, G(x,z))\right] \\ &+ \mathbb{E}_{x,y,z}\left[\|y - G(x,z)\|_1\right] \\ &\Rightarrow G^* = \arg\min_G \max_D \mathcal{L}_{cGAN}(G,D) + \lambda \mathcal{L}_{L1}(G) \end{aligned} \tag{4.26}$$

4.6 Applications in condensed matter

The main results presented in this section were published in [54, 106]

4.6.1 Charge density predictions with cGANs

We have introduced the exact diagonalization method and its computational implementation in Section 3.6. While this approach offers the highest accuracy for calculating the ground state eigenvalues and eigenfunctions of a many-body system, it is also computationally demanding. Along with the machine learning revolution in all fields that deal with analyzing large amounts of data, there has also been a call for combining ML techniques with traditional algorithms in computational physics. In reference [54], we explored the possibility to use cGANs to make predictions about the charge density profiles for interacting many particle systems.

The quantum system we studied is comprised of N electrons confined to a randomly generated potential configuration V_{xy}. The configuration is defined on a 2D

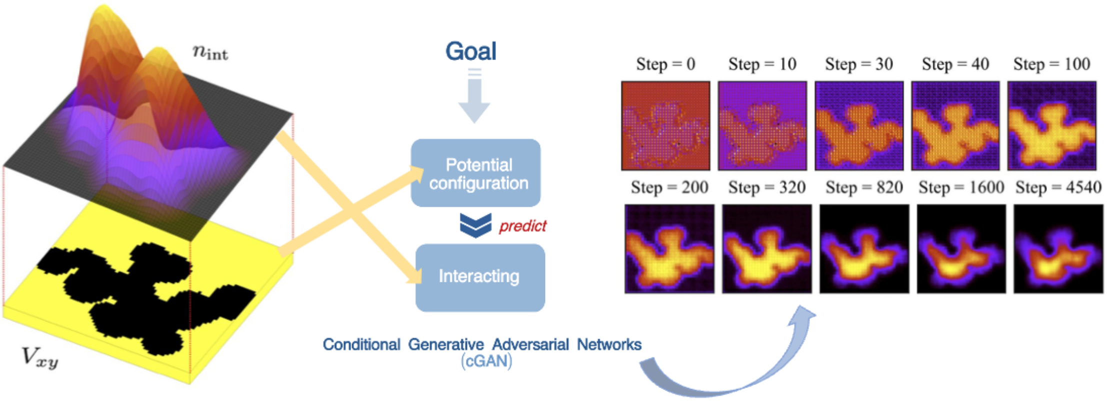

FIGURE 4.12: Prediction of interacting charge densities with an image translation ML model .

square region of area $L \times L$, as displayed in Figure 4.12 . The confining potential was obtained by assembling connected quantum wells, with potential $\mathrm{V}_0 = 0\,\mathrm{eV}$, while the step potential is set at $\mathrm{V}_\mathrm{s} = 0.5\,\mathrm{eV}$. A set of 5000 potential mappings were generated, in order to have enough data for the subsequent training of the ML model. These configurations resemble systems of interacting QDs such as two-dimensional self-assembled functionalized graphene QDs [107], randomly distributed QDs for memristive elements [108] or random geometric graphs of QDs [109].

For the case of $N = 2$ particles, using the reference cGAN configuration described in [105], we looked at mappings such as: (i) $V_{xy} \mapsto \tilde{n}_0$, (ii) $V_{xy} \mapsto \tilde{n}_{\text{int}}$, where the $'\sim'$ symbol stands for the generated quantities. The potentials $\{V_{xy}\}$ are available as input data and the non-interacting densities, $\{n_0\}$, can be easily calculated through one-particle calculations. The interacting densities, $\{n_{\text{int}}\}$, are determined using the ED method. The second mapping, $V_{xy} \mapsto \tilde{n}_{\text{int}}$, is of the highest importance, since it produces the profile of the charge density of a system with interaction without any diagonalization procedure. The result is almost instant, once the model was thoroughly trained and the loss metrics were monitored to avoid under/overfitting. Visually, the mappings depicted in Figure 4.13 reproduce the fundamental features of the reference (calculated) densities very well. The published paper [54] provides more details about the metrics we employed to measure the accuracy of the models in a quantitative manner.

As the particle number increases, the number of many-particle states also becomes considerably larger and the exact diagonalization calculations are even more computationally expensive. The accuracy in identifying the charge density maxima slightly decreases as the number of particle is increased, but the determination coefficient has higher values. When the number of electrons is raised even further, approaching the mean field case, the charge is more delocalized and it gradually takes the shape of the confining potential, which facilitates the prediction process.

4.6.2 ML models for molecular dynamics simulations

In article [106], we studied the collective motion of the embedded Calcium atoms in endohedral fullerenes cages and provided a consistent description of the correlated motion through extensive molecular dynamics calculations. For the purpose of identifying complex patterns in dynamics, we employed a hybrid numerical approach,

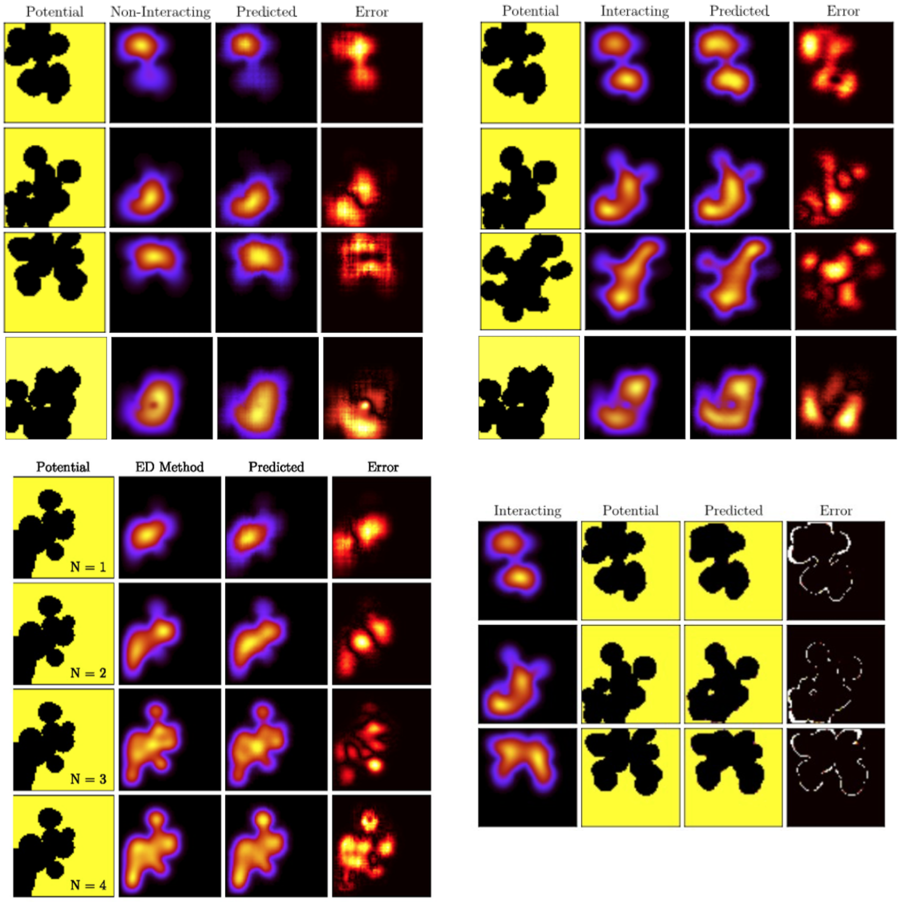

FIGURE 4.13: Results obtained with pix2pix. Upper row: Predicted non-interacting and interacting charge densities for different potential configurations. Bottom left corner: predicted charge densities for different electron numbers confined in the potential well. Bottom right corner: Predictions for the shape of the potential, with the charge densities as input.

employing efficient simulations based on *ab initio* molecular dynamics simulations (AIMD) and ML models.

The molecular dynamics simulations were done with the ORCA package, while the structural optimizations were performed in the framework of density functional theory (DFT). The computational load of molecular dynamics simulations is high, so we employed an ANN-based model in order to predict the dynamics. The ML model was used to determine the force field $\left\{\left(F_x, F_y, F_z\right)\right\}_i$ from the positions of the Ca atoms in the fullerene cage $\{(r, \theta, \phi)\}_i \rightarrow \left\{\left(F_x, F_y, F_z\right)\right\}_i$. Subsequently, using the predicted force field, we calculated the dynamics by means of Newton's laws, also accounting for the velocity rescaling induced by the thermostat. Our goal was to reproduce as accurately as possible the fundamental features of the trajectories and the correlated motion of the encapsulated atoms. The ANN architecture has four hidden layers, with $128, 1024, 512, 64$ neurons. We use the ReLU activation function in each layer, except for the last one, where it was determined that tanh was a better fit. Also, a dropout of 0.3 was applied to each hidden layer. The input layer contains $3 \times N_{\mathrm{Ca}}$ entries, corresponding to the spherical coordinates of the encapsulated Ca atoms multiplied by the number of samples in the training dataset. In this case, we choose to work with a multi-target regression model, such that the output layer was comprised also of 3 neurons, corresponding to the forces in Cartesian coordinates. We considered that, since the correlations between the embedded atoms in the cage are crucial, this approach would improve the accuracy of the ML model.

Also, we employed a regularization technique known as data augmentation, that we briefly discussed in section 4.2.3. Although the MD simulations were realized for an extended time interval, the Ca atoms actually occupy a small percentage of the space in the fullerene cage. We used data augmentation to enhance the sampling of trajectory space and we generated an extended training dataset by applying rotations to the Ca subsystem. The final dataset is obtained by considering 5500 MD steps multiplied by 7^3 rotations around the Cartesian axes, with an angular step size of $\pi/6$.

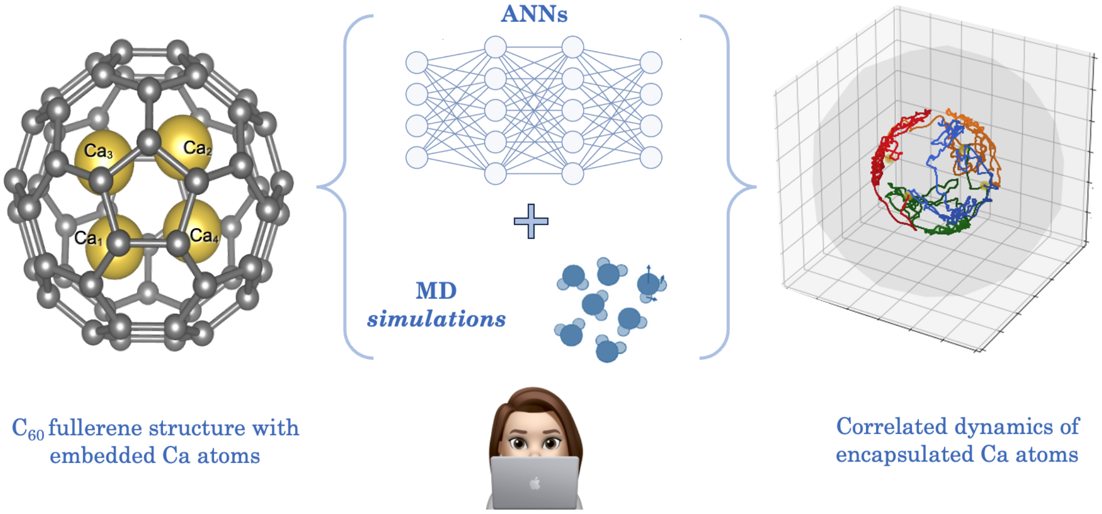

FIGURE 4.14: ML models employed to predict the dynamics of encapsulated Ca atoms in fullerene cages.

Part II

Results

5

R-matrix method for two particle scattering problems

>> The main results presented in this section were published in [3]

In the article [3] , we extended the R-matrix formalism to include two-particle scattering events. In this chapter, we shall briefly review the results introduced in the published work. The system is structurally similar to the one described in the case of the single-particle R-matrix formalism, which we presented in detail in Section 3.5. It consists of a number of leads connected to a central scattering region. The particles are identical fermions and our approach conserves the anti-symmetry of the fermionic wavefunction throughout the entire system. We obtained a consistent system of equations that yield the coefficients of the two-particle scattering scattering functions by choosing an appropriate initial Ansatz. To this end, the two-particle scattering functions are expanded in terms of anti-symmetrized products of one-particle scattering functions (when at least one particle is in the leads), or in terms of the two-particle eigenstates of the Hamiltonian (when both particles are in the scattering region).

We make the following assumptions

- The particles interact with each other through a potential of the type $V^{(\Omega_c)}\left(\mathbf{r}_1, \mathbf{r}_2\right) \equiv V^{(\Omega_c)}\left(|\mathbf{r}_1 - \mathbf{r}_2|\right)$, which depends on the distance between the two fermions. Also, we consider an interaction potential only if both of the particles are in the scattering region ($\mathbf{r}_1, \mathbf{r}_2 \in \Omega_c$).
- When both particles are in the leads or one particle is in one of the leads and the other is in the central region, they do not interact with each-other.
- The interactions do not depend on the particle spin
- The total energy E is conserved

The main notations that are used throughout the formalism are summarized in Table 5.1.

Notation	
s=1,2,3...	lead index
$\mathbf{r_p}$	particle position vector
Ω_c	scattering region
Ω_s	lead s region
Γ_s	interface between lead Ω_s and the central region

TABLE 5.1: Notations employed in the bi-particle R-matrix formalism

Hamiltonian of the system and Hamiltonian eigenstates

In the lead s, the single-particle Hamiltonian is:

$$\hat{\mathcal{H}}^{(s)}(\mathbf{r}) = -\frac{\hbar^2}{2m^{(\Omega_s)}}\Delta + V^{(s)}(\mathbf{r}) \tag{5.1}$$

where m^{Ω_s} is the effective mass and and $V^{(s)}$ is the single-particle potential energy. Since we assume translational invariance along the transport direction, then $V^{(s)}(\mathbf{r}) \equiv V^{(s)}(x,y) \equiv V^{(s)}\left(\mathbf{r}_\perp\right)$. The bi-particle Hamiltonian is:

$$\hat{\mathcal{H}}^{(2,\Omega_s)}\left(\mathbf{r}_1,\mathbf{r}_2\right) = \hat{\mathcal{H}}^{(\Omega_s)}\left(\mathbf{r}_1\right) + \hat{\mathcal{H}}^{(\Omega_s)}\left(\mathbf{r}_2\right) \tag{5.2}$$

For the interaction region Ω_c, the single-particle Hamiltonian is:

$$\hat{\mathcal{H}}^{(\Omega_c)}(\mathbf{r})\Big|_{\mathbf{r}\in\Omega_c} = -\frac{\hbar^2}{2m^{(\Omega_c)}}\Delta + V^{(\Omega_0)}(\mathbf{r}),$$

while the two-particle Hamiltonian is:

$$\hat{\mathcal{H}}^{(2,\Omega_c)}\left(\mathbf{r}_1,\mathbf{r}_2\right) = \hat{\mathcal{H}}^{(\Omega_0)}\left(\mathbf{r}_1\right) + \hat{\mathcal{H}}^{(\Omega_c)}\left(\mathbf{r}_2\right) + V_2^{(\Omega_c)}\left(\mathbf{r}_1,\mathbf{r}_2\right) \tag{5.3}$$

where $V_2^{(\Omega_c)}\left(\mathbf{r}_1,\mathbf{r}_2\right)$ was introduced above. Therefore, for the entire system $\mathcal{T} \equiv \Omega_c \bigcup \Omega_s$, we can define a non-interacting single particle Hamiltonian $\hat{\mathcal{H}}^{(\mathcal{T})}(\mathbf{r})$, the the two-particle Hamiltonian $\hat{\mathcal{H}}^{(2,\mathcal{T})}\left(\mathbf{r}_1,\mathbf{r}_2\right)$ and an ideal two particle Hamiltonian $\hat{\mathcal{H}}_0^{(2,\mathcal{T})}\left(\mathbf{r}_1,\mathbf{r}_2\right)$:

$$\begin{cases} \hat{\mathcal{H}}^{(\mathcal{T})}(\mathbf{r}) \equiv \hat{\mathcal{H}}^{(\Omega_s)}(\mathbf{r}) + \hat{\mathcal{H}}^{(\Omega_c)}(\mathbf{r}), \\ \hat{\mathcal{H}}^{(2,\mathcal{T})}\left(\mathbf{r}_1,\mathbf{r}_2\right) \equiv \hat{\mathcal{H}}^{(2,\Omega_s)}\left(\mathbf{r}_1,\mathbf{r}_2\right) + \hat{\mathcal{H}}^{(2,\Omega_c)}\left(\mathbf{r}_1,\mathbf{r}_2\right), \\ \hat{\mathcal{H}}_0^{(2,\mathcal{T})}\left(\mathbf{r}_1,\mathbf{r}_2\right) \equiv \hat{\mathcal{H}}^{(\mathcal{T})}\left(\mathbf{r}_1\right) + \hat{\mathcal{H}}^{(\mathcal{T})}\left(\mathbf{r}_2\right), \end{cases} \tag{5.4}$$

The orbital component of the eigenstate of the single-particle Hamiltonian at energy E, $\Psi_i^{(in,s,E)} = 1$ and $\Psi_j^{(in,s',E)} = 0$ for any $s' \neq s, j \neq i$ is:

$$\Psi_i^{(1,s,\mathcal{T},E)}(\mathbf{r}) \equiv \sum_{s',j}\left[\delta_{ij}\delta_{ss'}e^{-ik_j^{(s',E)}z} + \psi_{j(s,i)}^{(out,s',E)}e^{ik_j^{(s',E)}z}\right]\phi_j^{(s')}(\mathbf{r}) + \sum_l a_{l(s,i)}^{(E)}\chi_l(\mathbf{r}) \tag{5.5}$$

where $\chi_l(\mathbf{r})$ are the Wigner-Eisenbud functions, while the coefficients $\psi_{j(s,i)}^{(out,s',E)}$ and $a_{l(s,i)}^{(E)}$ can be determined as we highlighted in a detailed manner in Section 3.5.

The Ansatz that we propose for $\Psi^{(\pm,2,T,E)}\left(\mathbf{r}_1,\mathbf{r}_2\right)$ in the exterior region (see Figure 5.1), such that it satisfies energy conservation and the continuity equations is:

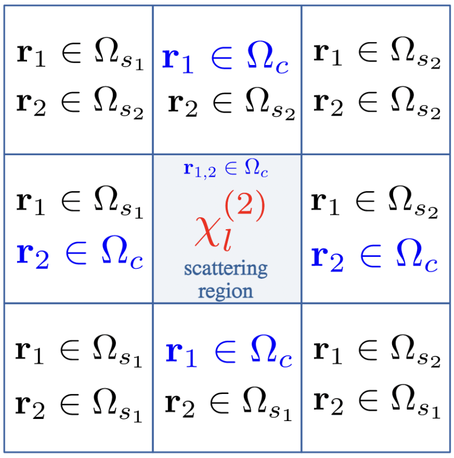

FIGURE 5.1: The 2D schematic representation of the 6D coordinate space of the system, where leads Ω_{s1} and Ω_{s2} are attached to the scattering region Ω_c. The coordinates corresponding to the two electrons,$\mathbf{r}_1$ and $\mathbf{r}_2$, can be in any of the three regions, Ω_{s1}, Ω_{s2}, or Ω_c. We call the *exterior region* the eight marginal squares, where at least one of the coordinates ($\mathbf{r}_1$ or $\mathbf{r}_2$) is not in the central region Ω_c. We consider that the particles are independent and non-interacting in the exterior region. The two particle potential acts only in the *interior region*, which is represented by the middle square with blue background.

$$\Psi^{(\pm,0,2,\mathcal{T},E)}\left(\mathbf{r}_1,\mathbf{r}_2\right) = \int_0^E \frac{dE_1}{E} \sum_{s,s',i,j} C_{i,j}^{(\pm,s,E_1,s',E-E_1)} \times \left[\Psi_i^{(1,s,\mathcal{T},E_1)}\left(\mathbf{r}_1\right)\Psi_j^{(1,s',\mathcal{T},E-E_1)}\left(\mathbf{r}_2\right) \pm \Psi_i^{(1,s,\mathcal{T},E_1)}\left(\mathbf{r}_2\right)\Psi_j^{(1,s',\mathcal{T},E-E_1)}\left(\mathbf{r}_1\right)\right]. \tag{5.6}$$

In the interior region, the two-particle wavefunction can be written as:

$$\Psi^{(\pm,2,\Omega_c,E)}\left(\mathbf{r}_1,\mathbf{r}_2\right) = \sum a_l^{(\pm,2,E)} \chi_l^{(\pm,2)}\left(\mathbf{r}_1,\mathbf{r}_2\right) \tag{5.7}$$

The eigenfunctions $\chi_l^{(\pm,2)}\left(\mathbf{r}_1,\mathbf{r}_2\right)$ satisfy the Schrödinger equation:

$$\hat{\mathcal{H}}^{(2,\mathcal{T})}\left(\mathbf{r}_1,\mathbf{r}_2\right)\chi_l^{(\pm,2)}\left(\mathbf{r}_1,\mathbf{r}_2\right) = E_l^{(\pm,2,\Omega_c)}\chi_l^{(\pm,2)}\left(\mathbf{r}_1,\mathbf{r}_2\right), \qquad \text{for } \mathbf{r}_1,\mathbf{r}_2 \in \Omega_c,$$

and the boundary conditions

$$\left[\hat{\mathbf{n}}_{\Gamma_s}\left(\mathbf{r}_1\right)\cdot\nabla_1\chi_l^{(\pm,2)}\left(\mathbf{r}_1,\mathbf{r}_2\right)\right]_{\mathbf{r}_1\in\Gamma_s} = \left[\hat{\mathbf{n}}_{\Gamma_s}\left(\mathbf{r}_2\right)\cdot\nabla_2\chi_l^{(\pm,2)}\left(\mathbf{r}_1,\mathbf{r}_2\right)\right]_{\mathbf{r}_2\in\Gamma_s} = 0,$$

whereas $\chi_l^{(\pm,2)}\left(\mathbf{r}_1,\mathbf{r}_2\right) = 0$ if $\mathbf{r}_1$ or $\mathbf{r}_2 \notin \Omega_c$. The functions $\chi_l^{(\pm,2)}\left(\mathbf{r}_1,\mathbf{r}_2\right)$ are the bi-particle analogue to the single particle Wigner-Eisenbud eigenfunctions $\chi_l(\mathbf{r})$ introduced in Section 3.5. Using a method similar to the one described in 3.5, we obtain the expression for the expansion coefficients:

$$\begin{aligned}
&a_l^{(\pm,2,E)}\left(E-E_l^{(2)}\right) = -\frac{\hbar^2}{2m^{(\Omega_c)}}\cdot \\
&\sum_s \left(\int_{\Omega_c} d\mathbf{r}_2 \int_{\Gamma_s} d\Gamma_s \left\{ \hat{\mathbf{n}}_{\Gamma_s}(\mathbf{r}_1)\cdot \left[\chi_l^{(\pm,2)^*}(\mathbf{r}_1,\mathbf{r}_2)\, \nabla_1 \Psi^{(\pm,2,\mathcal{T},E)}(\mathbf{r}_1,\mathbf{r}_2) \right] \right\}_{\mathbf{r}_1\in\Gamma_{s\Omega_0}} \right. \\
&\left. + \int_{\Omega_0} d\mathbf{r}_1 \int_{\Gamma_s} d\Gamma_s \left\{ \hat{\mathbf{n}}_{\Gamma_s}(\mathbf{r}_2)\cdot \left[\chi_l^{(\pm,2)^*}(\mathbf{r}_1,\mathbf{r}_2)\, \nabla_2 \Psi^{(\pm,2,\mathcal{T},E)}(\mathbf{r}_1,\mathbf{r}_2) \right] \right\}_{\mathbf{r}_2\in\Gamma_{s\Omega_0}} \right).
\end{aligned} \tag{5.8}$$

Continuity of the wavefunction when one particle is the scattering region and the other one is on the interface

From the continuity condition of the wavefunction we get an equation for $a_l^{(\pm,2,E)}$ [3]:

$$\begin{aligned}
&\sum_l a_l^{(\pm,2,E)} \int_{\Omega_0} d\mathbf{r}_2 \chi_{l_0}^*(\mathbf{r}_2) \int_{\Gamma_{s_1}} d\Gamma_{s_1} \left[\phi_k^{(s_1)^*}(\mathbf{r}_{1\perp})\, \chi_l^{(\pm,2,E)}(\mathbf{r}_1,\mathbf{r}_2) \right]_{\mathbf{r}_1\in\Gamma_{s_1\Omega_0}} \\
&= \frac{1}{\sqrt{2}} \int_0^E \frac{dE_1}{E} \sum_{s,s',i,j} C_{i,j}^{(\pm,s,E_1,s',E-E_1)} \mathcal{B}_{i,j,k,l_0}^{(\pm,s,E_1,s',E-E_1,s_1)}
\end{aligned} \tag{5.9}$$

with

$$\begin{aligned}
&\mathcal{B}_{i,j,k,l_0}^{(\pm,s,E_1,s',E-E_1,s_1)} \equiv \left\{ a_{l_0}\left(\Psi_j^{(1,s',\mathcal{T},E-E_1)}\right) \left[\delta_{ik}\delta_{ss_1} + \psi_k^{(\text{out},s_1,E)}\left(\Psi_i^{(1,s,\mathcal{T},E)}\right) \right] \right. \\
&\left. \pm a_{l_0}\left(\Psi_i^{(1,s,\mathcal{T},E)}\right) \left[\delta_{jk}\delta_{s's_1} + \psi_k^{(\text{out},s_1,E-E_1)}\left(\Psi_j^{(1,s',\mathcal{T},E-E_1)}\right) \right] \right\}
\end{aligned} \tag{5.10}$$

Continuity of the probability flux when one particle is the scattering region and the other one is on the interface

Let us now consider that $\mathbf{r}_2 \in \Omega_c$ and $\mathbf{r}_1 \in \Gamma_{s_1}$. We impose the condition:

$$\frac{1}{m^{(\Omega_c)}} \frac{\partial \Psi^{(\pm,2,\mathcal{T},E)}(\mathbf{r}_1,\mathbf{r}_2)}{\partial z_1} \Bigg|_{\mathbf{r}_1\in\Gamma_{S_1\Omega_c},\mathbf{r}_2\in\Omega_c} = \frac{1}{m^{(\Omega_s)}} \frac{\partial \Psi^{(\pm,0,2,\mathcal{T},E)}(\mathbf{r}_1,\mathbf{r}_2)}{\partial z_1} \Bigg|_{\mathbf{r}_1\in\Gamma_{s_1\Omega_s},\mathbf{r}_2\in\Omega_c} \tag{5.11}$$

From this, we obtained [3]:

$$\frac{\partial \Psi^{(\pm,2,\mathcal{T},E)}(\mathbf{r}_1,\mathbf{r}_2)}{\partial z_2} \Bigg|_{\mathbf{r}_1\in\Omega_0,\mathbf{r}_2\in\Gamma_{s_2\Omega_0}} = -\frac{m^{(\Omega_0)}}{m^{(\Omega_s)}} \frac{1}{\sqrt{2}} \int_0^E \frac{dE_1}{E} \sum_{s,s',i,j} C_{i,j}^{(\pm,s,E_1,s',E-E_1)} \mathcal{A}_{i,j}^{(\pm,s,E_1,s',E-E_1,s_2)}(\mathbf{r}_2,\mathbf{r}_1) \tag{5.12}$$

where

$$\begin{aligned}
&\mathcal{A}_{i,j}^{(\pm,s,E_1,s',E-E_1,s_1)}\left(\mathbf{r}_1,\mathbf{r}_2\right) \equiv \left.\frac{\partial\Psi_i^{(1,s,\mathcal{T},E_1)}\left(\mathbf{r}_1\right)}{\partial z_1}\right|_{\Gamma_{s_1}\Omega_s} \Psi_j^{(1,s',\mathcal{T},E-E_1)}\left(\mathbf{r}_2\right) \pm \\
&\Psi_i^{(1,s,\mathcal{T},E_1)}\left(\mathbf{r}_2\right) \left.\frac{\partial\Psi_j^{(1,s',\mathcal{T},E-E_1)}}{\partial z_1}\left(\mathbf{r}_1\right)\right|_{\Gamma_{s_1}\Omega_s} \\
&= \sum_{i_1}\left(-ik_{i_1}^{(s_1,E_1)}\left[\delta_{ii_1}\delta_{ss_1} - \psi_{i_1}^{(out,s_1,E_1)}\left(\Psi_i^{(1,s,\mathcal{T},E_1)}\right)\right]\phi_{i_1}^{(s_1)}\left(\mathbf{r}_1\right)\right)\Psi_j^{(1,s',\mathcal{T},E-E_1)}\left(\mathbf{r}_2\right) \pm \Psi_i^{(1,s,\mathcal{T},E_1)}\left(\mathbf{r}_2\right) \\
&\times \sum_{i_1}\left(-ik_{i_1}^{(s_1,E-E_1)}\left[\delta_{ji_1}\delta_{s's_1} - \psi_{i_1}^{(\mathrm{out}\,,s_1,E-E_1)}\left(\Psi_j^{(1,s',\mathcal{T},E-E_1)}\right)\right]\phi_{i_1}^{(s_1)}\left(\mathbf{r}_1\right)\right)
\end{aligned} \tag{5.13}$$

Final equations for coefficients C

Using the results from the continuity conditions and the expression for the expansion coefficients, we obtained:

$$\int_0^E \frac{dE_1}{E} \sum_{s,s',i,j} C_{i,j}^{(\pm,s,E_1,s',E-E_1)} \mathcal{D}_{i,j,s_1,k,l_0}^{(\pm,s,E_1,s',E-E_1)} = 0, \tag{5.14}$$

where

$$\begin{aligned}
&\mathcal{D}_{i,j,s_1,k,l_0}^{(\pm,s,E_1,s',E-E_1)} \equiv -\frac{\hbar^2}{m^{(\Omega_s)}} \sum_l \left\{ \int_{\Omega_0} d\mathbf{r}_2 \sum_{s_1} \int_{\Gamma_{s_1}} d\Gamma_{s_1} \left[\chi_l^{(\pm,2)*}\left(\mathbf{r}_1,\mathbf{r}_2\right) \mathcal{A}_{i,j}^{(\pm,s,E_1,s',E-E_1,s_1)}\left(\mathbf{r}_1,\mathbf{r}_2\right)\right]_{\mathbf{r}_1\in\Gamma_{s_1}} \right\} \\
&\times \frac{\int_{\Omega_0} d\mathbf{r}_2 \chi_{l_0}^{*}\left(\mathbf{r}_2\right) \int_{\Gamma_{s_1}} d\Gamma_{s_1} \left[\phi_k^{(s_1)*}\left(\mathbf{r}_{1\perp}\right)\chi_l^{(\pm,2)}\left(\mathbf{r}_1,\mathbf{r}_2\right)\right]_{\mathbf{r}_1\in\Gamma_{s_1}}}{E-E_l^{(2)}} - \mathcal{B}_{i,j,k,l_0}^{(\pm,s,E_1,s',E-E_1,s_1)}
\end{aligned} \tag{5.15}$$

We present the logic of our method in Figure 5.2 where one can easily follow the workflow with the main steps ar equations to be solved.

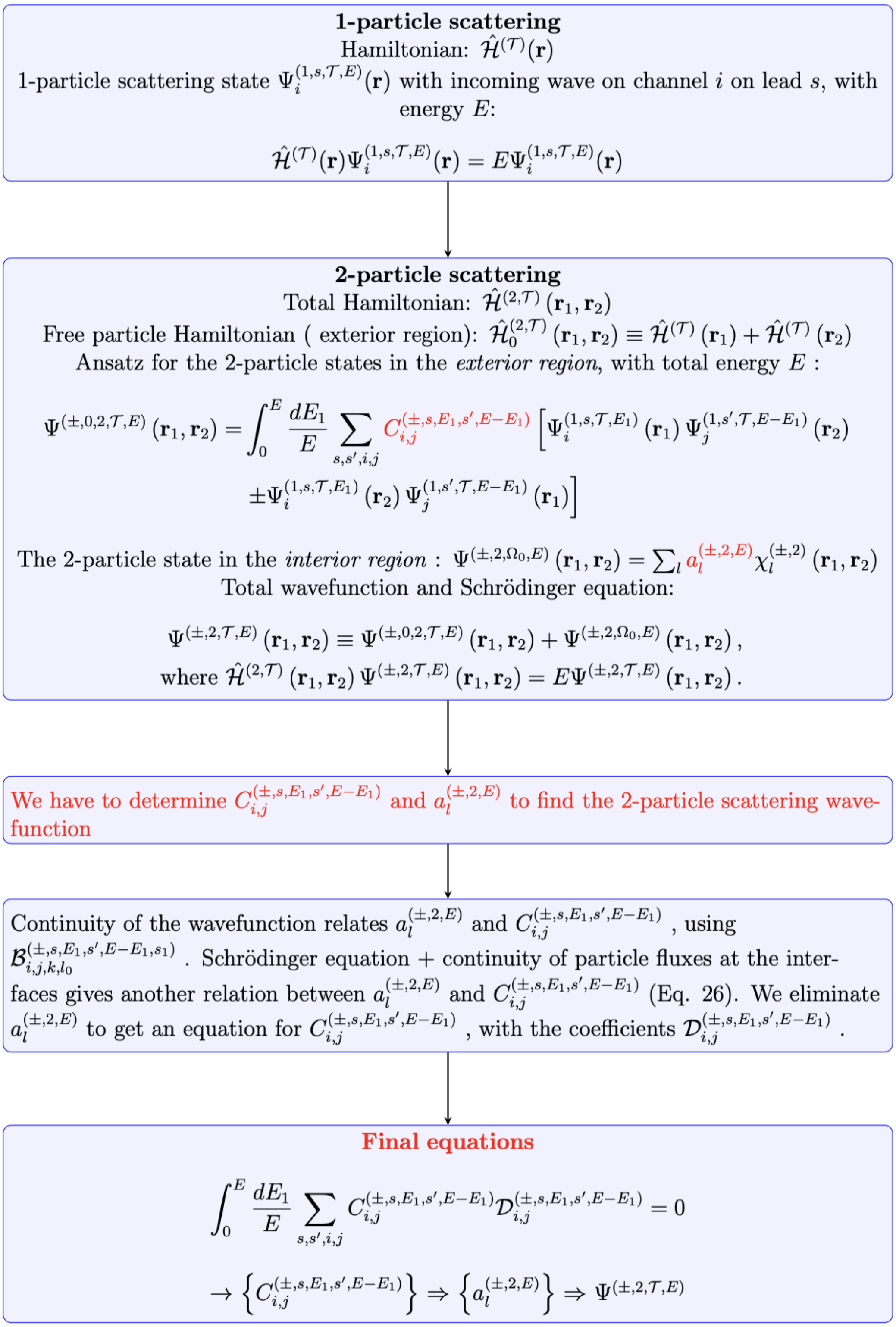

1-particle scattering

Hamiltonian: $\hat{\mathcal{H}}^{(\mathcal{T})}(\mathbf{r})$

1-particle scattering state $\Psi_i^{(1,s,\mathcal{T},E)}(\mathbf{r})$ with incoming wave on channel i on lead s, with energy E:

$$\hat{\mathcal{H}}^{(\mathcal{T})}(\mathbf{r})\Psi_i^{(1,s,\mathcal{T},E)}(\mathbf{r}) = E\Psi_i^{(1,s,\mathcal{T},E)}(\mathbf{r})$$

2-particle scattering

Total Hamiltonian: $\hat{\mathcal{H}}^{(2,\mathcal{T})}(\mathbf{r}_1,\mathbf{r}_2)$

Free particle Hamiltonian (exterior region): $\hat{\mathcal{H}}_0^{(2,\mathcal{T})}(\mathbf{r}_1,\mathbf{r}_2) \equiv \hat{\mathcal{H}}^{(\mathcal{T})}(\mathbf{r}_1) + \hat{\mathcal{H}}^{(\mathcal{T})}(\mathbf{r}_2)$

Ansatz for the 2-particle states in the *exterior region*, with total energy E :

$$\Psi^{(\pm,0,2,\mathcal{T},E)}(\mathbf{r}_1,\mathbf{r}_2) = \int_0^E \frac{dE_1}{E} \sum_{s,s',i,j} C_{i,j}^{(\pm,s,E_1,s',E-E_1)} \Big[\Psi_i^{(1,s,\mathcal{T},E_1)}(\mathbf{r}_1)\,\Psi_j^{(1,s',\mathcal{T},E-E_1)}(\mathbf{r}_2) \pm\Psi_i^{(1,s,\mathcal{T},E_1)}(\mathbf{r}_2)\,\Psi_j^{(1,s',\mathcal{T},E-E_1)}(\mathbf{r}_1)\Big]$$

The 2-particle state in the *interior region* : $\Psi^{(\pm,2,\Omega_0,E)}(\mathbf{r}_1,\mathbf{r}_2) = \sum_l a_l^{(\pm,2,E)}\chi_l^{(\pm,2)}(\mathbf{r}_1,\mathbf{r}_2)$

Total wavefunction and Schrödinger equation:

$$\Psi^{(\pm,2,\mathcal{T},E)}(\mathbf{r}_1,\mathbf{r}_2) \equiv \Psi^{(\pm,0,2,\mathcal{T},E)}(\mathbf{r}_1,\mathbf{r}_2) + \Psi^{(\pm,2,\Omega_0,E)}(\mathbf{r}_1,\mathbf{r}_2)\,,$$

$$\text{where } \hat{\mathcal{H}}^{(2,\mathcal{T})}(\mathbf{r}_1,\mathbf{r}_2)\,\Psi^{(\pm,2,\mathcal{T},E)}(\mathbf{r}_1,\mathbf{r}_2) = E\Psi^{(\pm,2,\mathcal{T},E)}(\mathbf{r}_1,\mathbf{r}_2)\,.$$

We have to determine $C_{i,j}^{(\pm,s,E_1,s',E-E_1)}$ and $a_l^{(\pm,2,E)}$ to find the 2-particle scattering wavefunction

Continuity of the wavefunction relates $a_l^{(\pm,2,E)}$ and $C_{i,j}^{(\pm,s,E_1,s',E-E_1)}$, using $\mathcal{B}_{i,j,k,l_0}^{(\pm,s,E_1,s',E-E_1,s_1)}$. Schrödinger equation + continuity of particle fluxes at the interfaces gives another relation between $a_l^{(\pm,2,E)}$ and $C_{i,j}^{(\pm,s,E_1,s',E-E_1)}$ (Eq. 26). We eliminate $a_l^{(\pm,2,E)}$ to get an equation for $C_{i,j}^{(\pm,s,E_1,s',E-E_1)}$, with the coefficients $\mathcal{D}_{i,j}^{(\pm,s,E_1,s',E-E_1)}$.

Final equations

$$\int_0^E \frac{dE_1}{E} \sum_{s,s',i,j} C_{i,j}^{(\pm,s,E_1,s',E-E_1)}\mathcal{D}_{i,j}^{(\pm,s,E_1,s',E-E_1)} = 0$$

$$\to \left\{C_{i,j}^{(\pm,s,E_1,s',E-E_1)}\right\} \Rightarrow \left\{a_l^{(\pm,2,E)}\right\} \Rightarrow \Psi^{(\pm,2,\mathcal{T},E)}$$

FIGURE 5.2: The logic of the method published in [3] is presented in the form of a workflow where one can follow the main equations that lead to determination of the coefficients for the two-particle scattering function.

6

Device modeling

6.1 Two dimensional systems: gate arrays

The main results presented in this section were published in [110]

We begin the introduction of this chapter with the presentation of a many-particle system that marked the beginning of our computational studies of 2D quantum many-body systems with possible applications to quantum computing, namely a gate array controlled quantum dot system [110]. Quantum dot arrays are viable prototypes for quantum computing architectures, due to their versatility in controlling the ground state with voltages applied to the top gates. To this end, investigating the spectra of many-electron systems becomes a prerequisite to designing such devices, an endeavor which requires a significant computational effort. Our aim was not only to highlight the properties of a bi-particle 2D gate array system, but also to employ machine learning techniques to predict the many-electron eigenvalues and eigenfunctions.

6.1.1 Model system

The proposed architecture is displayed in Figure 6.1a, where we consider a set of N-particle quantum systems (N = 2) defined on a finite two-dimensional square shaped region. Each gate voltage can take two values (0 or V_g), defining a configuration that controls the potential energy in the plane where the electrons are confined. The many-body eigenstates are determined by the voltages applied on the top gates and the Coulomb interaction between electrons is fully accounted for. The fundamental features of the many-body system are captured in this description, but we ignore for now any additional screening effects that would emerge due to the gate electrodes.

The number of systems depends on the number of gates (N_g) and is 2^{N_g}. Since the Coulomb potential is given by:

$$V_{\mathrm{C}}\left(\mathbf{r}-\mathbf{r}'\right)=\frac{1}{4\pi\bar{\epsilon}_0\bar{\epsilon}_r}\frac{e^2}{|\mathbf{r}-\mathbf{r}'|}, \tag{6.1}$$

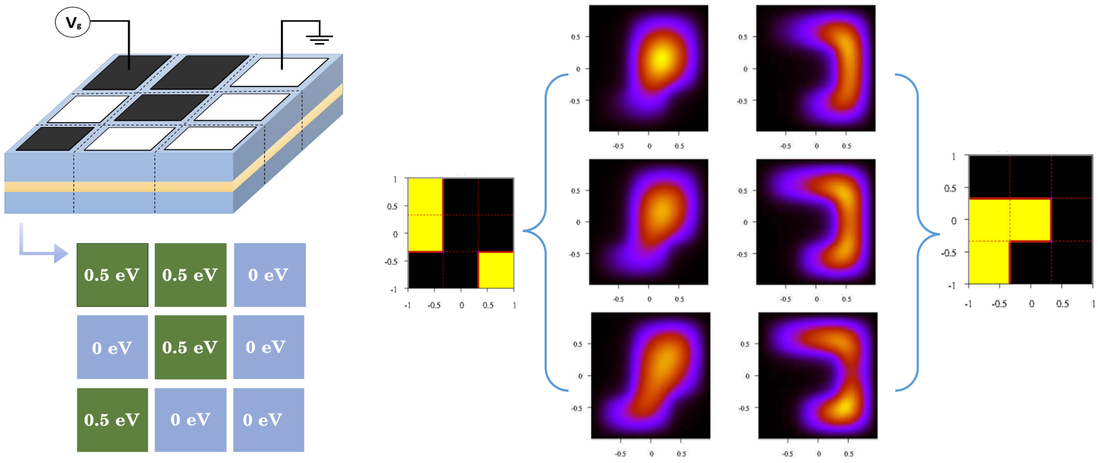

(A) (B)

FIGURE 6.1: (A) The gate-array controlling the 2D many-body system. (B) Two potential configurations, corresponding to a system without (left) a central potential block and one with a central potential block, respectively (right).

it follows that the relative strength of the Coulomb interaction can be adjusted by modifying the relative permittivity $\bar{\epsilon}_r$. The maximum Coulomb interaction $\left(V_C^0\right)$ is obtained for $\bar{\epsilon}_r = 1$, so $V_C = V_C^0/\bar{\epsilon}_r$. Also, one can also vary the effective mass m_{eff} and the geometrical confinement, which controls the strength of the electrostatic potential relative to the single-particle energy level spacings. Other external conditions can be applied, such as in-plane electric fields, and we will explore this in Section 6.3. In the subsequent calculations, we considered that the number of top gates is $N_g = 3^2$, the applied potentials are $V_g = 0$ and $0.5\,\text{eV}$, the linear size of the confinement region is $L = 30$ nm and the effective mass is $m_{\text{eff}} = 0.0655 m_0$, corresponding to GaAs. Also, note that a small Zeeman term was added to order the spin-states properly.

6.1.2 Computational methods

Description of bi-particle states with the exact diagonalization method

The energy spectra of the bi-particle electronic Hamiltonian are obtained using the exact diagonalization method, introduced in Section 3.6. The N-particle Hamiltonian is:

$$\mathcal{H}\Psi_n = E_n \Psi_n,$$

where E_n and $\Psi_n \equiv \Psi_n\left(\mathbf{r}_1, \sigma_{\mathbf{z1}}, \ldots, \mathbf{r}_\text{N}, \sigma_{\mathbf{zN}}\right)$ are the eigenvalues and eigenfunctions of the many-body system. The N-particle eigenvalue problem is solved in the occupation number representation and the basis elements are given by the eigenvectors of the non-interacting system. In the ED code, they are represented as binary strings. If we take one of these basis elements as a many-electron state denoted by $|\psi_k\rangle$, then:

$$|\psi_k\rangle = \left|n_1^{(k)} n_2^{(k)} \ldots n_s^{(k)} \ldots\right\rangle,$$

where $n_s^{(k)} = 0$ or 1 and $s \leq N_{\text{SES}}$ (N_{SES} is the number of single particle states).

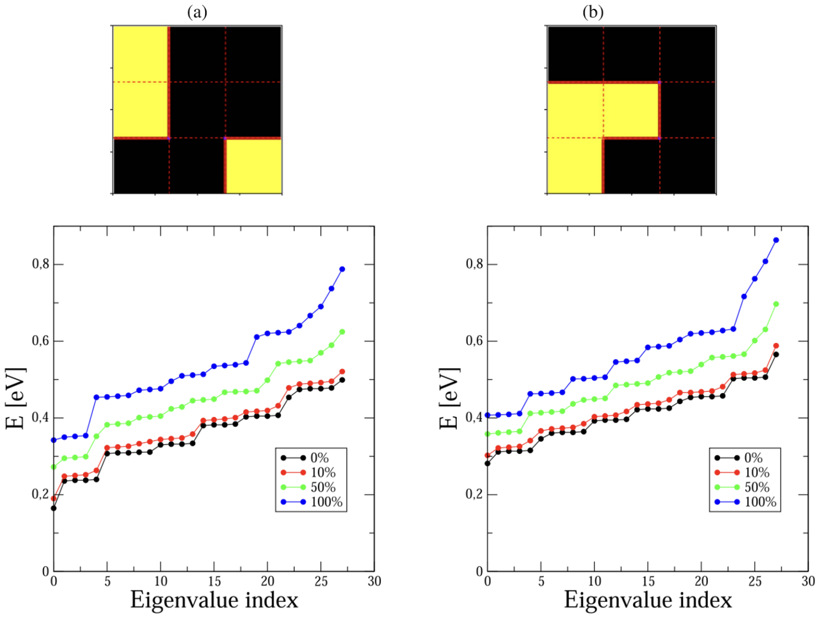

FIGURE 6.2: Two potential configurations induced by the top-gate array and the corresponding eigenvalues for different strengths of the Coulomb interaction, namely $v_c = 0, 0.1, 0.5, 1.0$.

Therefore,

$$\Psi_n = \sum_k C_{nk} \psi_k, \tag{6.2}$$

where k counts the many-particle states ($N_{\text{MES}} = C^{N}_{N_{\text{SES}}}$). In our calculations, we considered $N_{\text{SES}} = 8$ single particle states, leading to $N_{\text{MES}} = 28$. Relevant observables (charge and spin) for a certain eigenstate n, can be written as [110]:

$$\begin{aligned}\bar{\rho}_n(\mathbf{r}) &= \sum_k |C_{nk}|^2 \sum_{p=1}^{2} \left[\left|\phi_{i_p,\uparrow}\right|^2 + \left|\phi_{i_p,\downarrow}\right|^2 \right] \\ \bar{\sigma}_{z,n}(\mathbf{r}) &= \sum_k |C_{nk}|^2 \sum_{p=1}^{2} \left[\left|\phi_{i_p,\uparrow}\right|^2 - \left|\phi_{i_p,\downarrow}\right|^2 \right]\end{aligned} \tag{6.3}$$

where ϕ_{i_p} are the single-particle states.

Since our focus is to develop multi-target regression models to predict the energy spectra of such 2D many-body systems, we performed exact diagonalization calculations for all the possible potential configurations. These results were subsequently used to assess the performance of the ML approaches. For each potential map, we considered 21 values for the strength of the Coulomb interaction. By varying V_C in small incremental steps, we generated over 10 000 systems to analyze. The single-particle eigenvalue problem is solved with basis set of $2 \times N_{\text{bx}} \times N_{\text{by}}$ functions, with $N_{\text{bx}} = N_{\text{by}} = 30$, on a real-space grid of $N_x = N_y = 60$ points.

Machine learning techniques

The problem formulated here has two generic coordinates: the list of potentials given by all the possible top gate configurations $\{V_{xy}(i_V)\}$ and the relative strength of the Coulomb interaction v_C. The Coulomb interaction, v_C is a continuous variable,

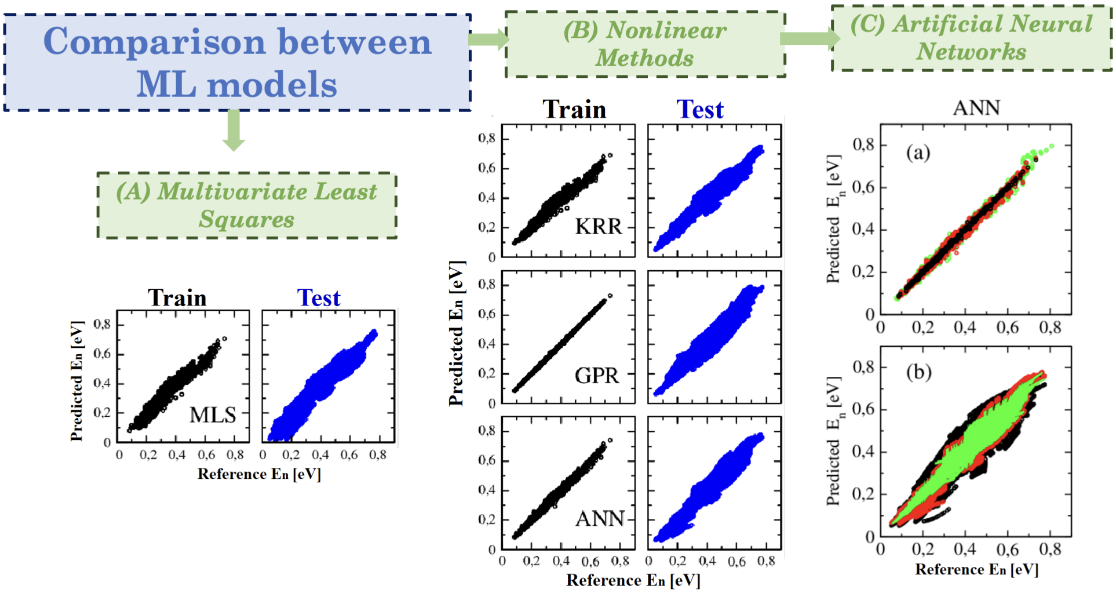

FIGURE 6.3: Comparison between multiple ML models employed for the prediction of the many-body energy spectra.

while the set of 2^{N_g} potentials are represented as binary strings in an N_g-dimensional space. Therefore, the features are constructed as $(N_g + 1)$-dimensional vectors, containing a combination of discrete and continuous feature representations that allow for a direct connection between the system information and the target quantities. Also, note that the full set of 512 potentials includes several equivalent systems that can be obtained through rotations and mirroring, leaving only 102 non-equivalent potential maps. However, to maximize the use of training data, we incorporated all the equivalent configurations, since this approach should drive the models towards integrating the symmetry of the 2D system naturally. For predicting the set of eigenvalues, we explored a couple of ML techniques:

- The method of least squares (MLS) ⇒ It is a fundamental linear regression method, consisting of fitting the parameters of an overdetermined linear model by minimizing the sum of the squared residuals. This method is already implemented in the SciKit library.

- Kernel Ridge Regression (KRR) ⇒ It combines ridge regression with the kernel trick, which implies learning a nonlinear function by performing linear regression after projecting the data in a high dimensional feature space. The method is implemented with the SciKit library in Python, using the radial basis function (RBF) kernel and maximum regularization (which is specified by the parameter $\alpha = 1$).

- Gaussian process regression (GPR) ⇒ It is a method of computing distributions over continuous functions that conform to a finite number of observations or measured values. The GPR model, also implemented directly in Python, uses a kernel similar to the one employed in KRR, with $\sigma_0 = 0.5$ and 5 optimization restarts.

- Artificial Neural Networks (ANNs) ⇒ The ANN architecture is comprised of only one hidden layer with 25 neurons. The learning process was performed for 5000 epochs, with a batch size of 25 and a learning rate of 0.001. The loss

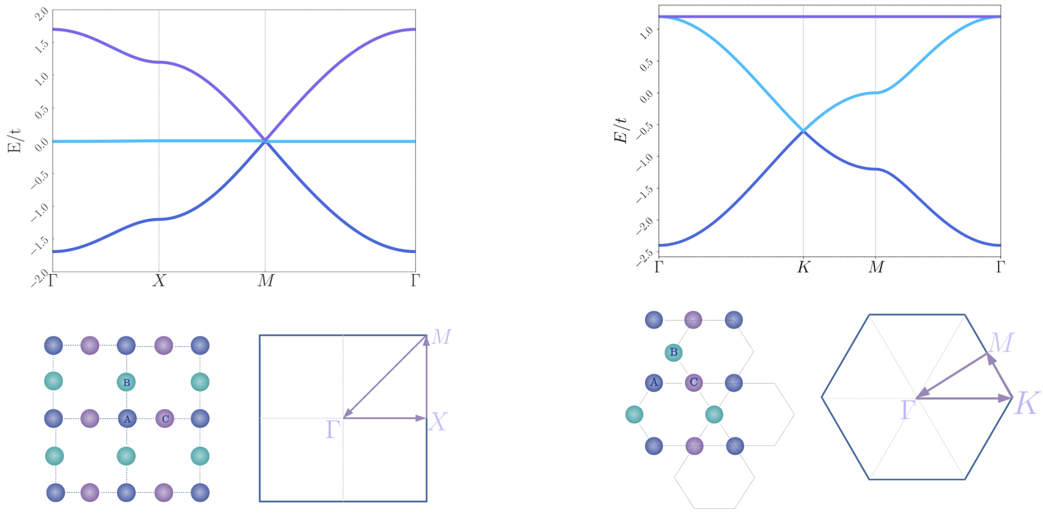

(A)

(B)

FIGURE 6.4: (A) Bandstructure of an ideal Lieb lattice with NN interactions, along with the first Brillouin zone. (B) Bandstructure of an ideal Kagome lattice with NN interactions, along with the first Brillouin zone.

function is the mean squared error and the optimizer that we chose was Adam. For the evaluation of the train and test errors, we use the R^2 coefficient of determination.

The train set contains $N_{\text{train}} = N_V \times N_{\text{int}}$ examples, where N_V is the number of potential configurations and N_{int} is the number of relative Coulomb interactions selected for the learning process (namely $v_C = 0.1, 0.5, 0.9$). The results are indicated in Figure 6.3. The linear method (MLS) gives a reasonable coefficient of determination ($R^2 = 0.85$), but, as it was expected, it is outperformed by the non-linear methods: KRR(0.91), GPR (0.92) and ANN (0.96). Although the R^2 values are comparable, the ANN performs better overall. In Figure 6.3 we also represented how the coefficient of determination for the ANN model varies for different sizes of the training sets. As expected, the R^2 value is the highest when the size of the training set is increased ($R^2 = 0.97$).

Our study shows that it is possible for this class of ML models to predict the entire many-particle spectrum of 28 eigenvalues with quite high accuracy, having as input an $N_g + 1$ feature vector. The non-linear methods, like KRR, GPR, ANN, bring a considerable improvement (almost 10%) in the accuracy as measured by R^2, which could be pivotal in the design of optoelectronic devices.

6.2 Two-dimensional systems with periodic boundary conditions -Lieb lattices

6.2.1 Introduction

Two dimensional topological lattices, such as Lieb and Kagome lattices have been extensively studied due to their exotic features related to the Dirac cones and flatbands that emerge in their band structures. Non-trivial flatbands, driven by destructive interference, are investigated in the context of highly degenerated single particle

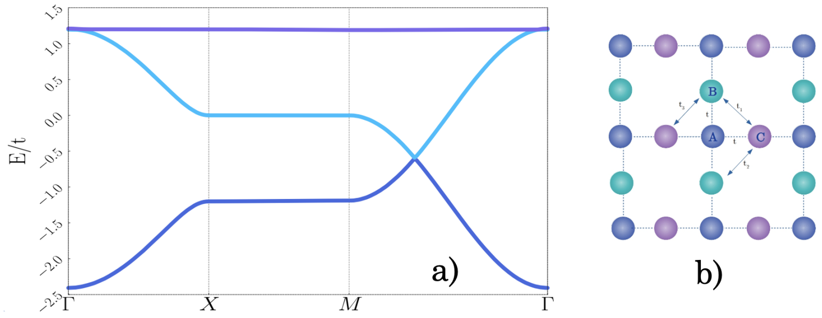

FIGURE 6.5: A Lieb lattice transitions into a Kagome-like structure if the hopping parameters are modified in a manner that favours the overlap between the orbital wavefunctions on the B and C sites.

states leading to strongly correlated phenomena, topological states, superconductivity, strong suppression of magnetic coupling [111, 112]. In Lieb and Kagome lattices, both of these peculiar features coexist in different arrangements due to their similar geometrical structures. Lieb lattices are edge centered squared lattices, while Kagome lattices are 2D triangular corner-sharing networks [113] (see Figures 6.4). Two dimensional lattices are also suitable candidates for the study of YSR (Yu-Shiba-Rusinov) states which emerge after a magnetic impurity is placed on a superconducting substrate, but display a high decay rate in 3D structures.

The distinctive feature of the Lieb lattice is the flatband which lies between the upper and lower dispersive bands and the Dirac cone at point M, where all the energy bands touch to form a cone-like dispersion relation, similar to the one in graphene (see Figure 6.4a). The dispersion relation of a structure (the energy band) encompasses the fundamental electronic properties of a solid. The common case is when the energy is parabolic and displays a quadratic dependence on k. A linear dependence on k, such as the one encountered in graphene, which leads to the emergence of the so-called massless Dirac particles. This linear dispersion relation is at the root of the most defining properties of graphene, such as its semi-metallic state and high electronic mobility. Recently, graphene has become important also from the perspective of topological effects. One last type of dispersion relation is the flatband, with quenched kinetic energy that suppresses wave transport. However, flatbands that are the result of destructive interference are rare and they require a certain symmetry or fine tuning of the couplings. The flatbands are interesting for multiple reasons, for example they are prone to electronic instabilities and spontaneous symmetry breaking when they are close to half filling and they lead to highly correlated phenomena. The presence of the flatband does not only depend on the lattice symmetry, but also on the hoppings that are included in the model. In the case of the Lieb lattice, the flatband actually becomes dispersive if the next-nearest hoppings are included.

While Lieb lattices do not occur naturally, the option to design artificial materials in the lab combined with the growing interest in the theoretical formalisms that explain 2D mesoscopic structures, topological lattices have become an exciting platform of research in condensed matter. The design of atomically precise nanostructures, where the position of each atom can be accurately controlled is an ongoing pursuit in the research community. The possibility to create artificial structures opens a path for designing materials with tunable band structures and implicitly tunable electronic properties [114]. From an experimental point of view, this is

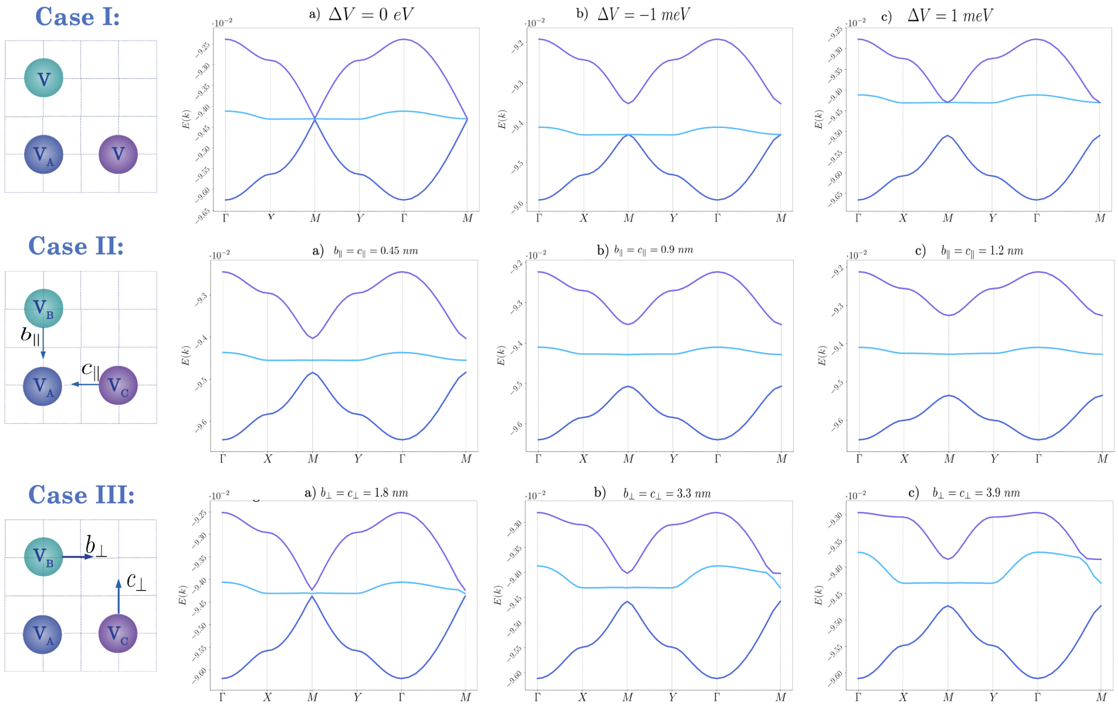

FIGURE 6.6: Bandstructures obtained numerically with a continuous model for the three configurations I, II, III.

achievable now by the use of scanning tunneling microscope (STM), atomic force microscope (AFM), lithography techniques. While some of this methods are not viable for an eventual industrial level of production, they offer the ideal opportunity to test and gain better insight into topological properties and how they could be exploited technologically. In [115], the authors have demonstrated that the characteristic features of a Lieb lattice can emerge from an experimentally synthesized phthalocyanine-based metal organic structure. In 2017, Drost *et al.* [116] presented an experimental technique to create custom band structures with the STM, by recreating the geometry of the Lieb lattice with chlorine vacancies on a Cu(100) surface.

In order to achieve novel experimental results, one also needs a good understanding of the key theoretical concepts and mainly how the symmetry of a lattice controls the band structure. To this point, the theoretical formalism that we rely on is the tight binding (TB) model [45]. However, the assumptions of the TB model are idealized and it is challenging to achieve all the conditions in a real material. In the Lieb lattice, for example, the flatland becomes dispersive when the next nearest neighbors are accounted for. The main difficulty is that we have no clear theoretical picture that could lead to an experimental discovery and the nontrivial topological properties are elusive for the experimental community [115]. Also, the tight binding parameters are not directly related to parameters that can be controlled experimentally.

6.2.2 Results

We focus here on tuning the electron band structure of Lieb-like lattices using a continuous model, which is more realistic from the perspective of the lithography technique. Each atom in the lattice now corresponds to a potential well of given (circular) shape and, by imposing periodic boundary conditions, and by tuning the potential wells accordingly, we first reproduced the band structure of an ideal Lieb lattice. For different potential configurations, we also obtain the gapped band structures with flat bands, predicted by the tight binding models. By varying the essential parameters (potential energy, radius, distance, shape and position of the quantum wells etc.) we can create classes of similar systems which may be further explored efficiently by employing machine learning techniques.

If the system is periodic and translational invariance is preserved, we can rewrite the Hamiltonian as follows:

$$\begin{gathered}\hat{H}_{\mathbf{k}} u_{\mathbf{k}}(\mathbf{r}) = \left[\frac{\hbar^2}{2m}(-i\nabla + \mathbf{k})^2 + U(\mathbf{r})\right] u_{\mathbf{k}}(\mathbf{r}) = \varepsilon_{\mathbf{k}} u_{\mathbf{k}}(\mathbf{r}) \\ \psi(\mathbf{r}) = e^{i\mathbf{k}\cdot\mathbf{r}} u(\mathbf{r}) \quad u_{\mathbf{k}}(\mathbf{r}) = u_{\mathbf{k}}(\mathbf{r} + \mathbf{R}),\end{gathered} \tag{6.4}$$

where

$$U(\mathbf{r} = V_A(\mathbf{r}) + V_B(\mathbf{r}) + V_C(\mathbf{r}). \tag{6.5}$$

Using this formulation of the Hamiltonian and imposing periodic boundary conditions, we can diagonalize it numerically and obtain the bandstructure. We used this appraoch to study the possible tuning of the bandstrutcture of Lieb-like lattices. For this particular case, we ignored the Coulomb interaction and the potential $U(\mathbf{r})$ is composed of the three circular quantum wells V_A, V_B and V_C, in order to mimic the symmetry of the Lieb lattice. We explored three cases, varying the depth of the potential wells and the distances between them, slightly altering the symmetry of Lieb lattice.

In this first case, we studied the change in the band structure when the quantum well potential $\mathrm{V_A}$ is varied, while potentials $\mathrm{V_B}$ and $\mathrm{V_C}$ remain equal. The reference potential is $\mathrm{V_B} = \mathrm{V_C} = -0.2\,\mathrm{eV}$, and we distinguished two cases: (i) $\mathrm{V_A} > \mathrm{V_B}$: there is a gap between the 2nd band (flatband) and 3rd band and (ii) $\mathrm{V_A} < \mathrm{V_B}$: the gap appears between the 1st band and 2nd band (flatband). Similar results were obtained from tight binding and atomistic models.

In the second case, we studied the change in the band structure when the quantum wells B and C are brought closer to the corner of the structure (quantum well A), while all the potentials remain equal to the reference value of -0.2 eV . The flatband (2nd band) is now found in the middle of the gap formed by the other two bands (1st and 3rd bands).

In this third case, we investigated the influence of the displacement of quantum wells B and C towards the centre, while all the potentials remain equal to the reference value of -0.2 eV . By comparison to the geometry of the Kagome Lattice, one would expect to see a flatband at the top. However, the shape of the quantum wells has to be also adjusted, in order to increase the overlap between the states localized at B and C sites. The results are presented in Figure 6.6.

We modified the shape of the quantum wells B and C, so that they have elliptical shapes which would lead to a greater overlap between the wavefunctions. In this configuration we came closer to recreating a Kagome band structure from a square geometry (see Figure 6.7 (a)).

Employing ML approaches, we also aimed to predict whether a particular quantum well configuration would exhibit a dispersionless band. The ANN-based model uses as features the potential difference between quantum wells A and B/C and the the displacements of quantum wells B and C. The output to be predicted is the bandwidth of the second band, which we define as the difference between the maximum

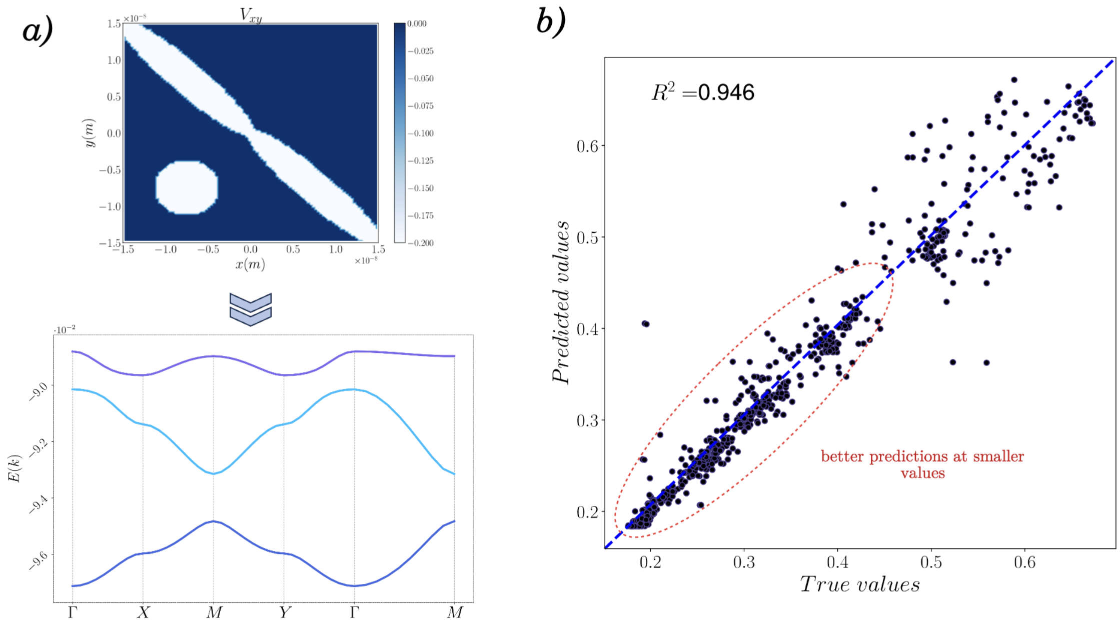

FIGURE 6.7: a) Bandstructure of the configuration displayed above, where we modified the shapes of the potential wells in order to approach a Kagome-like lattice type. b) The results obtained with ANNs for predicting the system geometries and potential well depths that favour the formation of flatbands.

and minimum point of the $E(\mathbf{k})$ curve. The artificial neural network was trained on 5250 potential configurations and we used a set of 750 systems for testing.The network has 5 hidden layers and we used the "ReLU" activation function between all of them. Also, the model was trained for 1200 epochs, with a batch size of 20. We obtained a coefficient of determination of 94.6% and the plot of predicted values versus ground truth is displayed in 6.7(b).

6.3 Quantum interconnects

» The main results presented in this section were published in [117]

6.3.1 Introduction

Neuromorphic computing refers to systems that are inspired by the biological structure of the human brain and it aims for a higher capacity of data storage and processing, while demanding lower power consumption than conventional computing hardware devices. Neuromorphic systems should, by definition, try to mimic the type of information processing in the human brain. These systems are usually comprised of electronic neural architectures that implement circuits with neurons as their building blocks and synapses as their connections. While this is, of course, strikingly similar to how we described the architecture of an ANN, this concept is distinct from ML and AI techniques because rather than being based entirely on software development, it deals with actual hardware implementations of the abstract concept at hand [118]. A precise definition of neuromorphic computing is still somewhat controversial [118]. It ranges from demanding a very accurate similarity to the principles of neuroscience to loosely biologically-inspired principles that are translated to simple linear algebra concepts, such as having an input vector multiplied by a matrix of synaptic weights.

In this section, we explored multiple configurations of neuromorphic electron waveguides, venturing into the new and exciting fields of neuromorphic computing and quantum interconnects [117]. The many-electron states in the 2D systems were rigorously described through the ED method, presented theoretically in section 3.6.

We focused on the charge localization in the dendritic-like structures and investigated the control of the electronic states by external fields, which is highly relevant from the perspective of switching the charge density between inputs and guiding the transport to the output register. In parallel, a cGAN approach was implemented in order to achieve potential-to-charge mappings. From an experimental point of view, the charge distribution can be extracted from the tunneling current measured in a perpendicular direction. The reconfigurable device we proposed enables an efficient design of quantum interconnects (QIs), aided by image-to-image translation techniques.

6.3.2 Model system and methods

The quantum interconnects are assembled on a square shaped area $2d \times 2d$, where d is half the size of the square side, similar to our approach for the 2D system of the previous section. The crucial difference comes into play when we define the confining potential, using $N_{\mathrm{wg}} = 4$ input waveguides with shapes defined by the generalized logistic function, also known as the Richards curve:

$$f(x) = A + \frac{K - A + L}{\left(C + Qe^{-B(x-M)}\right)^{1/v}}. \tag{6.6}$$

The parameters $B = 6.0/d$ (growth rate), $C = 1, K = d/2, Q = 1/2, v = 1/2$ are fixed and they set the curvature of the waveguides. Meanwhile, $A = -3d/4, -d/4, d/4,$

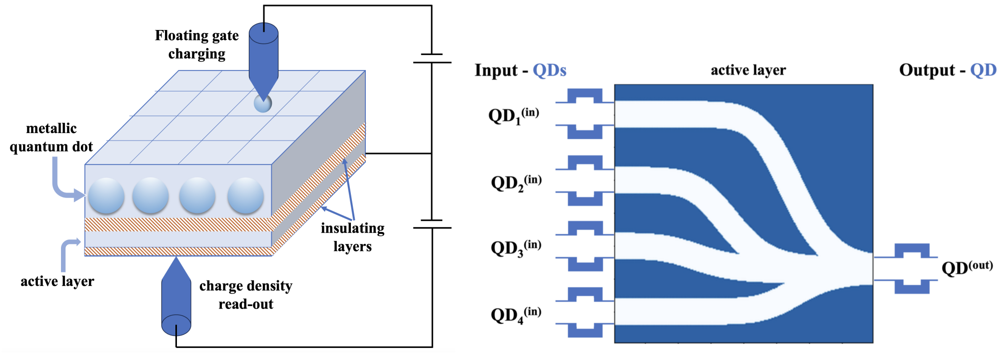

(A) (B)

FIGURE 6.8: Schematic representation of the reconfigurable 2D system. (A) A layer with floating gate array of quantum dots controls the confinement potential in the active layer, while the STM tip performs both the charging of the floating gate QDs and the read-out of the charge densities. (B) Top view of the active layer, where the quantum interconnects are represented. Quantum dot registers are connected to the input and output terminals, supplying and collecting electrons [117].

and $3d/4$ represent the y positions for each of the four waveguides. The L parameter sets the y-position of the outgoing lead, while the M parameters influence the x-positions of the branching points. A large class of QI systems can be generated in this manner by varying the L and M parameters. For a given QI, $L = r_1 \cdot d/2$, with $r_1 \in (-2.5, 0.5)$ is a random number. For each waveguide, we choose $M = (\delta + r_2/2) \cdot d$, where $r_2 \in (0, 1)$ and $\delta = 0$ for outer leads (in_1, in_4) and $\delta = -1/2$ for the inner ones (in_2, in_3). The outcome is the waveguide structure with four incoming leads merging into one outgoing lead, as one can see in Figure 6.8b.

The width of the waveguides Δ_{wg} is kept constant for all leads. In order to keep the constant width of the waveguide, they were carved out of a potential block of height V_b, using a circular shape with radius R_0 while moving along the path given by Equation 6.6, so that we obtain a uniform $\Delta_{\text{wg}} = 2R_0$. The theoretical design proposed here makes use of existing technologies like floating gate arrays and STM.

Experimentally, the manipulation of the many electron states in the proposed device can be realized by varying the confining potential in order to increase charge localization in the desired output terminals. To describe the many-body quantum system theoretically, we employ the exact diagonalization method that we discussed in detail in Section 3.6.

6.3.3 Convoluting Charge Density Maps

The read out process of the charge density profile could be achieved by measuring the tunneling current detected with the aid of scanning tunneling microscopy. STM imaging is based on tunneling phenomena between the metallic tip of the instrument and the sample, leading to a tunneling electrical current. The current depends on the local density of states and, similarly to this case, we assume that the tunneling current map corresponding to the quantum interconnects directly depends on the charge density distribution of the many-particle ground state. The workflow of our approach is described schematically in Figure 6.9. Our assumption is that the tunneling current map (TCM) can be simulated by a convoluted image of the charge

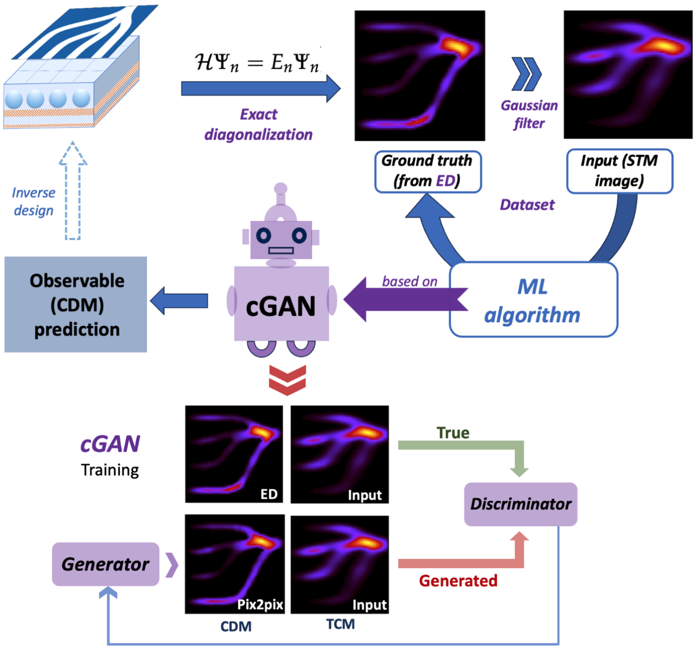

FIGURE 6.9: Workflow displaying the steps of this computational study of QIs. The exact diagonalization method gives the charge density maps of the 2D system and the TCMs are obtained by applying a Gaussian filter to the images. Using a ML algorithm based on cGANs, the TCMs are deconvoluted back into CDMs.

density map (CDM) that was exactly determined through accurate numerical methods. In short, we create a blurred version of the ground state density and consider this to be the input for a ML model that aims to deconvolute experimentally obtained charge density profiles.

The simplest filter that we could employ is a two dimensional Gaussian filter, defined as:

$$G(x,y) = \frac{1}{2\pi\sigma_x\sigma_y} \exp\left[-\left(\frac{x^2}{2\sigma_x^2} + \frac{y^2}{2\sigma_y^2}\right)\right]. \tag{6.7}$$

where σ_x and σ_y are the standard deviations along the x and y directions. In order to try to mimic a more experimentally realistic situation, we will look more closely into the cases where $\sigma_x \neq \sigma_y$ and also account for the influence of random noise (denoted by σ_n). The Python code used to blur the images is presented the Appendix H and one can check Figure 6.12 for reference.

6.3.4 Results and discussions

Predicting Charge Localization and deconvoluting Tunneling Current Maps

We studied closely two categories of QIs, depending on the width of the input and output leads ($R_0 = 10$ nm for the narrow leads and $R_0 = 20$ nm for the wide leads), as can be seen in Figure 6.11. Let us begin with the simplest case, that corresponding to one single electron being injected into the quantum interconnects. From the first row of Figure 6.11, one notices that the charge is localized into one area, in the region where the incoming and outgoing leads meet. There is no electrostatic interaction in this case, which means the system tends to simply minimize the kinetic energy and

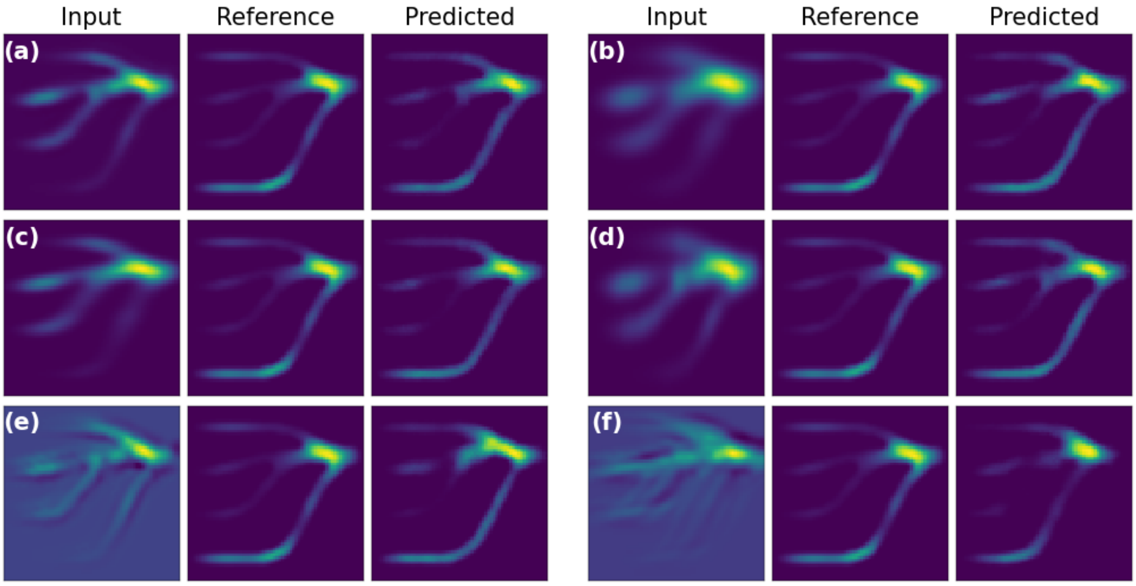

FIGURE 6.10: Deconvoluting tunneling current maps (TCMs) and comparison with the reference CDMs (charge density maps): (a) $\sigma_x = \sigma_y = 1, \sigma_n = 0.01$; (b) $\sigma_x = \sigma_y = 3, \sigma_n = 0$; (c) $\sigma_x = 3, \sigma_y = 1, \sigma_n = 0$; (d) $\sigma_x = 1$, $\sigma_y = 3, \sigma_n = 0$; $(e)\sigma_x = \sigma_y = 1, \sigma_n = 0.1$; $(f)\sigma_x = 3, \sigma_y = 1, \sigma_n = 0.1$

there is no interplay between the kinetic and potential terms of the Hamiltonian. Also, the single particle case is easily scalable to simplified many-particle configurations with null Coulomb interactions.

As more electrons are being taken into account (in this study we went up to four particles), the Coulomb repulsion drives the charge density to regions with stronger confinement. Notice from the following three rows in Figure 6.11 that the charge density distribution shifts towards the leads as there are multiple peaks in the profile. There is now a trade-off between the kinetic energy, which increases in more confined areas, and the electrostatic interaction, which in turn decreases when there is a larger separation between the charged particles. This exchange between the defining terms in the Hamiltonian is evident when comparing the case of the narrow leads to the case of the wider ones. As the number of electrons is increased, we expect to see a smoother distribution since we are approaching a mean field description of the quantum system.

Since the ED simulations are demanding from a computational perspective and the number of possible neuromorphic configurations increases abruptly with the parameters that determine the confining potential, we explored an efficient and accurate ML approach based on cGANs. This machine learning algorithm which predicts the charge density maps for different potential maps almost instantly once it was trained. The image-to-image translation is implemented using the pix2pix method developed by Isola *et al.* [105], the same ML technique we employed in [54].

The cGAN architecture is basically defined by the generator and discriminator networks, as we described more thoroughly in Section 4.5.1. The input size of the image is 64 × 64 × 1 (one color channel), which goes into the U-Net of the generator. The encoder of the U-Net has 6 layers, using the LeakyReLU activation function, and the decoder has the same parameters, with the caveat that the activation functions are ReLU (for the first 5 layers) and tanh (for the last layer). The discriminator is a PatchGAN classifier with 5 layers, input size of 64 × 64 × 2 (because it is dealing

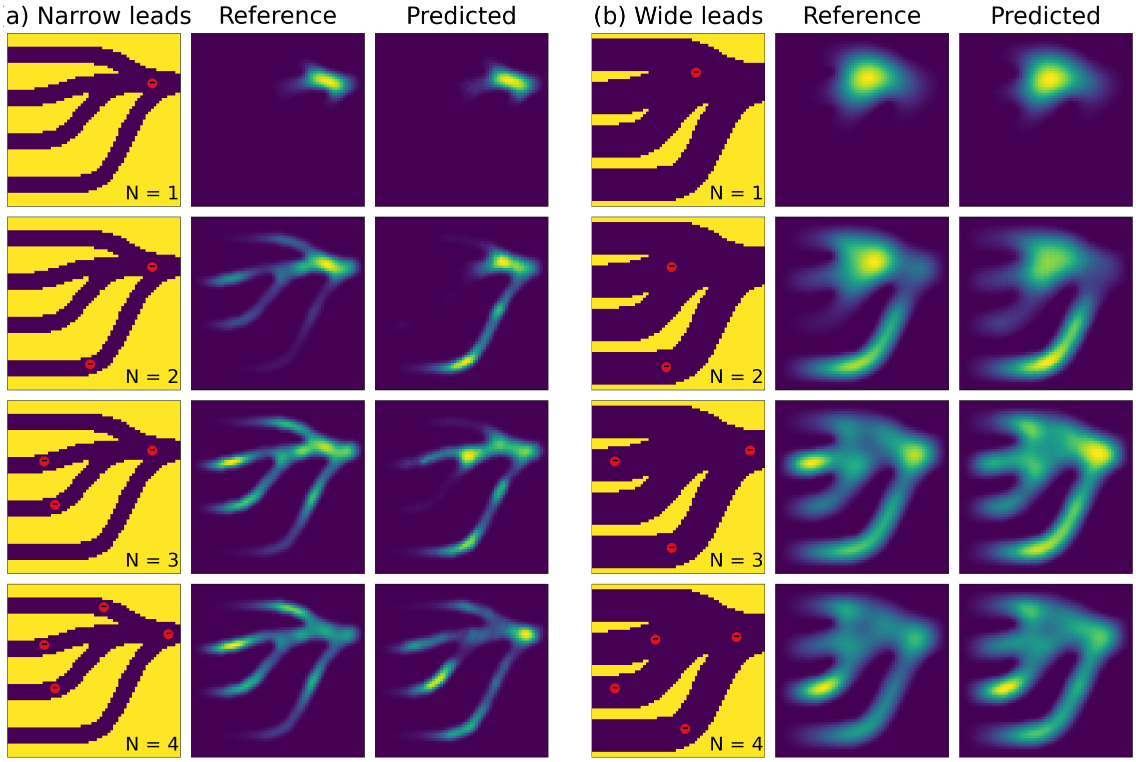

FIGURE 6.11: The reference (ground truth) and predicted charge density maps for $N = 1, 2, 3, 4$ confined electrons, in systems with (a) narrow leads, $R_0 = 10$ nm and (b) wide leads, $R_0 = 20$ nm. The effect of the Coulomb interaction is evidenced in the extension of the charge distribution, as discussed in the current section.

in image pairs), zero-padding and a stride sequence of $(2, 2, 2, 1, 1)$. The ADAM optimizer was employed, as per usual, with a learning rate of 10^{-4} and momentum parameters $\beta_1 = 0.5$ and $\beta_2 = 0.999$.

In figure 6.11, the predicted charge densities are shown alongside the ground truth images. The simplest case is the non-interacting one, where the highly localized charge density is easily reproduced by the ML model. The algorithm exhibits higher errors as we slightly increase the number of particles in the system. The pix2pix code has to predict peaks that appear randomly distributed to a model that has no a priori knowledge about the physical intricacies of the quantum device. As the number of particles increases even further and the charge density extends all throughout the two dimensional system, the cGAN finds it again easier to make accurate predictions. More details on the metrics that we employed to measure the accuracy of the model are given in the articles we published on this topic [54, 117].

Also, we investigated how efficient the cGANs are at deconvoluting the TCMs. The simplest case is represented by a two-dimensional Gaussian filter with equal standard deviations $\sigma_x = \sigma_y = \sigma$. As you can see in Figure 6.12, for a small value of $\sigma = 1$, there is a barely noticeable change in the TCM compared to the reference. Even by increasing the standard deviation $\sigma = 3$, the image translation method provides a similar accuracy, as the kernel of the Gaussian filter remains symmetric. Even asymmetric kernels, with a larger standard deviation on either the x-direction $(\sigma_x = 3, \sigma_y = 1\ )$ or on the y-direction $(\sigma_x = 1, \sigma_y = 3)$, do not lead to significant and noticeable errors in the prediction accuracy. We can conclude that the standard Gaussian kernel is easily recognizable by the cGAN. However, the noise has a

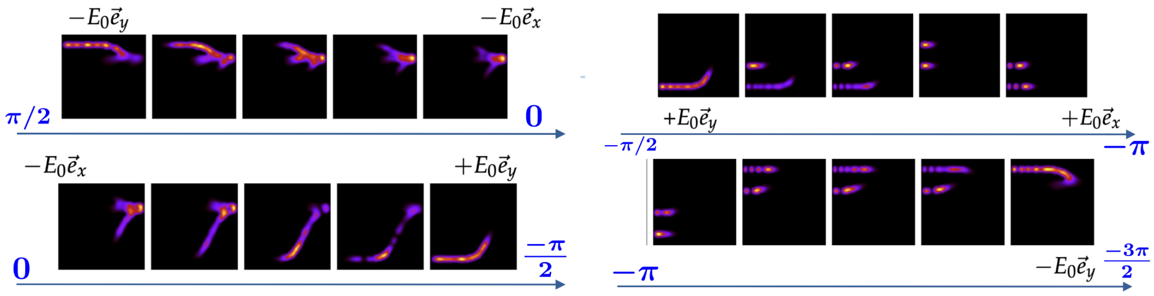

FIGURE 6.12: Switching of the charge density localization induced by a rotating in plane electric field, where $E_x = -E_0 \cos(\theta)$, $E_y = -E_0 \sin(\theta)$ and $E_0 > 0$.

more significant impact. A symmetric kernel $\left(\sigma_x = \sigma_y = 1\right)$, which, in addition, has a noise component with $\sigma_n = 0.1$, transforms the CDM into a rather different map. In this case, although, overall, the predicted image well resembles the reference, the prediction accuracy is visibly lower.

Manipulation of many-body states by in-plane electric fields

Next we modified the confining potential by adding in-plane electric fields in the range of $[-50, 50]$ meV in both directions $\vec{e_{x,y}}$, such that:

$$V_{\text{conf}}(x, y; E) = V_{\text{conf},0}(x, y) + \Delta V(x, y; E), \tag{6.8}$$

where $V_{\text{conf},0}(x, y)$ is the potential profile in the case if zero electric field. The purpose is to investigate the possibility to manipulate the localization of the charge density without using any magnetic fields, only by slightly modifying the confining potentials. We looked at the single particle case and also the interacting bi-particle case in this analysis.

When the field is oriented along the $\vec{e_x}$ direction, the charge is gradually driven towards the input terminals, as one can see in Figures 6.13 and 6.12. When the in-plane field is oriented along the $\vec{e_y}$ direction, the switching occurs between the outer terminals along the vertical direction. At maximum values of the electric field, the outer input terminals are the most populated. We have noticed that the output terminal is typically depleted if it is placed in the middle of the active region. Since in Figure 6.13 (b), the output terminal is placed in the upper half, it retains a considerable amount of charge.

6.3.5 Conclusions

We proposed a reconfigurable two-dimensional device and a cGAN-based methodology in order to efficiently design neuromorphic systems, that can successfully transfer charge and spin between quantum dot registers. The system we studied can also perform the functions of active switching elements. Moreover, the approach we presented is highly versatile and can be employed for the inverse design of quantum multi-terminal devices.

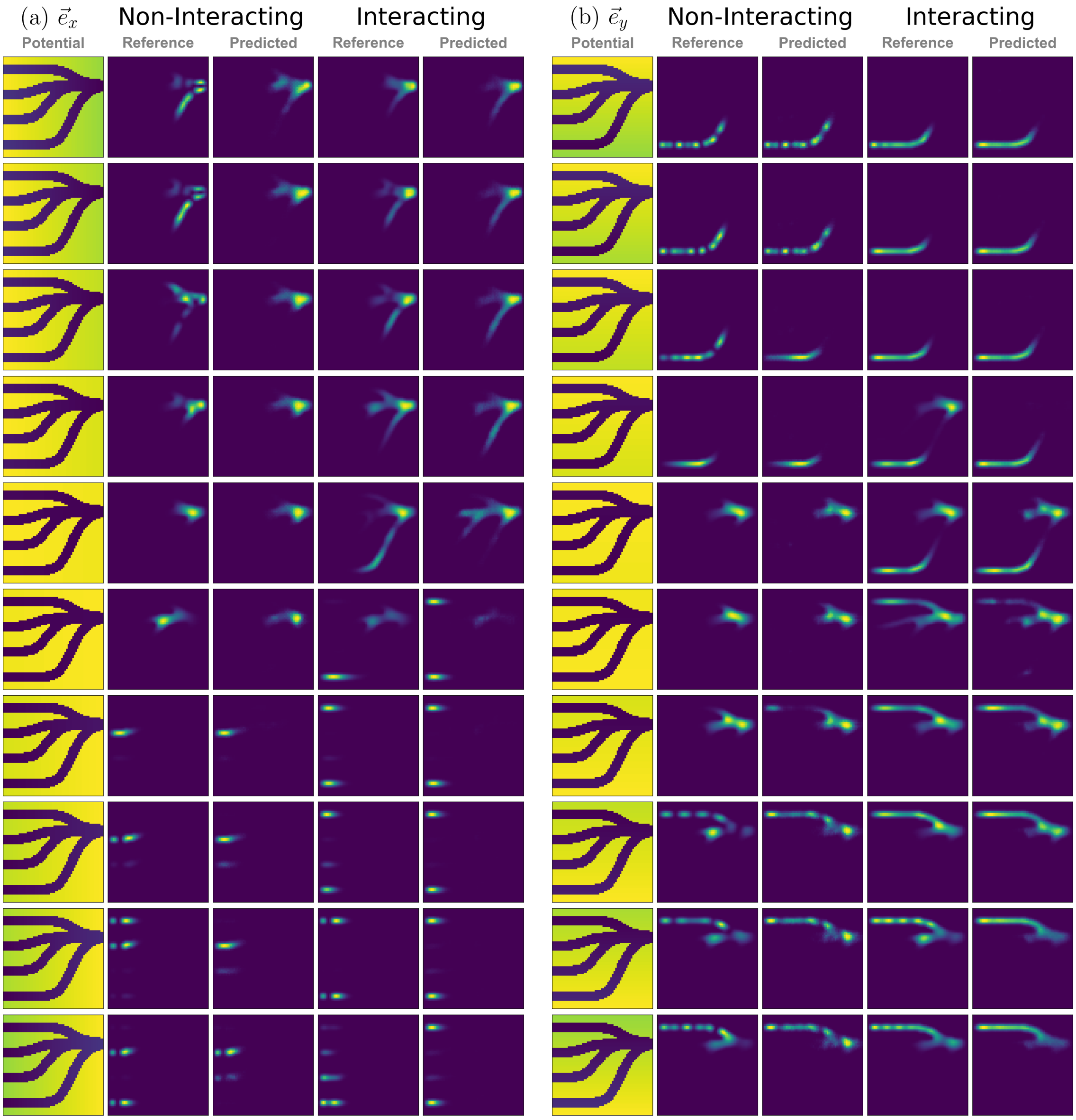

FIGURE 6.13: Switching of the charge density localization induced by in-plane electric fields oriented along: (a) $\vec{e}_x$ and (b) $\vec{e}_y$. For each case, we depicted the confinement potential in the first column, followed by the charge densities for the non-interacting single particle $(N = 1)$ and interacting $(N = 2)$ bi-particle cases. The second and fourth columns correspond to the ground truth (reference) particle density, while the third and fifth columns represent the predictions made with pix2pix. The green shade in the potential map denotes a lower potential energy and the yellow one depicts the transition to larger values of the potential energy.

6.4 Double channel nanotransistor

▶ >> The main results presented in this section were published in [119]

6.4.1 Introduction

Moore's law has been the governing principle of the semiconductor industry since the 1960s [120], stating that the number of transistors that can be fit into a microprocessor doubles approximately every two years. However, this principle is already beginning to falter, as semiconductor processing technology passed the sub-10 nm mark [121, 122]. Therefore, the development of nano-transistors which overcome the short channel effects that emerge along with their reduced sized is critical in the current technological landscape [123, 124].

Along with the down-scaling of electronics devices, ballistic transport has become the dominant transport mechanism in nanoscale transistors, since the conventional drift-diffusion models are no longer suitable for describing the carriers in the mesoscopic channels. Also, low dimensional materials and alternative designs for the field effect transistors have become an essential field of research in the las decade. This chapter is solely focused on a double channel nanotransistor that could overcome some of the challenges of downscaling and open up the way to low operating voltages that are highlysuitable for low energy applications [119].

6.4.2 Nanotransistors in the Landauer-Büttiker formalism

As we have already pointed out, the prominent progress of the semiconductor industry in the last couple of decades has warranted extensive interest in both the experimental and theoretical aspects of quantum transport. Once the channel lengths of the transistors decreased below 20-40 nm, short channel effects become significant and below 10 nm quantum transport becomes the dominant transport regime. Short channel effects arise due to a decrease in electrostatic control of the device through the gate potential and manifest themselves as a lowering of the threshold voltage when the gate length is reduced or the drain potential is increased [125, 126].

From this perspective, a description of nanotransistors in the framework of the Landauer-Büttiker (LB) formalism is a suitable approach for the transport problem. Several papers were published on this subject, working with a compact transistor model based on the fundamentals of the LB theory and, also, the R-matrix and NEGF formalisms adapted to a multi-terminal quantum system [126, 127, 128, 129].

We briefly describe here the R-matrix based approach for a two-terminal device as the one represented in figure 6.14, that encapsulates the structural elements of a traditional MOSFET. The source and drain are modeled as conventional leads of a multi-terminal system (Ω_s), with the potential energy in the region taking de form:

$$V\left(\vec{r} \in \Omega_s\right) = V_s\left(\vec{r}_{\perp;s}\right) - eU_{s/d}, \tag{6.9}$$

where $U_{s/d}$ is the source/drain potential. The scattering solutions originating from contact s can be written as:

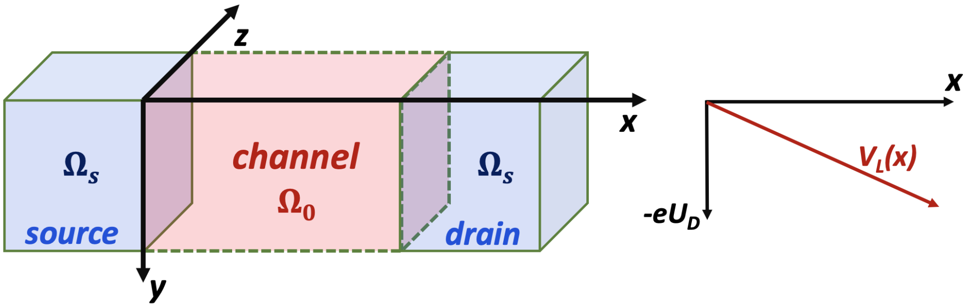

FIGURE 6.14: (a) Simple scheme of a nanotransistor modeled from the point of view of quantum transport, where the channel region acts as the central scattering region and the source and drain contacts are represented as right and left leads. (b) Variation of the longitudinal potential (V_L) in the scattering region, with respect to the channel length, according to equations 6.17, where U_D is the drain potential.

$$\Psi^{sn}\left(\vec{r} \in \Omega_{s'}, E\right) = \exp\left(-ik_{sn}z_s\right)\Phi_{sn}\left(\vec{r}_{\perp;s}\right)\delta_{s,s'} + \sum_{n'} S_{s'n',sn}(E)\exp\left(ik_{s'n'}z_{s'}\right)\Phi_{s'n'}\left(\vec{r}_{\perp;s'}\right), \tag{6.10}$$

where s, s' are the lead indices, n, n' account for the transverse modes in the lead and $S_{s'n',sn}$ is the S matrix. The transverse modes are solutions of the following eigenvalue problem:

$$\left[-\frac{\hbar^2}{2m^*}\Delta_{\vec{r}_{\perp;s}} + V_s\left(\vec{r}_{\perp;s}\right) - eU_d - E_\nu^\perp\right]\Phi_\nu\left(\vec{r}_{\perp;s}\right) = 0, \tag{6.11}$$

where we defined $\nu = (s, n)$ as a composite index, for simplicity of the notation. The total electrical current in terminal s is:

$$I_s = \frac{2e}{h}\sum_{s'}\int_{-\infty}^{\infty} dE\left[f\left(E - \mu_s\right) - f\left(E - \mu_{s'}\right)\right) T_{s's}(E) \tag{6.12}$$

The total transmission between the terminals s and s' can be written as as a sum:

$$T_{ss'}(E) = \sum_i T_{ss'}^{\mathbf{2D}}\left(E - E_i\right) \tag{6.13}$$

where $T^{\mathbf{2D}}$ is the transmission for an ideal 2D transport problem and

$$E_i = i^2\left(\frac{\hbar^2}{2m^*}\right)\left(\frac{\pi}{L_z}\right)^2 \tag{6.14}$$

are the energy levels for the transverse modes in the leads, modeled as the solutions for a simple particle in a box problem, with L_z being the width of the transistor. If one works in the single mode approximation where strong transverse quantization is assumed, then only the lowest transverse energy level is taken into account.

This model does not take into account tunneling currents to the gate and also assumes a separable form for the potential in the scattering area:

$$V\left(\vec{r} \in \Omega_0\right) = V_L(x) + V_T(y), \tag{6.15}$$

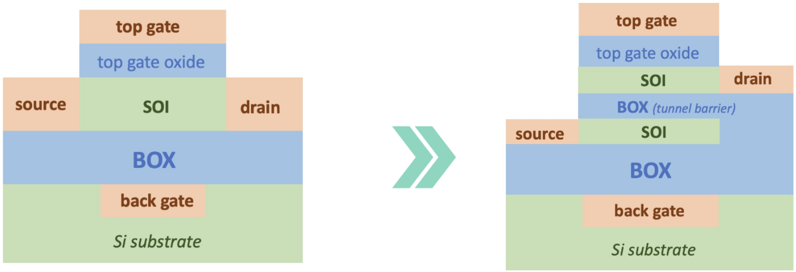

FIGURE 6.15: In a double-channel nanotransistor, an extra buried oxide substrate is added to the standard SOI wafer.

where V_T is the confinement potential in the channel that would be present in a MOS structure without any source/drain contacts attached. This potential was thoroughly discussed in [130, 131]. The longitudinal potential arises from the applied source-drain voltages. Assuming that $V_S = 0$, $V_G = 0$ and that the voltage drop across the channel varies linearly, one can consider the following equation for V_L:

$$V_L(x) = -\frac{x}{L} eU_D \tag{6.16}$$

The effective scattering potential in the device can be summarized as follows [124]:

$$\bar{V}^{ef}(x) = \begin{cases} 0 & \text{for } x < 0 \\ -eU_D x/L & \text{for } 0 \leq x \leq L \\ -eU_D & \text{for } x > L \end{cases} \tag{6.17}$$

All these assumptions make the quantum system easier to solve analytically, but, as we will discuss in the next section, we will shift to a more detailed numerical description in order to obtain better results for the two channel nano-FET.

6.4.3 Double-channel nanoFET

The device we study is a Si/SiO_2-based field effect nanotransistor, which exploits of the tunneling between two parallel conduction channels and allows for the switching of the drain current with small gate voltages, thus opening the way to low-energy applications. We call this proposed device a two-channel tunneling field effect transistor (2CTFET). This 2CTFET can be realized on a double silicon-on-insulator (SOI) substrate which is shown schematically in Figure 6.16. In [119], we explain how the 2CTFET can be derived from an SOI transistor. In a standard Silicon-On-Insulator (SOI) transistor, the fundamental structural components include the silicon (Si) substrate, the buried oxide (BOX) layer, and the silicon film. Subsequently, the source, drain, back gate, top gate oxide, and top gate are incorporated. In a double SOI substrate nanotransistor, an additional buried oxide layer is introduced into the standard SOI wafer (see Figure 6.15). As a result, the silicon film is divided into two distinct layers, which can be as thin as 2 nm. These layers function as two quantum wells, coupled by the thin buried oxide layer, which serves as a tunneling barrier. The quantum well in the lower SOI layer is selectively connected to the source, while the quantum well in the upper SOI layer is selectively connected to the drain. In this proposed model for the 2CTFET, the drain current only occurs

Quantity	Notation	Value
Well thickness	D_W	3 nm
Effective mass	m^*	$0.32 \times m_0$
Channel length	L	30 nm
Height of tunneling barrier	V_B	$[1,2]eV$
Top gate potential	V_G	$[-0.2,0]eV$
Drain voltage	U_D	$[0,0.2]$ V
Device temperature	T	10 K
Tunneling barrier thickness	D_B	$[1,3]$ nm
Gate insulator thickness	D_G	8 nm

TABLE 6.1: Relevant quantities and notations for the nanoFET

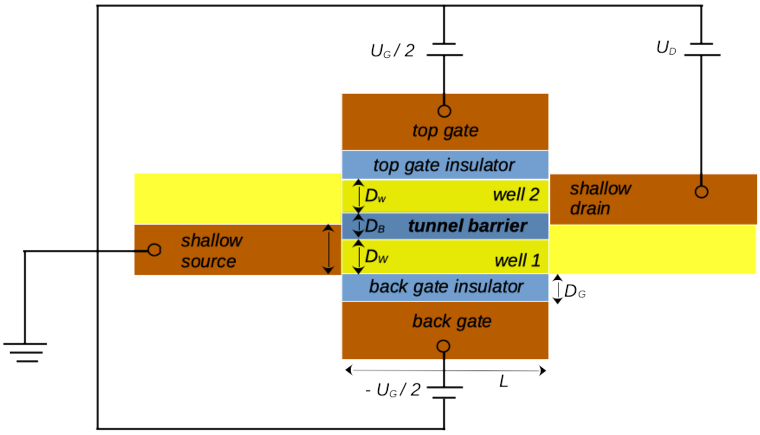

FIGURE 6.16: 2D scheme of the two-channel nanotransistor proposed in [119].

under lateral resonant tunneling conditions, which leads to the resonant tunneling peak in the transfer characteristics, as we shall see in the following.

In our simulations, we are mainly interested in the transmission function and, by means of the Landauer-Büttiker formalism, the drain current. We analyze the results for one configuration, where the lateral dimension of the source/drain contacts is $D_C = 3$ nm, the height of the central tunneling barrier is varied between 1 and 2 eV, the thickness of the barrier is set at $D_B = 2$ nm and the channel length is considered $L = 30$ nm. Also, we consider in our simulations an isotropic effective mass of $m^* = 0.32m_0$. The configuration of the double channel nanotransistor is represented in Figure 6.16 and the relevant quantities are introduced in Table 6.1.

Potential map from the Poisson equation

Along with the reduction in size of the MOSFETs and the implicit quantum effects that arise, one needs to take into account the effect of quantum confinement on the carrier charge distribution. Since quantum confinement directly impacts the distribution of free charge carriers, then the electrostatic potential is also modified, which in turn affects the density profile of the charge carriers. This self-consistent cycle is implemented through a variety of methods, each one searching for an ideal balance between computational cost, system dimensionality, numerical accuracy and convergence of the calculations. For example, the NEGF formalism coupled with the Poisson equation in a self consistent cycle is widely used to analyze quantum

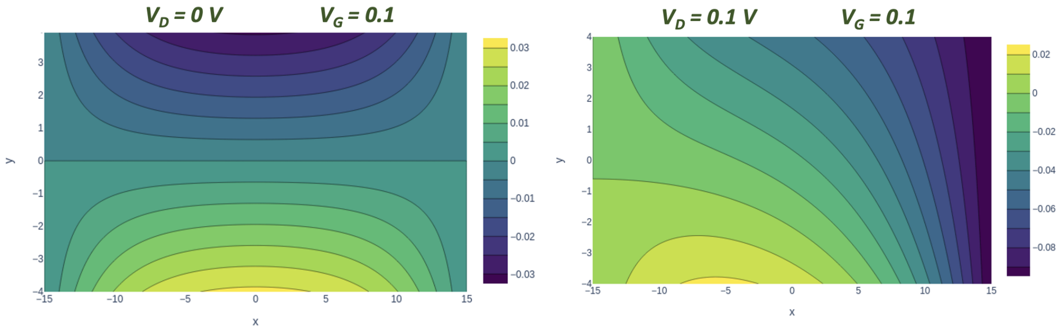

FIGURE 6.17: Potential maps from the Poisson equation

transport in semiconductor nanodevices. The core of the self-consistent calculations lies in the fact that the electrostatic potential modifies the values of the diagonal entries of the Hamiltonian matrix, while the source terms of the Poisson equation are given by the results of the NEGF simulations [132]. Continuum models based on the $k \cdot p$ theory have also been proposed, aiming to reduce the computational load while maintaining accurate results [133]. The coupled Schrodinger-Poisson equations were also solved for the case of a cylindrical nanotransistor with the R-matrix formalism in [134]. The R-matrix method possesses numerical advantages when dealing with large energy sets, as we discussed previously, but it is not suited yet for simulations at higher temperatures. Besides discussions about numerical implementations and appropriate theoretical quantum transport models, solving the Schrodinger-Poisson equation also requires increased attention to the boundary conditions. Dirichlet boundary conditions correspond a fixed applied potential, while von Neumann conditions impose that the electric field orthogonal to the boundary is zero. Usually, the gate electrode is described by Dirichlet boundary conditions. However, the nature of ballistic transport and the open boundary conditions of the NEGF formalism impose Neumann type boundary conditions for the source and drain contacts, in order to maintain charge neutrality, as it is discussed in [132, 135, 136].

$$\begin{aligned} -\nabla \cdot (\epsilon \nabla \phi) &= q(-n + p + N), \quad \text{in } \Omega_0, \\ \phi &= \phi_{\text{electrode}}\,, \qquad\qquad \text{on } \Gamma_{\text{D/S}}, \\ \frac{\partial \phi}{\partial \vec{m}} &= 0, \quad \text{on } \Gamma_{\text{G}}. \end{aligned} \tag{6.18}$$

Applying drain and gate (V_d, V_g) potentials modifies the scattering potential in a more complicated manner than the simple linear model assumed in the theoretical model.

For our simulations, we considered a simplified version of the system and solved the Poisson equation for the scattering region of the nanotransistor with null source term. The Dirichlet type boundary conditions were defined on a rectangular shaped region, defined by the intersection of the scattering region with the drain/source electrodes (to the left and right of the system) and with the top and bottom gates. We have analyzed the system in two different configurations, one in which the top and bottom gates have applied voltages of $\pm V_g/2$ and the second one where the potential on the bottom gate was always null and the top gate controlled the transport. Without the barrier that separates the two conduction channels, some of the potentials maps are represented in Figure 6.17, for the symmetric configuration. For an efficient calculation of the solutions of the differential equation, we employed the

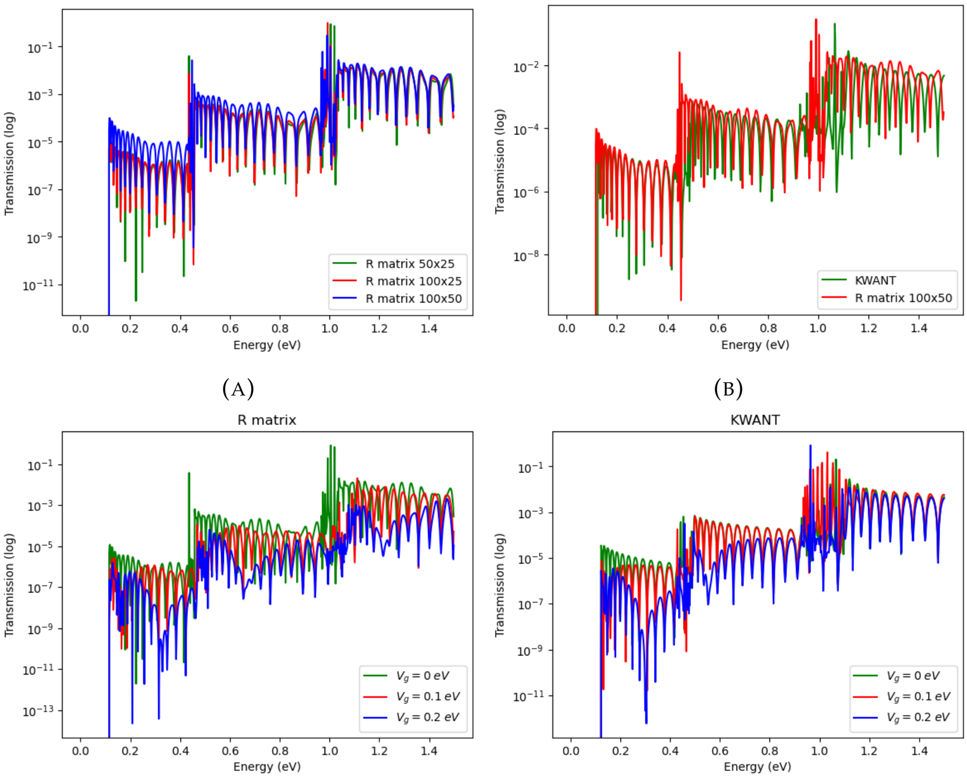

(A) (B) (C) (D)

FIGURE 6.18: Transmission function (source-to-drain) with no applied voltages, $(V_d, V_g) = (0, 0)$; comparative analysis between R-matrix and KWANT. Transmission funcrion at $V_d = 0$ eV si $V_g = 0, 0.1, 0.2$ eV; comparative analysis between R-matrix and KWANT

Python package *scipy*, which includes effective routines for solving linear systems with the aid of sparse matrices. To this potential profile, we add the energy offset from the constant barrier in centered in the middle of the scattering region.

$$\begin{aligned} -\nabla \cdot (\epsilon \nabla \phi) &= 0, \quad \text{in } \Omega_0, \\ \phi &= \phi_{\text{electrode}}, \quad \text{on } \Gamma_{D/S/G}, \end{aligned} \tag{6.19}$$

Numerical simulations

The first step in our analysis is to compute the I-V characteristics of the 2CTFET. We are interested in the low voltage properties, so we will only examine drain and gate voltages between $[0, 0.2]$ V. The R-matrix code outputs the transmission through the device, and using the subroutine in Appendix I, we computed the current employing the Landauer-Büttiker (see equations 6.12, 6.13 and 6.14). While the structure of the output characteristic is similar to that of a MOSFET, we notice that the drain current in the case of the 2CTFET actually decreases with an increasing gate voltage.

In order to run multiple simulations as time efficiently as possible, we use the MPI library to approach multiple $I_d(V_d, V_g)$ pairs at once. We compute transmission functions and currents for 2000 voltage configurations and recreate the output characteristic of the 2CTFET in Figures 6.20. The figures mentioned before correspond to two possible configurations of the device: in the first we apply a top gate potential

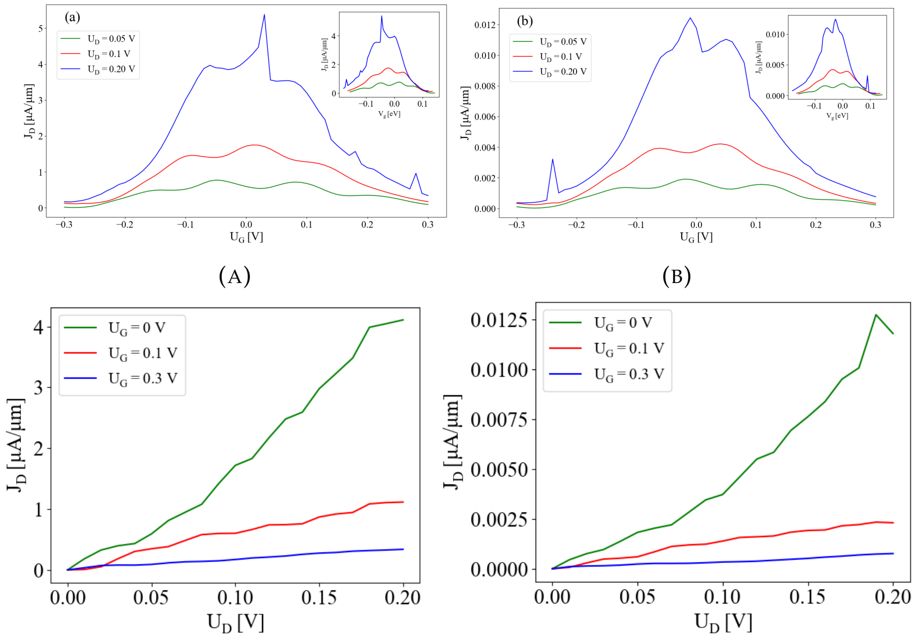

(A) (B)

(C) (D)

FIGURE 6.19: (A), (B) Drain current vs. gate voltage for several drain voltages, $U_D = 0.05, 0.1, 0.2$ V, calculated using the tight-binding model, for (A) $V_b = 1$eV and (B) $V_b = 2$eV. Notice the decrease of J_D with U_G. The insets show the same data plotted against the potential energy, V_g, found at $x = L/2$ (the edge of the upper channel, $y = 0$).(B), (C) Drain current vs. drain voltage for several gate voltages, $U_G = 0, 0.1, 0.3$ V, for (C) $V_b = 1$eV and (D) $V_b = 2$eV. Notice the almost linear increase is at low U_D voltages.

of $V_g/2$ and a bottom gate potential of $-V_g/2$, while in the second we only apply a potential on the top gate.

While the accuracy of the R-matrix based numerical model depends on the number of components of the Fourier basis, The KWANT package becomes comparable to a continuous model once the lattice constant is decreased enough. For the two channel nanotransistor, we studied the efficiency of both models for a wide set of different configurations and the results are highly similar.

Discussion and Results

In Figure 6.19(A,B) we represent the drain current as a function of the gate voltage for three values of the drain bias and for two values of the barrier between the two channels ($V_b = 1$ eV and for $V_b = 2$ eV). Note that at $U_G = 0$ the characteristic displays a peak even for small drain voltages. Our assumption is that at zero gate voltage the two quantum wells in the device are symmetric and the wavefunctions are localized in both of the channels. This leads to a significant drain current. When the relative asymmetry between the two quantum wells increases (by increasing the gate voltage, for example), the lateral tunneling current between the source and drain is highly diminished and the transistor switches from the ON to the OFF state. By varying the drain voltage, there is an almost linear increase in the drain current for the same two barrier sizes (see Figures 6.19C,D). Again, it is evident that increasing the gate voltage leads to a steep decrease in the drain current, reflecting the ON-OFF transition of the nanotransistor. The same is evident from Figures 6.20,

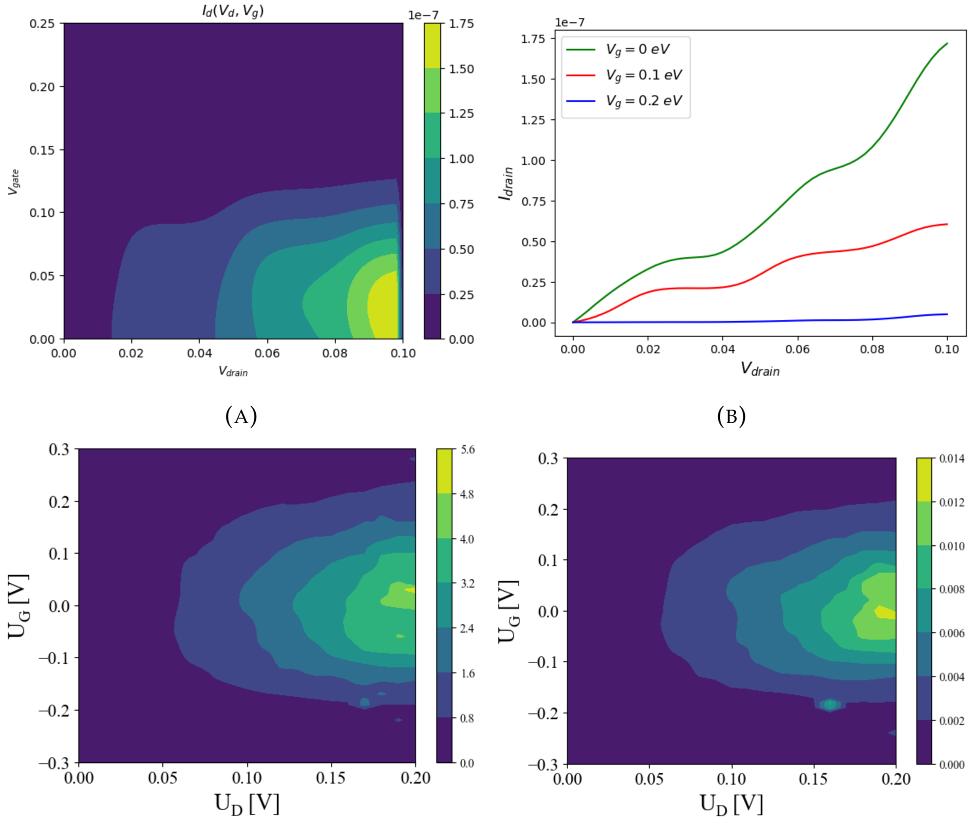

(A) (B)

(C) (D)

FIGURE 6.20: (A) The drain current I_d as a function of the drain voltage V_d and top gate voltage, in a configuration where the top-gate voltage is $(V_g/2)$, the bottom-gate voltage is 0 and $V_b = 2\text{eV}$. (B) The drain current as a function of the drain voltage for the same configuration described in subfigure (A). (C), (D) Heat maps of the drain current vs. (U_D, U_G) voltages, for (C) $V_b = 1\text{eV}$ and (D) $V_b = 2\text{eV}$. Notice that a peak in J_D emerges for large U_D voltage and low values of U_G. The ON state of the 2CTFET can be switched to an OFF state by increasing $|U_G|$.

where the contour-plots confirm the narrow maxima in the drain current around the set of values $(U_G, U_D) = (0, 0.2)\ V$. Note that in the numerical simulations the solution of the Poisson equation included the top and bottom buffer oxide layers, which decrease the potential drop on the active region. For a proper comparison with the analytical model presented in reference [119] , we plotted in the insets of Figure 6.19 the drain currents against the potentials found at the upper edge of the drain channel ($x = L/2, y = 0$).

The transmission functions in Figures 6.18 present a series of sharp peaks and are all represented in logarithmic scale due to their small values. In order to gain a better understanding of this, we represented the absolute values of the wavefunctions in the nanotransistor in Figure 6.21, for a set of energies that correspond to minima and maxima in the transmission functions. For each transverse mode, we noticed that there is a matching condition between the maxima and minima of the quasi-stationary waves in the two channels occurs for certain values of the total energy. If this matching condition is met, the probability of lateral tunneling between the two quantum wells increases and narrow peaks in the transmissions emerge. We called

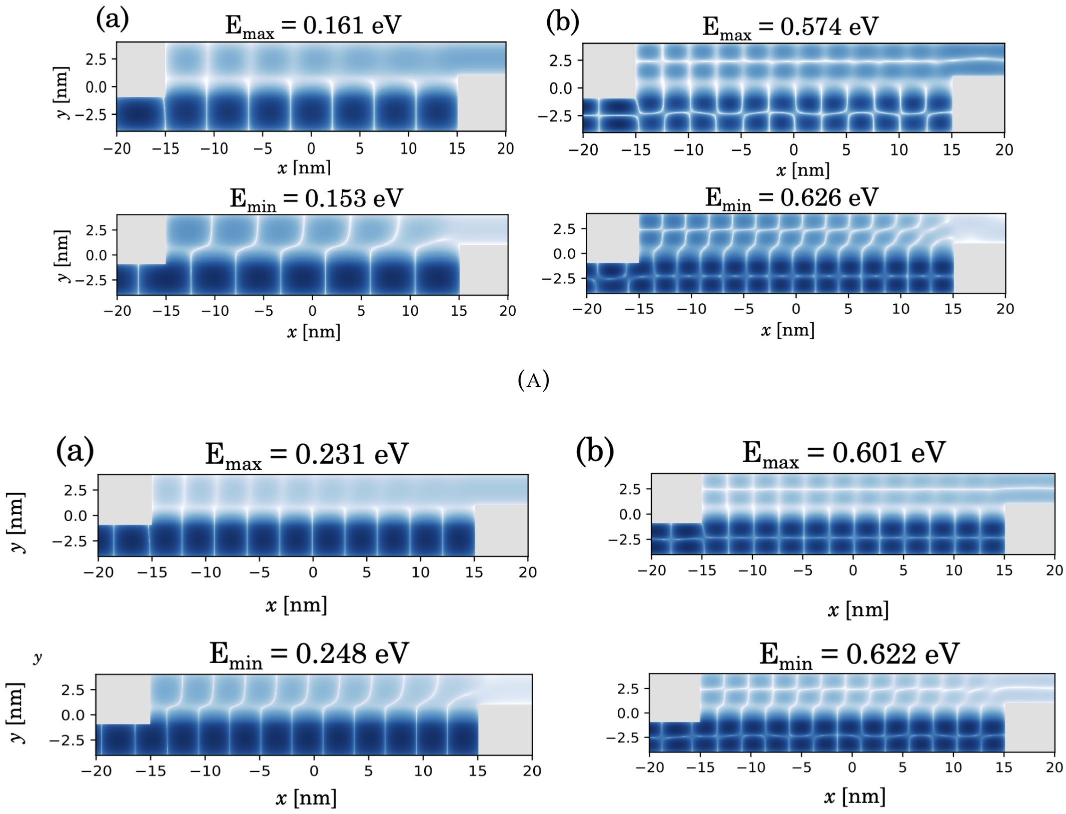

(A)

(B)

FIGURE 6.21: (A), (B) In-phase and out-of-phase matching of quasi-stationary wave functions (absolute value) in the two channels, obtained for $V_b = 1\text{eV}$. (C), (D) In-phase and out-of-phase matching of quasi-stationary wave functions (absolute value) in the two channels, obtained for $V_b = 2\text{eV}$: (C) energies $E = 0.231\text{eV}$ and 0.248 eV ; (D) energies $E = 0.601\text{eV}$ and $E = 0.622\text{eV}$. These correspond to peaks and dips in the transmission function.

this the in-phase wave function-matching condition and it is exemplified in Figure 6.21 for two values of the barriers between the transport channels.

In [119], a more detailed discussion is presented about the features of the 2CTFET which are favorable for technological applications. One important characteristic is that the lateral resonant tunneling effect which stands at the core of the 2CTFET does not depend strongly on temperature. Since thermal effects play a minor role, the tunneling peaks that define the transfer characteristic persist even at room temperature. In future studies, we will also explore a double-barrier nanotransistor, where we observe conventional resonant tunneling effects, with peaks in the transmission functions that come close to unity.

6.4.4 Machine learning techniques

Solving scattering problems for complex systems is computationally demanding and requires resources and time. While one cannot bypass the high throughput computing completely, integrating machine learning algorithms into the research process can accelerate the calculations and push for the discovery of novel devices. To this end, we have explored possible machine learning applications built upon the data we have obtained with the Kwant and R matrix simulations.

Artificial Neural Networks

We have tested the efficiency of ANNs in predicting the drain current from the values of the gate and drain potentials. After the simulations performed with parallel the R-matrix code we had at our disposal a set of 2600 data tuples for (V_d, V_g, I_d), that we have divided into 2080 training data (80% of the total dataset) and 520 test

Layer	Nr. of neurons	Activation function
Input	2	-
Hidden layer	10	ReLU
Hidden layer	30	ReLU
Hidden layer	50	ReLU
Hidden layer	100	ReLU
Output	1	-

ANN Parameters	
N_{train}	2080
N_{test}	520
Epochs	1200
Batch size	16
Optimizer	ADAM
Loss	R^2

(A)

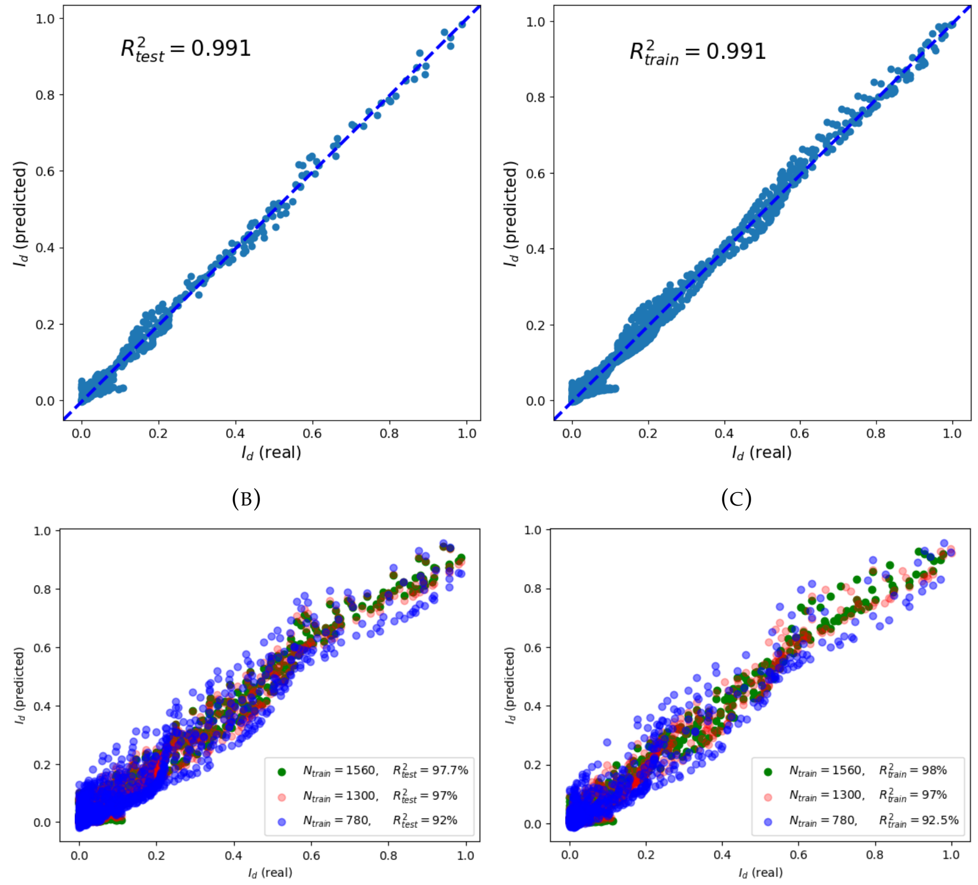

(B) (C)

(D) (E)

FIGURE 6.22: (A) Architecture of the ANN employed for drain current prediction. (B, C) Graphical analysis of the ANN performance for the prediction of drain currents for test (C) and train (C) data. (D,E) Graphical analysis of the ANN performance for the prediction of drain currents for varying sizes of the trainig dataset for test (D) and train (E) data

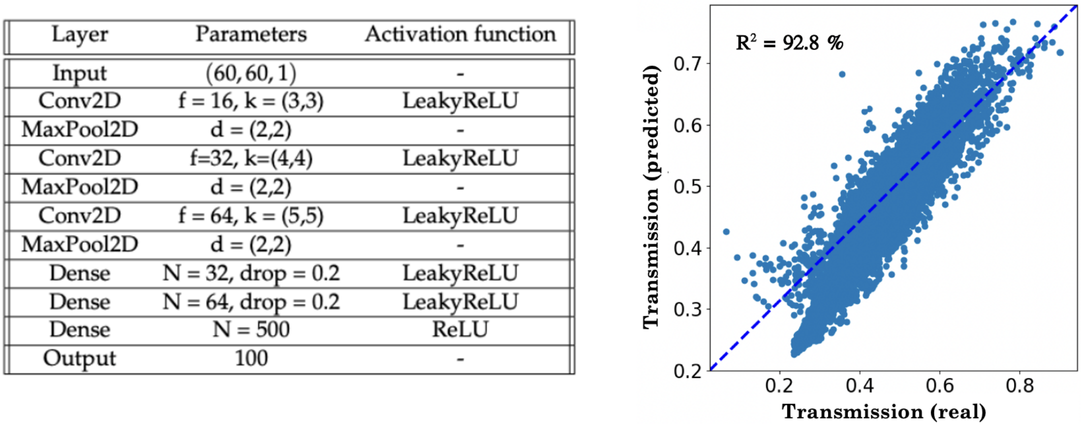

Layer	Parameters	Activation function
Input	(60, 60, 1)	-
Conv2D	f = 16, k = (3,3)	LeakyReLU
MaxPool2D	d = (2,2)	-
Conv2D	f=32, k=(4,4)	LeakyReLU
MaxPool2D	d = (2,2)	-
Conv2D	f = 64, k = (5,5)	LeakyReLU
MaxPool2D	d = (2,2)	-
Dense	N = 32, drop = 0.2	LeakyReLU
Dense	N = 64, drop = 0.2	LeakyReLU
Dense	N = 500	ReLU
Output	100	-

FIGURE 6.23: (a) The architecture of the NN and the relevant parameters. Notation f denotes the number of filters employed in the convolutional layer and k is the dimension of the kernel. Also, "drop" stand for dropout, a method we described in Section 4.2.3.

data (the remaining 20%). Out of the test data, 20% were also set aside by the network for validation. The gate potential was varied between 0 eV and 0.25 eV, with a step of 0.005 eV, and the values for the drain potential were set between 0 eV and 0.1 eV, with a step of 0.002 eV. To optimize the training process, the input data was preprocessed, which involves data scaling, checking the statistical distribution of the data and eliminating the possible outliers. Also, the analyzed systems should possess a certain degree of similarity, therefore we chose nanotransistorrs with the same barrier height (V_b) and we kept the same effective masses and dimensions.

The architecture of the neural network is presented in the Table 6.22a. The training process was carried out for 1200 epochs, with a batch size of 16 and the optimizer we chose was ADAM. The efficiency of the model was measured by employing the coefficient of determination as a metric, which we computed for the training data as well (see Figure 6.22). By tracking the coefficient of determination throughout the training, one can avoid a potential case of overfitting. Despite the fact the many of the configurations result in a null drain potential and the dataset is not very large, the artificial neural network performs very well and reaches coefficients of determination of 99%. We have also tested the same ANN architecture for datasets of reduced dimensions, namely $N_{\text{train}} = 1560, 1300, 780$, and the coefficient of determination has remained over 90%, although a decrease in performance is noticeable, as one expected.

Convolutional Neural Networks

The oscillations of the transmission function evident in Figures 6.18 are a defining characteristic of the double channel nanoFET. For this reason, we oriented ourselves towards a machine learning model that would be able to predict the transmission function itself on a given interval. Convolutional neural networks stood out as an appropriate choice, since they are actively being used not only for image processing and classification problems, but also for image translation algorithms. In our case, the change in the architecture of a traditional CNN arises in the last layer of the network, where we have to define enough neurons to correspond to each point of the transmission curve.

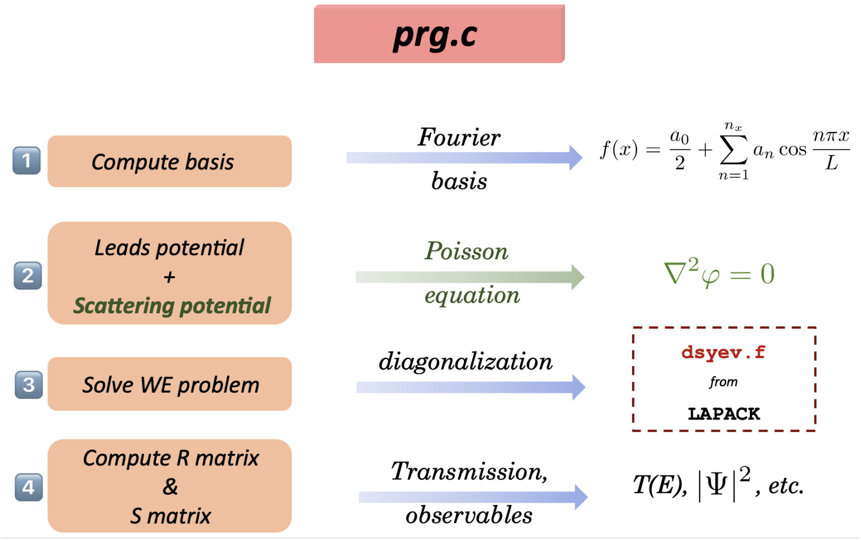

FIGURE 6.24: Brief workflow of how the R matrix code is built

For this quantum device, the input data are the potential maps obtained through numerically solving the Poisson equation. After multiple sessions of trial and error, we concluded that it is better to consider as input image the whole potential profile, including the buffer regions that account for the top and bottom gate insulators. In the numerical simulations, we only considered the scattering region with the two channel separated by the barrier. For the gathering of data for the machine learning model, we solved the Poisson equation with a grid of 0.1, to decrease the computational load and time, and subsequently the images were reduced to a smaller dimension of 60×60, to make the training process smoother.

The output data were the transmission functions in the energy interval of $[0.2, 0.4]$ eV. Due to the fact that the values of the transmission function are in the narrow interval of $[10^{-4}, 10^{-8}]$ (for a nanoFET with a tunneling barrier of 1 eV, we applied the logarithm to the transmission values and multiplied the result with -1, such that we end up with a set of positively valued input data. Also, the transmission function was mediated on intervals of 10^{-3} eV, to decrease the number of output neurons. The structure of the CNN is represented in table 6.23, where we specified the relevant parameters, namely the dimensions of the input and output layers, the structure of the convolutional layers and the number of neurons in the hidden intermediary layers. The model was trained for 6000 epochs, with a batch size of 32, and the chosen optimizer is ADAM, with a learning rate of 10^{-4}. We had at our disposal a set of 5000 entries, out of which 10% were used for testing and 20% of the training data was employed for validation. To evaluate the performance of the model, we used the coefficient of determination and we obtained a value of 92% (Figure 6.23). Some of the results were also shown in Figure 6.25.

6.4.5 Conclusions

The transport properties of field effect nanotransistor device we studied in this thesis can be explained by the lateral resonant tunneling between two parallel conduction channels. In the transfer characteristics we find narrow resonant tunneling peaks around zero control voltage allowing to switch the drain current with small control voltages, which opens the way to low-energy applications.

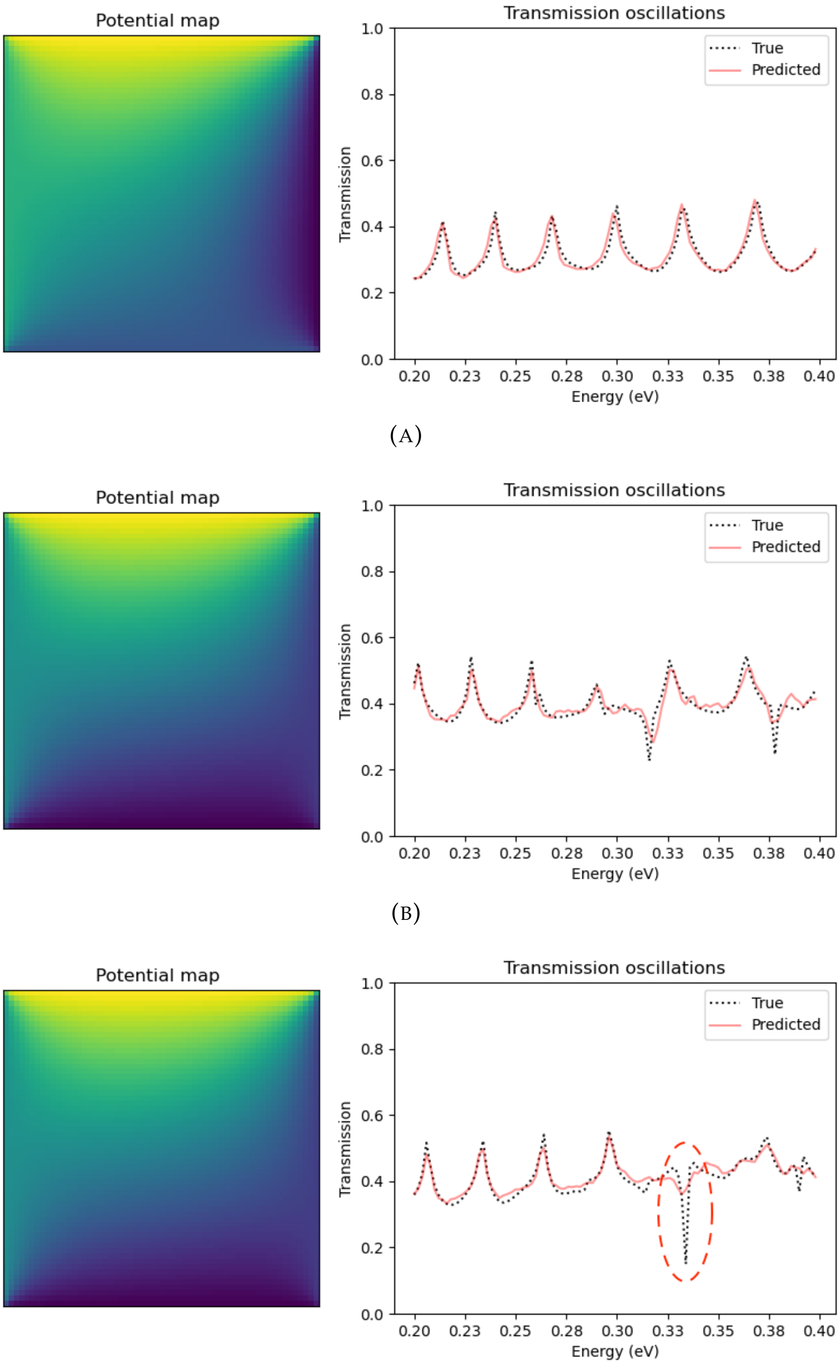

(A)

(B)

(C)

FIGURE 6.25: A series of results after training the CNNs. On the left - the potential map is displayed and on the right - the corresponding predicted transmission function (logarithmic scale). We notice that higher errors arise where the transmission has abrupt variations and narrow peaks.

7

Quantum Sorters

7.1 Probabilistic quantum sorter

>> The main results presented in this section were published in [137]

7.1.1 Introduction

Information theory is a fundamental pillar of technological advancement and has consistently been a focal point of interest in theoretical physics, engineering, and research and development. Its primary objective is to enable the realization of physical devices that process information with greater efficiency and at increasingly smaller physical scales. From an experimental standpoint, achieving this goal implies a precise understanding and control of both solid-state and optical components of the device. The field of quantum information emerged from the need to reformulate information processing exclusively through the principles of quantum mechanics. Its rapid development in recent decades has been driven by the potential to harness quantum phenomena—such as interference, superposition, and entanglement—within (nano-)electronic devices. Unlike classical computing, where the fundamental unit of information, the bit, is defined by two discrete logical states (0/1 or ON/OFF), quantum information employs the qubit, which exists as a superposition of both states [138].

While the exploitation of quantum effects for technological innovation is well established—exemplified by the Tsu-Esaki diode, superconductors, Josephson junctions, and topological materials—the development of large-scale quantum computers presents significant challenges. A crucial requirement is the ability to maintain coherent quantum channels for reliable information transmission. Consequently, quantum information research can be broadly categorized into two domains: one focusing on theoretical aspects, such as quantum algorithms, protocols, cryptography, and entanglement, and the other concerned with condensed matter physics and photonics, investigating various materials and techniques for realizing quantum devices [139].

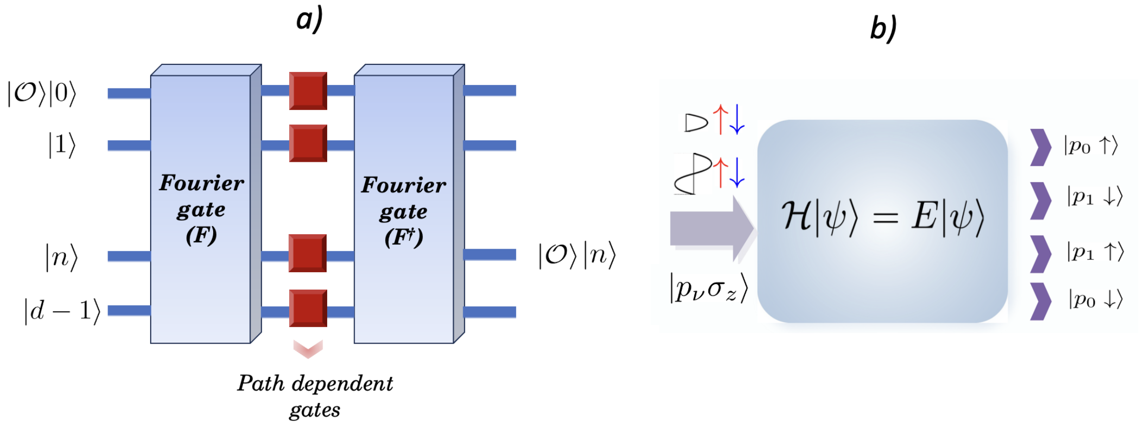

FIGURE 7.1: (a) Universal quantum sorter proposed in [158, 157], unitary and hence reversible. Incoming particles are incident on spatial mode 0 and they are subsequently sorted according to the value of the observable $\mathcal{O}$. In this ideal quantum sorter, a particle with $\mathcal{O} = n$ will exit on output port n with maximum probability; (b) Mesoscopic quantum sorter that we proposed.

Many applications in quantum information, including logic operations, quantum key distribution, and teleportation, fundamentally require the characterization of a multi-dimensional Hilbert space to accurately describe the quantum system. In quantum information processing, a crucial step involves sorting the multiple degrees of freedom that define the system, followed by precise measurement [140].

This field has seen significant advancements, particularly in quantum optics, where the study of quantum sorters has gained considerable attention due to their efficiency and applicability in quantum communication and cryptography. These quantum sorters employ photons as information carriers, leveraging different degrees of freedom such as polarization and orbital angular momentum [141, 142, 143, 144, 145, 146, 147], total angular momentum [148], radial modes [149, 150, 151], Laguerre-Gaussian modes [152], spin and radial quantum numbers [153], full-field mode sorting [154], multimode fiber sorting [155], and all-fiber in-line mode sorting [156]. However, these quantum sorters are designed to function only for specific photon properties. A generalized quantum sorter, capable of utilizing any degree of freedom within a D-level system, was introduced in [157], though it was constructed for a single input port. Further advancements led to the proposal of a multi-input-port quantum sorter, designed to perform the simultaneous sorting of D-level systems [158, 159].

Parallel to the development of quantum optics as a prolific exploratory ground for quantum information, solid state physics has also positioned itself at the forefront of research into more energy efficient and versatile electronics involving the investigation of advanced quantum mechanical effects, including entanglement, tunneling and spin orbit interaction [160]. Widespread charge base devices such as tunneling field effect transistors or resonant tunneling diodes have already exploited the quantum mechanical nature of charge carriers and proved their value not only in information processing, but also information storage. In the last decades, spintronics has also emerged as a promising field, with spin based logic devices and spin based memories, exploiting the electron spin as a degree of freedom in quantum information. Quantum dots, which are spatially confined electronic systems, could be used for realizing new quantum computing architectures. Since electronic spin is the fundamental platform for the implementation of qubits, similarly to how photons can be sorted, electrons could also be sorted according to their orbital angular momentum [161].

The quantum sorter we propose provides a straightforward method to measure observables, by sorting the output states into different ports according to the eigenvalues and subsequently using particle detectors in each output lead.

7.1.2 Simulation of a probabilistic quantum sorter

Theoretical considerations

A quantum state in the qubit system can be represented as a column vector in the $\mathbb{C}^2$ plane, spanned by the following two basis state:

$$|0\rangle = \begin{bmatrix} 1 \\ 0 \end{bmatrix}, \quad |1\rangle = \begin{bmatrix} 0 \\ 1 \end{bmatrix}$$

Therefore, the general state $|\psi\rangle$ can be written as:

$$|\psi\rangle = \alpha|0\rangle + \beta|1\rangle = \begin{bmatrix} \alpha \\ 0 \end{bmatrix} + \begin{bmatrix} 0 \\ \beta \end{bmatrix} = \begin{bmatrix} \alpha \\ \beta \end{bmatrix}$$

where $|\alpha|^2 + |\beta|^2 = 1$.

Consider the situation of two qubit systems that are independently prepared in states $|\psi\rangle = (\alpha_0, \alpha_1)^T \in \mathbb{C}^2$ and $|\phi\rangle = (\beta_0, \beta_1)^T \in \mathbb{C}^2$. Then, the total state of the composite system is described by a vector in $\mathbb{C}^4$, obtained as the tensor product of $|\psi\rangle$ and $|\phi\rangle$ [139]:

$$|\psi\rangle \otimes |\phi\rangle = \begin{pmatrix} \alpha_0|\phi\rangle \\ \alpha_1|\phi\rangle \end{pmatrix} = \begin{pmatrix} \alpha_0\beta_0 \\ \alpha_0\beta_1 \\ \alpha_1\beta_0 \\ \alpha_1\beta_1 \end{pmatrix} \in \mathbb{C}^4 \tag{7.1}$$

Therefore, we have four possible computational basis states, namely $|00\rangle, |01\rangle, |10\rangle, |11\rangle$. We can thus write the general form of the two-qubit state as follows:

$$|\psi\rangle = \alpha_{00}|00\rangle + \alpha_{01}|01\rangle + \alpha_{10}|10\rangle + \alpha_{11}|11\rangle \tag{7.2}$$

where $|\alpha_{00}|^2 + |\alpha_{01}|^2 + |\alpha_{10}|^2 + |\alpha_{11}|^2 = 1$.

This can be generalized further to the qudit system. Specifically, a state in the d-dimensional qudit system is a superposition of d basis states:

$$|\psi\rangle = \alpha_1|1\rangle + \alpha_2|2\rangle + \cdots + \alpha_d|d\rangle, \tag{7.3}$$

where $|\alpha_1|^2 + \cdots + |\alpha_d|^2 = 1$. In theory, any qudit system could be constructed using only qubits.

To analyze a quantum sorter type of system, consider two D-dimensional Hilbert spaces $\mathcal{H}_{\text{system}}$ and $\mathcal{H}_{\text{port}}$, where the first Hamiltonian is associated to a qudit system, while the second one to the states of the D input and output ports. From [158], rigorously, a multi-input-port quantum sorter is a device acting in the Hilbert space $\mathcal{H}_{\text{system}} \otimes \mathcal{H}_{\text{port}}$, that performs the unitary transformation

$$|s\rangle|k\rangle \longrightarrow |s\rangle|s\rangle, \quad \text{with } s, k = 0, 1, \ldots, D-1$$

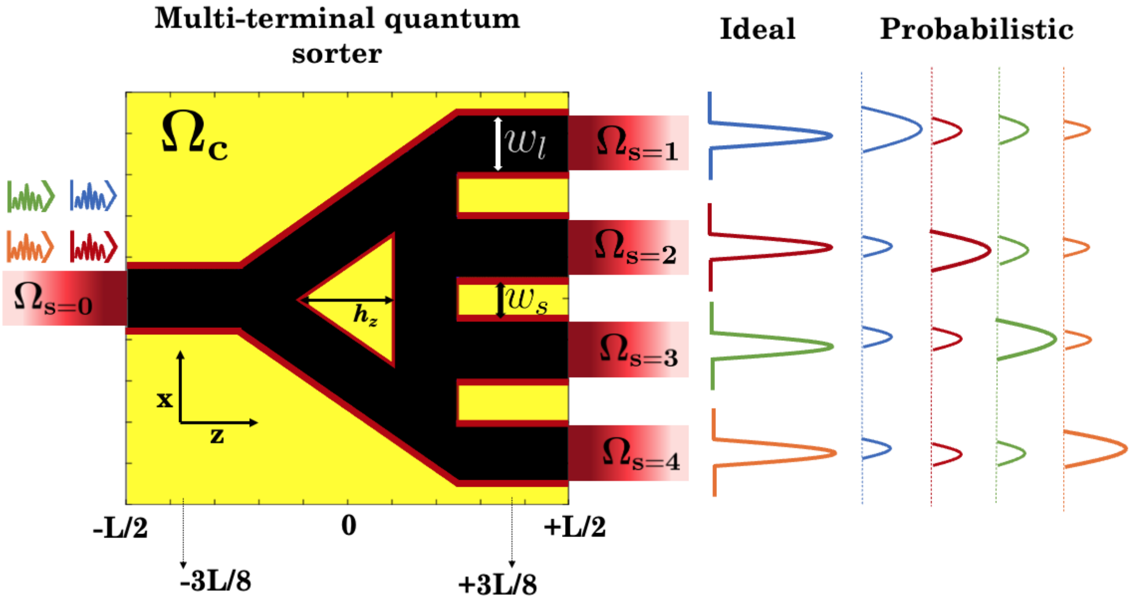

FIGURE 7.2: Proposed multi-terminal design of the quantum sorter and the qualitative transmission probabilities in the ideal and probabilistic case. Ideally, each incoming spin-resolved mode is transmitted into a separate outgoing lead [137].

Also note that each computational gate is a unitary operator, which is a reversible transformation by nature. However, in [158] it was proved than an ideal multi-input-port quantum sorter is forbidden by the laws of quantum mechanics, hence we focus on the implementation of a probabilistic quantum sorter.

The system that we propose here as a concrete version of the quantum sorter is defined as a multi-terminal 2D mesoscopic system, with only one input lead and four outputs. The incoming particle is described, quantum mechanically, with two quantum numbers, namely the spin and the channel (transverse mode). Therefore, we can describe the incoming state as a superposition of $|k_\nu \sigma_z\rangle$, where $\nu = 1, 2$ and $\sigma_z = \uparrow, \downarrow$.

In references [158, 157], the quantum sorter selects the particles characterized by the property $|s\rangle$ of the quantum system by directing them into the same output port-state, which is denoted by $|s\rangle$. In the case of the quantum sorter device we proposed, we work solely in a single-particle framework and assume that in an experimental setting, one injects sequentially multiple electrons, at the same energy, but different transverse modes and with different spin degrees of freedom. After repeating this for a large amount of times, each of the four possible input states of the incoming particle is transmitted into a different output lead. **Our goal in this work is to define a system that works as a probabilistic quantum sorter in a concrete manner, by choosing an interaction Hamiltonian that enables the device to separate the eigenstates into multiple output ports. To this end, identifying a quantum state does not imply measuring the observable, but detecting of a particle in one particular output lead.** While the device we propose is not reversible, we maintain the name of "quantum sorter" since it describes best the purpose of the proposed device.

To model this type of device, we need to calculate transmission probability for the electrons coming into the left lead into each of the output leads. The wavefunctions in the reservoirs are represented in the basis of eigenstates $|\uparrow\rangle, |\downarrow\rangle$ of σ_z . The basis functions are $|k_x, k_y, \sigma\rangle$, where k_x and k_y are the wave vector components in the reservoirs and $\sigma = \uparrow, \downarrow$.

In the left reservoir $(x < 0)$, the wave function is

$$\left|\psi^{(L)}_{k_x k_y,\sigma}\right\rangle = \left|k_x, k_y, \sigma\right\rangle + \sum_{\sigma'} r_{\sigma,\sigma'} \left|-k_x, k_y, \sigma'\right\rangle,$$

where $\left|k_x, k_y, \sigma\right\rangle$ is the state vector of incident electrons. The wave function of transmitted electrons $(x > d)$ is

$$\left|\psi^{(R)}_{k_x k_y,\sigma}\right\rangle = \sum_{\sigma'} t_{\sigma,\sigma'} \left|k_x, k_y, \sigma'\right\rangle.$$

Here, $r_{s,s'}$ and $t_{\sigma,\sigma'}$ are the reflection and transmission matrices. If a spin-polarized electron is injected into an ideal lead, with no spin orbit coupling or magnetic terms, semi-infinite in the x direction and with a transversal confinement potential in the y direction, each transport channel is, from a quantum mechanical perspective, a tensor product between the (orbital) transverse mode and the spin degree of freedom. In quantum information terms, this is a separable pure quantum state:

$$\begin{aligned} \left|\psi^{(injected)}_{k_n,\sigma}\right\rangle &= \langle \mathbf{r}|k_n^{\pm}\sigma\rangle = \Phi_n(y)\cdot \exp^{\pm i k_n x} \otimes |\sigma\rangle, \\ |IN\rangle &= |k_n\sigma\rangle. \end{aligned} \tag{7.4}$$

The outgoing state in one particular lead will be pure, but nonseparable and it can be expressed as [162]:

$$|OUT\rangle = \sum_{n'\sigma'} t_{n'n,\sigma'\sigma} \left|k_{n'}\right\rangle \otimes \left|\sigma'\right\rangle. \tag{7.5}$$

One important thing to note is that an electron injected into the left lead in mode $|n\rangle$ and spin state $|\sigma\rangle$ will be scattered into one of the output leads into mode $|n'\rangle$ and spin $|\sigma'\rangle$. The quantity that can be measured experimentally is the particle current in each lead, so our objective is to find a configuration of the scattering region Hamiltonian that will ensure that a particular injected state is transmitted with high probability into one lead, while the current it generates in all the other leads is negligible.

7.1.3 Multi-terminal model system

The prototype device that we propose is defined on a square-shaped scattering region of dimensions $L_x = L_y = L = 2d = 1\mu$m which is divided into three regions: the continuation of the left $(x < -3d/4)$ and right leads $(x > 3d/4)$, and the active region in the center [137]. The lead areas in the scattering region have the same characteristics as the ideal semi-infinite leads. The leads are defined by quantum wells with constant potential of width $w_l = 3d/10 = 150$ nm, carved out from a base potential barrier of height $V_b = 100$ meV and the distance between two consecutive leads is $w_s = d/5 = 100$ nm. We perform the simulations o a material with a small effective mass (namely InSb, with $m^* = 0.023 m_0$) in order to increase the separation between quantum levels .

In the active region, a triangular shaped potential barrier acts as a central scatterer that guides the incoming electrons to the output leads. The dimensions of the central triangle and also the barrier height are parameters that we tune in order to find the ideal quantum sorter configuration. The shape of this central scatterer can also be modified with top gate voltages in an experimental setup. For a clean separation between the up and down spin components, we consider a magnetic barrier

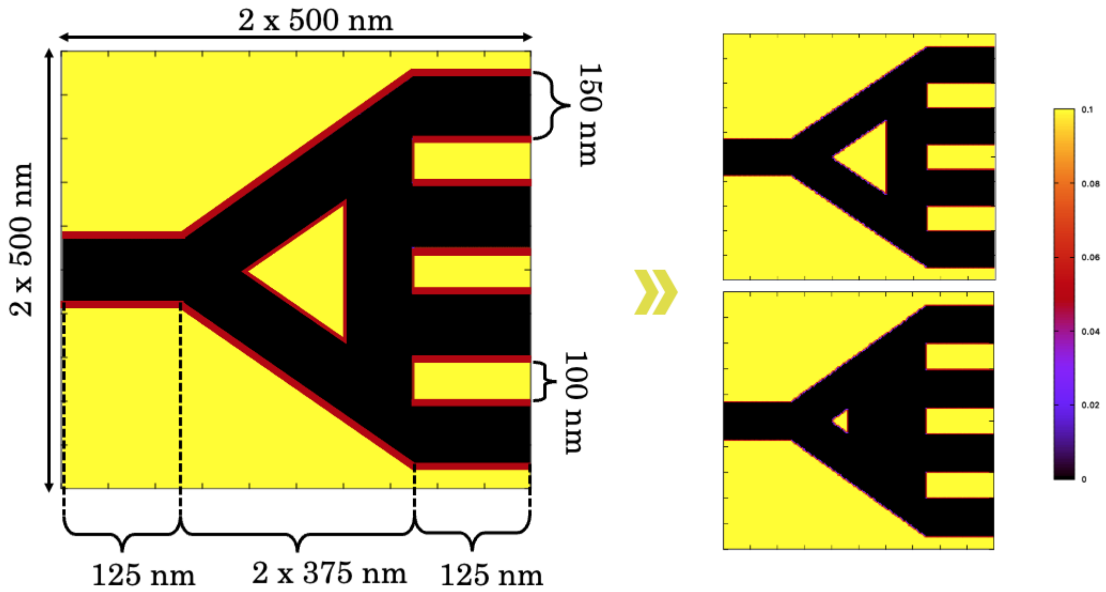

FIGURE 7.3: The the potential map in the scattering region, with a triangular scatterer along with the system dimensions. The geometrical parameter that is varied is the area of the central triangular scatterer.

on top of the output leads that induces a Zeeman splitting of $V_Z = \pm 100$ meV. To avoid the downshift of energy levels for one spin component, we compensate with an electrostatic potential equal to half of the splitting. In this way, the energy levels corresponding to one of the spin component will remain unchanged, while for the other spin component, the energy levels will shift to higher energies, essentially leading to a cutoff of the respective spin component.

R-matrix simulations

The quantum sorter device we propose is represented in Figure 7.2. As we already mentioned, the device has one input terminal and multiple output terminals, with the scattering region in-between. The geometry and scale of the system is defined by the dimensions of the interaction region $d = 500$ nm, the triangular central potential barrier is set at $V_0 = 0.1$ eV and the effective mass is that of InSb $m^* = 0.023 m_0$ [137].

The coherent transport is described in the framework of the R-matrix method, which was described extensively in section 3.5. This formalism efficiently provides the transmission for a wide energy range and its computational implementation also allows for easy parallelization (employing the MPI library), such that we can study multiple system configurations effectively. The diagonalization of the Wigner-Eisenbud problem in the scattering region is the most time consuming, but is also computationally stable and highly versatile. The method easily allows for the inclusion of Rashba spin orbit interaction, magnetic fields and the geometrical tuning of the potential in the scattering region. In the final step, the R-matrix and scattering matrix are computed, leading to the transmission function through the system at any chosen energy.

The time independent Schrodinger equation defines the scattering problem in the entire system:

$$\mathcal{H}\Psi(\mathbf{r}) = E\Psi(\mathbf{r}), \quad \mathbf{r} \in \Omega_0 \cup \Omega_s \tag{7.6}$$

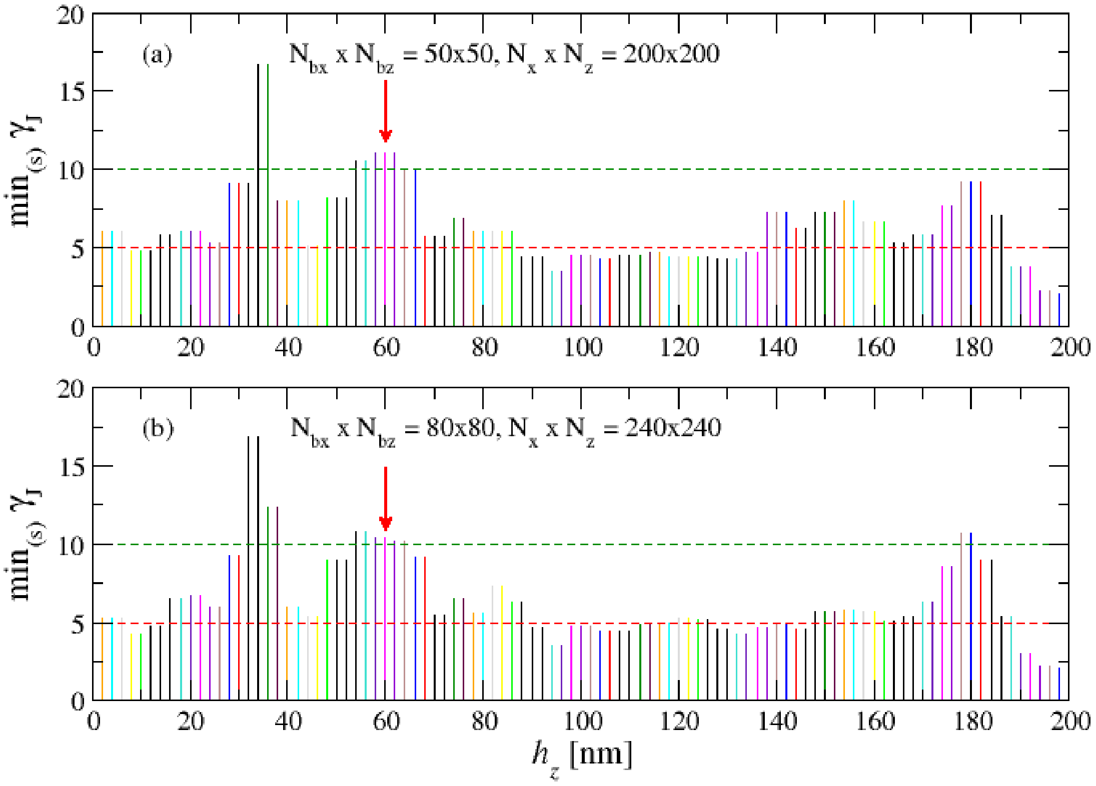

FIGURE 7.4: Minimum current ratios for a sequence of $N_{\text{scat}} = 100$ scatterer configurations set by the parameter h_z. We checked the results for two different sets of basis size and grid points: (a) $N_{\text{bx}} \times N_{\text{bz}} = 50 \times 50$, $N_x \times N_z = 200 \times 200$. Notice that both results are similar, therefore the calculations have converged. The red arrow marks the reference system, which leads to a highly effective probabilistic quantum sorter (obtained for $h_z = 60$ nm) [137].

with asymptotic boundary conditions for the input/output leads.

The Hamiltonian in the scattering region includes the scattering potential and the spin-orbit coupling term (Rashba SOI)

$$\mathcal{H}_0 = -\frac{\hbar^2}{2m^*}\nabla^2 + V\left(\mathbf{r} \in \Omega_0; \mathcal{P}\right), \tag{7.7}$$

where $\mathcal{P}$ is a set of tunable parameters related to the geometry of the potential and the height of the central barrier it induces. By varying these parameters, we search for an optimal quantum sorter configuration.

The Hamiltonian inside the left lead is:

$$\mathcal{H}_{s=0} = -\frac{\hbar^2}{2m^*}\nabla^2 + V_{s=0}\left(\mathbf{r} \in \Omega_s\right) \tag{7.8}$$

where $V_s\left(\mathbf{r} \in \Omega_s\right)$ is the confinement potential in the leads, with a longitudinal component that is translationally invariant in the direction of transport and a transverse component which gives rise to the transversal modes in the leads.

In the right leads, we added a Zeeman term to the Hamiltonian in order to facilitate the separation of different spin states:

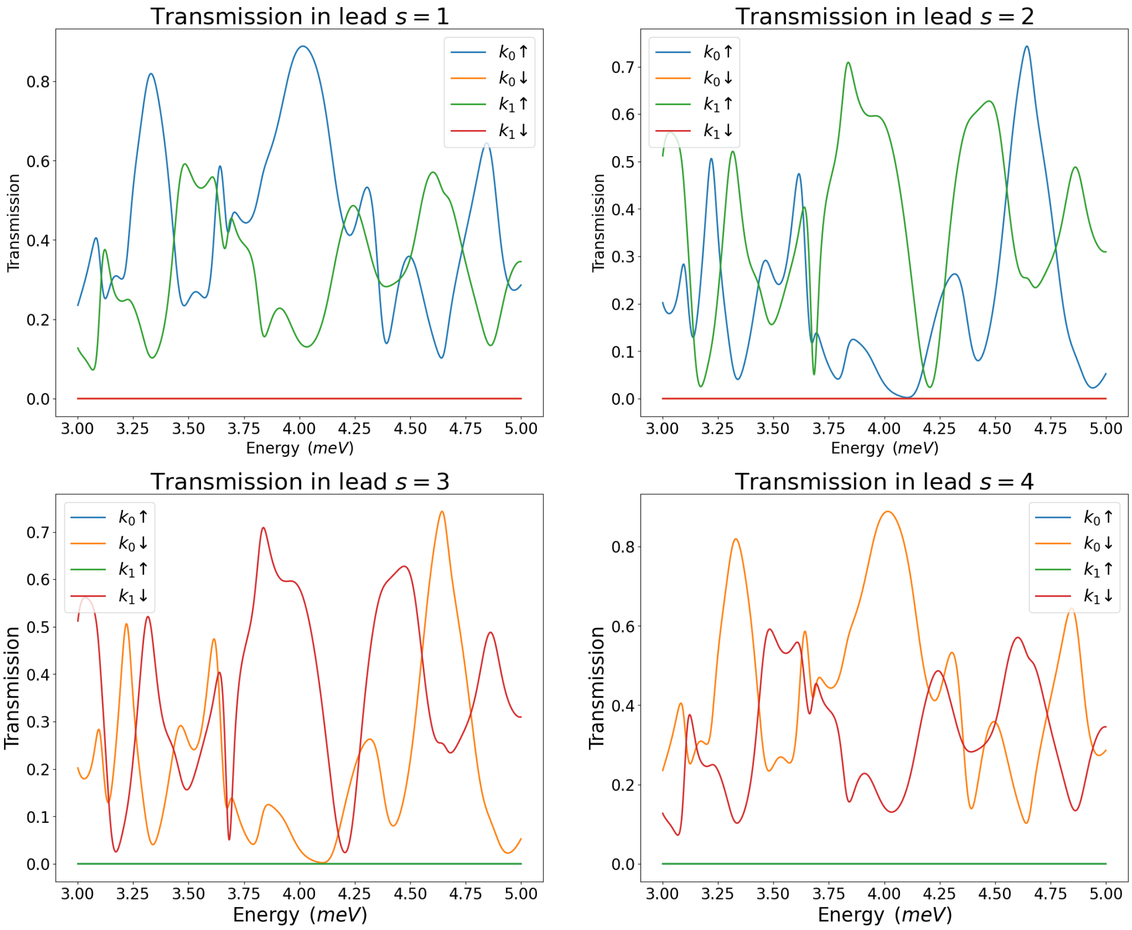

FIGURE 7.5: Transmission functions for each incoming mode in all of the output leads. These results are obtained with R-matrix simulations.

$$\begin{aligned}\mathcal{H}_{s=1,2} &= -\frac{\hbar^2}{2m^*}\nabla^2\mathbb{I}_2 + V_{s=1,2}\left(\mathbf{r}\in\Omega_s\right)\mathbb{I}_2 + \frac{E_z\sigma_z}{2} + \frac{E_z\sigma_0}{2} \\ \mathcal{H}_{s=3,4} &= -\frac{\hbar^2}{2m^*}\nabla^2\mathbb{I}_2 + V_{s=3,4}\left(\mathbf{r}\in\Omega_s\right)\mathbb{I}_2 - \frac{E_z\sigma_z}{2} + \frac{E_z\sigma_0}{2}\end{aligned} \tag{7.9}$$

where $E_z = 50 \cdot 10^{-3}$ eV.

Searching for the ideal QS configuration

In typical multi-terminal devices, one expects a non-zero transmission in all of the output ports, since elastic scattering greatly impacts the transversal momentum of the electrons. Therefore, to identify an effective quantum sorter prototype, we need to first establish valid minimal criteria for the transmission functions in the leads [137].

We settled on calculating the ratios between the currents of each propagating mode in all of the output leads. For example, we calculated for the current ratios between a mode i_1 and mode i_2, where $i_2 \neq i_1$, at given total energy E

$$\gamma_J\left(s, i_1, i_2\right) = j\left(s, i_1\right) / j\left(s, i_2\right),$$

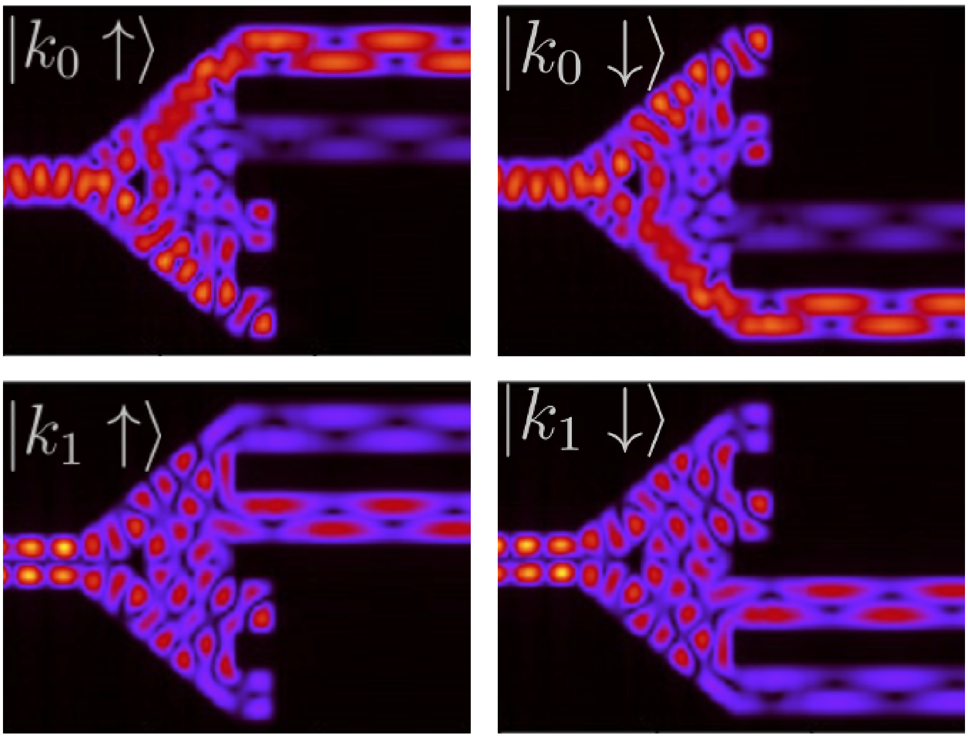

FIGURE 7.6: The absolute value squared of the wavefunctions for the incoming modes, calculated using the R-matrix method. The modes $|k_0 \uparrow\rangle$ and $|k_0 \downarrow\rangle$ are mostly transmitted into the outer $s = 1$ and $s = 4$ leads, while the $|k_1 \uparrow\rangle$ and $|k_1 \downarrow\rangle$ are scattered with greater probability into the inner leads ($s = 2, 3$).

in a lead denoted by s. Due to the spin symmetry enforced by the magnetic barriers, we only need to determine the ratios for $s = 1$ and $s = 2$:

$$\begin{aligned} \gamma_{J,1} &\equiv \gamma_J(\text{s=1}, 0, 1) = j(1, 0)/j(1, 1), \\ \gamma_{J,2} &\equiv \gamma_J(\text{s=2}, 1, 0) = j(2, 1)/j(2, 0). \end{aligned} \tag{7.10}$$

We impose a minimum ratio, such that $\min_s \gamma_{J,s} > \gamma_{\text{min}}$, where γ_{min} is taken to be 5. One can also define the ratios between the transmission functions at a given energy, $\gamma_T(s, i_1, i_2) = T(s, i_1)/T(s, i_2)$, but we are mainly focused on the current ratios because the current is the experimentally measured quantity.

We proceed by tuning the geometrical parameter (in our case, h_z) that defines the size triangular central scatterer, as we highlighted in Figure 7.4. We found a minimal current ratio of $\gamma_{\text{min}} = 10.46$ for the case with $h_z = 60$ nm, (see Figure 7.4). The transmission functions for each incoming mode, obtained with the R-matrix simulations, are represented in Figure 7.5 . In the energy range of $[3, 5]$ meV we find an optimal device configuration at $E = 4.04$ meV. The mode $|k_0 \uparrow\rangle$ is dominant in $s = 1$, while mode $|k_1 \uparrow\rangle$ is dominant in lead $s = 2$. This result is mirrored in the other two leads, $s = 3, 4$, as one notices also from the transmission functions.

Other criteria should be accounted for if one aims to design a quantum sorter device. For example, the stability of the system with respect to the tunable parameter is a key aspect. For this reason, the results displayed in Figure 7.4 are highly relevant, since they emphasize the fact that around $h_z = 60$ nm, the systems exhibit similar values for γ_J. As a result, a slight inaccuracy in the manufacturing process would not become a hindrance for the desired functionality of the device.

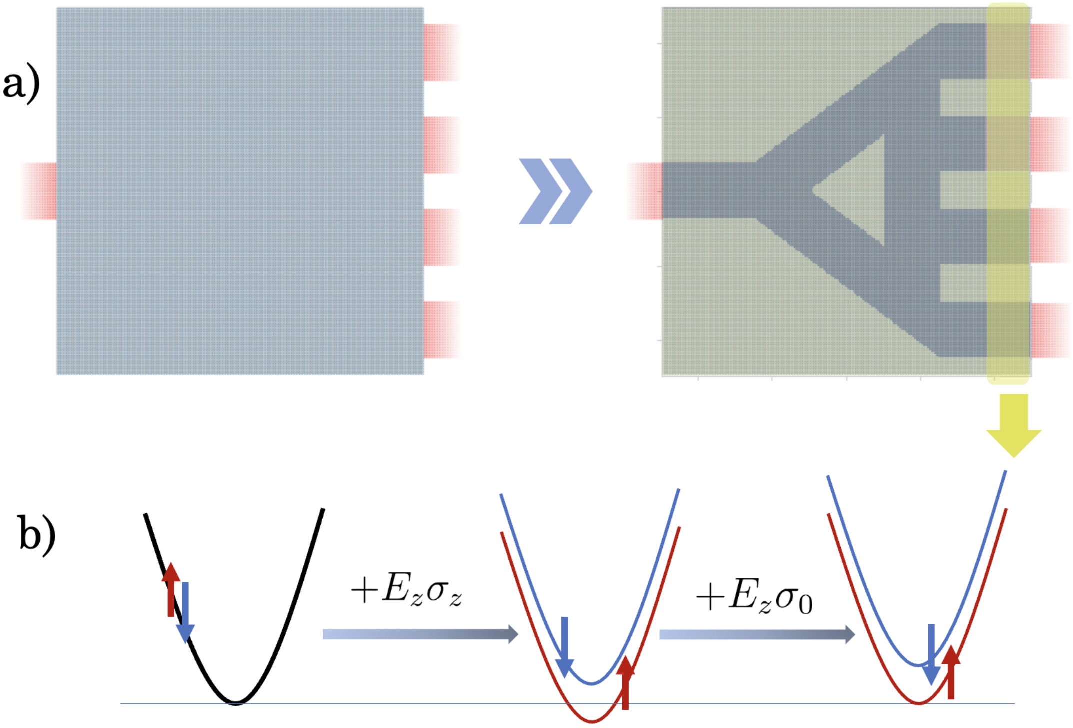

FIGURE 7.7: (a) tight-binding model, implemented with Kwant, showing the positioning of magnetic barriers (yellow) and the attached leads (red) (b) The impact of the Zeeman term on the bandstructure.

KWANT simulations

The Kwant package [61] has acquired a great deal of popularity in recent years. It is a Python library based on the tight binding model, focusing on quantum transport calculations and using the wavefunction matching method to solve the scattering problem. We have discussed this approach in detail in section 3.8. The Kwant library is also popular due to its versatility and its transparent syntax that allows the user great flexibility when it comes to the geometrical properties of the system, incorporating spin orbit-coupling and magnetic fields and even transitioning to more exotic Hamiltonians.

For our system, the Hamiltonian operator is:

$$\mathbf{H} = \sum_{\langle ij\rangle,\sigma\sigma'} t^{\sigma\sigma'}\sigma_0 \left|i,\sigma\right\rangle \left\langle j,\sigma'\right| + \sum_{i\in S,\sigma\sigma'} V_i\sigma_0 \left|i,\sigma\right\rangle \left\langle i,\sigma'\right| + \sum_{i\in Z,\sigma\sigma'} \frac{g\mu_B}{2}\mathbf{B}\boldsymbol{\sigma} \left|i,\sigma\right\rangle \left\langle i,\sigma'\right|, \tag{7.11}$$

where the sum over $\langle ij\rangle$ is taken over nearest neighbors only, $(\sigma_0, \boldsymbol{\sigma})$ denote the identity matrix and the Pauli vector that incorporates the Pauli matrices ($\boldsymbol{\sigma} = (\sigma_x, \sigma_y, \sigma_z)$), and $\mathbf{B}$ is the external magnetic field. S stands for the whole scattering region and Z denotes the area where the Zeeman term is applied (see Figure 7.7 a). In contrast to the R-matrix approach, in the tight binding based approach we only include the in-plane magnetic field in the scattering region, right before it comes in contact with the leads. The Kwant code demands that the leads maintain translational invariance, since they are modeled as ideal semi-infinite contacts, therefore magnetic fields are not added to the terminals.

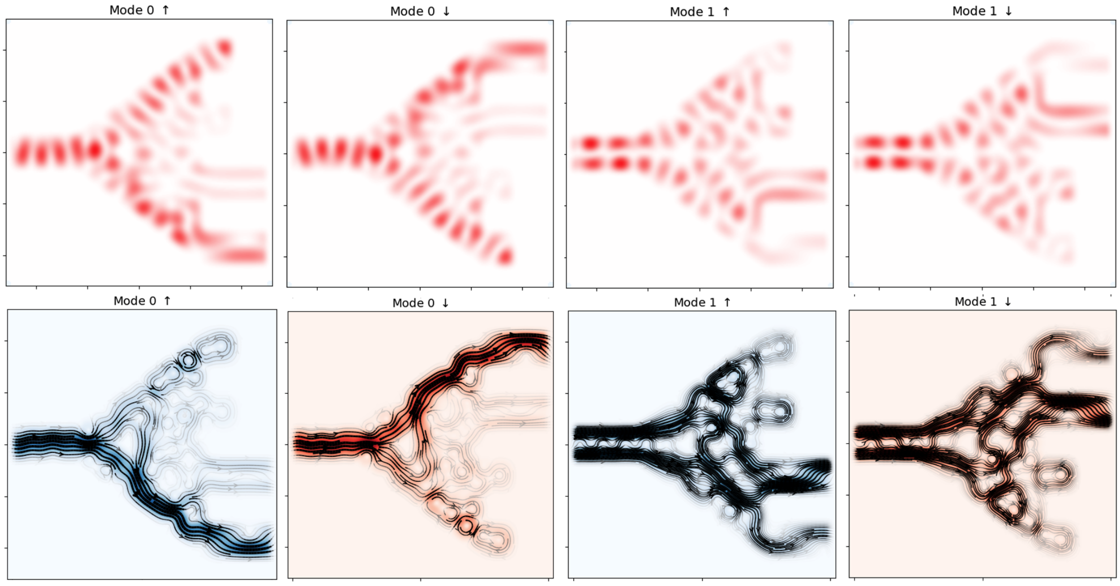

FIGURE 7.8: Wavefunctions (absolute value squared) for the incoming modes and current density maps, calculated using Kwant [137].

The effects of an external, time-independent, homogeneous magnetic field, **B**, are included in theoretical model through the Peierls substitution and the Zeeman energy term. The Peierls substitution changes the wavevector $\mathbf{k} \rightarrow \mathbf{k} + (|e|/\hbar)\mathbf{A}$, where **A** is the vector potential and it adds a phase to the tight binding Hamiltonian. The Zeeman term accounts for the interaction of the atomic orbital angular momentum and spin and can be written as

$$E_{\text{Zeeman}} = \vec{E}_z \vec{\sigma} \tag{7.12}$$

While the presence of a Zeeman term should modify the kinetic momentum ($\vec{p}$) to the canonical momentum ($\vec{p} + |e|\vec{A}$). However, in the weak field limit, its effect can be neglected for in-plane magnetic fields [163].

The tight-binding model corresponding to a spinful system naturally exhibits a 2x2-matrix structure of onsite energies and hopping terms (note that in the code in Appendix L we selected $n_{\text{orbs}} = 2$). Also, it is important to note that the Zeeman Hamiltonian adds to the onsite terms (since we ignore the Peierls phase), in contrast to a Rashba spin-orbit term that, due to the derivative operators involved in its expression, adds to the hopping terms. In the code added in Appendix L you can also see how to add SOC in a Kwant code, though we did not employ any Rashba interaction in this case (the Rashba coefficient is set to zero).

The (spin) charge density at site i with energy E is defined as follows:

$$\rho_i(E) = \sum_{\sigma,\sigma'} \psi^{\dagger}_{i\sigma}(\mu) M_{\sigma,\sigma'} \psi_{i\sigma'}(E) \tag{7.13}$$

where $\psi_i(E)$ is an eigenstate of the Hamiltonian and M is a quantum operator. In order to calculate this quantity, it is necessary to find the scattering wavefunction of the system. In Kwant, the wave function in one of the leads is calculated as shown in the code snippet:

```
# Hf is the Hamiltonian of the system and E is the energy of interest
wf = kwant.wave_function(fsyst, energy=E)
```

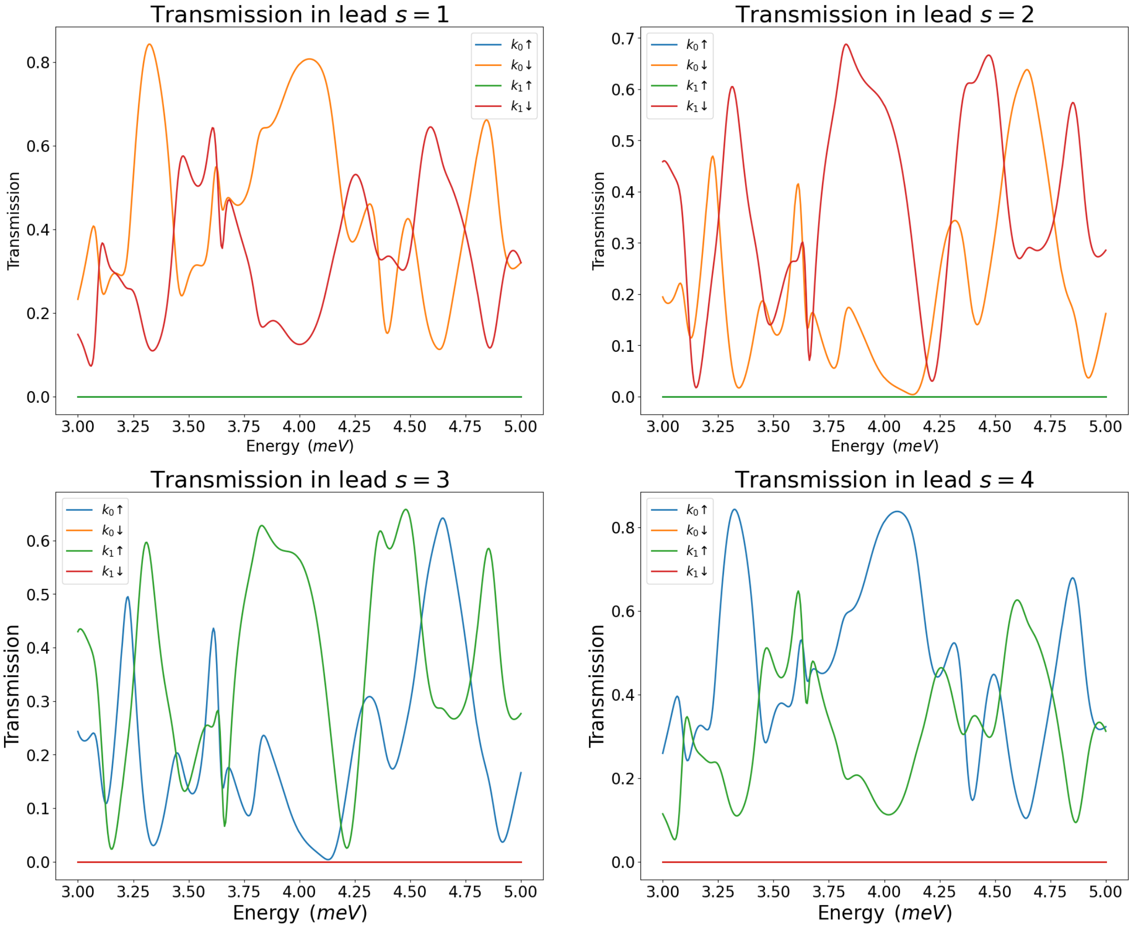

FIGURE 7.9: Transmission functions for each incoming mode in all of the output leads. These results are obtained with Kwant simulations.

```
# lead indicates the lead number and mode the desired mode
phiw = wf(lead)[mode]
```

For the case when $M = \mathbb{I}$, the n-th mode of the charge at energy E for a system with spin is expressed as:

$$\rho_i^n(E) = e\left|\psi_{i\uparrow}^n(E)\right|^2 + \left|\psi_{i\downarrow}^n(E)\right|^2$$

The total charge density is:

$$\rho_{c,i}(E) = e\sum_{i,n}\rho_n(E)$$

In order to obtain the spin density we should replace M by a chosen Pauli matrix σ^z. Let's say we want the spin projected along z:

$$\rho_{s,k}^n(E) = \begin{pmatrix}\psi_{k\uparrow}^{n\dagger}(E)\\ \psi_{k\downarrow}^{n\dagger}(E)\end{pmatrix}^T \sigma_z \begin{pmatrix}\psi_{k\uparrow}^n(E)\\ \psi_{k\downarrow}^n(E)\end{pmatrix},$$

where $k \equiv (a, b)$ stands for lattice indices, E is the energy and n is the index of the incoming transversal mode. Employing the same quantities discussed above, one can also define local current flowing from site b to site a :

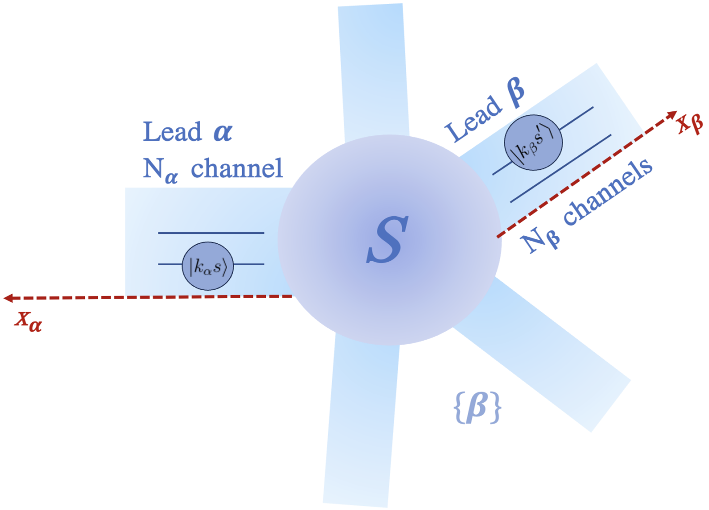

FIGURE 7.10: An electron injected into the input lead α can be scattered into any channel (and spin state, as long as we accout for spin-dependent scattering processes, such as spin-orbit interactions) in lead β. To compute the probability that an injected electron scatters into a particular output lead, one needs to sum over all the channels in the lead and sum over the spin states.

$$J_{ab} = i\left(\psi_b^\dagger \left(\mathbf{H}_{ab}\right)^\dagger \mathbf{M}\psi_a - \boldsymbol{\psi}_a^\dagger \mathbf{M}\mathbf{H}_{ab}\psi_b\right),$$

where $\mathbf{H}_{ab}$ is the hopping matrix from site b to site a.

Spin and mode resolved transmission

The total transmission function, derived from the scattering matrix, is:

$$T = \sum_{\sigma\sigma'} \sum_{m\in \mathrm{I}, n\in \mathrm{O}} T^{\sigma'\sigma}_{n\leftarrow m}, \tag{7.14}$$

where I is the left input lead ($s = 0$) and O stands for the set of four output terminals (see also Figure 7.10). The spin and mode resolved transmissions are computed as follows:

$$\begin{aligned}
T_{k_0\uparrow} &= \sum_{\sigma'} \sum_{0\in \mathrm{I}, n\in \mathrm{O}} T^{\sigma'\uparrow}_{n\leftarrow 0} = \sum_{0\in \mathrm{I}, n\in \mathrm{O}} T^{\uparrow\uparrow}_{n\leftarrow 0} + T^{\downarrow\uparrow}_{n\leftarrow 0}\\
T_{k_0\downarrow} &= \sum_{\sigma'} \sum_{0\in \mathrm{I}, n\in \mathrm{O}} T^{\sigma'\downarrow}_{n\leftarrow 0} = \sum_{0\in \mathrm{I}, n\in \mathrm{O}} T^{\uparrow\downarrow}_{n\leftarrow 0} + T^{\downarrow\downarrow}_{n\leftarrow 0}\\
T_{k_1\uparrow} &= \sum_{\sigma'} \sum_{1\in \mathrm{I}, n\in \mathrm{O}} T^{\sigma'\uparrow}_{n\leftarrow 1} = \sum_{1\in \mathrm{I}, n\in \mathrm{O}} T^{\uparrow\uparrow}_{n\leftarrow 1} + T^{\downarrow\uparrow}_{n\leftarrow 1}\\
T_{k_1\downarrow} &= \sum_{\sigma'} \sum_{1\in \mathrm{I}, n\in \mathrm{O}} T^{\sigma'\downarrow}_{n\leftarrow 1} = \sum_{1\in \mathrm{I}, n\in \mathrm{O}} T^{\uparrow\downarrow}_{n\leftarrow 1} + T^{\downarrow\downarrow}_{n\leftarrow 1}
\end{aligned} \tag{7.15}$$

and the Python code is presented in L.

7.1.4 Conclusions

We designed a two-dimensional multi-terminal mesoscopic system that works as probabilistic quantum sorter, by identifying a scattering Hamiltonian that separates the eigenstates into multiple output ports. The transmission functions through the system were computed numerically with a C code based on the R-matrix formalism. The results were subsequently compared with Kwant calculations. The input states are qudits with degrees of freedom are defined by the transverse momentum and spin state of the injected electron. The device was optimized by tuning the geometry of the central scatterer. We believe that this approach could also be employed in an experimental realization of the device, where by tuning a top gate potential could facilitate the practical implementation of the QS.

7.2 Topological quantum sorter

7.2.1 Introduction

We have touched on the technological and industry driven demand to produce smaller and smaller electronic device in Section 6.4, where we introduced the two channel nanotransistor. Traditional information processing in electronic devices is done employing the highly popular CMOS (complementary metal oxide semiconductor) architecture, but the challenges that come with scaling these transistors may become insurmountable due to physical constraints. Researchers and engineers alike are searching for device implementations that set a new standard for low power and efficient computing and hence the interest in new categories of materials has increased exponentially in the last years. From this perspective, topological materials are promising candidate due to their exotic properties, that we briefly introduced in Section 2.3. These properties that make topological insulators (TIs) fit for low power transistors, spin filter devices and architectures for quantum computing pave the way for a "post-CMOS" technological revolution [164].

In the previous section, 7.1, we simulated a wide range of candidate systems and took full advantage of the computational resources at our disposal in order to identify an ideal configuration for the quantum sorter prototype device. However, the computational load would be reduced tremendously if one was able to design a quantum sorter that exploits the spin-momentum locking characteristics of TIs. Hence, this section is solely focused on simulations of hybrid trivial and topological systems, modeled by means of the BHZ Hamiltonian.

7.2.2 Model Hamiltonian and Kwant simulations

The quantum transport simulations were performed using the Kwant Python package. The 2D system was created in a similar manner as the probabilistic quantum sorter presented in the previous section, but using library known as *kwant.continuum*, which facilitates the discretization of the Hamiltonian. This library allows the user to write the Hamiltonian as a symbolic expression, specify the symmetry of the lattice and the lattice constant which defines the grid and the discretization is performed automatically. This is a useful approach when we deal with more complicated systems and it is popular for simulations with topological Hamiltonians. In our case, we employed a position dependent BHZ Hamiltonian in order to describe both the trivial and topological regions of the device.

The four band Hamiltonian is implemented in the Python code in the following manner:

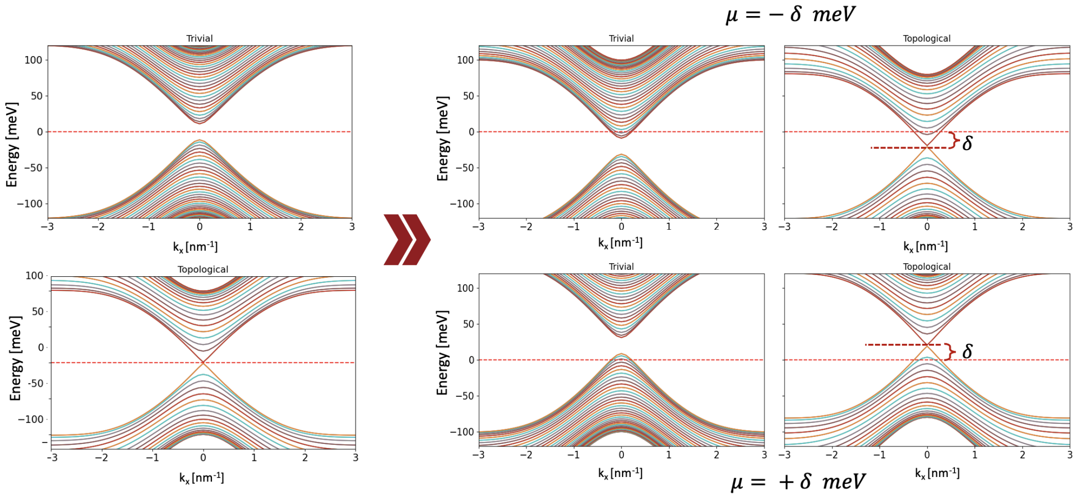

FIGURE 7.11: The effect that a $\pm\delta$ shift of the chemical potential has on the band structure in the trivial (top line) and topological case (bottom line). The red dashed line is set at a reference value of 0 meV.

```
# BHZ hamiltonian

bhz_continuum = '''
    + mu * kron(sigma_0, sigma_0)
    + M * kron(sigma_0, sigma_z)
    - B * (k_x**2 + k_y**2) * kron(sigma_0, sigma_z)
    - D * (k_x**2 + k_y**2) * kron(sigma_0, sigma_0)
    + A * k_x * kron(sigma_z, sigma_x)
    - A * k_y * kron(sigma_0, sigma_y)
    '''
```

Hence, the BHZ Hamiltonian has the form we presented in section 2.3.3:

$$\boldsymbol{H} = \begin{pmatrix} \varepsilon_{\hat{k}} + M(\hat{\boldsymbol{k}}) & A\hat{k}_- & 0 & 0 \\ A\hat{k}_+ & \varepsilon_{\hat{k}} - M(\hat{\boldsymbol{k}}) & 0 & 0 \\ 0 & 0 & \varepsilon_{\hat{k}} + M(\hat{\boldsymbol{k}}) & -A\hat{k}_+ \\ 0 & 0 & -A\hat{k}_- & \varepsilon_{\hat{k}} - M(\hat{\boldsymbol{k}}) \end{pmatrix} \tag{7.16}$$

where $\boldsymbol{k} = (k_x, k_y)$ is the in-plane momentum operator, $\varepsilon_{\boldsymbol{k}} = C - D(k_x^2 + k_y^2)$, $M(k) = M(x,y) - B(k_x^2 + k_y^2)$, $\boldsymbol{k}_\pm = \boldsymbol{k}_x \pm \mathrm{i}\boldsymbol{k}_y$, and A, B, D, and M are parameters describing the band structure of the HgTe/CdTe QWs. We consider the following parameters for the QWs: $A = 364.5\,\mathrm{meV\cdot nm}$, $B = -686\,\mathrm{meV\cdot nm^2}$, $D = 0$, $C = 0$ and $M = +10\,\mathrm{meV}$. The topological phases are distinguished by the signs of parameter M, which in the case of HgTe/CdTe QWs is determined by the width of the heterostructure, as we discussed in 2.3.3. Usually, the parameter D is $-512\,\mathrm{meV\cdot nm^2}$, but we consider $D = 0$ in order to have a band-structure that is symmetric around $E_F = 0$. To account for the effect of the top gate, one has to add a diagonal term:

$$\begin{aligned} \boldsymbol{H} &= \boldsymbol{H}_{\mathbf{BHZ}} + eV_g \boldsymbol{I}_{4\times4} \\ \text{where} \qquad eV_g \boldsymbol{I}_{4\times4} &= \begin{pmatrix} eV_g & 0 & 0 & 0 \\ 0 & eV_g & 0 & 0 \\ 0 & 0 & eV_g & 0 \\ 0 & 0 & 0 & eV_g \end{pmatrix} \end{aligned} \tag{7.17}$$

The wavefunction in a TI system described by the four band BHZ model is a four component spinor $\Psi(x, y)$. The eigenvalue problem is discretized in a square lattice with a constant a, which defines the grid spacing in the x and y directions. The choice for the lattice constant is a trade-off between the computational cost of a finer grid and the accuracy it provides. As we detailed in Section 2.3.3, the discrete Hamiltonian can be written as:

$$\begin{aligned} H^{m,m}_{n,n} &= \left[(eV_g)\sigma_0 \otimes \sigma_0 + M\sigma_z \otimes \sigma_0 - 4\frac{B\sigma_z \otimes \sigma_0}{a^2} \right], \\ H^{m,m}_{n,n+1} &= \left[\frac{B\sigma_z \otimes \sigma_0}{a^2} + \frac{iA\sigma_x \otimes \sigma_0}{2a} \right], \\ H^{m,m+1}_{n,n} &= \left[\frac{B\sigma_z \otimes \sigma_0}{a^2} - \frac{iA\sigma_y \otimes \sigma_0}{2a} \right], \\ H^{m,m}_{n,n-1} &= \left(H^{m,m}_{n,n+1} \right)^\dagger, \\ H^{m,m-1}_{n,n} &= \left(H^{m,m+1}_{n,n} \right)^\dagger. \end{aligned} \tag{7.18}$$

where $\sigma_x, \sigma_y, \sigma_z$ are the Pauli matrices. The discretization procedure employed by Kwant was detailed in section 2.3.3 in Chapter 2.

The effect of the gate potential $\pm eV_g$ on the band-structure is represented in Figure 7.11. In order to interpret the simulation results and highlight the ideal quantum sorter configuration, we compute a set of relevant physical quantities for each proposed system:

- the local density of states
- the spin resolved charge density and the spin polarized current
- the spin and mode resolved transmission functions

Local density of states

The local density of states (LDOS) at site i is defined as:

$$\text{LDOS}(E) = \sum_l |\langle i \mid l \rangle|^2 \delta\left(E - E_l\right), \tag{7.19}$$

where the summation is performed over all electronic eigenstates $|l\rangle$ of the Hamiltonian H with energy E_l. This is evaluated numerically by Kwant using Chebyshev polynomials and the kernel polynomial method. The LDOS of the topological quantum sorter is represented in Figure 7.16.

Charge (Spin) Density and Current

The charge (spin) density is computed similarly to Eq. 7.13, but the projection operator is extended to a four-dimensional Hilbert space:

$$\rho_i(E) = \sum_{\sigma,\sigma'} \psi^\dagger_{i\sigma}(E) P_{\sigma,\sigma'} \psi_{i\sigma'}(E), \tag{7.20}$$

In the equation above we used $P_{x,y,z;\pm} = \frac{1}{2}\left(\sigma_0 \pm \sigma_{x,y,z}\right) \otimes \sigma_0$, defined as the projector operator in the subspace of the $S_{x,y,z}$ states. Explicitly, the charge and current operators are implemented as follows in the code:

```
    # Define current operators in Kwant
J_0 = kwant.operator.Current(sys)
J_x = kwant.operator.Current(sys, np.kron(sigma_x, sigma_0))
J_z = kwant.operator.Current(sys, np.kron(sigma_z, sigma_0))
# up and down spin components
J_up = kwant.operator.Current(sys, np.kron((sigma_0+sigma_z)/2, sigma_0))
J_down = kwant.operator.Current(sys, np.kron((sigma_0-sigma_z)/2, sigma_0))
# +1 and -1 x-components
J_xplus = kwant.operator.Current(sys, np.kron((sigma_0+sigma_x)/2, sigma_0))
J_xminus = kwant.operator.Current(sys, np.kron((sigma_0-sigma_x)/2,
    sigma_0))

# Density operators in Kwant
D_0 = kwant.operator.Density(sys)
D_x = kwant.operator.Density(sys, np.kron(sigma_x, sigma_0))
D_y = kwant.operator.Density(sys, np.kron(sigma_y, sigma_0))
D_z = kwant.operator.Density(sys, np.kron(sigma_z, sigma_0))
# up and down spin components
D_up = kwant.operator.Density(sys, np.kron((sigma_0+sigma_z)/2, sigma_0))
D_down = kwant.operator.Density(sys, np.kron((sigma_0-sigma_z)/2, sigma_0))
# +1 and -1 x-components
D_xplus = kwant.operator.Density(sys, np.kron((sigma_0+sigma_x)/2, sigma_0))
D_xminus = kwant.operator.Density(sys, np.kron((sigma_0-sigma_x)/2,
    sigma_0))
```

7.2.3 TI hybrid systems as ideal spin filters

One can easily model a system composed of a nanowire (1D) and a 2D topological insulator. The edge states in a TI ca be described, in the low energy approximation, by a simple 1D Dirac Hamiltonian:

$$H_{\mathrm{II}} = i\hbar v_F \sigma_z \partial_x \tag{7.21}$$

with $k_x = E/\hbar v_F$, where E is the energy of the injected electron.

The Hamiltonian of the nanowire is:

$$H_{\mathrm{I}} = \left(-\frac{\hbar^2}{2m}\partial_x^2\right)\sigma_0, \tag{7.22}$$

with $k'_x = \sqrt{2mE/\hbar^2}$.

Consider that a pure spin-up state $|\uparrow\rangle$ is injected into the nanowire (denoted as region *I*) and is transmitted into the TI (region *II*). The wavefunction in the two regions separated by a boundary situated at $x = 0$ is:

$$\begin{cases} \Psi_I^{x<0} = e^{+ik_x x}\left|\uparrow\right\rangle + r_\uparrow e^{-ik_x x}\left|\uparrow\right\rangle + r_\downarrow e^{-ik_x x}\left|\downarrow\right\rangle, \\ \Psi_{II}^{x>0} = t_\uparrow e^{+ik'_x x}\left|\uparrow\right\rangle + t_\downarrow e^{-ik'_x x}\left|\downarrow\right\rangle, \end{cases} \tag{7.23}$$

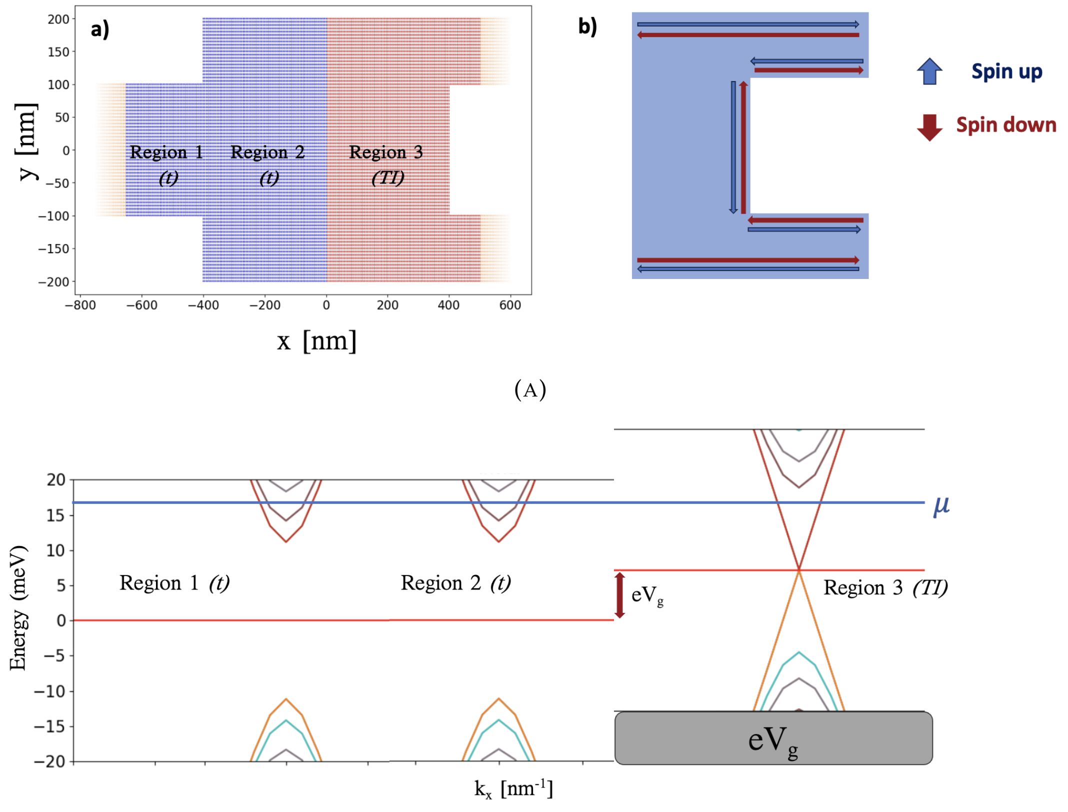

(A)

(B)

FIGURE 7.12: (A) a) Scheme of a t-t-TI junction (trivial material - trivial material - topological material). (b) Helical edge states in the topological region. (B) The bandstuctures of the three regions that compose the hybrid t-t-TI device. A top gate (V_g) shifts the bandstructure in the TI region.

where $|\uparrow\rangle = (1 \quad 0)^T$ and $|\downarrow\rangle = (0 \quad 1)^T$. The reflection and transmission coefficients are determine in a straightforward manner by imposing the well-known boundary conditions:

$$\begin{aligned} \Psi_{\mathrm{I}}|_{x=0_-} &= \Psi_{\mathrm{II}}|_{x=0_+}\,, \\ \partial_x \Psi_{\mathrm{I}}|_{x=0_-} &= \partial_x \Psi_{\mathrm{II}}|_{x=0_+}\,, \end{aligned} \tag{7.24}$$

and we obtain that $r_\downarrow = t_\downarrow = 0$, hence there is no transmission into the spin-down channel. This result is expected, since the TI Hamiltonian commutes with σ_z. This simple model does not fully describe the more complex structures of the multi-terminal systems we propose, but it highlights the potential of hybrid topological insulator-trivial conductor devices to act as ideal spin filters.

The transmission functions are computed in the same manner explained previously in 7.1:

$$T = \sum_{\sigma\sigma'} \sum_{m \in \mathrm{I}, n \in \mathrm{O}} T^{\sigma'\sigma}_{n \leftarrow m} \tag{7.25}$$

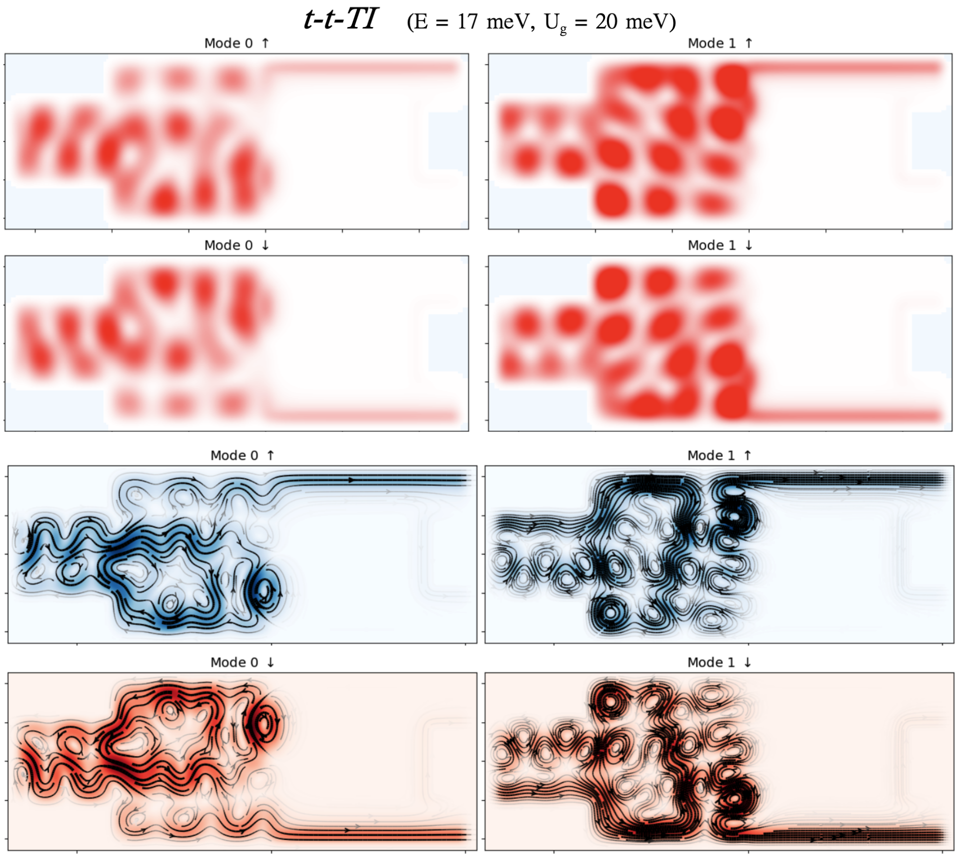

FIGURE 7.13: Representation of the spin and mode resolved wavefunctions and currents in the t-t-TI device. Notice the nearly ideal spin separation induced by the helical edge transport in the topological region.

$$
\begin{aligned}
T_{k_0\uparrow} &= \sum_{\sigma'} \sum_{0\in \mathrm{I}, n\in \mathrm{O}} T^{\sigma'\uparrow}_{n\leftarrow 0} = \sum_{0\in \mathrm{I}, n\in \mathrm{O}} T^{\uparrow\uparrow}_{n\leftarrow 0} + T^{\downarrow\uparrow}_{n\leftarrow 0} \\
T_{k_0\downarrow} &= \sum_{\sigma'} \sum_{0\in \mathrm{I}, n\in \mathrm{O}} T^{\sigma'\downarrow}_{n\leftarrow 0} = \sum_{0\in \mathrm{I}, n\in \mathrm{O}} T^{\uparrow\downarrow}_{n\leftarrow 0} + T^{\downarrow\downarrow}_{n\leftarrow 0} \\
T_{k_1\uparrow} &= \sum_{\sigma'} \sum_{1\in \mathrm{I}, n\in \mathrm{O}} T^{\sigma'\uparrow}_{n\leftarrow 1} = \sum_{1\in \mathrm{I}, n\in \mathrm{O}} T^{\uparrow\uparrow}_{n\leftarrow 1} + T^{\downarrow\uparrow}_{n\leftarrow 1} \\
T_{k_1\downarrow} &= \sum_{\sigma'} \sum_{1\in \mathrm{I}, n\in \mathrm{O}} T^{\sigma'\downarrow}_{n\leftarrow 1} = \sum_{1\in \mathrm{I}, n\in \mathrm{O}} T^{\uparrow\downarrow}_{n\leftarrow 1} + T^{\downarrow\downarrow}_{n\leftarrow 1}
\end{aligned}
\tag{7.26}
$$

To design an optimized quantum sorter, first we analyzed two hybrid systems made of trivial and topological regions, aimed for effective spin and mode separation: a *t-t-TI* system and a *t-constriction-TI* system.

Normal-TI junction

In the case of the probabilistic quantum sorter proposed in section 7.1, successful spin separation was achieved with the aid of the Zeeman field applied to the leads. In practice, this can be created using ferromagnetic leads or magnetic stripes applied on top of the leads to directly control the direction of magnetization. The effective separation of the propagating modes was determined by the central scattering potential, defined by a set of geometrical parameters that we determined mainly through exhaustive high-throughput computing and quantitative observations. However, moving forward, we aimed to explore configurations of devices that could generate spin-polarized currents by exploiting the edge transport of topological insulators. In HgTe-based TIs, the counter-propagating spin states form a Kramers doublet protected by time reversal symmetry, which no backscattering and high spin coherence lengths that are advantageous for information processing.

Firstly, we shall study a hybrid system composed of a trivial conductor region and a TI region, which we denote as *t-t-TI*. The scheme of the system is presented in Figure 7.12a, with dimensions:

$$\text{Leads} = \begin{cases} \text{s=0}, & z \in [-\infty, 650]\ \text{nm}, \quad y \in [-100, 100]\ \text{nm} \\ \text{s=1}, & z \in [500, +\infty]\ \text{nm}, \quad y \in [100, 200]\ \text{nm} \\ \text{s=2}, & z \in [500, +\infty]\ \text{nm}, \quad y \in [-200, -100]\ \text{nm} \end{cases} \tag{7.27}$$

Regions 1 and 2 are described by a trivial BHZ Hamiltonian, the only difference being the width of the two regions which leads to a slight difference in the separation between the transverse bands describing the propagating modes. The TI region (region 3) is highlighted with red in Figure 7.12a and is characterized by a negative M parameter in the four-band Hamiltonian (as discussed in section 2.3.3). In Figure 7.12a (b) we highlighted the trademark characteristic of thee TI system, an insulating bulk with helical spin states that travel in clockwise and anti-clockwise directions, respectively. This unique property also stands at the core of the almost ideal spin polarization and separating in the outgoing terminals denoted by R_1 and R_2.

At thermal equilibrium, the chemical potential in all three regions stabilizes at the same value. However, if the chemical potential is not in the bulk gap of the TI, the characteristic edge transport does not emerge. The purpose of the gate potential is therefore to tune the chemical potential such that the incoming states from the trivial region are transmitted into the helical edge states in the TI region (as suggested in Figure 7.12b). As one can see in Figure 7.13, the spin currents are symmetrical in the two output leads, but they exhibit opposite spin polarization. Due to this result, a *t-t-TI* 2D system can be employed as a spin filter and, also, as a spin separator. A similar setup was proposed in [165], and the authors reached a similar conclusion.

Normal-constriction-TI junction

In the setup described above, the first and second transverse modes are not selectively transmitted into the output leads. In order to control the transversal mode that is transmitted into the TI region, we propose a device comprised of a trivial region connected to another trivial region of lower width (a constriction) and continuing into the topological region. The system is presented in Figure 7.14a and the leads have the same dimensions as in the case of the *t-t-TI* system:

$$\text{Leads} = \begin{cases} \text{s=0}, & z \leq -650\ \text{nm}, \quad y \in [-100, 100]\ \text{nm} \\ \text{s=1}, & z \geq 500\ \text{nm}, \quad y \in [100, 200]\ \text{nm} \\ \text{s=2}, & z \geq 500\ \text{nm}, \quad y \in [-200, -100]\ \text{nm} \end{cases} \tag{7.28}$$

The constriction in the middle region has a width of 100 nm. The spin charge density is represented in Figure 7.14b.

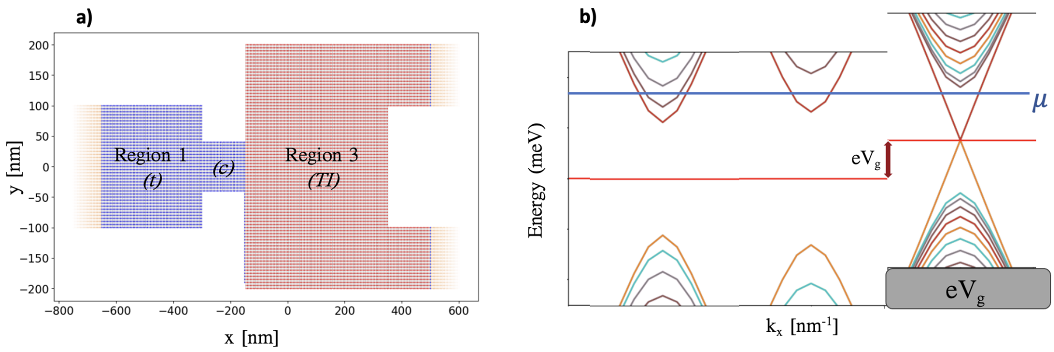

(A) (a)Scheme of the t-c-TI device (trivial-constriction-topological). The orange regions represent the semi-infinite leads, the blue shaded regions correspond to materials with trivial bandstructures and the red region indicates the presence of a TI. (b) The effect of the top-gate on the bandstructure of the TI.

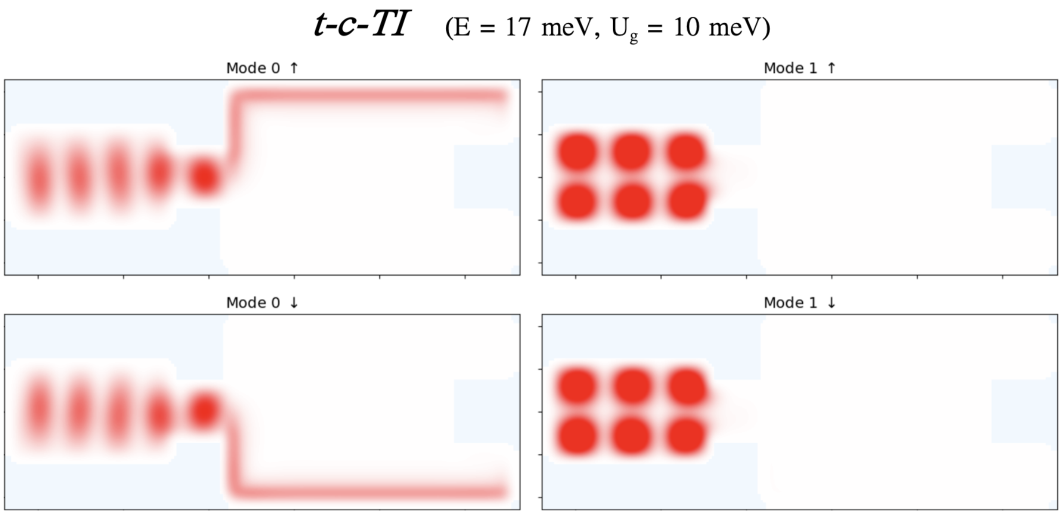

(B)

FIGURE 7.14: Mode and spin-resolved wavefunctions in the 2D t-c-TII device. The constriction does not allow for the transmission of higher energy modes, while the TI region ensures ideal spin selectivity. The wavefunctions (absolute value square) are computed at an energy $E = 17$ meV and the top-gate on the TI region induces an energy shift of $U_g = 10$ meV.

7.2.4 Model system of a topological quantum sorter

With these considerations in mind, we simulated the optimized model of a 2D multi-terminal system comprised of one input lead and four output leads (the same approach as the trivial probabilistic quantum sorter), but the central region of the device is a material that exhibits the characteristics of a topological insulator. The device is displayed in Figure 7.15(a), where:

$$\text{Leads} = \begin{cases} \text{s=0}, & z \leq -650 \text{ nm}, \quad y \in [-100, 100] \text{ nm} \\ \text{s=1}, & z \geq 500 \text{ nm}, \quad y \in [300, 400] \text{ nm} \\ \text{s=2}, & z \geq 500 \text{ nm}, \quad y \in [100, 200] \text{ nm} \\ \text{s=3}, & z \geq 500 \text{ nm}, \quad y \in [-200, -100] \text{ nm} \\ \text{s=4}, & z \geq 500 \text{ nm}, \quad y \in [-400, -300] \text{ nm} \end{cases} \tag{7.29}$$

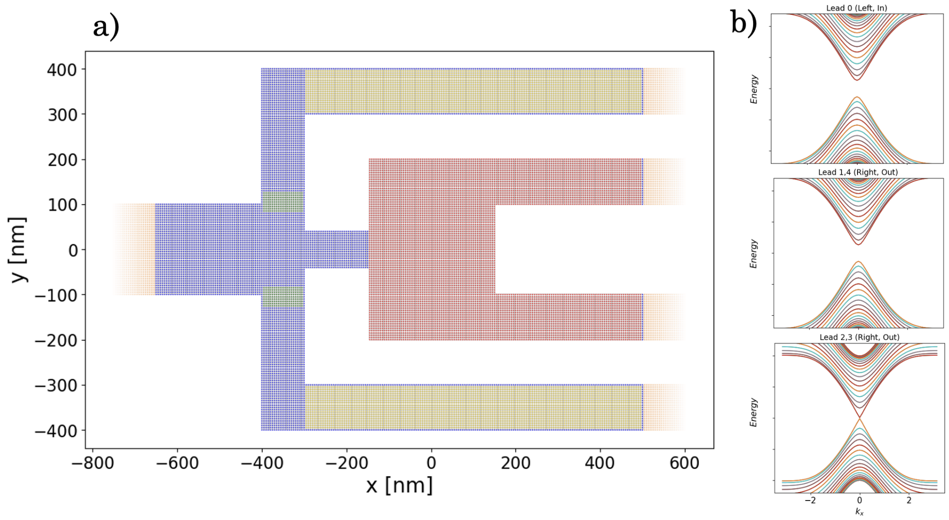

FIGURE 7.15: (a) The proposed scheme of the topological quantum sorter, with one incoming lead and four ourput ports. The red shaded region indicates a topological material, while the blue regions exhibit trivial bandstructures. The yellow regions indicate the presence of magentic barriers that induce a Zeeman term that separates the energy dispersion brances of up/down projections of the spin along the z direction. The green regions represent two barriers induced by top-gates that reduce the transmission probability of lower-energy electrons in the outer leads. (b) The bandstructures of the five leads, where leads 2 and 3 are topological.

The central region is cut from a rectangular area with $z \in (-650, 500)$ nm and $y \in (-400, 400)$ nm. The blue shaded region in Figure 7.15 denotes a trivial material, the red highlighted part represents the topological part of the system and the yellow region indicate the effect of a magnetic polarization that would facilitate the spin separation. In Figure 7.15 (b), we represented the band structures of the input lead (first row), the first and fourth leads (trivial band structure) and the middle leads (topological band structure). Notice that for the middle leads we have the defining zero energy propagating helical edge states that exhibit spin-momentum locking. Our approach was to exploit this robust edge states in order to separate the lowest energy propagating mode from the second transverse mode.

```
# BHZ hamiltonian

bhz_continuum = '''
    + mu * kron(sigma_0, sigma_0)
    + M * kron(sigma_0, sigma_z)
    - B * (k_x**2 + k_y**2) * kron(sigma_0, sigma_z)
    - D * (k_x**2 + k_y**2) * kron(sigma_0, sigma_0)
    + A * k_x * kron(sigma_z, sigma_x)
    - A * k_y * kron(sigma_0, sigma_y)
    + Delta * Gamma_so
    + pol*(kron(vx*sigma_x + vz*sigma_z + vy*sigma_y, sigma_0))
    '''
```

The position dependent parameters (of the scattering region) are:

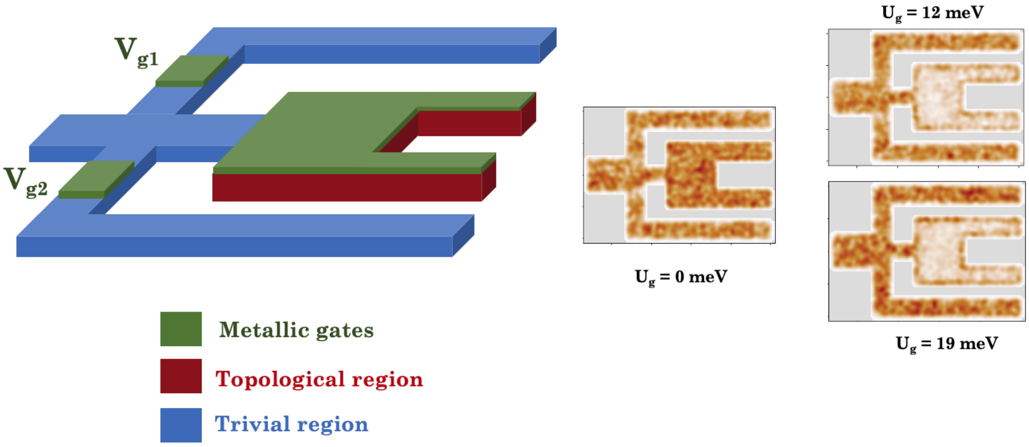

FIGURE 7.16: Right: A 3D scheme of the topological quantum sorter. Left: The local density of states in three cases, $U_g = 0$ meV (b)$U_g = 12$ meV (c) $U_g = 19$ meV with the respective local density of states in the central region. Notice that for $U_g \in [12, 19]$ meV there is helical edge transport in the TI region.

$$V(x,y) = \begin{cases} eV_{g1}, & \text{if } (x,y) \in \mathcal{G}_1 \\ eV_{g2}, & \text{if } (x,y) \in \mathcal{G}_2 \\ eV_g, & \text{if } (x,y) \in \mathcal{R} \\ 0, & \text{elsewhere} \end{cases} \tag{7.30}$$

$$M(x,y) = \begin{cases} 10\,\text{meV}, & \text{if } (x,y) \in \mathcal{B} \\ -10\,\text{meV}, & \text{if } (x,y) \in \mathcal{R} \end{cases} \tag{7.31}$$

where the regions $\mathcal{G}_1, \mathcal{G}_2, \mathcal{R}, \mathcal{B}$ are the regions highlighted in Figure 7.15. A schematic illustration of the device we simulated is shown in Figure 7.16. Two top gates are deposited onto the upper and lower terminals of the cross junction where the incoming electrons are injected (denoted with V_{g1} and V_{g2}), in order to decrease the probability that lower energy particles propagate into the marginal leads. Also, another gate on top of the topological region is inserted to control the chemical potential and induce a band shift. The goal of this setup is to modulate the band alignment in a manner that makes the lowest mode from the trivial input terminal to propagate as a chiral helical edge state along the margins of the topological region. Due to the spin separation in the SQHE phase, the spin degrees of freedom are transmitted into separate output leads without the influence of external magnetic fields. The influence that a positive/negative voltage on the top gates has on the bands of a topological insulator is displayed in Figure 7.11.

In equations 7.32 listed below, we exemplify the discretized Hamiltonian of the BHZ model in the case of an external perpendicular magnetic field (case (a)) and in the simpler case where we consider the influence of a magnetic barrier which controls the spin polarization of the charge carriers. A magnetic field that is perpendicular to the plane of the quantum well, $\mathbf{B}_z = B\mathbf{e}_z$, will affect the transport properties by means of the Zeeman and orbital terms. The Zeeman term will lift the degeneracy of spin polarized bands and it is introduced as a diagonal term $\mu_B B_z \Sigma_z/2$, where $\Sigma_z = \text{diag}(g_e, g_e, -g_h, -g_h)$. This accounts for the fact that electrons and holes have

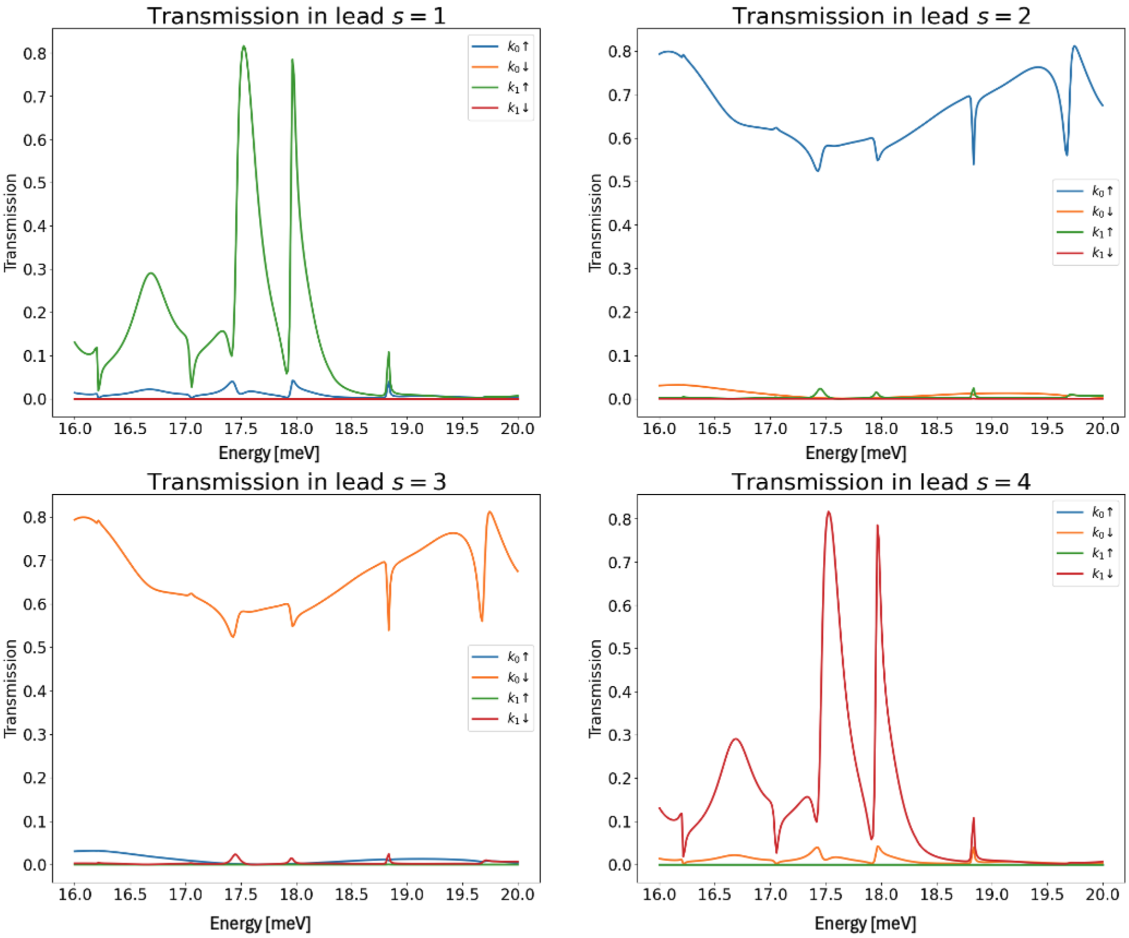

FIGURE 7.17: Spin and mode resolved transmission functions for the quantum sorter proposed in Figure 7.15.

different effective g-factors. The orbital effect of a magnetic field is introduced in the tight binding model by means of the Peierls phase which modifies the hopping terms between adjacent sites. The Peierls substitution is defined in terms of the line integral of the potential vector, namely $e/\hbar \int d\boldsymbol{l} \cdot \boldsymbol{A}$. In the Landau gauge, for example, the vector potential is $\mathbf{A}(\mathbf{r}) = -B_z y \mathbf{e_x}$ and the hopping matrix elements between sites (n, m) and (n, m+1) will be affected.

In our model for the quantum sorter, we considered that magnetic barriers placed along the outer leads will modify the spin polarization and ensure the transmission of spin up/down electrons in leads s_1 and s_4. We consider, in this particular case, that the magnetic barrier polarizes the spin along the **z** direction, since S_z is a good quantum number for the edge states in the BHZ model, due to the symmetry of the Hamiltonian. Therefore, the term $\boldsymbol{\mathcal{P}\sigma} = \mathcal{P}_x\sigma_x + \mathcal{P}_y\sigma_y + \mathcal{P}_z\sigma_z$ reduces to $\mathcal{P}_z\sigma_z$, where $\mathcal{P}_z$ is a position dependent parameter with positive/negative values in leads $s = 1$ and $s = 4$, respectively.

The spin and mode resolved transmission functions in each of the four output leads are represented in Figure 7.17. The four states are selectively transmitted with high probability into only one particular output port, meeting the main criteria of the probabilistic quantum sorter we proposed. These results are also robust to slight modifications in the geometry and also to weak disorder, which leads to a more stable device from the perspective of experimental realization.

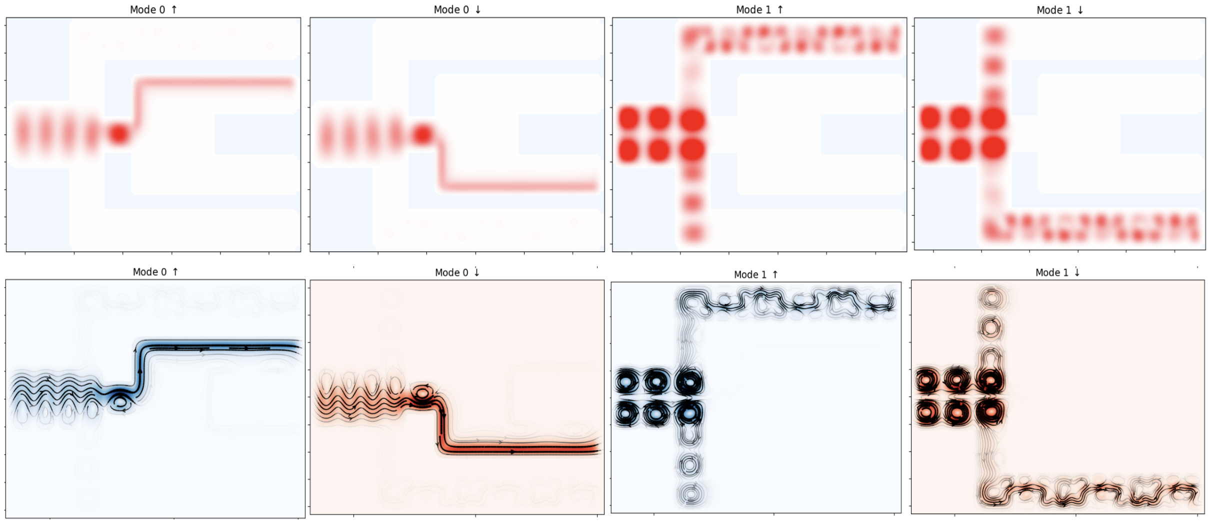

FIGURE 7.18: Wavefunctions and currents of the four incoming modes for the quantum sorter prototype described in Figure 7.15

a) Perpendicular magnetic field **b) Magnetic barrier**

$$\begin{array}{lcl}
H^{m,m}_{n,n} = \left[M\sigma_z \otimes \sigma_0 - 4\dfrac{B\sigma_z \otimes \sigma_0}{a^2} + \underbrace{\dfrac{\mu_B B_z \Sigma_z}{2}}_{\textbf{Zeeman}} \right] & \Rightarrow & H^{m,m}_{n,n} = \left[M\sigma_z - 4\dfrac{B\sigma_z}{a^2} + \boldsymbol{\mathcal{P}}\boldsymbol{\sigma} \otimes \sigma_0 \right] \\
H^{m,m}_{n,n+1} = \left[\dfrac{B\sigma_z \otimes \sigma_0}{a^2} + \dfrac{iA\sigma_x \otimes \sigma_0}{2a} \right] \underbrace{e^{ima^2(eB/\hbar)}}_{\textbf{Peierls}} & \Rightarrow & H^{m,m}_{n,n+1} = \left[\dfrac{B\sigma_z \otimes \sigma_0}{a^2} + \dfrac{iA\sigma_x \otimes \sigma_0}{2a} \right] \\
H^{m,m+1}_{n,n} = \left[\dfrac{B\sigma_z \otimes \sigma_0}{a^2} - \dfrac{iA\sigma_y \otimes \sigma_0}{2a} \right] & \Rightarrow & H^{m,m+1}_{n,n} = \left[\dfrac{B\sigma_z \otimes \sigma_0}{a^2} - \dfrac{iA\sigma_y \otimes \sigma_0}{2a} \right] \\
H^{m,m}_{n,n-1} = \left(H^{m,m}_{n,n+1} \right)^{\dagger} & \Rightarrow & H^{m,m}_{n,n-1} = \left(H^{m,m}_{n,n+1} \right)^{\dagger} \\
H^{m,m-1}_{n,n} = \left(H^{m,m+1}_{n,n} \right)^{\dagger} & \Rightarrow & H^{m,m-1}_{n,n} = \left(H^{m,m+1}_{n,n} \right)^{\dagger} .
\end{array} \tag{7.32}$$

Another rendition of the device is presented in 7.19a. All the relevant parameters are maintained, but the first and fourth output leads are perpendicular to the transport direction. In this configuration, the energy range for which the system exhibits quantum sorter functionality is increased, since shorter propagation distances in the trivial regime also imply less scattering and higher transmission probabilities. These devices also have high functionality for spin selectivity (see Figure 7.20), which is a crucial element in the field of spintronics. For this reason, HgTe-based topological insulators are considered to be promising candidates for spintronic devices. Another advantage is that, as opposed to the Datta-Das spin transistor, they do not rely on Rashba SOI to control charge flow, hence there is no spin relaxation induced by the interfacial effects that arise in a heterostructre device.

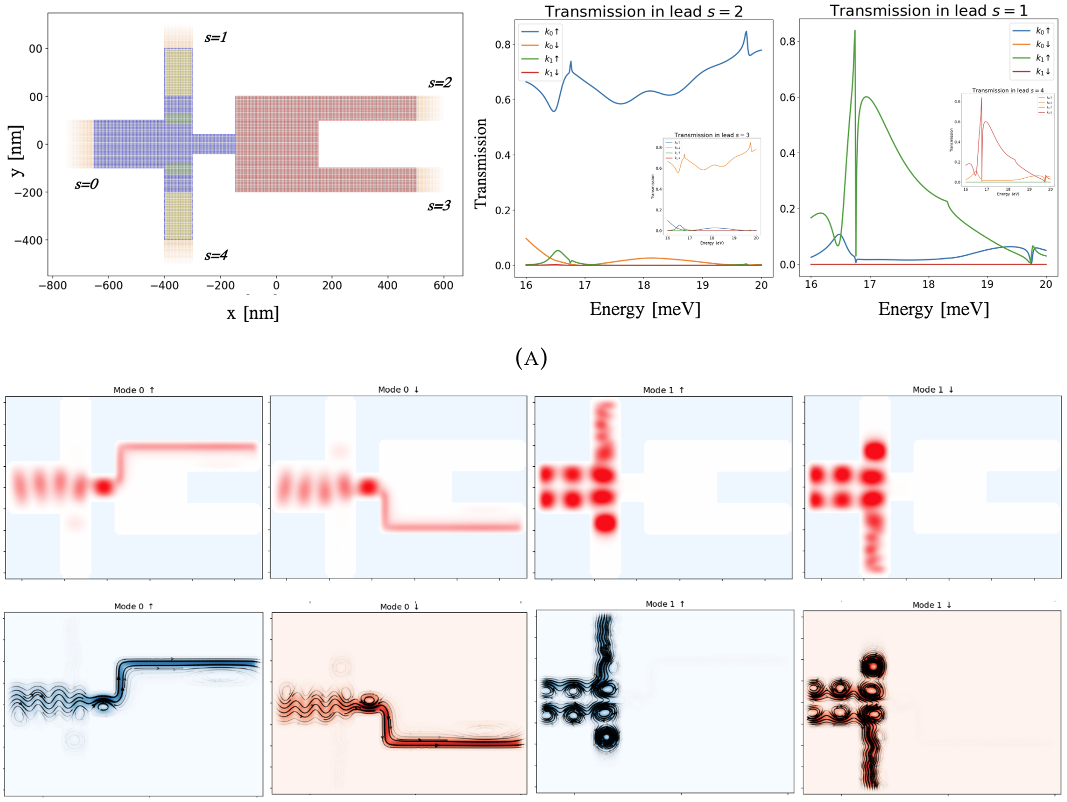

(A)

(B)

FIGURE 7.19: (A) Model device of a quantum sorter with different output leads configuration and the corresponding spin and mode resolved transmission functions. (B) The wavefunctions and currents in the device proposed in subfigure (A).

7.2.5 Conclusions

We aimed to exploit the helical edge channel transport of TIs, robust against scattering and disorder, in order to propose a quantum sorter with improved performance. In a 1D QSHE (quantum spin Hall effect) system, the helical edge states emerge when the Fermi energy lies in the bulk gap. In order to find the set of V_g that optimize the transmission of the incoming states into the topological bulk gap, we compute the local density of states in the scattering region. The spin charge density and current of the topological quantum sorter for a set of top gate values (namely $U_g = 12$ meV and $U_{g1,g2} = 10$ meV) are represented in Figure 7.18. Our topological quantum sorter proposal relies on an electrical operation by electrostatic gates on a hybrid system composed of trivial and topological regions that is able to select with a high level of efficiency the incoming spin resolved transverse modes and sort them into separate output leads. With the aid of electrostatic gates, the edge transport of the TI material can be employed for quantum information applications.

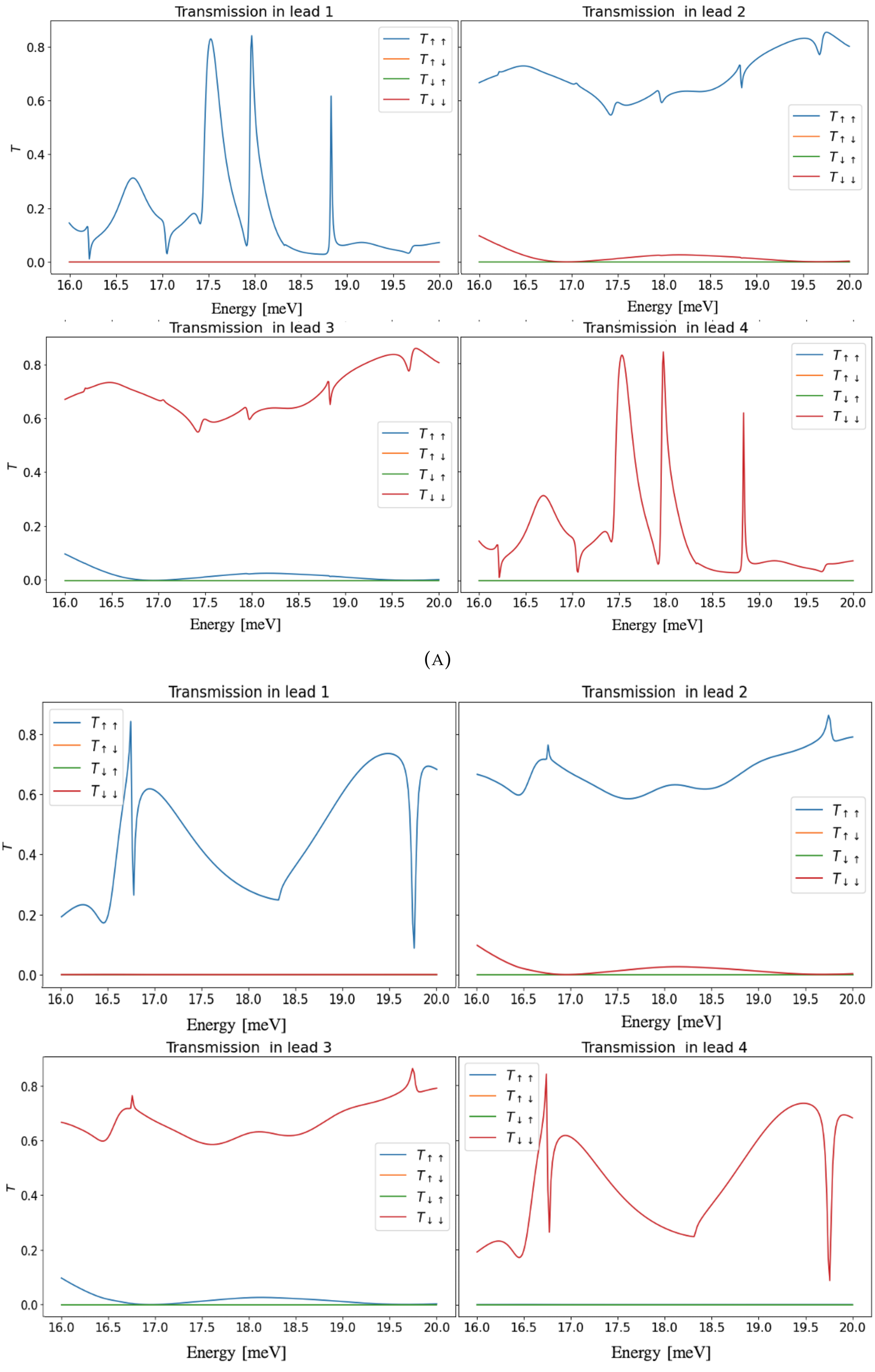

(A)

(B)

FIGURE 7.20: Spin resolved transmissions for the topological quantum sorter prototypes in Figure 7.19a (A) and Figure 7.15 (B)

8

Summary and conclusions

The first part of the thesis focused on introducing the fundamental theoretical concepts that are employed in quantum transport and also outlined the main approximation methods and simulation tools that we employed throughout this work. My goal was to present essential theoretical formalisms, such as the Landauer-Buttiker approach and the non-equilibrium Green's functions method in a pedagogical yet fairly rigorous manner. Also, all the computational methods that were employed in this thesis were presented thoroughly in the first chapters, ranging from the well-known density functional theory to the R-matrix theory, which has not been widely used up until to this point, but has notable advantages. Since in our work we coupled the conventional simulation tools with machine learning techniques, I also introduced the widely used ML methods based on artificial neural networks. Throughout the theoretical part of the thesis, applications of the methods that were discussed have also been presented. To exemplify the use of such simulation tools and ML techniques, I presented original results obtained by working alongside the computational physics group from IFIN-HH.

The second part of the thesis introduces in more detail the work done with regards to quantum transport in low-dimensional quantum systems, with the focus on devices that could bring advancements to the field of quantum information processing. The results are partitioned in a manner that highlights the research process, starting from simpler many-body systems and moving on to multi-terminal configurations that have great potential to be integrated in spintronic devices, a new class of nanotransistors for low energy applications and quantum information technologies.

Firstly, we briefly reviewed the original results in [3], where we presented an extension of the R-matrix formalism towards bi-particle scattering problems. The two particles are identical fermions that interact with each-other only inside the boundaries of the scattering region. When at least one particle is in the leads, the two particles do not interact with each-other. In the case when at least one particle is in the central region, the two-particle eigenfunctions of the Hamiltonian are written as a linear combination of antisymmetrized products of two single-particle eigenstates of the Hamiltonian that describes the whole device. These combinations involve several single-particle eigenstates, entangled because of the interaction in the scattering region. The Ansatz that was proposed is crucial for describing entangled states in the multi-particle scattering problem, which is a essential for applications in the realm of quantum information technology.

Then, we move towards more computationally oriented research that focuses on two-dimensional systems. We started our study of low-dimensional devices by solving a large class of two-electron problems based on a quantum dot system, controlled by a top-gate array [110]. The energy spectra of the quantum systems were directly determined by both external and material dependent factors: the binary valued gate voltages and the strength of the Coulomb interaction. Using the exact diagonalization technique, we solve the bi-particle problem with high accuracy and obtained also the charge and spin densities, alongside the energy spectra. Coupled with ML algorithms based on artificial neural networks, the approach we explored in [110] can assist the design process of novel low-dimensional quantum devices. The methods can be extended to systems where the exhaustive computation of the many-body states is computationally unfeasible. Moreover, we investigated periodic systems and reproduced the band structure of the Lieb lattices. This points towards a direction of highly tunable devices, that are easily connected to experimental structures. Through the variation of relevant parameters, such as the depth of the potential wells, their shape and positions on the grid, we can modify the bandgaps, as well as the bandwidths of the energy bands. We showed that, by modifying the shape of the quantum wells, the band structure can be adjusted to a Kagome-like lattice. Again, we employed machine learning techniques, namely artificial neural networks, to predict the bandwidth of the middle energy band with good accuracy.

Furthermore, we also explored 2D devices in the form of neuromorphic device structures, described in the framework of the many-body formalism coupled with cGAN based image-to-image translation approaches [117]. We proposed a two-dimensional reconfigurable device, suitable to optimize the design process of neuromorphic systems and also function as reprogrammable multi-terminal system for charge transfer between quantum dot registers. Since assessing the charge distribution of a multi-particle system along with the switching properties is a difficult task from a computational perspective, the optimization process requires a large number of configurations to be analyzed. This is where machine learning techniques could bring significant advantages.

Also, we studied the transport properties of field effect nanotransistor devices based on lateral resonant tunneling between two parallel conduction channels. We found narrow resonant tunneling peaks around zero control voltage, allowing for the switching of the drain current with small control voltages and opening up the way to low-energy applications. The simulation results, carried out within the R-matrix and tight binding formalisms, aligned with the theoretical results presented in detail in [119]. Through a joint computational and theoretical study we provided an in-depth understanding of the tunneling process that dominates the transport properties of the two-channel nanotransistor.

In the last chapter of the results section, we discussed a 2D mesoscopic system that works as probabilistic quantum sorter. By choosing an appropriate scattering Hamiltonian, the device separates the eigenstates into multiple output ports. In order to compute the spin and mode resolved transmission functions, we used the R-matrix formalism for multi-terminal transport and also compared the results with Kwant simulations. The input states are described as qudits with four degrees of freedom, defined by their transverse momentum and the spin component. A tunable geometrical parameter defines the scattering potential and the QS was optimized in terms of this chosen parameter by means of high throughput computations. We believe this approach can be employed as a means to a practical realization of such a device. Our study paves the way for further designing of quantum devices that enables a desired mode-lead pairing in the output ports and could function as a solid state device for efficient quantum state identification. We extended this proposal to more exotic systems, based on two-dimensional topological insulators described in the framework of the BHZ model. Such a topological quantum sorter provides an even better spin-mode separation and could even function as an almost ideal spin filter. This 2D system exploits the characteristic properties of TIs, namely the spin-momentum locking of the robust edge states, protected by time-reversal symmetry.

The research introduced in this thesis aims to present new insights into an effective device modeling paradigm that exploits complementary numerical methods of quantum transport in tandem with machine learning techniques. Spin and charge manipulation, control of the electronic wavefunction and an in depth understanding of the quantum mechanical phenomena that govern transport in low dimensional systems are essential for effective inverse design of novel devices. We believe that the approach we highlighted throughout this thesis, that integrates advanced computational methods with machine learning techniques in order to gather crucial physical insights could lead to the design of low dimensional systems with multiple applications in quantum information technologies.

A

Derivation of the Kohn-Sham equations

We have seen in section 3.1 that in the Kohn-Sham approach the electrons density is given by the non-interacting KS orbitals:

$$n(\mathbf{r}) = \sum_{i=1}^{N} |\phi_i(\mathbf{r})|^2, \tag{A.1}$$

and that the total energy is a functional of the ground state density:

$$E_{\mathrm{KS}}[n] = 2\sum_{i=1}^{N} \int \phi_i^*(\mathbf{r}) \left(-\frac{1}{2}\nabla^2\right) \phi_i(\mathbf{r}) d\mathbf{r} + E_H[n] + E_{\mathrm{ext}}[n] + E_{\mathrm{xc}}[n] \tag{A.2}$$

We also mentioned that, in accordance with the variational principle, we need to minimise the energy with respect to the (ground state) density to find the ground state energy. Also, we need to conserve the orthonormality of the Kohn Sham orbitals, so we have to solve a minimisation problem with constraints. To this end, we employ the method of the Lagrange multipliers, and the expression that we have to minimize is:

$$\Omega_{\mathrm{KS}}[n] = E_{\mathrm{KS}}[n] - \sum_{i,j} \epsilon_{ij} \left(\int \phi_i^*(\mathbf{r})\phi_j(\mathbf{r}) d\mathbf{r} - \delta_{ij} \right) \tag{A.3}$$

We use the chain rule to calculate the derivative of the energy functional with respect to the KS orbitals:

$$\frac{\delta \Omega_{\mathrm{KS}}[n]}{\delta \phi_j^*(\mathbf{r})} = \frac{\delta \Omega_{\mathrm{KS}}[n]}{\delta n(\mathbf{r})} \frac{\partial n(\mathbf{r})}{\partial \phi_j^*(\mathbf{r})} \tag{A.4}$$

From equation A.1, we know that:

$$\frac{\partial n(\mathbf{r})}{\partial \phi_j^*(\mathbf{r})} = 2\phi_j(\mathbf{r}) \tag{A.5}$$

Hence,

$$\frac{\delta\Omega_{\text{KS}}[n]}{\delta\phi_j^*(\mathbf{r})} = \frac{\delta\Omega_{\text{KS}}[n]}{\delta n(\mathbf{r})} 2\phi_j(\mathbf{r}) \tag{A.6}$$

Using the formula for the energy E_{KS} and the fact that the orbitals that minimize it must satisfy the condition:

$$\frac{\delta\Omega_{\text{KS}}[n]}{\delta\phi_j^*(\mathbf{r})} = 0, \tag{A.7}$$

we can write the following equation:

$$0 = \frac{\delta E_{kin}^{non}}{\delta\phi_i^*(\mathbf{r})} + \left[\frac{\delta E_{\text{ext}}}{\delta n(\mathbf{r})} + \frac{\delta E_H}{\delta n(\mathbf{r})} + \frac{\delta E_{xc}}{\delta n(\mathbf{r})}\right] \frac{\delta n(\mathbf{r})}{\delta\phi_i^*(\mathbf{r})} - \sum_j \varepsilon_{ij}\phi_j(\mathbf{r}) \tag{A.8}$$

Now we can use the following equalities:

$$\frac{\delta E_{kin}^{non}}{\delta\phi_i^*(\mathbf{r})} = -\nabla_i^2\phi_i(\mathbf{r}) \quad \text{and} \quad U_{xc}[n(\mathbf{r})] = \frac{\delta E_{xc}[n(r)]}{\delta n(\mathbf{r})} \tag{A.9}$$

along with equations A.5 and A.6. We obtain the following system:

$$\begin{aligned} \left(-\frac{1}{2}\nabla_i^2 + U_{ext} + U_H + U_{xc} - \lambda_i\right)\phi_i(\mathbf{r}) = 0 \\ \left(-\frac{1}{2}\nabla_i^2 + U_{eff} - \varepsilon_i\right)\phi_i(r) = 0 \\ \Rightarrow \left[-\frac{1}{2}\nabla_i^2 + U_{eff}(\mathbf{r})\right]\phi_i(\mathbf{r}) = \varepsilon_i\phi_i(\mathbf{r}) \\ \rightarrow \hat{H}_{KS}\phi_i(\mathbf{r}) = \varepsilon_i\phi_i(\mathbf{r}) \end{aligned} \tag{A.10}$$

As a last observation, formally speaking the Lagrange multiplier ε_{ij} can be identified as energies of the orbitals only after diagonalization of ϕ_i with a unitary transformation. However, we can simply replace them with ε_i intuitively, since equations A.10 make sense as Schrodinger equations only in this case [30, 32].

B

Bond current and the total current

Todorov [42] defined a projector operator

$$P_n = \sum_{\gamma} |\phi_{n\gamma}\rangle \langle\phi_{n\gamma}| , \tag{B.1}$$

and the expectation value of the projector is interpreted as the charge of the atom at site n:

$$q_n(t) = e \langle\psi(t)\, |P_n|\, \psi(t)\rangle \tag{B.2}$$

The rate of change of the charge is net current flux flowing from all the neighboring sites into n. We can write [1]:

$$\frac{\mathrm{d}q_n(t)}{\mathrm{d}t} = \frac{e}{\mathrm{i}\hbar} \langle\psi(t)\, |[P_n, H]|\, \psi(t)\rangle \tag{B.3}$$

Todorov identified here the operaator J_n

$$J_n = \frac{e}{\mathrm{i}\hbar}[P_n, H] = \frac{1}{\mathrm{i}\hbar}\sum_{n'}[P_n H P_{n'} - P_{n'} H P_n]$$

and then defined the quantity

$$J_{n',n} = \frac{e}{\mathrm{i}\hbar}[P_n H P_{n'} - P_{n'} H P_n] \tag{B.4}$$

as the current flowing from site n to site n', or the bond current [2].

The net current flowing across the system requires us to compute the current flowing through a particular cross section of the device, which is a sum of all the bond currents:

---

[1] The density-matrix analogue of the Schrödinger equation

$$i\hbar\frac{\partial\hat{\rho}}{\partial t} = [\hat{H}, \hat{\rho}], \quad \text{where} \quad \hat{\rho} = |\Psi\rangle\langle\Psi|$$

[2] This particular equation is only valid in the case of an orthogonal basis, since it implies overlap between neighboring sites and it becomes more difficult to define the rate of change in the charge

$$J_S = \frac{e}{\mathrm{i}\hbar} \sum_{n' \in L, n \in R} J_{n',n}, \tag{B.5}$$

The observed value is evaluated as a statistical expectation value:

$$\begin{aligned} I_{n'n} &= \operatorname{Tr}\left\{J_{n'n} \rho\left(V_{\text{bias}}\right)\right\}, \\ J_S &= \operatorname{Tr}\left\{J_S \rho\left(V_{\text{bias}}\right)\right\}. \end{aligned} \tag{B.6}$$

where $\rho(V_bias)$ is the density matrix which depend on the bias voltage. In a lead-device-lead system, the density matrix can be defined as:

$$\rho\left(V_{\text{bias}}\right) = \int \left[f_1(E) D_1(E) + f_2(E) D_2(E)\right] \mathrm{d}E, \tag{B.7}$$

The partial density operators are[3]:

$$\begin{aligned} D_1(E) &= \sum_1 \left|\psi_1\right\rangle \delta\left(E - E_1\right)\left\langle\psi_1\right| \\ D_2(E) &= \sum_2 \left|\psi_2\right\rangle \delta\left(E - E_2\right)\left\langle\psi_2\right| \end{aligned} \tag{B.8}$$

The total density of stayes can be written in terms of the Green's functions of the system:

$$D(E) = \frac{\mathrm{i}}{2\pi}\left[G^{\mathrm{r}} - G^{\mathrm{a}}\right] \tag{B.9}$$

This is also related to the spectral function:

$$\begin{aligned} A(E) &= i\left(G^r(E) - G^a(E)\right) \\ &= 2\pi \sum_n \left|\Psi_n(E)\right\rangle\left\langle\Psi_n(E)\right| \\ &= 2\pi D(E) \end{aligned} \tag{B.10}$$

---

[3] The partial density opertors are associated to the incoming states from lead 1 and from lead 2 respectively

C

Tight binding model for the Lieb lattice

C.1 Tight binding formalism in Dirac notation

The time-independent Schrödinger equation for the lattice:

$$H|\psi\rangle = E|\psi\rangle, \tag{C.1}$$

where we write $|\psi\rangle$ using the Bloch Ansatz:

$$|\psi\rangle = \sum_{\mathbf{R}'_{\alpha'}} c_{\alpha'} e^{i\mathbf{k}\cdot\mathbf{R}'} \left|\mathbf{R}'_{\alpha'}\right\rangle . \tag{C.2}$$

Substituting equation C.2 into the Schrödinger equation, we obtain:

$$H \sum_{\mathbf{R}'_{\alpha'}} c_{\alpha'} e^{i\mathbf{k}\cdot\mathbf{R}'} \left|\mathbf{R}'_{\alpha'}\right\rangle = \sum_{\mathbf{R}'_{\alpha'}} c_{\alpha'} e^{i\mathbf{k}\cdot\mathbf{R}'} H \left|\mathbf{R}'_{\alpha'}\right\rangle = E \sum_{\mathbf{R}'_{\alpha'}} c_{\alpha'} e^{i\mathbf{k}\cdot\mathbf{R}'} \left|\mathbf{R}'_{\alpha'}\right\rangle . \tag{C.3}$$

We then project the state $\langle \mathbf{R}_\alpha|$ onto the eigenvalue problem above:

$$\sum_{\mathbf{R}'_{\alpha'}} c_{\alpha'} e^{i\mathbf{k}\cdot\mathbf{R}'} \langle \mathbf{R}_\alpha| H \left|\mathbf{R}'_{\alpha'}\right\rangle = E \sum_{\mathbf{R}'_{\alpha'}} c_{\alpha'} e^{i\mathbf{k}\cdot\mathbf{R}'} \left\langle \mathbf{R}_\alpha \mid \mathbf{R}'_{\alpha'}\right\rangle . \tag{C.4}$$

Next, we write the Hamiltonian H as the sum of an isolated atomic Hamiltonian and a potential term in the form

$$H = H^{\text{at}}_{\mathbf{R}_\alpha} + \Delta U_{\mathbf{R}_\alpha}.$$

where the atomic Hamiltonian obeys the eigenvalue relation

$$H^{\text{atom}}_{\mathbf{R}_\alpha} \left|\mathbf{R}_\alpha\right\rangle = E^{at}_\alpha \left|\mathbf{R}_\alpha\right\rangle$$

We then substitute this Hamiltonian into Equation C.4:

$$\sum_{\mathbf{R}'_{\alpha'}} c_{\alpha'} e^{i\mathbf{k}\cdot\mathbf{R}'} \left(E^{\text{atom}}_\alpha \left\langle \mathbf{R}_\alpha \mid \mathbf{R}'_{\alpha'}\right\rangle + \langle \mathbf{R}_\alpha| \Delta U_{\mathbf{R}_\alpha} \left|\mathbf{R}'_{\alpha'}\right\rangle\right) = E \sum_{\mathbf{R}'_{\alpha'}} c_{\alpha'} e^{i\mathbf{k}\cdot\mathbf{R}'} \left\langle \mathbf{R}_\alpha \mid \mathbf{R}'_{\alpha'}\right\rangle$$

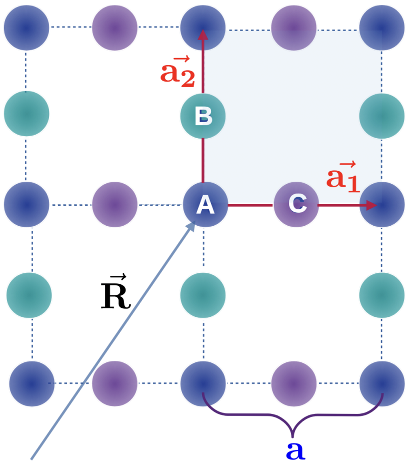

FIGURE C.1: Structure of the Lieb lattice, with a three-atom basis. The basis vectors are $\mathbf{a_1} = a\mathbf{x}$ and $\mathbf{a_2} = a\mathbf{y}$, where a is the lattice constant.

Next, we combine the like $\langle \mathbf{R}_\alpha \mid \mathbf{R}'_{\alpha'} \rangle$ terms, which produces

$$\sum_{\mathbf{R}'_{\alpha'}} c_{\alpha'} e^{i\mathbf{k}\cdot\mathbf{R}'} \langle \mathbf{R}_\alpha | \Delta U_{\mathbf{R}_\alpha} | \mathbf{R}'_{\alpha'} \rangle = \left(E - E^{\text{atom}}_\alpha\right) \sum_{\mathbf{R}'_{\alpha'}} c_{\alpha'} e^{i\mathbf{k}\cdot\mathbf{R}'} \langle \mathbf{R}_\alpha \mid \mathbf{R}'_{\alpha'} \rangle .$$

We decompose the sum on the right-hand side of the equation above and use $\langle \mathbf{R}_\alpha \mid \mathbf{R}_\alpha \rangle = 1$ to obtain:

$$\sum_{\mathbf{R}'_{\alpha'}} c_{\alpha'} e^{i\mathbf{k}\cdot\mathbf{R}'} \langle \mathbf{R}_\alpha | \Delta U_{\mathbf{R}_\alpha} | \mathbf{R}'_{\alpha'} \rangle = \left(E - E^{\text{atom}}_\alpha\right) \left(c_\alpha e^{i\mathbf{k}\cdot\mathbf{R}} + \sum_{\mathbf{R}'_{\alpha'} \neq \mathbf{R}_\alpha} c_{\alpha'} e^{i\mathbf{k}\cdot\mathbf{R}'} \langle \mathbf{R}_\alpha \mid \mathbf{R}'_{\alpha'} \rangle \right) .$$

$$\begin{aligned} &\langle \mathbf{R}_\alpha | \Delta U_{\mathbf{R}_\alpha} | \mathbf{R}_\alpha \rangle c_\alpha e^{i\mathbf{k}\cdot\mathbf{R}} + \sum_{\mathbf{R}'_{\alpha'} \neq \mathbf{R}_\alpha} \langle \mathbf{R}_\alpha | \Delta U_{\mathbf{R}_\alpha} | \mathbf{R}'_{\alpha'} \rangle c_{\alpha'} e^{i\mathbf{k}\cdot\mathbf{R}'} \\ &= \left(E - E^{\text{atom}}_\alpha\right) \left(c_\alpha e^{i\mathbf{k}\cdot\mathbf{R}} + \sum_{\mathbf{R}'_{\alpha'} \neq \mathbf{R}_\alpha} c_{\alpha'} e^{i\mathbf{k}\cdot\mathbf{R}'} \langle \mathbf{R}_\alpha \mid \mathbf{R}'_{\alpha'} \rangle \right) \end{aligned} \tag{C.5}$$

One orbital per unit cell

In the simplest case of one electronic orbital per unit cell, we may discard the index α, and introduce the tight-binding integrals as:

$$\begin{aligned} \langle \mathbf{R} | \Delta U_{\mathbf{R}} | \mathbf{R} \rangle &= \beta, \\ \langle \mathbf{R} | \Delta U_{\mathbf{R}} | \mathbf{R}' \rangle &= t\left(\mathbf{R}' - \mathbf{R}\right), \\ \langle \mathbf{R}_\alpha \mid \mathbf{R}'_{\alpha'} \rangle &= S, \end{aligned} \tag{C.6}$$

where β is the Coulombian integral, t is the exchange (hopping) integral and S is the overlap integral. Also, we will consider the case of only nearest neighbors hopping and denote with $\mathbf{\Delta}$ the distance to the NNs. Therefore, the eigenvalue problem is rewritten as:

$$E(\mathbf{k}) = E^{\text{at}} + \frac{\beta + \sum_{\mathbf{\Delta}} t(\mathbf{\Delta}) e^{i\mathbf{k}\cdot\mathbf{\Delta}}}{1 + \sum_{\mathbf{\Delta}} S(\mathbf{\Delta}) e^{i\mathbf{k}\cdot\mathbf{\Delta}}} \approx E_{at} + \beta + \sum_{\mathbf{\Delta}} t(\mathbf{\Delta}) e^{i\mathbf{k}\cdot\mathbf{\Delta}} \tag{C.7}$$

C.2 The bandstructure of the Lieb lattice

The Lieb lattice is 2D square lattice (see Figure C.1) with three atoms in the primitive unit cell. Hence, when writing the lattie wavefunction, we account for three different orbitals:

$$|\psi\rangle = \sum_{\mathbf{R}'} \Big\{ c_A \,|\mathbf{R}'_\mathbf{A}\rangle + c_B \,|\mathbf{R}'_\mathbf{B}\rangle + c_C \,|\mathbf{R}'_\mathbf{C}\rangle \Big\} e^{i\mathbf{k}\mathbf{R}'}, \tag{C.8}$$

where

$$\begin{aligned} |\mathbf{R}'_\mathbf{A}\rangle &= |\mathbf{R}'\rangle \\ |\mathbf{R}'_\mathbf{B}\rangle &= |\mathbf{R}' + \frac{\mathbf{a_2}}{2}\rangle \\ |\mathbf{R}'_\mathbf{A}\rangle &= |\mathbf{R}' + \frac{\mathbf{a_1}}{2}\rangle \end{aligned} \tag{C.9}$$

The nearest neighbors of the three atoms in the unit cell of a Lieb lattice:

- Atom A ⇒ one NN of type B and one of type C, both in unit cell $\mathbf{R}'$ + one NN of type B in unit cell $\mathbf{R}' - \mathbf{a_2}$ + one NN of type C in unit cell $\mathbf{R}' - \mathbf{a_1}$
- Atom B ⇒ one NN of type A in unit cell $\mathbf{R}'$ and one NN of type A in unit cell $\mathbf{R}' + \mathbf{a_2}$
- Atom C ⇒ one NN of type A in unit cell $\mathbf{R}'$ and one NN of type A in unit cell $\mathbf{R}' - \mathbf{a_1}$

We'll use formula:

$$\langle \mathbf{R}_\alpha |\, \Delta U_{\mathbf{R}_\alpha} \,|\mathbf{R}_\alpha\rangle\, c_\alpha e^{i\mathbf{k}\cdot\mathbf{R}} + \sum_{\mathbf{R}'_{\alpha'} \neq \mathbf{R}_\alpha} \langle \mathbf{R}_\alpha |\, \Delta U_{\mathbf{R}_\alpha} \,|\mathbf{R}'_{\alpha'}\rangle\, c_{\alpha'} e^{i\mathbf{k}\cdot\mathbf{R}'} = \left(E - E^{\text{at}}_\alpha\right) c_\alpha e^{i\mathbf{k}\cdot\mathbf{R}}, \tag{C.10}$$

derived in the previous section and assume that all Coulombian integrals, as well as all the eigenvalues of the atomic Hamiltonians ($E^{\text{at}}_{A,B,C} = E^{\text{at}}$) are equal. Therefore:

$$\sum_{\mathbf{R}'_{\alpha'} \neq \mathbf{R}_\alpha} \langle \mathbf{R}_\alpha |\, \Delta U_{\mathbf{R}_\alpha} \,|\mathbf{R}'_{\alpha'}\rangle\, c_{\alpha'} e^{i\mathbf{k}\cdot\mathbf{R}'} = \left(E - E^{\text{atom}}_\alpha - \beta\right) c_\alpha e^{i\mathbf{k}\cdot\mathbf{R}}. \tag{C.11}$$

For the Lieb lattice, we obtain the following three equations:

$$\begin{aligned} tc_B e^{i\mathbf{k}\mathbf{R}} + tc_B e^{i\mathbf{k}(\mathbf{R}-\mathbf{a}_2)} + tc_B e^{i\mathbf{k}\mathbf{R}} + tc_C e^{i\mathbf{k}(\mathbf{R}-\mathbf{a}_1)} &= \left(E - E^{\text{at}} - \beta\right) c_A e^{i\mathbf{k}\cdot\mathbf{R}} \\ tc_A e^{i\mathbf{k}\mathbf{R}} + tc_A e^{i\mathbf{k}(\mathbf{R}+\mathbf{a}_2)} &= \left(E - E^{\text{at}} - \beta\right) c_B e^{i\mathbf{k}\cdot\mathbf{R}} \\ tc_A e^{i\mathbf{k}\mathbf{R}} + tc_A e^{i\mathbf{k}(\mathbf{R}+\mathbf{a}_1)} &= \left(E - E^{\text{at}} - \beta\right) c_C e^{i\mathbf{k}\cdot\mathbf{R}} \end{aligned} \tag{C.12}$$

$$\begin{aligned} tc_B + tc_B e^{-i\mathbf{k}\mathbf{a}_2} + tc_B + tc_C e^{-i\mathbf{k}\mathbf{a}_1} &= \left(E - E^{\text{at}} - \beta\right) c_A \\ tc_A + tc_A e^{i\mathbf{k}\mathbf{a}_2} &= \left(E - E^{\text{at}} - \beta\right) c_B \\ tc_A + tc_A e^{i\mathbf{k}\mathbf{a}_1} &= \left(E - E^{\text{at}} - \beta\right) c_C \end{aligned} \tag{C.13}$$

This can be written as:

$$\begin{pmatrix} E^{\text{at}} + \beta - E & t(1 + e^{-i\mathbf{k}\mathbf{a}_2}) & t(1 + e^{-i\mathbf{k}\mathbf{a}_1}) \\ t(1 + e^{i\mathbf{k}\mathbf{a}_2}) & E^{\text{at}} + \beta - E & 0 \\ t(1 + e^{i\mathbf{k}\mathbf{a}_1}) & 0 & E^{\text{at}} + \beta - E \end{pmatrix} \begin{pmatrix} c_A \\ c_B \\ c_C \end{pmatrix} = \mathbf{0}. \tag{C.14}$$

We denote $E^{\text{at}} + \beta$ as $\tilde{E}$ and solve the determinant:

$$\begin{aligned}&\left(\tilde{E} - E(\mathbf{k})\right) \cdot \\ &\left[\left(\tilde{E} - E(\mathbf{k})\right)^2 - t^2\left(1 + e^{-i\mathbf{k}\mathbf{a_1}}\right)\left(1 + e^{i\mathbf{k}\mathbf{a_1}}\right) - t^2\left(1 + e^{-i\mathbf{k}\mathbf{a_2}}\right)\left(1 + e^{i\mathbf{k}\mathbf{a_2}}\right)\right] = 0\end{aligned} \tag{C.15}$$

$$\begin{aligned}&\left(\tilde{E} - E(\mathbf{k})\right) \cdot \\ &\left[\left(\tilde{E} - E(\mathbf{k})\right)^2 - 4t^2\left(\cos^2(\frac{k_x a}{2}) + \cos^2(\frac{k_y a}{2})\right)\right] = 0\end{aligned} \tag{C.16}$$

Therefore, he spectrum of the Lieb lattice has two dispersive bands ($E_{1,2}(k)$) and one flatband ($E_3(k)$):

$$\begin{aligned}&E_{1,2}(k) = \pm 2t\sqrt{\cos^2(\frac{k_x a}{2}) + \cos^2(\frac{k_y a}{2})} \\ &E_3(k) = 0\end{aligned} \tag{C.17}$$

D

Spin averages

The spin observable $\vec{S}$ is mathematically expressed by a vector with matrix components:

$$\vec{S} = \frac{\hbar}{2}\vec{\sigma}$$

where the vector $\vec{\sigma}$ contains the Pauli matrices $\sigma_{\mathrm{x}}, \sigma_{\mathrm{y}}, \sigma_{\mathrm{z}}$:

$$\vec{\sigma} = \begin{pmatrix} \sigma_{\mathrm{x}} \\ \sigma_{\mathrm{y}} \\ \sigma_{\mathrm{z}} \end{pmatrix}, \sigma_{\mathrm{x}} = \begin{pmatrix} 0 & 1 \\ 1 & 0 \end{pmatrix}, \sigma_{\mathrm{y}} = \begin{pmatrix} 0 & -i \\ i & 0 \end{pmatrix}, \sigma_{\mathrm{z}} = \begin{pmatrix} 1 & 0 \\ 0 & -1 \end{pmatrix}$$

A general spinor state can be written as:

$$\alpha|\uparrow\rangle + \beta|\downarrow\rangle = \begin{pmatrix} \alpha \\ \beta \end{pmatrix}, \quad |\alpha|^2 + |\beta|^2 = 1$$

where

$$|\uparrow\rangle = \begin{pmatrix} 1 \\ 0 \end{pmatrix}, \quad |\downarrow\rangle = \begin{pmatrix} 0 \\ 1 \end{pmatrix}$$

$$I_{\sigma=} \begin{pmatrix} 1 & 0 \\ 0 & 1 \end{pmatrix}; \qquad I_\sigma = |\uparrow\rangle\langle\uparrow| + |\downarrow\rangle\langle\downarrow| \tag{D.1}$$

$$\sigma_x = \begin{pmatrix} 0 & 1 \\ 1 & 0 \end{pmatrix}; \qquad \sigma_x = |\uparrow\rangle\langle\downarrow| + |\downarrow\rangle\langle\uparrow| \tag{D.2}$$

$$\sigma_y = \begin{pmatrix} 0 & -i \\ i & 0 \end{pmatrix}; \qquad \sigma_y = i|\downarrow\rangle\langle\uparrow| - i|\uparrow\rangle\langle\downarrow| \tag{D.3}$$

$$\sigma_z = \begin{pmatrix} 1 & 0 \\ 0 & -1 \end{pmatrix}; \qquad \sigma_z = |\uparrow\rangle\langle\uparrow| - |\downarrow\rangle\langle\downarrow| \tag{D.4}$$

$$\begin{aligned} S_x &= \tfrac{\hbar}{2}(|\uparrow\rangle\langle\downarrow| + |\downarrow\rangle\langle\uparrow|) \\ S_y &= i\tfrac{\hbar}{2}(|\downarrow\rangle\langle\uparrow| - |\uparrow\rangle\langle\downarrow|) \\ S_z &= \tfrac{\hbar}{2}(|\uparrow\rangle\langle\uparrow| - |\downarrow\rangle\langle\downarrow|) \end{aligned} \tag{D.5}$$

$$(S_x)_{ij} = \frac{\hbar}{2}\begin{pmatrix} 0 & 1 \\ 1 & 0 \end{pmatrix} \tag{D.6}$$

$$\left(S_y\right)_{ij} = \frac{\hbar}{2}\begin{pmatrix} 0 & -i \\ i & 0 \end{pmatrix} \tag{D.7}$$

$$(S_z)_{ij} = \frac{\hbar}{2}\begin{pmatrix} 1 & 0 \\ 0 & -1 \end{pmatrix} \tag{D.8}$$

$$S_z \begin{cases} |\uparrow\rangle & \left(\frac{\hbar}{2}\right) \\ |\downarrow\rangle & \left(-\frac{\hbar}{2}\right) \end{cases} \tag{D.9}$$

$$S_x \begin{cases} \frac{1}{\sqrt{2}}(|\uparrow\rangle + |\downarrow\rangle) \\ \frac{1}{\sqrt{2}}(|\uparrow\rangle - |\downarrow\rangle) \end{cases} \tag{D.10}$$

$$S_y \begin{cases} \frac{1}{\sqrt{2}}(|\uparrow\rangle + i|\downarrow\rangle) \\ \frac{1}{\sqrt{2}}(|\uparrow\rangle - i|\downarrow\rangle) \end{cases} \tag{D.11}$$

$$\langle\sigma_\alpha\rangle = \langle\psi\,|\sigma_\alpha|\,\psi\rangle \quad \alpha = x, y, z \tag{D.12}$$

$$\begin{aligned} \sigma_z\psi &= (|\uparrow\rangle\langle\uparrow| - |\downarrow\rangle\langle\downarrow|)\cdot\left(\psi_\uparrow|\uparrow\rangle + \psi_\downarrow|\downarrow\rangle\right) \\ &= \psi_\uparrow|\uparrow\rangle - \psi_\downarrow|\downarrow\rangle \end{aligned} \tag{D.13}$$

$$\begin{aligned} \langle\psi\mid\sigma_z\psi\rangle &= \left\langle\psi_\uparrow^*\,|\uparrow\right\rangle + \psi_\downarrow^*|\downarrow\rangle\Big)\left(\psi_\uparrow|\uparrow\rangle - \psi_\downarrow|\downarrow\rangle\right) \\ &= |\psi_\uparrow|^2 - |\psi_\downarrow|^2 \end{aligned} \tag{D.14}$$

$$\begin{aligned} \sigma_x\psi &= (|\uparrow\rangle\langle\downarrow| + |\downarrow\rangle\langle\uparrow|)\cdot\left(\psi_\uparrow|\uparrow\rangle + \psi_\downarrow|\downarrow\rangle\right) \\ &= \langle\psi_\uparrow\,|\downarrow\rangle + \psi_\downarrow|\uparrow\rangle \end{aligned} \tag{D.15}$$

$$\begin{aligned} \langle\psi\mid\sigma_x\psi\rangle &= \left(\psi_\uparrow^*|\uparrow\rangle + \psi_\downarrow^*|\downarrow\rangle\right)\cdot\left(\psi_\uparrow|\downarrow\rangle + \psi_\downarrow|\uparrow\rangle\right) \\ &= \psi_\uparrow^*\psi_\downarrow + \psi_\downarrow^*\psi_\uparrow = \langle\psi\mid\sigma_x\psi\rangle^* \end{aligned} \tag{D.16}$$

$$\begin{aligned} \sigma_y\psi =&(i|\downarrow\rangle\langle\uparrow| - i|\uparrow\rangle\langle\downarrow|)\cdot\left(\psi_\uparrow|\uparrow\rangle + \psi_\downarrow|\downarrow\rangle\right) \\ &= i\psi_\uparrow|\downarrow\rangle - i\psi_\downarrow|\uparrow\rangle \end{aligned} \tag{D.17}$$

$$\begin{aligned} \langle\psi\mid\sigma_y\psi\rangle &= \left(\psi_\uparrow^*|\uparrow\rangle + \psi_\downarrow^*|\downarrow\rangle\right)\left(i\psi_\uparrow|\downarrow\rangle - i\psi_\downarrow|\uparrow\rangle\right) \\ &= i\psi_\downarrow^*\psi_\uparrow - i\psi_\uparrow^*\psi_\downarrow = \langle\psi\mid\sigma_y\psi\rangle^* \end{aligned} \tag{D.18}$$

E

Rashba and Dresselhaus SOI in the R-matrix formalism

In order to implement Rashba and Dresselhaus SOIs within an R-matrix method, it is important to include the Bloch operators in order to maintain the Hermiticity of the Hamiltonian operators. For these particular SOCs, we explicitly calculate here the action of the Bloch operators onto the spin wavefunctions and the Wigner-Eisenbud wavefunctions.

For the Rashba SOI, the results are:

$$\begin{aligned}
\mathcal{L}_{\mathcal{R}} \left|\Psi\right\rangle &= \mathcal{L}_{\mathcal{R}} \left(\sum_{\sigma} \Psi_{\sigma} \left|\sigma\right\rangle \right) = \sum_{\sigma} \Psi_{\sigma} \mathcal{L}_{\mathcal{R}} \left|\sigma\right\rangle \\
&= \frac{\alpha}{2} \sum_{s,\sigma} \eta_s \delta(x - x_s) i \left(\left|\downarrow\right\rangle \left\langle\uparrow\right| - \left|\uparrow\right\rangle \left\langle\downarrow\right| \right) \left[\Psi_{\uparrow} \left|\uparrow\right\rangle + \Psi_{\downarrow} \left|\downarrow\right\rangle \right] \\
&= \frac{\alpha}{2} \left(\Psi_{\uparrow} \left|\downarrow\right\rangle - \Psi_{\downarrow} \left|\uparrow\right\rangle \right)
\end{aligned} \tag{E.1}$$

$$\begin{aligned}
\left\langle \chi_l \middle| \mathcal{L}_{\mathcal{R}} \Psi \right\rangle &= \frac{\alpha}{2} \left\langle \left(\chi_{l\uparrow} \left|\uparrow\right\rangle + \chi_{l\downarrow} \left|\downarrow\right\rangle \right) \middle| \left(\Psi_{\uparrow} \left|\downarrow\right\rangle - \Psi_{\downarrow} \left|\uparrow\right\rangle \right) \right\rangle \\
&= \frac{\alpha}{2} \left(-\chi_{l\uparrow} \Psi_{\downarrow} + \chi_{l\downarrow} \Psi_{\uparrow} \right) \\
&= \frac{\alpha}{2} \sum_{\sigma} \sigma \chi_{l,-\sigma} \Psi_{\sigma}
\end{aligned} \tag{E.2}$$

Similarly, for the Dresselhaus SOI, we get a similar result:

$$\begin{aligned}
\mathcal{L}_{\mathcal{D}} \psi &= \mathcal{L}_{\mathcal{D}} \left(\sum_{\sigma} \Psi_{\sigma} \left|\sigma\right\rangle \right) = \sum_{\sigma} \Psi_{\sigma} \mathcal{L}_{\mathcal{D}} \left|\sigma\right\rangle \\
&= \frac{\beta}{2} \sum_{s,\sigma} \eta_s \delta(x - x_s) i \left(\left|\uparrow\right\rangle \left\langle\downarrow\right| - \left|\downarrow\right\rangle \left\langle\uparrow\right| \right) \left[\Psi_{\uparrow} \left|\uparrow\right\rangle + \Psi_{\downarrow} \left|\downarrow\right\rangle \right] \\
&= \frac{\beta}{2} \left(\Psi_{\uparrow} \left|\downarrow\right\rangle + \Psi_{\downarrow} \left|\uparrow\right\rangle \right)
\end{aligned} \tag{E.3}$$

$$\begin{aligned}
\langle \chi_l | \mathcal{L}_{\mathcal{D}} \Psi \rangle &= \frac{\beta}{2} \left\langle \left(\chi_{l\uparrow} \left| \uparrow \right\rangle + \chi_{l\downarrow} \left| \downarrow \right\rangle \right) \,|\, \left(\Psi_{\uparrow} \left| \downarrow \right\rangle + \Psi_{\downarrow} \left| \uparrow \right\rangle \right) \right\rangle \\
&= \frac{\beta}{2} \left(\chi_{l\uparrow} \Psi_{\downarrow} + \chi_{l\downarrow} \Psi_{\uparrow} \right) \\
&= \frac{\beta}{2} \sum_{\sigma} \chi_{l,-\sigma} \Psi_{\sigma}
\end{aligned} \tag{E.4}$$

F

Bandstucture of the Lieb lattice (Python code)

LISTING F.1: TB code for the ideal Lieb lattice

```
from __future__ import print_function
from pythtb import * # import TB model class
import numpy as np
import matplotlib.pyplot as plt

import pybinding as pb
import matplotlib.pyplot as plt
from math import pi

from cycler import cycler

plt.rcParams["figure.figsize"] = (15,15)

pb.pltutils.use_style()

# Version 1

def lieb(d=1, delta=0, t=0.6, t_p=0.01):
    lat = pb.Lattice(a1=[2*d, 0], a2=[0, 2*d])
    lat.add_sublattices(
        ('A', [0, 0], -delta),
        ('B', [0, d], delta),
        ('C', [d, 0], delta),
    )
    lat.add_hoppings(
        ([ 0,  0], 'A', 'B', t),
        ([ 0,  0], 'A', 'C', t),
        ([ 0,  0], 'B', 'C', t_p),
        ([ 0, -1], 'A', 'B', t),
        ([ -1, 0], 'A', 'C', t))
    return lat
```

```
lattice = lieb()
lattice.plot()
plt.show()
plt.savefig('Lieb_lattice_structure.eps')

lattice.plot_brillouin_zone()
plt.show()

model = pb.Model(lieb(), pb.translational_symmetry())
solver = pb.solver.lapack(model)

#Path in k space

Gamma = [0, 0]
X = [0,0.5*pi]
M = [0.5*pi, 0.5*pi]


bands = solver.calc_bands(Gamma, X, M, Gamma)
bands.plot(point_labels=[r'$\Gamma$', r'$X$', 'M', r'$\Gamma$'])
plt.show()

from turtle import color


plt.rcParams["figure.figsize"] = (10,7)

default_cycler = (cycler(color=['r', 'g', 'b', ]) +
                cycler(linestyle=['-', '--', ':']))

plt.rc('lines', linewidth=4)
plt.rc('axes', prop_cycle=default_cycler)

model = pb.Model(lieb(), pb.translational_symmetry())
solver = pb.solver.lapack(model)

Gamma = [0, 0]
X = [0,0.5*pi]
M = [0.5*pi, 0.5*pi]


bands = solver.calc_bands(Gamma, X, M, Gamma)
bands.plot(point_labels=[r'$\Gamma$', r'$X$', 'M', r'$\Gamma$'])
plt.show()

# Version 2 => this version was adapted from the PythTB documentation:
    https://www.physics.rutgers.edu/pythtb/examples.html

# define lattice vectors
d = 1

lat=[[1.0,0.0],[0.0,1.0]]

# define coordinates of orbitals
orb=[[0.0,0.0],[0,0.5], [0.5,0]]

# make two dimensional tight-binding model
```

```
my_model=tb_model(2,2,lat,orb)

# set model parameters

delta=1
t=0.6
t_p = 0.01

# set on-site energies
my_model.set_onsite([0,0,0])
# set hoppings (one for each connected pair of orbitals)
# (amplitude, i, j, [lattice vector to cell containing j])
my_model.set_hop(t, 0, 1, [ 0, 0])
my_model.set_hop(t, 0, 2, [ 0, 0])
my_model.set_hop(t_p, 1, 2, [ 0, 0])
my_model.set_hop(t, 0, 1, [ 0, -1])
my_model.set_hop(t, 0, 2, [ -1, 0])

# print tight-binding model

my_model.display()

# generate list of k-points following a segmented path in the BZ
# list of nodes (high-symmetry points) that will be connected
path=[[0, 0], [0, 0.5], [0.5, 0.5], [0, 0]]
# labels of the nodes
label=(r'$\Gamma $',r'$X$', r'$M$', r'$\Gamma $')
# total number of interpolated k-points along the path
nk=200

# call function k_path to construct the actual path
(k_vec,k_dist,k_node)=my_model.k_path(path,nk)
# inputs:
#   path, nk: see above
#   my_model: the pythtb model
# outputs:
#   k_vec: list of interpolated k-points
#   k_dist: horizontal axis position of each k-point in the list
#   k_node: horizontal axis position of each original node

print('---------------------------------------')
print('starting calculation')
print('---------------------------------------')
print('Calculating bands...')

# obtain eigenvalues to be plotted

evals=my_model.solve_all(k_vec)

# figure for bandstructure

fig, ax = plt.subplots()
# specify horizontal axis details
# set range of horizontal axis
ax.set_xlim(k_node[0],k_node[-1])
# put tickmarks and labels at node positions
```

```
ax.set_xticks(k_node)
ax.set_xticklabels(label)
# add vertical lines at node positions
for n in range(len(k_node)):
  ax.axvline(x=k_node[n],linewidth=0.7, color=’k’)
# put title
ax.set_title("Lieb lattice band structure")
ax.set_xlabel("Path in k-space")
ax.set_ylabel("Band energy")

# plot first, second band and third band

ax.plot(k_dist,evals[0])
ax.plot(k_dist,evals[1])
ax.plot(k_dist,evals[2])

# save figure with plot
fig.tight_layout()
#fig.savefig("Kagome_to_lieb.jpg")

print(’Done.\n’)
```

G

Bandstructure of the Kagome lattice (Python code)

LISTING G.1: TB code for the ideal Kagome lattice

```
from __future__ import print_function
from pythtb import * # import TB model class
import numpy as np
import matplotlib.pyplot as plt

import pybinding as pb
import matplotlib.pyplot as plt
from math import pi

from cycler import cycler

default_cycler = (cycler(color=[’r’, ’g’, ’b’, ]) +
                cycler(linestyle=[’-’, ’--’, ’:’]))

plt.rc(’lines’, linewidth=4)
plt.rc(’axes’, prop_cycle=default_cycler)

plt.rcParams.update({’axes.labelsize’: ’large’})

plt.rcParams["figure.figsize"] = (10,7)

def kagome_ideal(d=1,delta=0,t=1):

    # create a lattice with 2 primitive vectors
    lat = pb.Lattice(
        a1=[np.sqrt(3)*d/2, -0.5*d],
        a2=[d*np.sqrt(3)/2, d * 0.5]
    )

    lat.add_sublattices(
        # name and position
        (’A’, [0, 0], -delta),
        (’B’, [np.sqrt(3)*d/4, -0.25*d], delta),
```

```
        ('C', [d*np.sqrt(3)/4, d * 0.25], delta)
    )

    lat.add_hoppings(
        # inside the main cell
        ([0,  0], 'A', 'B', t),
        ([0,  0], 'A', 'C', t),
        ([0,  0], 'B', 'C', t),
        # between neighboring cells
        ([1, 0], 'B', 'A', t),
        ([-1, 1], 'C', 'B', t),
        ([0, -1], 'A', 'C', t),
    )

    return lat


lattice = kagome_ideal()
lattice.plot()
plt.show()

def kagome_ideal_v2(d=1,delta=0,t=1):

    # create a lattice with 2 primitive vectors
    lat = pb.Lattice(
        a1=[2*d, 0],
        a2=[d, d * np.sqrt(3)]
    )

    lat.add_sublattices(
        # name and position
        ('A', [0, 0], -delta),
        ('B', [d/2, d/2*np.sqrt(3)], delta),
        ('C', [d, 0], delta)
    )

    lat.add_hoppings(
        # inside the main cell
        ([0,  0], 'A', 'B', t),
        ([0,  0], 'A', 'C', t),
        ([0,  0], 'B', 'C', t),
        # between neighboring cells
        ([1, 0], 'B', 'A', t),
        ([-1, 1], 'C', 'B', t),
        ([0, -1], 'A', 'C', t),


        #([1, -1], 'B', 'C', t),
        #([0, -1], 'A', 'B', t),
        #([-1, 0], 'B', 'C', t),
        #([-1, 0], 'A', 'C', t),
        #([0, -1], 'C', 'B', t),
    )

    return lat
```

```
# lattice = kagome_ideal_v2()
# lattice.plot()
# plt.show()

lattice.plot_brillouin_zone()
plt.show()

model = pb.Model(kagome_ideal(), pb.translational_symmetry())
solver = pb.solver.lapack(model)

Gamma = [0,0]
M = [pi*2/np.sqrt(3), 0]
K = [2*pi/np.sqrt(3),-2/3*pi]

#bands = solver.calc_bands(Gamma, M, K, X, Gamma)
bands = solver.calc_bands(Gamma, K, M, Gamma)
#bands.plot(point_labels=[r'$\Gamma$', r'$M$', 'K', 'X', r'$\Gamma$'])
bands.plot(point_labels=[r'$\Gamma$', r'$K$', 'M', r'$\Gamma$'], color =
    'k')
plt.title('Ideal Kagome lattice band structure', fontsize=20)
plt.show()

model.lattice.plot_brillouin_zone(decorate=False)
#bands.plot_kpath(point_labels=[r'$\Gamma$', r'$M$', 'K','X', r'$\Gamma$'])
bands.plot_kpath(point_labels=[r'$\Gamma$', r'$K$', 'M', r'$\Gamma$'])

# Version 2 => this version was adapted from the PythTB documentation:
    https://www.physics.rutgers.edu/pythtb/examples.html

# define lattice vectors
d = 1

#lat=[[2.0,0.0],[1.0,np.sqrt(3)]]

lat=[[np.sqrt(3.0)/2.0,-0.5],[np.sqrt(3.0)/2.0,0.5]]

# define coordinates of orbitals
orb=[[0.0,0.0],[0.5,0], [0,0.5]]

# make two dimensional tight-binding model

my_model=tb_model(2,2,lat,orb)

# set model parameters

delta=0
t=0.6


# set on-site energies
my_model.set_onsite([0,0,0])
# set hoppings (one for each connected pair of orbitals)
# (amplitude, i, j, [lattice vector to cell containing j])

 #atom A hopping terms;
my_model.set_hop(t, 1, 0, [ 0, 0])
my_model.set_hop(t, 1, 0, [ 1, 0])
```

```
#atom B hopping terms;
my_model.set_hop(t, 2, 1, [ 0, 0])
my_model.set_hop(t, 2, 1, [-1, 1])

 #atom C hopping terms;
my_model.set_hop(t, 0, 2, [ 0, 0])
my_model.set_hop(t, 0, 2, [ 0,-1])



# print tight-binding model

my_model.display()

# generate list of k-points following a segmented path in the BZ
# list of nodes (high-symmetry points) that will be connected

#path=[[0, 0], [0.67*pi, 0], [0.5*pi, 0.5*pi*np.sqrt(3)/3], [0, 0]]

path=[[0.,0.],[2./3.,1./3.],[.5,.5], [0, 0] ]
# labels of the nodes
label=(r’$\Gamma $’,r’$K$’, r’$M$’, r’$\Gamma $’)
# total number of interpolated k-points along the path
nk=300

# call function k_path to construct the actual path
(k_vec,k_dist,k_node)=my_model.k_path(path,nk)
# inputs:
#   path, nk: see above
#   my_model: the pythtb model
# outputs:
#   k_vec: list of interpolated k-points
#   k_dist: horizontal axis position of each k-point in the list
#   k_node: horizontal axis position of each original node

print(’---------------------------------------’)
print(’starting calculation’)
print(’---------------------------------------’)
print(’Calculating bands...’)

# obtain eigenvalues to be plotted

evals=my_model.solve_all(k_vec)

# figure for bandstructure

fig, ax = plt.subplots()
# specify horizontal axis details
# set range of horizontal axis
ax.set_xlim(k_node[0],k_node[-1])
# put tickmarks and labels at node positions
ax.set_xticks(k_node)
ax.set_xticklabels(label)
# add vertical lines at node positions
for n in range(len(k_node)):
  ax.axvline(x=k_node[n],linewidth=0.7, color=’k’)
```

```
# put title
ax.set_title("Ideal Kagome lattice band structure")
ax.set_xlabel("Path in k-space")
ax.set_ylabel("Band energy")

# plot first, second band and third band

ax.plot(k_dist,evals[0])
ax.plot(k_dist,evals[1])
ax.plot(k_dist,evals[2])

# save figure with plot
fig.tight_layout()
fig.savefig("Kagome_ideal.jpg")

print('Done.\n')
```

H

Gaussian filter (Python code)

LISTING H.1: Python code to apply Gaussian filter on charge density maps

```
from scipy.ndimage import gaussian_filter
import numpy as np
import matplotlib.pyplot as plt
import os
from statistics import stdev

# Load image as array

charge_den =
    np.loadtxt('/Users/amapreda/Exact_diagonalization_ML_PCE/output/RUN_0100
/charge_density_0.dat').reshape(64,64)

# Functions needed:

def convolution(oldimage, kernel):
    image_h = oldimage.shape[0]
    image_w = oldimage.shape[1]


    kernel_h = kernel.shape[0]
    kernel_w = kernel.shape[1]


    image_pad = np.pad(oldimage, pad_width=((kernel_h // 2, kernel_h //
        2),(kernel_w // 2, kernel_w // 2)), mode='constant',
        constant_values=0).astype(np.float32)


    h = kernel_h // 2
    w = kernel_w // 2
```

```
    image_conv = np.zeros(image_pad.shape)

    for i in range(h, image_pad.shape[0]-h):
        for j in range(w, image_pad.shape[1]-w):
            #sum = 0
            x = image_pad[i-h:i-h+kernel_h, j-w:j-w+kernel_w]
            x = x.flatten()*kernel.flatten()
            image_conv[i][j] = x.sum()
    h_end = -h
    w_end = -w

    if(h == 0):
        return image_conv[h:,w:w_end]
    if(w == 0):
        return image_conv[h:h_end,w:]
    return image_conv[h:h_end,w:w_end]


def GaussianBlurImage(image, sigma_x, sigma_y, noise):
    #print(image)
    if(sigma_x == sigma_y):
        filter_size = 2 * int(4 * sigma_x + 0.5) + 1
        gaussian_filter = np.zeros((filter_size, filter_size), np.float32)
        m = filter_size//2
        n = filter_size//2
    else:
        filter_size_x = 2 * int(4 * sigma_x + 0.5) + 1
        filter_size_y = 2 * int(4 * sigma_y + 0.5) + 1
        gaussian_filter = np.zeros((filter_size_x, filter_size_y),
            np.float32)
        m = filter_size_x//2
        n = filter_size_y//2


    if(sigma_x==sigma_y):
        for x in range(-m, m+1):
            for y in range(-n, n+1):
                x1 = 2*np.pi*(sigma_x**2)
                x2 = np.exp(-(x**2 + y**2)/(2* sigma_x**2))
                gaussian_filter[x+m, y+n] = (1/x1)*x2
    else:
        for x in range(-m, m+1):
            for y in range(-n, n+1):
                x1 = 2*np.pi*(sigma_x*sigma_y)
                x2 = np.exp(-(x**2/(2*sigma_x**2)+ y**2/(2*sigma_y**2)))
                gaussian_filter[x+m, y+n] = (1/x1)*x2

    ### Add noise to gaussian filter if noise = 1

    if(noise!=0):
        len = (2*m+1)*(2*n+1)
        exponent= np.zeros(len)

        if(sigma_x==sigma_y):
            i=0
            for x in range(-m, m+1):
                for y in range(-n, n+1):
```

```
                    x1 = 2*np.pi*(sigma_x**2)
                    x2 = np.exp(-(x**2 + y**2)/(2* sigma_x**2))
                    exponent[i] = (1/x1)*x2
                    i=i+1

        else:
            i=0
            for x in range(-m, m+1):
                for y in range(-n, n+1):
                    x1 = 2*np.pi*(sigma_x*sigma_y)
                    x2 = np.exp(-(x**2/(2*sigma_x**2)+ y**2/(2*sigma_y**2)))
                    exponent[i] = (1/x1)*x2
                    i=i+1

        # max = np.amax(exponent)
        # min = np.amin(exponent)
        # noise_deviation = 0.1 * (max- min)                         # make
            sure the noise is not too large
        # noise_deviation = stdev(exponent)

        noise_add = np.random.normal(0, noise, gaussian_filter.shape) #
            Random noise to add to the filter
        new_signal = gaussian_filter + noise_add                         #
            new filter
        # print(gaussian_filter[0])                                  # to
            check how filter with/without noise looks
        # print(noise[0])
        # print(np.shape(gaussian_filter))
        im_filtered = np.zeros_like(image)
        im_filtered[:, :] = convolution(image[:, :], new_signal)     #
            filter with noise

    else:
        im_filtered = np.zeros_like(image)
        im_filtered[:, :] = convolution(image[:, :], gaussian_filter)


    return im_filtered

# Apply functions

sigma_x = 1
sigma_y = 1

# Set here the standard deviation for the random noise added to the filter.
    If noise=0, no noise is added
noise = 0.001

# Generate image with filter

filtered_image = GaussianBlurImage(image=charge_den, sigma_x = sigma_x,
    sigma_y = sigma_y, noise=noise )

# Check

fig = plt.figure()
plt.gray() # show the filtered result in grayscale
```

```
ax1 = fig.add_subplot(121) # left side
ax2 = fig.add_subplot(122) # right side
ax1.imshow(charge_den)
ax2.imshow(filtered_image)
title = "Sx = " + str(sigma_x)+ ", Sy = " + str(sigma_y)+ ", noise = " +
    str(noise)
ax2.set_title(title)
if (noise ==0):
    save_title = "Without_noise"
else:
    save_title = "With_Noise"
plt.savefig(save_title)
plt.show()
```

I

Computation of the current in the nanotransistor (C subroutine)

LISTING I.1: C subroutine for the computation of the current through the tw-channel nanotransistor

```
#include <stdio.h>
#include <stdlib.h>
#include <math.h>

double fermi(double E, double Ef, double T, double kb);
double step(double E, double Ef);
long return_index(double En, double dE, double En_new, double E0);


double fermi(double E, double Ef, double T, double kb){
   return 1/(1+exp((E-Ef)/kb*T));
}

double step(double E, double Ef){
   if (E < Ef) {return 1;}
   else {return 0;}
}


// compute index of (E-Ei); where E-Ei has to be a multiple of dE

long return_index(double En, double dE, double En_new, double E0){
   if (En < dE){En_new = 0;}

    if (fmod(En,dE) > dE/2) {En_new = En - fmod(En,dE) + dE;}
    else {En_new = En - fmod(En,dE);}

    //return index for En= E - Ei

    return (long)((En_new - E0)/dE); //ni
```

```
}

double compute_current( long N_energies, double *Energies, double *trans,
    double Vd, double Vg, double T, double Lz) {
    //constants
    const double kb = 8.617333262e-5; // eV/K Boltzmann constant
    const double e = 1.60217663e-19; //C electron charge
    const double pi = 3.14169265;
    const double hbar = 6.582119569e-16;//eV s
    const double em0 = 9.109534e-31;
    const double hbar_J = 1.054571817e-34; //hbar in J s
    const double joule_to_eV = 6.24150907e18;
    const double effmass = 0.5;




    //variables
    double E;
    double Ef, muL, muR;
    double I, I_total, I_final;
    double a,b, limit1, limit2; //integration limits
    double Ei, En_new, E0, E_final, dE, En;
    FILE *file;
    long n = N_energies;
    long na, nb;
    double deltaE = Energies[1]-Energies[0];
    long i, j, k, index, ni;
    double Ez[10];
    double C;



     C = 4*e*pi/hbar;
     E0 = Energies[0];
     E_final = Energies[N_energies-1];


     I_total = 0;        //integral / intensity

     //Set integration limits as multiples of dE
     /*

     if (a < dE){limit1 = 0;}
     if (b < dE){limit2 = 0;}

     if (a%dE > dE/2) {limit1 = Ei - Ei%dE + dE;}
     else {limit1 = Ei - Ei%dE;}

     if (b%dE > dE/2) {limit2 = Ei - Ei%dE + dE;}
     else {limit2 = Ei - Ei%dE;}
    */

     // compute E_i

     for (i=0; i<1; i++){
```

```
        Ez[i] = joule_to_eV *i*i *
            (hbar_J*hbar_J/(2*effmass*em0))*(pi/Lz)*(pi/Lz);
     }
     //set index for integration limits

     //na = (limit1 - E0)/dE;
     //nb = (limit2 - E0)/dE;

     muL = 0.2;
     muR = 0.2 - Vd;

     //compute integral

     for (k=0; k<1; k++){
        Ei = Ez[k];
        na = return_index(Ez[k],deltaE, En_new, E0);
        nb = (E_final-E0)/deltaE;
        I=0;
     for(i=na;i<=nb; i++){
        En = Energies[i] - Ei;
        index = return_index(En,deltaE, En_new, E0);

// printf( "i index %li %li\n", i, index);
        if (T > 30){
        I = I + (fermi(Energies[i], muL, T, kb) - fermi(Energies[i], muR, T,
            kb)) * trans[index] * deltaE;
//       I = I + trans[index] * deltaE;
//       printf("I=%.6e\n", I);

   }
        else{
            I = I + (step(Energies[i], muL) - step(Energies[i], muR)) *
                trans[index] * deltaE;}
     }
     I_total = I_total + I;
 }

I_final = I_total * C;

//FILE *f = fopen("Current_Vd_Vg.txt", "w");
//fprintf(f,"%f %f %f\n",I_total*C,Vd,Vg);
//fclose(f);

return I_final;
}
```

J

Nanotransistor (KWANT code)

LISTING J.1: KWANT code for the multi-terminal quantum sorter device

```
import matplotlib.pyplot as plt
from math import exp
import numpy as np
import pandas as pd
import kwant
from scipy.sparse import csc_matrix
from scipy.sparse.linalg import inv
import scipy
import scipy.linalg
import time
import matplotlib.pyplot

# CONSTANTS

kB = scipy.constants.value("Boltzmann constant in eV/K")  # unit: eV/K
qe = scipy.constants.value("elementary charge")           # unit: C
me = scipy.constants.value("electron mass")/qe*1e-18      # unit: eV*s^2/nm^2
hP = scipy.constants.value("Planck constant in eV s")     # unit: eV*s
hbar = hP/(2*scipy.pi)                                    # unit: eV*s
eps0 = scipy.constants.value("electric constant")*qe*1e-9 # unit:
    C^2/(eV*nm)

# DEVICE parameters:

# Nanotransistor parameters

D_w = 3 # well nm
D_B = 2 # tunnel barrier
D_tgi = 8 # top gate insulator layer
D_bgi = 8 # back gate insulator layer
```

```
y_scat = 2* D_w + D_B
y_device_int = 2* D_w + D_B + D_bgi + D_tgi
L_device_int = 30           # nm

top = 0.3      # top gate
bottom = 0    # bottom gate
source = 0    # source
drain = 0.2     # drain

V_barrier = 2.0   # barrier height eV

h = 0.05           # delta x for Poisson equation

# KWANT tight bindind parameters


a = 0.05               # lattice constant
m = 0.32               # effective mass

W = 4             # width/2 of scattering region [-W, W]
L = 20            # length/2 of scattering region [-L, L]
L_central = 15    # Length/2 of the cenral region

lead_scat = 5
block_lead = 3


t = hbar**2/(2*me*m*a**2)      # units: eV

E_min = 0
E_max = 1.5
N_en = 1000

def Solve_Poisson(L_x, W_y, h, top, bottom, drain, source):

    # Define system

    xmax=L_x
    ymax=W_y
    h=h

    # Set Nx, Ny

    Nx = int (xmax/h)
    Ny = int (ymax/h)


    nx = Nx-1
    ny = Ny-1
    n = (nx)*(ny) #number of unknowns


    # Set boundary conditions
    v_top = top    # y = max, x = all V top gate
    v_bottom = bottom # y = 0, x = all V bottom gate
    v_left = source # x= 0, y = all, Vsource
    v_right = drain  # x = max, y = all, Vd drain
```

```
d = np.ones(n) # diagonals
b = np.zeros(n) #RHS
d0 = d*-4
d1 = d[0:-1]
d5 = d[0:-ny]

# Plot parameters:

x = np.linspace(0, xmax, Nx + 1)
y = np.linspace(0, ymax, Ny + 1)

X, Y = np.meshgrid(x, y)

# Create 2D potential map

vv = np.zeros_like(X)


# set the imposed boudary values
vv[-1,:] = v_top
vv[0,:] = v_bottom
vv[:,0] = v_left
vv[:,-1] = v_right


# Defining the A matrix


d = np.ones(n) # diagonals
b = np.zeros(n) #RHS
d0 = d*-4
d1 = d[0:-1]
d5 = d[0:-ny]

A = scipy.sparse.diags([d0, d1, d1, d5, d5], [0, 1, -1, ny, -ny], format
    = 'csr')

# set elements to zero in A matrix where BC are imposed
for k in range(1,nx):
    j = k*(ny)
    i = j - 1
    A[i, j], A[j, i] = 0, 0
    b[i] = -v_top


b[-ny:]+=-v_right #set the last ny elements to -vright
b[-1]+=-v_top    #set the last element to -vtop
b[0:ny-1]+=-v_left #set the first ny elements to -vleft
b[0::ny]+=-v_bottom #set every ny-th element to -vbottom


sol = scipy.sparse.linalg.spsolve(A,b)


for j in range(1,ny+1):
    for i in range(1, nx + 1):
```

```
            vv[j, i] = sol[j + (i-1)*ny - 1]

    return vv

def scat_pot(vv_poisson, D_tg_buffer, barrier, h, L_x, w_y):
    vv = vv_poisson
    vv_pot = vv * (-1)

    # Cut the top gate/back gate insulator region

    N_tgi = int(D_tg_buffer/h)

    x_scat_min = -L_x/2
    x_scat_max = L_x/2

    y_max_scat = w_y/2
    y_min_scat = -w_y/2


    Nx_cut = int((x_scat_max - x_scat_min)/h) + 1
    Ny_cut = int((y_max_scat- y_min_scat)/h) + 1

    v_cut = np.zeros((Ny_cut,Nx_cut))

    v_cut[:,:] = vv_pot[N_tgi:N_tgi+Ny_cut,:]

    # Create the scattering region for the R matrix code, including some of
        the leads

    V_b = barrier

    y_min_int = -4
    y_max_int = 4

    y_min_bar = -1
    y_max_bar = 1

    N_y_bar = int((y_max_bar - y_min_bar)/h) + 1
    Ny_int = int((y_max_int - y_min_int)/h) + 1

    # Add the potential barrier

    v_scat_bar = v_cut

    N_add = int((Ny_int-N_y_bar)/2)
    v_scat_bar[N_add+1: N_add + N_y_bar-1,: ] = v_cut[N_add+1: N_add +
        N_y_bar-1,: ] + V_b

    return v_scat_bar

def central_region():


    # Solve the Poisson equation:

    vv = Solve_Poisson(L_x = L_device_int, W_y = y_device_int, h=h, top=top,
        bottom=bottom, drain=drain, source=source)
```

```
    vv_scat = scat_pot(vv_poisson = vv, D_tg_buffer = D_tgi, barrier =
        V_barrier, h=h, L_x = L_device_int, w_y = y_scat)

    return vv_scat

potential = central_region()

# x = np.linspace(-15, 15, 301)
# y = np.linspace(-4, 4, 81)

# X, Y = np.meshgrid(x, y)

# fig,ax=plt.subplots(1,1)
# cp = ax.contourf(X, Y, potential)
# fig.colorbar(cp) # Add a colorbar to a plot
# ax.set_title('Contour plot')
# ax.set_xlabel('x (cm)')
# ax.set_ylabel('y (cm)')
# # plt.savefig('Contour_plot.png')
# plt.show()

# Kwant

lat = kwant.lattice.square(a, norbs = 1)
syst = kwant.Builder()

def pot(x,y, potential):
    index_x = int(abs(-15-x)/h)
    index_y = int(abs(-4-y)/h)
    return potential[index_y, index_x]

def onsite(site):
    x,y = site.pos
    if (-(L-lead_scat) <= x <= L-lead_scat and -W <= y <= W):
        return 4*t + pot(x=x,y=y, potential=potential)
    if (-L <= x <= -(L-lead_scat) and (-W <= y <= -(W-block_lead))):
        return 4*t -source
    if (L-lead_scat <= x <= L and (W-block_lead <= y <= W)):
        return 4*t -drain



def scattering_region(pos):
    (x,y) = pos
    poisson_rectangle = (-(L-lead_scat) <= x <= L-lead_scat and -W <= y <= W)
    lead_1 = (-L <= x <= -(L-lead_scat) and (-W <= y <= -(W-block_lead)))
    lead_2 = (L-lead_scat <= x <= L and (W-block_lead <= y <= W))
    return poisson_rectangle or lead_1 or lead_2

syst[lat.shape(scattering_region, (0,0))] = onsite
syst[lat.neighbors()] = -t


sym = kwant.TranslationalSymmetry((-a,0))

# Add leads:
```

```
lead_left = kwant.Builder(sym)
def left(pos):
    (x,y) = pos
    return (-W <= y <= -(W-block_lead))

i = int(-L_central/a)
j = int(-1/a)
# print(i)
lead_left[lat.shape(left, lat(i,j).pos)] = 4*t - source
lead_left[lat.neighbors()] = -t
syst.attach_lead(lead_left)

lead_right = kwant.Builder(sym)
def right(pos):
    (x,y) = pos
    return (W-block_lead <= y <= W)

k = int(L_central/a)
l = int(1/a)

lead_right[lat.shape(right, lat(k,l).pos)] = 4*t - drain
lead_right[lat.neighbors()] = -t
syst.attach_lead(lead_right.reversed())

kwant.plot(syst);

fsyst = syst.finalized()

# Color the sites accroding to their onsite potential (= their onsite
    hamiltonian value)

kwant.plot(fsyst, site_color = lambda i: fsyst.hamiltonian(i,i));

# Check band dispersion in the leads

kwant.plotter.bands(fsyst.leads[0]);

Es = np.linspace(0,1.5,1000)
gs = []

start_time = time.time()

for E in Es:
    S = kwant.smatrix(fsyst, E)
    gs.append(S.transmission(1,0))

print("time: %3.2f"%(time.time()-start_time))

# f = plt.figure(figsize=(8, 5))
# plt.plot(Es, gs, 'k-')
# plt.ylabel("$g \quad [e^2/h]$")
# plt.xlabel("$E \quad [t] $")
# # plt.savefig(out_dir+"transmission-prob.png", dpi=300,
    bbox_inches='tight')
# plt.show();
# plt.close()
```

```
dir = "/Users/amapreda/Kwant_transport/Nanotransistor_dense_grid/"

# plot transmission curve
f = plt.figure(figsize=(8, 5))
plt.plot(Es, gs, 'k-')
plt.ylabel("Transmission probability")
plt.xlabel("Energy (eV)")
name = "Vb = " + str(V_barrier)+ ", Vd = " + str(drain) + ", Vg = " +
    str(top) + ", Vg_bottom = " + str(bottom)
plt.title(name)
name_save = "Vb-" + str(V_barrier)+ "_Vd-" + str(drain) + "_Vg-" + str(top)
    + ".png"
# plt.savefig(dir + name_save, dpi=300, bbox_inches='tight')
plt.show()
plt.close()

f = plt.figure(figsize=(8, 5))
plt.plot(Es, gs, 'k-')
plt.ylabel("Transmission probability")
plt.xlabel("Energy (eV)")
plt.yscale('log')
name = "Vb = " + str(V_barrier)+ ", Vd = " + str(drain) + ", Vg_top = " +
    str(top) + ", Vg_bottom = " + str(bottom)
plt.title(name)
name_save = "Vb-" + str(V_barrier)+ "_Vd-" + str(drain) + "_Vg-" + str(top)
    + "_log.png"
# plt.savefig(dir + name_save, dpi=300, bbox_inches='tight')
plt.show()
plt.close()


# Write to file

filename = "/Users/amapreda/Nanotransistor_simulations/Nonsymmetric_Vg/
Transmission_Vg03Vd02Vb2_kwant.dat"
textToSave= "a = " + str(a) + "\n" + "m_eff = " + str(m) + "\n" + "Vb = " +
    str(V_barrier)+ "\n" + "Vd = " + str(drain) + "\n" + "Vg_top = " +
    str(top) + "\n" + "Vg_bottom = " + str(bottom) + "\n" + "Energy
    Transmission" + "\n"
n=0
for i in range(0,len(Es)):
    textToSave+="{0:.6f}".format(Es[n])+ " " + '{:.6e}'.format(gs[n])
    textToSave+="\n"
    n=n+1
outfile = open(filename, 'w')
outfile.write(textToSave)
outfile.close() # Close the file


index_list_min = np.zeros(np.shape(min)[0])
index_list_max = np.zeros(np.shape(max)[0])

for i in range(np.shape(min)[0]):
    index_list_min[i] = gs.index(min[i])


for i in range(np.shape(min)[0]):
```

```
    index_list_max[i] = gs.index(max[i])

# Plot wavefunctions

mode = int(0)

for i in range(np.shape(index_list_min)[0]):
    i = int(index_list_min[i])
    wf = kwant.wave_function(fsyst, Es[i])
    wave_function_right = wf(1)[mode]
    wave_function_left = wf(0)[mode]
    density_left = np.abs(wave_function_left)**2
    density_right = np.abs(wave_function_right)**2
    density_log_left = np.log(density_left)
    density_log_right = np.log(density_right)

    fig = plt.figure()
    ax = kwant.plotter.map(fsyst, density_log_left,cmap='Blues')
    name_save_3 = "Vb-" + str(V_barrier)+ "_Vd-" + str(drain) + "_Vg-" +
        str(top) + "E = " + str(round(Es[i],3)) + "_wf_log.pdf"
    ax.savefig('./Wavefunction_vg03_vd02_vb2_left/Mode_' + str(mode) +
        '/Min_log/' + name_save_3)
    plt.close()


for i in range(np.shape(index_list_max)[0]):
    i = int(index_list_max[i])
    wf = kwant.wave_function(fsyst, Es[i])
    wave_function_right = wf(1)[mode]
    wave_function_left = wf(0)[mode]
    density_left = np.abs(wave_function_left)**2
    density_right = np.abs(wave_function_right)**2
    density_log_left = np.log(density_left)
    density_log_right = np.log(density_right)

    fig = plt.figure()
    ax = kwant.plotter.map(fsyst, density_log_left,cmap='Blues')
    name_save_3 = "Vb-" + str(V_barrier)+ "_Vd-" + str(drain) + "_Vg-" +
        str(top) + "E = " + str(round(Es[i],3)) + "_wf_log.pdf"
    ax.savefig('./Wavefunction_vg03_vd02_vb2_left/Mode_' + str(mode) +
        '/Max_log/' + name_save_3)
    plt.close()
```

K

CNN for transmission function prediction

LISTING K.1: KWANT code for the multi-terminal quantum sorter device

```
import math
import os
from matplotlib import pyplot as plt
import numpy as np
import pandas as pd
from sklearn import metrics
import tensorflow as tf
from tensorflow.python.data import Dataset
from keras.utils import np_utils
from sklearn.model_selection import train_test_split
from sklearn.metrics import r2_score

tfk = tf.keras
tfkl = tf.keras.layers

N_jobs =2601
N_jobs_extra = 1886
N_x = 60
N_y = 60

path = '/home/apreda/Nanotransistor/CNN/Poisson_CNN_new'
path_extra = '/home/apreda/Nanotransistor/CNN/Poisson_CNN_new_part2'

run_zzz = "poisson_red-000"
run = "poisson_red-"
run_z = "poisson_red-0"
run_zz = "poisson_red-00"

List = [0] * (N_jobs + N_jobs_extra)
complete_path = [0] * (N_jobs+ N_jobs_extra)

List[0] = run_zz + str(0)
```

```
# complete_path[0] = os.path.join(path, str(List[0]))

for i in range(0,10):
    List[i] = run_zzz + str(i) + ".txt"

for i in range(10,100):
    List[i] = run_zz + str(i) + ".txt"

for i in range(100,1000):
    List[i] = run_z + str(i) + ".txt"

for i in range(1000,N_jobs+ N_jobs_extra):
    List[i] = run + str(i) + ".txt"


for k in range(0,N_jobs):
    complete_path[k] = os.path.join(path, str(List[k]))

for k in range(0, N_jobs_extra):
    complete_path[k+N_jobs] = os.path.join(path_extra, str(List[k]))

N_all = N_jobs + N_jobs_extra


    # Read all images as 3D arrays

pot_cut = np.loadtxt(complete_path[0])

input_potentials = np.zeros((N_all,N_y,N_x))
for k in range(N_all):
    n=0
    pot_cut = np.loadtxt(complete_path[k])
    for i in range(0,N_x):
        for j in range(0, N_y):
            input_potentials[k,j,i]=pot_cut[n]
            n=n+1

            # Normalize the data in all the arrays

x_features = np.zeros((N_all,N_y,N_x))
min = np.amin(input_potentials)
max = np.amax(input_potentials)
scale =max-min

for k in range(0,N_all):
    min_val = np.amin(input_potentials[k])
        for i in range(0,N_x):
        for j in range(0, N_y):
            x_features[k,j,i]=(input_potentials[k,j,i]-min_val)/scale

path = '/home/apreda/Nanotransistor/CNN/T_mean_log_all_v2.txt'
data = np.loadtxt(path)

data_pos = data * (-1)
data_res = data_pos.reshape(N_all,-1)
y_target = np.zeros_like(data_res)
```

```
# print(data_res[100])

#for i in range(N_all):
#    max = np.amax(data_res[i][:])
#    y_target[i] = data_res[i]/max

max_t = np.amax(data_res)
#min_t = np.amin(data_res)

scale_t = max_t

for i in range(N_all):
    # max = np.amax(data_res[i][:])
   # min_loc = np.amin(data_res[i][:])
    # scale = max - min
    y_target[i] = (data_res[i])/scale_t


# print(y_target[100])
#x_features_t = tf.convert_to_tensor(x_features)
#y_target_t= tf.convert_to_tensor(y_target)
# Split data into training, test and validation

# Create images where borders are at the center

def flip(array):
    x_features_centered = np.zeros((60,60))
    b1 = array[0:30,0:30]
    b2 = array[0:30,30:60]
    b3 = array[30:60,0:30]
    b4 = array[30:60,30:60]

    b1_flip = np.flip(b1, axis=0)
    b2_flip = np.flip(b2, axis=0)
    b3_flip = np.flip(b3, axis=0)
    b4_flip = np.flip(b4, axis=0)

    x_features_centered[0:30,0:30] = b1_flip
    x_features_centered[0:30,30:60] = b2_flip
    x_features_centered[30:60,0:30] = b3_flip
    x_features_centered[30:60,30:60] = b4_flip

    return x_features_centered

x_features_flip = np.zeros_like(x_features)
for i in range(N_jobs):
    input = x_features[i]
    out = flip(array = input)
    x_features_flip[i] = out




x_train, x_test, y_train, y_test = train_test_split(x_features, y_target,
    test_size=0.1, random_state=45)
```

```
x_train, x_val, y_train, y_val = train_test_split(x_train, y_train,
    test_size=0.2, random_state=45)

#Set random seed
tf.random.set_seed(42)

#Create model
model = tf.keras.Sequential([

    tf.keras.layers.Conv2D(filters=16, kernel_size=(3,3), padding="same",
        activation= tf.keras.layers.LeakyReLU(alpha=0.3),
                         input_shape=(N_y,N_x,1)),
    tf.keras.layers.MaxPool2D(pool_size=(2,2)),
    tf.keras.layers.Conv2D(filters = 32,kernel_size=(4,4), padding="same",
        activation=tf.keras.layers.LeakyReLU(alpha=0.8)),
    tf.keras.layers.MaxPool2D(pool_size=(2,2)),
    tf.keras.layers.Conv2D(filters = 64,kernel_size=(5,5), padding="same",
        activation=tf.keras.layers.LeakyReLU(alpha=0.8)),
    tf.keras.layers.MaxPool2D(pool_size=(2,2)),
    tf.keras.layers.Flatten(),
    tf.keras.layers.Dense(32, activation="relu"),
    tf.keras.layers.Dropout(0.2),
    tf.keras.layers.Dense(64, activation="relu"),
    tf.keras.layers.Dropout(0.2),
    tf.keras.layers.Dense(500, activation="relu"),
    tf.keras.layers.Dense(100, activation="relu"),
    ])

#Compile the model

model.compile(loss="mse",
             optimizer=tf.keras.optimizers.Adam(learning_rate = 0.0001),
             metrics=["mse"])

#Show summary

model.summary()

# Fit the model
epochs = 6000
batch = 32

history = model.fit(x_train, y_train,
                  epochs=epochs,batch_size=batch,
                  validation_data=(x_val,y_val), verbose=1
                  )
y_pred = model.predict(x_test)

test_dim_1 = np.shape(y_test)[0]
test_dim_2 = 100

filename = "Tfunction_test_predicted.txt"
textToSave=""
for i in range(0,test_dim_1):
    for j in range (0, test_dim_2):
        a = float(y_test[i][j])
        b = float(y_pred[i][j])
```

```
        textToSave+="{0:.6e}".format(a)+ " " + "{0:.6e}".format(b) + "\n"
    textToSave+="\n"

outfile = open(filename, 'w')
outfile.write(textToSave)
outfile.close() # Close file


filename = "Potential_test.txt"
textToSave=""
for i in range(0,test_dim_1):
    x = x_test[i]
    a = x.flatten()
    for j in range (0, N_y*N_x):
        b = float(a[j])
        textToSave+="{0:.6e}".format(b)+ " " + "\n"
    textToSave+="\n"

outfile = open(filename, 'w')
outfile.write(textToSave)
outfile.close()

# Calculate and plot R2 score

def r2_coef(y_true, y_pred):
    y_pred = tf.convert_to_tensor(y_pred, np.float32)
    y_true = tf.convert_to_tensor(y_true, np.float32)
    SS_res = tfk.backend.sum(tfk.backend.square(y_true - y_pred))
    SS_tot = tfk.backend.sum(tfk.backend.square(y_true -
        tfk.backend.mean(y_true)))
    return (1 - SS_res/(SS_tot + tfk.backend.epsilon()) )
    # stabilize the division with a small epsilon

r2 = r2_coef(y_test, y_pred)              #you can also use r2_score from
    scikit learn, if y_test and y_pred are numpy arrays
r2_coeff = math.floor(r2*1000)/1000

print("R2 coeff: ", r2_coeff)


print(r2_score(y_test, y_pred))

if (r2_coeff > 0):
    plt.rcParams["figure.figsize"] = (7,7)
    plt.scatter(y_test, y_pred)
    plt.text(0.9,0.4, r'$R^{2} = $' + str(r2_coeff), fontsize = 14)
    plt.ylabel(r"I_drain predicted", fontsize = 15)
    plt.xlabel(r"I_drain real ", fontsize = 15)
    plt.xticks(fontsize = 20)
    plt.yticks(fontsize = 20)
    lineStart = y_pred.min()
    lineEnd = y_test.max()
    y_lim = plt.ylim()
    x_lim = plt.xlim()
    plt.plot(x_lim, y_lim, '--', color = 'b', linewidth = 3)
    plt.ylim(y_lim)
    plt.xlim(x_lim)
```

```
    plt.savefig("Transmission_prediction_R2.png")
   # plt.show()

plt.figure(figsize=(7,7))
plt.plot(np.arange(epochs),history.history['loss'], label="Training")
plt.plot(np.arange(epochs), history.history['val_loss'],
    label="validation", c="darkorange")
plt.xlabel("epoch")
plt.ylabel("loss")
plt.legend()
plt.savefig("CNN_loss_trfunction.png")

#functions to plot testing data and the prediction (vs actual data)

test =[10,30,40,50,70,90,100, 150, 200]

for i in range(len(test)):
    name = "./Predictions/Predictions_oscillations_" + str(i) + ".png"
    test_case = test[i]
    plt.figure(figsize=[10, 3])
    plt.subplot(1, 2, 1)
    plt.imshow(x_test[test_case, :, :])
    plt.title('Poisson potential ')
    plt.subplot(1, 2, 2)
    plt.plot(y_test[test_case, :], ls=':', c='k', label='True', alpha=0.9)
    plt.plot(y_pred[test_case, :], c='red', label='Pred.', alpha=0.4)
    plt.ylim([0, 1])
    plt.title('Transmission oscillation prediction')
    plt.legend()
    plt.savefig(name)
```

L
Quantum sorter (KWANT code)

LISTING L.1: KWANT code for the multi-terminal quantum sorter device

```
import matplotlib.pyplot as plt
from math import exp
import numpy as np
import pandas as pd
import kwant
from scipy.sparse import csc_matrix
from scipy.sparse.linalg import inv
import scipy
import scipy.linalg
import time
import tinyarray

# CONSTANTS

kB = scipy.constants.value("Boltzmann constant in eV/K")  # unit: eV/K
qe = scipy.constants.value("elementary charge")            # unit: C
me = scipy.constants.value("electron mass")/qe*1e-18       # unit:
    eV*s^2/nm^2 !!!
hP = scipy.constants.value("Planck constant in eV s")      # unit: eV*s
hbar = hP/(2*scipy.pi)                                     # unit: eV*s
mu_B = scipy.constants.value(’Bohr magneton in eV/T’)
eps0 = scipy.constants.value("electric constant")*qe*1e-9 # unit:
    C^2/(eV*nm)

# Pauli matrices

sigma_0 = tinyarray.array([[1, 0], [0, 1]])
sigma_x = tinyarray.array([[0, 1], [1, 0]])
sigma_y = tinyarray.array([[0, -1j], [1j, 0]])
sigma_z = tinyarray.array([[1, 0], [0, -1]])

h=5
```

```
# Read potential from file


v2D = pd.read_table("./Comparisons/data_run_000/v2D.dat", delimiter = ' ',
    names=['x', 'y', 'pot'], usecols = [0,1,2])
v2D.head()
v2D_arr = v2D['pot'].to_numpy()
print(np.shape(v2D_arr))
v2D_reshaped = v2D_arr.reshape(200,200)
v2D_rotate = np.rot90(v2D_reshaped, k=1, axes=(0,1))
plt.imshow(v2D_rotate)
plt.show()

# Function to add potential to onsite terms in the TB model

def pot(x,y, potential):
    index_x = int(abs(-497.5-x)/h)
    index_y = int(abs(-497.5-y)/h)
    return potential[index_y, index_x]

# Check

pot(x = -497.5, y = -497.5, potential = v2D_reshaped)

# System dimensions

L= 497.5
W = L           #nm
# L = 375
lead_scat = 0
# W = 500
block_lead = 50

a=5
m = 0.023
t = hbar**2/(2*me*m*a**2)      # units: eV
alpha = 0.0 * 10**(-3)


# B_up = B_eV
# B_down = -B_eV

Ez = 50 * 10**(-3) * 0.5


B_up = 0.4
B_down = -0.4

lat = kwant.lattice.square(a, norbs = 2)
syst = kwant.Builder()

# Add Zeeman term

def onsite_spin_dep(site):
    x,y = site.pos
    if ((-L<= x<=L) and (-L<= y <=L)):
        if (L-125<=x<=L):
```

```
            if ((300<=y<=450) or (50<=y<=200)):
                return ( 4*t * sigma_0+ pot(x=x,y=y,
                    potential=v2D_rotate)*sigma_0 + Ez*sigma_z + Ez*sigma_0 )
            elif ((-47.5 >= y >=-197.5) or (-297.5>=y>=-447.5)):
                return ( 4*t * sigma_0+ pot(x=x,y=y,
                    potential=v2D_rotate)*sigma_0 - Ez*sigma_z + Ez*sigma_0)
            else: return ( 4*t+ pot(x=x,y=y, potential=v2D_rotate))*sigma_0
        else: return ( 4*t+ pot(x=x,y=y, potential=v2D_rotate))*sigma_0
    else: return 0


def scattering_region(pos):
    (x,y) = pos
    poisson_rectangle = (-(L-0) <= x <= L+0 and -W <= y <= W)
    lead_1 = (-L <= x <= -(L-0) and (-75 <= y <= 75))
    lead_2 = (L<= x <= L + lead_scat and ( 300 <= y <= 450))
    lead_3 = (L <= x <= L + lead_scat and (50 <= y <= 200))
    lead_4 = (L <= x <= L + lead_scat and (-50 >= y >= -200))
    lead_5 = (L <= x <= L + lead_scat and (-300 >= y >= -450))
    return poisson_rectangle or lead_1 or lead_2 or lead_3 or lead_4 or
        lead_5

syst[lat.shape(scattering_region, (0,0))] = onsite_spin_dep

# syst[lat.neighbors()] = hopping             ## no rashba SOI

# For Rashba SOI, we define x,y direction hopping parameters:

# hoppings in x-direction
syst[kwant.builder.HoppingKind((1, 0), lat, lat)] = -t * sigma_0- 1j *
    alpha * sigma_y
# hoppings in y-directions
syst[kwant.builder.HoppingKind((0, 1), lat, lat)] = -t * sigma_0 + 1j *
    alpha * sigma_x

sym = kwant.TranslationalSymmetry((-a,0))

# Add leads:

lead_left = kwant.Builder(sym, conservation_law=-sigma_z)

def left(pos):
    (x,y) = pos
    return (-75 <= y <= 75)


lead_left[lat.shape(left, lat(-L/a,75/a).pos)] = 4*t*sigma_0          #
    Lead_0
lead_left[lat.neighbors()] = -t*sigma_0
syst.attach_lead(lead_left)

lead_right_1 = kwant.Builder(sym, conservation_law=-sigma_z)
lead_right_2 = kwant.Builder(sym, conservation_law=-sigma_z)
lead_right_3 = kwant.Builder(sym, conservation_law=-sigma_z)
lead_right_4 = kwant.Builder(sym, conservation_law=-sigma_z)

def right_1(pos):
```

```
    (x,y) = pos
    return ( 300 <= y <= 450)

def right_2(pos):
    (x,y) = pos
    return   (50 <= y <= 200)

def right_3(pos):
    (x,y) = pos
    return  (-50 >= y >= -200)

def right_4(pos):
    (x,y) = pos
    return  (-300 >= y >= -450)


def lead_onsite(site):
    return sigma_z


lead_right_1[lat.shape(right_1, lat((L + lead_scat)/a,450/a).pos)] =
    4*t*sigma_0
lead_right_2[lat.shape(right_2, lat((L + lead_scat)/a,200/a).pos)] =
    4*t*sigma_0
lead_right_3[lat.shape(right_3, lat((L + lead_scat)/a,-200/a).pos)] =
    4*t*sigma_0
lead_right_4[lat.shape(right_4, lat((L + lead_scat)/a,-450/a).pos)] =
    4*t*sigma_0

lead_right_1[lat.neighbors()] = -t*sigma_0
lead_right_2[lat.neighbors()] = -t*sigma_0
lead_right_3[lat.neighbors()] = -t*sigma_0
lead_right_4[lat.neighbors()] = -t*sigma_0


syst.attach_lead(lead_right_1.reversed())
syst.attach_lead(lead_right_2.reversed())
syst.attach_lead(lead_right_3.reversed())
syst.attach_lead(lead_right_4.reversed())

kwant.plot(syst, num_lead_cells=20);

# Plot potential in the system

def V(site):
    Hd = onsite_spin_dep(site)
    # return (Hd[0,0] - Hd[1,1]).real
    return (Hd[0,0]).real
kwant.plotter.map(syst, V, cmap='inferno');

# Finalize system

fsyst = syst.finalized()

wave_funcs = kwant.wave_function(fsyst, energy=0.0037)
wf = wave_funcs(0)
```

```
# up and dw components
Dup = kwant.operator.Density(fsyst, (sigma_0+sigma_z)/2 )
Ddw = kwant.operator.Density(fsyst, (sigma_0-sigma_z)/2)

dens_up = Dup.bind()
dens_dn = Ddw.bind()

# kwant.plotter.current(fsyst, dens_up(wf[0]));
# kwant.plotter.current(fsyst, current_up(wf[1]));
# kwant.plotter.current(fsyst, current_dn(wf[2]));
# kwant.plotter.current(fsyst, current_dn(wf[3]));

fsat = 5 # saturation factor for color scale

fig, ax = plt.subplots(2,2, sharex=True, sharey=True, figsize=(15,10))
plt.rcParams.update({'font.size': 16})

density_1 = dens_up(wf[0]); vmax = fsat*np.abs(density_1).max()
kwant.plotter.density(fsyst, density_1, ax=ax[0,0], vmin=-vmax, vmax=vmax,
    cmap='bwr', background = 'aliceblue')
ax[0,0].set_title(R"Mode 0 $\uparrow$", fontsize=14)

density_2 = dens_up(wf[1]); vmax = fsat*np.abs(density_2).max()
kwant.plotter.density(fsyst, density_2, ax=ax[0,1], vmin=-vmax, vmax=vmax,
    cmap='bwr', background = 'aliceblue')
ax[0,1].set_title(R"Mode 1 $\uparrow$", fontsize=14)

density_3 = dens_dn(wf[2]); vmax = fsat*np.abs(density_3).max()
kwant.plotter.density(fsyst, density_3, ax=ax[1,0], vmin=-vmax, vmax=vmax,
    cmap='bwr', background = 'aliceblue')
ax[1,0].set_title(R"Mode 0 $\downarrow$", fontsize=14)

density_4 =dens_dn(wf[3]); vmax = fsat*np.abs(density_4).max()
kwant.plotter.density(fsyst, density_4, ax=ax[1,1], vmin=-vmax, vmax=vmax,
    cmap='bwr', background = 'aliceblue')
ax[1,1].set_title(R"Mode 1 $\downarrow$", fontsize=14)


plt.tight_layout()
plt.show()

incoming_lead = 0
outgoing_leads = [1,2,3,4]




E_min = 3 * 10**(-3)
E_max = 5 * 10**(-3)    #eV
N_en = 400


Es = np.linspace(E_min,E_max,N_en)

T_k0_up = np.zeros((4,len(Es)))
T_k0_down = np.zeros((4,len(Es)))
T_k1_up = np.zeros((4,len(Es)))
T_k1_down = np.zeros((4,len(Es)))
```

```
# Transmission for mode_1 spin_up:

for k in range(len(outgoing_leads)):
    out = int(outgoing_leads[k])
    for i in range(len(Es)):
        E = Es[i]
        # print(E)
        S = kwant.smatrix(fsyst, energy=E)
        S_out_0 = S.submatrix(out,0)
        prop_1 = int(S.num_propagating(out)/2)
        # print(prop_1)
        S_out0_up_up = S.submatrix((out, 0), (0, 0))
        S_out0_up_down = S.submatrix((out, 1), (0, 0))
        # print(np.shape( S_out0_up_up))
        # print(E)
        sum_1 = [np.linalg.norm(S_out0_up_up[j,0])**2 for j in range
            (prop_1)]
        trans_mode_0_upup = np.sum(sum_1)
        sum_2 = [np.linalg.norm(S_out0_up_down[j,0])**2 for j in range
            (prop_1)]
        trans_mode_0_updown = np.sum(sum_2)
        trans_all = trans_mode_0_upup + trans_mode_0_updown
        # trans_mode_0_up.append(trans_all)
        T_k0_up[k][i] = trans_all


# Transmission for mode_1 spin_down:

for k in range(len(outgoing_leads)):
    out = int(outgoing_leads[k])
    for i in range(len(Es)):
        E = Es[i]
        S = kwant.smatrix(fsyst, energy=E)
        S_out_0 = S.submatrix(out,0)
        prop_1 = int(S.num_propagating(out)/2)
        # print(prop_1)
        S_out0_down_up = S.submatrix((out, 0), (0, 1))
        S_out0_down_down = S.submatrix((out, 1), (0, 1))
        sum_1 = [np.linalg.norm(S_out0_down_up[j,0])**2 for j in range
            (prop_1)]
        trans_mode_0_upup = np.sum(sum_1)
        sum_2 = [np.linalg.norm(S_out0_down_down[j,0])**2 for j in range
            (prop_1)]
        trans_mode_0_updown = np.sum(sum_2)
        trans_all = trans_mode_0_upup + trans_mode_0_updown
        # trans_mode_0_up.append(trans_all)
        T_k0_down[k][i] = trans_all

# Transmission for mode_2 spin_up:

for k in range(len(outgoing_leads)):
    out = int(outgoing_leads[k])
    for i in range(len(Es)):
        E = Es[i]
        S = kwant.smatrix(fsyst, energy=E)
```

```
        S_out_0 = S.submatrix(out,0)
        prop_1 = int(S.num_propagating(out)/2)
        prop_in = S.num_propagating(0)
        # print(prop_1)
        S_out0_up_up = S.submatrix((out, 0), (0, 0))
        S_out0_up_down = S.submatrix((out, 1), (0, 0))
        if (prop_in >= 4):
            sum_1 = [np.linalg.norm(S_out0_up_up[j,1])**2 for j in range
                (prop_1)]
        else:
            sum_1 = 0
        trans_mode_0_upup = np.sum(sum_1)
        if (prop_in >= 4):
            sum_2 = [np.linalg.norm(S_out0_up_down[j,1])**2 for j in range
                (prop_1)]
        else:
            sum_2 = 0
        trans_mode_0_updown = np.sum(sum_2)
        trans_all = trans_mode_0_upup + trans_mode_0_updown
        # trans_mode_0_up.append(trans_all)
        T_k1_up[k][i] = trans_all

# Transmission for mode_2 spin_down:

for k in range(len(outgoing_leads)):
    out = int(outgoing_leads[k])
    for i in range(len(Es)):
        E = Es[i]
        S = kwant.smatrix(fsyst, energy=E)
        S_out_0 = S.submatrix(out,0)
        prop_1 = int(S.num_propagating(out)/2)
        prop_in = S.num_propagating(0)
        # print(prop_1)
        S_out0_down_up = S.submatrix((out, 0), (0, 1))
        S_out0_down_down = S.submatrix((out, 1), (0, 1))

        if (prop_in >= 4):
            sum_1 = [np.linalg.norm(S_out0_down_up[j,1])**2 for j in range
                (prop_1)]
        else:
            sum_1 = 0
        trans_mode_0_upup = np.sum(sum_1)
        if (prop_in >= 4):
            sum_2 = [np.linalg.norm(S_out0_down_down[j,1])**2 for j in range
                (prop_1)]
        else:
            sum_2 = 0
        trans_mode_0_updown = np.sum(sum_2)
        trans_all = trans_mode_0_upup + trans_mode_0_updown
        # trans_mode_0_up.append(trans_all)
        T_k1_down[k][i] = trans_all


fig, axs = plt.subplots(2, 2, figsize=(15, 10))
# fig = plt.figure(figsize=(40,40))

axs[0,0].plot(Es, T_k0_up[0], label='$s_{1}$')
```

```
axs[0,0].plot(Es, T_k0_up[1], label='$s_{2}$')
axs[0,0].plot(Es, T_k0_up[2], label='$s_{3}$')
axs[0,0].plot(Es, T_k0_up[3], label='$s_{4}$')
axs[0, 0].set_ylabel('Transmission')
axs[0, 0].set_xlabel('$E$')
# axs[0,0].set_xlim(11,13)
axs[0, 0].legend();
axs[0, 0].set_title("Transmission of mode $k_{0}up$")

axs[0, 1].plot(Es, T_k0_down[0], label='$s_{1}$')
axs[0, 1].plot(Es, T_k0_down[1], label='$s_{2}$')
axs[0, 1].plot(Es, T_k0_down[2], label='$s_{3}$')
axs[0, 1].plot(Es, T_k0_down[3], label='$s_{4}$')

axs[0, 1].set_ylabel('Transmission')
axs[0, 1].set_xlabel('$E$')
# axs[0,1].set_xlim(11,13)
axs[0, 1].legend();
axs[0, 1].set_title("Transmission of mode $k_{0}dn$")

axs[1, 0].plot(Es, T_k1_up[0], label='$s_{1}$')
axs[1, 0].plot(Es, T_k1_up[1], label='$s_{2}$')
axs[1, 0].plot(Es, T_k1_up[2], label='$s_{3}$')
axs[1, 0].plot(Es, T_k1_up[3], label='$s_{4}$')

axs[1, 0].set_ylabel('Transmission')
axs[1, 0].set_xlabel('$E$')
# axs[1,0].set_xlim(11,13)
# axs[1,0].axvspan(25,25.2, color = 'teal', alpha=0.3)
axs[1, 0].legend();
axs[1, 0].set_title("Transmission of mode $k_{1}up$")


axs[1,1].plot(Es, T_k1_down[0], label='$s_{1}$')
axs[1,1].plot(Es, T_k1_down[1], label='$s_{2}$')
axs[1,1].plot(Es, T_k1_down[2], label='$s_{3}$')
axs[1,1].plot(Es, T_k1_down[3], label='$s_{4}$')

axs[1,1].set_ylabel('Transmission')
axs[1,1].set_xlabel('$E$')
# axs[1,1].set_xlim(11,13)
# axs[1,1].axvspan(25,25.7, color = 'teal', alpha=0.3)
axs[1,1].legend();
axs[1,1].set_title("Transmission of mode $k_{1}dn$")

for ax in axs.flat:
    ax.set(xlabel='Energy', ylabel='Transmission')

    # # Hide x labels and tick labels for top plots and y ticks for right
        plots.
    # for ax in axs.flat:
    #     ax.label_outer()
    title = './Transmission_' + str('kwant') + '.png'
    plt.show()
    # fig.savefig(title)
    # plt.close()
```

Bibliography

[1] Walter Kohn. "An essay on condensed matter physics in the twentieth century". *Reviews of Modern Physics* 71.2 (1999), S59.

[2] Edwin Bedolla, Luis Carlos Padierna, and Ramón Castaneda-Priego. "Machine learning for condensed matter physics". *Journal of Physics: Condensed Matter* 33.5 (2020), 053001.

[3] Dragoş-Victor Anghel, Amanda Teodora Preda, and George Alexandru Nemnes. "The R-matrix formalism for two-particle scattering problems". *Physics Letters A* 425 (2022), 127865. ISSN: 0375-9601. DOI: `https://doi.org/10.1016/j.physleta.2021.127865`. URL: `https://www.sciencedirect.com/science/article/pii/S0375960121007295`.

[4] H. Bruus and K. Flensberg. *Many-Body Quantum Theory in Condensed Matter Physics: An Introduction*. Oxford Graduate Texts. OUP Oxford, 2004. ISBN: 9780198566335. URL: `https://books.google.ro/books?id=v5vhg1tYLC8C`.

[5] S. Datta. *Electronic Transport in Mesoscopic Systems*. Cambridge Studies in Semiconductor Physi. Cambridge University Press, 1997. ISBN: 9780521599436. URL: `https://books.google.ro/books?id=28BC-ofEhvUC`.

[6] B. J. van Wees, H. van Houten, C. W. J. Beenakker, J. G. Williamson, L. P. Kouwenhoven, D. van der Marel, and C. T. Foxon. "Quantized conductance of point contacts in a two-dimensional electron gas". *Phys. Rev. Lett.* 60 (9 Feb. 1988), 848–850. DOI: `10.1103/PhysRevLett.60.848`. URL: `https://link.aps.org/doi/10.1103/PhysRevLett.60.848`.

[7] D A Wharam, T J Thornton, R Newbury, M Pepper, H Ahmed, J E F Frost, D G Hasko, D C Peacock, D A Ritchie, and G A C Jones. "One-dimensional transport and the quantisation of the ballistic resistance". *Journal of Physics C: Solid State Physics* 21.8 (Mar. 1988), L209. DOI: `10.1088/0022-3719/21/8/002`. URL: `https://dx.doi.org/10.1088/0022-3719/21/8/002`.

[8] C.W.J. Beenakker and H. van Houten. "Quantum Transport in Semiconductor Nanostructures". *Semiconductor Heterostructures and Nanostructures*. Ed. by Henry Ehrenreich and David Turnbull. Vol. 44. Solid State Physics. Academic Press, 1991, pp. 1–228. DOI: `https://doi.org/10.1016/S0081-1947(08)60091-0`. URL: `https://www.sciencedirect.com/science/article/pii/S0081194708600910`.

[9] M. Büttiker. "Scattering theory of current and intensity noise correlations in conductors and wave guides". *Phys. Rev. B* 46 (19 1992), 12485–12507. DOI: `10.1103/PhysRevB.46.12485`. URL: `https://link.aps.org/doi/10.1103/PhysRevB.46.12485`.

[10] Mariana M. Odashima, Beatriz G. Prado, and E. Vernek. "Pedagogical introduction to equilibrium Green's functions: condensed-matter examples with numerical implementations". *Revista Brasileira de Ensino de Física* 39.1 (Sept. 2016). ISSN: 1806-1117. DOI: `10.1590/1806-9126-rbef-2016-0087`. URL: `http://dx.doi.org/10.1590/1806-9126-RBEF-2016-0087`.

[11] T. Lancaster and S. Blundell. *Quantum Field Theory for the Gifted Amateur*. OUP Oxford, 2014. ISBN: 9780199699339. URL: `https://books.google.ro/books?id=Y-0kAwAAQBAJ`.

[12] Klaus von Klitzing. "The quantized Hall effect". *Rev. Mod. Phys.* 58 (3 July 1986), 519–531. DOI: `10.1103/RevModPhys.58.519`. URL: `https://link.aps.org/doi/10.1103/RevModPhys.58.519`.

[13] David Tong. *Lectures on the Quantum Hall Effect*. 2016. arXiv: `1606.06687 [hep-th]`. URL: `https://arxiv.org/abs/1606.06687`.

[14] Klaus von Klitzing, Tapash Chakraborty, Philip Kim, Vidya Madhavan, Xi Dai, James McIver, Yoshinori Tokura, Lucile Savary, Daria Smirnova, Ana Maria Rey, Claudia Felser, Johannes Gooth, and Xiaoliang Qi. "40 years of the quantum Hall effect". *Nature Reviews Physics* 2.8 (2020), 397–401. DOI: `10.1038/s42254-020-0209-1`. URL: `https://doi.org/10.1038/s42254-020-0209-1`.

[15] C.L. Kane. "Chapter 1 - Topological Band Theory and the Z2 Invariant". *Topological Insulators*. Ed. by Marcel Franz and Laurens Molenkamp. Vol. 6. Contemporary Concepts of Condensed Matter Science. Elsevier, 2013, pp. 3–34. DOI: `https://doi.org/10.1016/B978-0-444-63314-9.00001-9`. URL: `https://www.sciencedirect.com/science/article/pii/B9780444633149000019`.

[16] Md Mobarak Hossain Polash, Shahram Yalameha, Haihan Zhou, Kaveh Ahadi, Zahra Nourbakhsh, and Daryoosh Vashaee. "Topological quantum matter to topological phase conversion: Fundamentals, materials, physical systems for phase conversions, and device applications". *Materials Science and Engineering: R: Reports* 145 (2021), 100620. ISSN: 0927-796X. DOI: `https://doi.org/10.1016/j.mser.2021.100620`. URL: `https://www.sciencedirect.com/science/article/pii/S0927796X21000152`.

[17] Steven Groves and William Paul. "Band Structure of Gray Tin". *Phys. Rev. Lett.* 11 (5 1963), 194–196. DOI: `10.1103/PhysRevLett.11.194`. URL: `https://link.aps.org/doi/10.1103/PhysRevLett.11.194`.

[18] Raphael C. Vidal, Giovanni Marini, Lukas Lunczer, Simon Moser, Lena Fürst, Julia Issing, Chris Jozwiak, Aaron Bostwick, Eli Rotenberg, Charles Gould, Hartmut Buhmann, Wouter Beugeling, Giorgio Sangiovanni, Domenico Di Sante, Gianni Profeta, Laurens W. Molenkamp, Hendrik Bentmann, and Friedrich Reinert. "Topological band inversion in HgTe(001): Surface and bulk signatures from photoemission". *Phys. Rev. B* 107 (12 Mar. 2023), L121102. DOI: `10.1103/PhysRevB.107.L121102`. URL: `https://link.aps.org/doi/10.1103/PhysRevB.107.L121102`.

[19] B. Andrei Bernevig, Taylor L. Hughes, and Shou-Cheng Zhang. "Quantum Spin Hall Effect and Topological Phase Transition in HgTe Quantum Wells". *Science* 314.5806 (2006), 1757–1761. DOI: `10.1126/science.1133734`. eprint: `https://www.science.org/doi/pdf/10.1126/science.1133734`. URL: `https://www.science.org/doi/abs/10.1126/science.1133734`.

[20] G. Dolcetto, M. Sassetti, and T. L. Schmidt. “Edge physics in two-dimensional topological insulators”. *La Rivista del Nuovo Cimento* 39.3 (2016), 113–154. ISSN: 0393697X, 0393697X. DOI: `10.1393/ncr/i2016-10121-7`. URL: `https://doi.org/10.1393/ncr/i2016-10121-7`.

[21] Bin Zhou, Hai-Zhou Lu, Rui-Lin Chu, Shun-Qing Shen, and Qian Niu. “Finite Size Effects on Helical Edge States in a Quantum Spin-Hall System”. *Physical Review Letters* 101.24 (2008). DOI: `10.1103/physrevlett.101.246807`. URL: `http://dx.doi.org/10.1103/PhysRevLett.101.246807`.

[22] G. Tkachov and E. M. Hankiewicz. “Spin-helical transport in normal and superconducting topological insulators”. *physica status solidi (b)* 250.2 (2013), 215–232. ISSN: 1521-3951. DOI: `10.1002/pssb.201248385`. URL: `http://dx.doi.org/10.1002/pssb.201248385`.

[23] Raffaele Battilomo, Niccoló Scopigno, and Carmine Ortix. “Spin field-effect transistor in a quantum spin-Hall device”. *Phys. Rev. B* 98 (7 2018), 075147. DOI: `10.1103/PhysRevB.98.075147`. URL: `https://link.aps.org/doi/10.1103/PhysRevB.98.075147`.

[24] Alexia Rod, Thomas L. Schmidt, and Stephan Rachel. “Spin texture of generic helical edge states”. *Phys. Rev. B* 91 (24 June 2015), 245112. DOI: `10.1103/PhysRevB.91.245112`. URL: `https://link.aps.org/doi/10.1103/PhysRevB.91.245112`.

[25] Xianxin Wu, Xin Liu, Ronny Thomale, and Chao-Xing Liu. “High-Tc superconductor Fe(Se,Te) monolayer: an intrinsic, scalable and electrically tunable Majorana platform”. *National Science Review* 9.3 (May 2021), nwab087. ISSN: 2095-5138. DOI: `10.1093/nsr/nwab087`. eprint: `https://academic.oup.com/nsr/article-pdf/9/3/nwab087/44252552/nwab087\_supplemental\_file.pdf`. URL: `https://doi.org/10.1093/nsr/nwab087`.

[26] Zunash Umar, Yasir Altaf, Fahim Ahmed, Najam Ul Hassan, Mushtaq Ali, Muhammad Zulfiqar, and Farhan Yousaf. “Band structure engineering to improve the optical and thermoelectric properties of Rb2AgXBr6 (X= Al, In, Ga) for energy applications within DFT framework”. *Materials Science and Engineering: B* 310 (2024), 117728.

[27] Fares KANOUNI, Farouk Laidoudi, and ARAB Fahima. “Density functional theory insights of phonons modes behaviours in AlScN for surface acoustic wave applications”. *Materials Today Communications* 36 (2023), 106753.

[28] P. Hohenberg and W. Kohn. “Inhomogeneous Electron Gas”. *Phys. Rev.* 136 (3B Nov. 1964), B864–B871. DOI: `10.1103/PhysRev.136.B864`. URL: `https://link.aps.org/doi/10.1103/PhysRev.136.B864`.

[29] W. Kohn and L. J. Sham. “Self-Consistent Equations Including Exchange and Correlation Effects”. *Phys. Rev.* 140 (4A Nov. 1965), A1133–A1138. DOI: `10.1103/PhysRev.140.A1133`. URL: `https://link.aps.org/doi/10.1103/PhysRev.140.A1133`.

[30] J.G. Lee. *Computational Materials Science: An Introduction, Second Edition*. CRC Press, 2016. ISBN: 9781498749756. URL: `https://books.google.ro/books?id=4eiVDQAAQBAJ`.

[31] E. Pavarini, E. Koch, F. Anders, and M. Jarrell. *Correlated electrons: from models to materials*. Reihe Modeling and Simulation, Vol. 2 (Forschungszentrum Jülich, 2012), 2012. URL: `http://www.cond-mat.de/events/correl12`.

[32] R.M. Martin. *Electronic Structure: Basic Theory and Practical Methods*. Cambridge University Press, 2004. ISBN: 9780521782852. URL: `https://books.google.ro/books?id=dmRTFLpSGNsC`.

[33] José M Soler, Emilio Artacho, Julian D Gale, Alberto García, Javier Junquera, Pablo Ordejón, and Daniel Sánchez-Portal. "The SIESTA method for ab initio order-N materials simulation". *Journal of Physics: Condensed Matter* 14.11 (2002), 2745.

[34] Alberto García, Nick Papior, Arsalan Akhtar, Emilio Artacho, Volker Blum, Emanuele Bosoni, Pedro Brandimarte, Mads Brandbyge, Jorge I Cerdá, Fabiano Corsetti, et al. "Siesta: Recent developments and applications". *The Journal of chemical physics* 152.20 (2020).

[35] Supriyo Datta. *Quantum Transport: Atom to Transistor*. Cambridge University Press, 2005.

[36] Dmitry Ryndyk. *Theory of Quantum Transport at Nanoscale*. Springer Cham, 2015.

[37] Mads Brandbyge, José-Luis Mozos, Pablo Ordejón, Jeremy Taylor, and Kurt Stokbro. "Density-functional method for nonequilibrium electron transport". *Phys. Rev. B* 65 (16 Mar. 2002), 165401. DOI: `10.1103/PhysRevB.65.165401`. URL: `https://link.aps.org/doi/10.1103/PhysRevB.65.165401`.

[38] M. Paulsson. *Non Equilibrium Green's Functions for Dummies: Introduction to the One Particle NEGF equations*. 2006. arXiv: `cond-mat/0210519 [cond-mat.mes-hall]`. URL: `https://arxiv.org/abs/cond-mat/0210519`.

[39] Calin-Andrei Pantis-Simut, Amanda Teodora Preda, Nicolae Filipoiu, Alaa Allosh, and George Alexandru Nemnes. "Electric-Field Control in Phosphorene-Based Heterostructures". *Nanomaterials* 12.20 (2022). ISSN: 2079-4991. DOI: `10.3390/nano12203650`. URL: `https://www.mdpi.com/2079-4991/12/20/3650`.

[40] Nick Papior. *sisl: v<fill-version>*. 2024. DOI: `10.5281/zenodo.597181`. URL: `https://doi.org/10.5281/zenodo.597181`.

[41] Hisao Nakamura. "First-Principles Study for Detection of Inelastic Electron Transport in Molecular Junctions by Internal Substitution". *The Journal of Physical Chemistry C* 114.28 (2010), 12280–12289. ISSN: 1932-7447. DOI: `10.1021/jp9114223`. URL: `https://doi.org/10.1021/jp9114223`.

[42] Tchavdar Todorov. "Tight-Binding Simulation of Current-Carrying Nanostructures". *Journal of Physics: Condensed Matter* 14 (Mar. 2002), 3049. DOI: `10.1088/0953-8984/14/11/314`.

[43] Nick Rübner Papior. *Computational Tools and Studies of Graphene Nanostructures*. English. 2016.

[44] Neil W Ashcroft, N David Mermin, and Sergio Rodriguez. "Solid state physics". *American Journal of Physics* 46.1 (1978), 116–117.

[45] W. P. Lima, F. R. V. Araújo, D. R. da Costa, S. H. R. Sena, and J. M. Pereira. "Tight-binding Model in First and Second Quantization for Band Structure Calculations". *Brazilian Journal of Physics* 52.2 (2022), 42. DOI: `10.1007/s13538-021-01027-x`. URL: `https://doi.org/10.1007/s13538-021-01027-x`.

[46] Alessandro Pecchia and Aldo Di Carlo. "Atomistic theory of transport in organic and inorganic nanostructures". *Reports on Progress in Physics* 67.8 (2004), 1497.

[47] J. C. Slater and G. F. Koster. “Simplified LCAO Method for the Periodic Potential Problem”. *Phys. Rev.* 94 (6 1954), 1498–1524. DOI: `10.1103/PhysRev.94.1498`. URL: `https://link.aps.org/doi/10.1103/PhysRev.94.1498`.

[48] Philip George Burke. *R-Matrix Theory of Atomic Collisions*. Springer Berlin, Heidelberg, 2021. DOI: `https://doi.org/10.1007/978-3-642-15931-2`.

[49] Jussi Behrndt, Hagen Neidhardt, Elena R. Racec, Paul N. Racec, and Ulrich Wulf. “On Eisenbud’s and Wigner’s R-matrix: A general approach”. *Journal of Differential Equations* 244.10 (2008), 2545–2577. ISSN: 0022-0396. DOI: `https://doi.org/10.1016/j.jde.2008.02.004`. URL: `https://www.sciencedirect.com/science/article/pii/S0022039608000636`.

[50] K. Varga. “*R*-matrix calculation of Bloch states for scattering and transport problems”. *Phys. Rev. B* 80 (8 2009), 085102. DOI: `10.1103/PhysRevB.80.085102`. URL: `https://link.aps.org/doi/10.1103/PhysRevB.80.085102`.

[51] Thushari Jayasekera, Michael A. Morrison, and Kieran Mullen. “*R*-matrix theory for magnetotransport properties in semiconductor devices”. *Phys. Rev. B* 74 (23 Dec. 2006), 235308. DOI: `10.1103/PhysRevB.74.235308`. URL: `https://link.aps.org/doi/10.1103/PhysRevB.74.235308`.

[52] Claude Bloch. “Une formulation unifiée de la théorie des réactions nucléaires”. *Nuclear Physics* 4 (1957), 503–528. ISSN: 0029-5582. DOI: `https://doi.org/10.1016/0029-5582(87)90058-7`. URL: `https://www.sciencedirect.com/science/article/pii/0029558287900587`.

[53] E. Anderson, Z. Bai, C. Bischof, S. Blackford, J. Demmel, J. Dongarra, J. Du Croz, A. Greenbaum, S. Hammarling, A. McKenney, and D. Sorensen. *LAPACK Users’ Guide*. Third. Philadelphia, PA: Society for Industrial and Applied Mathematics, 1999. ISBN: 0-89871-447-8 (paperback).

[54] Calin-Andrei Pantis-Simut, Amanda Teodora Preda, Lucian Ion, Andrei Manolescu, and George Alexandru Nemnes. “Mapping confinement potentials and charge densities of interacting quantum systems using conditional generative adversarial networks”. *Machine Learning: Science and Technology* 4.2 (May 2023), 025023. DOI: `10.1088/2632-2153/acd6d8`. URL: `https://dx.doi.org/10.1088/2632-2153/acd6d8`.

[55] T. Ando. “Quantum point contacts in magnetic fields”. *Phys. Rev. B* 44 (15 Oct. 1991), 8017–8027. DOI: `10.1103/PhysRevB.44.8017`. URL: `https://link.aps.org/doi/10.1103/PhysRevB.44.8017`.

[56] Maciej Zwierzycki, Petr Khomyakov, Anton Starikov, K. Xia, Mohand Talanana, Pengxiang Xu, Volodimir Karpan, Illya Marushchenko, I. Turek, G. Bauer, Geert Brocks, and Paul Kelly. “Calculating scattering matrices by wave function matching”. *physica status solidi (b)* 245 (Apr. 2008), 623–640. DOI: `10.1002/pssb.200743359`.

[57] Geert Brocks, Volodimir Karpan, Paul Kelly, Petr Khomyakov, Illya Marushchenko, Anton Starikov, Mohand Talanana, I. Turek, K. Xia, Pengxiang Xu, Maciej Zwierzycki, and G. Bauer. “9 SCIENTIFIC HIGHLIGHT OF THE MONTH: Calculating Scattering Matrices by Wave Function Matching Calculating Scattering Matrices by Wave Function Matching” (2007).

[58] Maciej Zwierzycki, Petr Khomyakov, Anton Starikov, K. Xia, Mohand Talanana, Pengxiang Xu, Volodimir Karpan, Illya Marushchenko, I. Turek, G. Bauer, Geert Brocks, and Paul Kelly. "Calculating scattering matrices by wave function matching". *physica status solidi (b)* 245 (Apr. 2008), 623–640. DOI: `10.1002/pssb.200743359`.

[59] Hocine Boumrar, Mahdi Hamidi, Hand Zenia, and Samir Lounis. "Equivalence of wave function matching and Green's functions methods for quantum transport: generalized Fisher–Lee relation". *Journal of Physics: Condensed Matter* 32.35 (June 2020), 355302. DOI: `10.1088/1361-648X/ab88f5`. URL: `https://dx.doi.org/10.1088/1361-648X/ab88f5`.

[60] P. A. Khomyakov, G. Brocks, V. Karpan, M. Zwierzycki, and P. J. Kelly. "Conductance calculations for quantum wires and interfaces: Mode matching and Green's functions". *Phys. Rev. B* 72 (3 2005), 035450. DOI: `10.1103/PhysRevB.72.035450`. URL: `https://link.aps.org/doi/10.1103/PhysRevB.72.035450`.

[61] Christoph W Groth, Michael Wimmer, Anton R Akhmerov, and Xavier Waintal. "Kwant: a software package for quantum transport". *New Journal of Physics* 16.6 (June 2014), 063065. ISSN: 1367-2630. DOI: `10.1088/1367-2630/16/6/063065`. URL: `http://dx.doi.org/10.1088/1367-2630/16/6/063065`.

[62] Qingtian Zhang, KS Chan, and Jingbo Li. "Spin-transfer torque generated in graphene based topological insulator heterostructures". *Scientific Reports* 8.1 (2018), 4343.

[63] Gongwei Hu, Yan Zhang, Lijie Li, and Zhong Lin Wang. "Piezotronic transistor based on topological insulators". *ACS nano* 12.1 (2018), 779–785.

[64] Vivekananda Adak, Krishanu Roychowdhury, and Sourin Das. "Spin Berry phase in a helical edge state: S z nonconservation and transport signatures". *Physical Review B* 102.3 (2020), 035423.

[65] Kristof Moors, Peter Schüffelgen, Daniel Rosenbach, Tobias Schmitt, Thomas Schäpers, and Thomas L Schmidt. "Magnetotransport signatures of three-dimensional topological insulator nanostructures". *Physical Review B* 97.24 (2018), 245429.

[66] Sanjib Kumar Das and Bitan Roy. "Quantized thermal and spin transports of dirty planar topological superconductors". *Physical Review B* 109.19 (2024), 195403.

[67] F Setiawan, Ady Stern, and Erez Berg. "Topological superconductivity in planar Josephson junctions: Narrowing down to the nanowire limit". *Physical Review B* 99.22 (2019), 220506.

[68] Jacob R Taylor, Jay D Sau, and Sankar Das Sarma. "Machine Learning the Disorder Landscape of Majorana Nanowires". *Physical Review Letters* 132.20 (2024), 206602.

[69] Barış Pekerten, Aykut Teker, Özgür Bozat, Michael Wimmer, and İnanç Adagideli. "Disorder-induced topological transitions in multichannel Majorana wires". *Physical Review B* 95.6 (2017), 064507.

[70] Thomas Kloss, Joseph Weston, Benoit Gaury, Benoit Rossignol, Christoph Groth, and Xavier Waintal. "Tkwant: a software package for time-dependent quantum transport". *New Journal of Physics* 23.2 (2021), 023025.

[71] Juan Carrasquilla and Roger G Melko. “Machine learning phases of matter”. *Nature Physics* 13.5 (2017), 431–434.

[72] D. Carvalho, N. A. García-Martínez, J. L. Lado, and J. Fernández-Rossier. “Real-space mapping of topological invariants using artificial neural networks”. *Phys. Rev. B* 97 (11 2018), 115453. DOI: `10.1103/PhysRevB.97.115453`. URL: `https://link.aps.org/doi/10.1103/PhysRevB.97.115453`.

[73] Joaquin F Rodriguez-Nieva and Mathias S Scheurer. “Identifying topological order through unsupervised machine learning”. *Nature Physics* 15.8 (2019), 790–795.

[74] Anton O Oliynyk, Erin Antono, Taylor D Sparks, Leila Ghadbeigi, Michael W Gaultois, Bryce Meredig, and Arthur Mar. “High-throughput machine-learning-driven synthesis of full-Heusler compounds”. *Chemistry of Materials* 28.20 (2016), 7324–7331.

[75] Yue Liu, Tianlu Zhao, Wangwei Ju, and Siqi Shi. “Materials discovery and design using machine learning”. *Journal of Materiomics* 3.3 (2017). High-throughput Experimental and Modeling Research toward Advanced Batteries, 159–177. ISSN: 2352-8478. DOI: `https://doi.org/10.1016/j.jmat.2017.08.002`. URL: `https://www.sciencedirect.com/science/article/pii/S2352847817300515`.

[76] Benjamin Sanchez-Lengeling and Alán Aspuru-Guzik. “Inverse molecular design using machine learning: Generative models for matter engineering”. *Science* 361.6400 (2018), 360–365.

[77] George Alexandru Nemnes, Tudor Luca Mitran, and Andrei Manolescu. “Gap Prediction in Hybrid Graphene-Hexagonal Boron Nitride Nanoflakes Using Artificial Neural Networks”. *Journal of Nanomaterials* 2019.1 (2019), 6960787.

[78] Nicolae Filipoiu and George Alexandru Nemnes. “Prediction of equilibrium phase, stability and stress-strain properties in Co-Cr-Fe-Ni-Al high entropy alloys using artificial neural networks”. *Metals* 10.12 (2020), 1569.

[79] George Alexandru Nemnes, Nicolae Filipoiu, and Valentin Sipica. “Feature selection procedures for combined density functional theory—artificial neural network schemes”. *Physica Scripta* 96.6 (2021), 065807.

[80] McCulloch W.S. and Pitts W. “A logical calculus of the ideas immanent in nervous activity”. *The bulletin of mathematical biophysics* 5 (1943), 115–133. DOI: `10.1007/BF02478259`.

[81] ROSENBLATT F. “The perceptron: a probabilistic model for information storage and organization in the brain”. *Psychol Rev.* 65 (1958), 386–408. DOI: `doi:10.1037/h0042519`.

[82] D.O. Hebb. *The organization of behavior*. John Wiley and Sons, 1949.

[83] Richard Brown. “Donald O. Hebb and the Organization of Behavior: 17 years in the writing”. *Molecular Brain* 13 (Dec. 2020). DOI: `10.1186/s13041-020-00567-8`.

[84] MIT. *Introduction to Machine Learning*. 2024. URL: `https://introml.mit.edu/_static/spring24/LectureNotes/6_390_lecture_notes_spring24.pdf`.

[85] Sagar Sharma, Simone Sharma, and Anidhya Athaiya. “Activation functions in neural networks”. *Towards Data Sci* 6.12 (2017), 310–316.

[86] Bin Ding, Huimin Qian, and Jun Zhou. “Activation functions and their characteristics in deep neural networks”. *2018 Chinese Control And Decision Conference (CCDC)*. 2018, pp. 1836–1841. DOI: `10.1109/CCDC.2018.8407425`.

[87] Tomasz Szandała. "Review and comparison of commonly used activation functions for deep neural networks". *Bio-inspired neurocomputing* (2021), 203–224.

[88] P Sibi, S Allwyn Jones, and P Siddarth. "Analysis of different activation functions using back propagation neural networks". *Journal of theoretical and applied information technology* 47.3 (2013), 1264–1268.

[89] Andrea Apicella, Francesco Donnarumma, Francesco Isgrò, and Roberto Prevete. "A survey on modern trainable activation functions". *Neural Networks* 138 (2021), 14–32.

[90] Sheng Qian, Hua Liu, Cheng Liu, Si Wu, and Hau San Wong. "Adaptive activation functions in convolutional neural networks". *Neurocomputing* 272 (2018), 204–212.

[91] Claude Elwood Shannon. "A mathematical theory of communication". *The Bell system technical journal* 27.3 (1948), 379–423.

[92] Mert Alagözlü. *Stochastic Gradient Descent Variants and Applications*. Feb. 2022. DOI: `10.13140/RG.2.2.12528.53767`.

[93] SVG Reddy, K Thammi Reddy, and V ValliKumari. "Optimization of deep learning using various optimizers, loss functions and dropout". *Int. J. Recent Technol. Eng* 7 (2018), 448–455.

[94] Diederik P. Kingma and Jimmy Ba. *Adam: A Method for Stochastic Optimization*. 2017. arXiv: `1412.6980 [cs.LG]`. URL: `https://arxiv.org/abs/1412.6980`.

[95] Girish Chandrashekar and Ferat Sahin. "A survey on feature selection methods". *Computers & electrical engineering* 40.1 (2014), 16–28.

[96] Geoffrey E Hinton and Ruslan R Salakhutdinov. "Reducing the dimensionality of data with neural networks". *science* 313.5786 (2006), 504–507.

[97] Siddharth Krishna Kumar. *On weight initialization in deep neural networks*. 2017. arXiv: `1704.08863 [cs.LG]`. URL: `https://arxiv.org/abs/1704.08863`.

[98] Xavier Glorot and Yoshua Bengio. "Understanding the difficulty of training deep feedforward neural networks". *Proceedings of the Thirteenth International Conference on Artificial Intelligence and Statistics*. Ed. by Yee Whye Teh and Mike Titterington. Vol. 9. Proceedings of Machine Learning Research. Chia Laguna Resort, Sardinia, Italy: PMLR, 2010, pp. 249–256. URL: `https://proceedings.mlr.press/v9/glorot10a.html`.

[99] Ian J. Goodfellow, Yoshua Bengio, and Aaron Courville. *Deep Learning*. `http://www.deeplearningbook.org`. Cambridge, MA, USA: MIT Press, 2016.

[100] David E. Rumelhart, Geoffrey E. Hinton, and Ronald J. Williams. "Learning internal representations by error propagation". 1986. URL: `https://api.semanticscholar.org/CorpusID:62245742`.

[101] Umberto Michelucci. *An Introduction to Autoencoders*. 2022. arXiv: `2201.03898`.

[102] Ian Goodfellow, Jean Pouget-Abadie, Mehdi Mirza, Bing Xu, David Warde-Farley, Sherjil Ozair, Aaron Courville, and Yoshua Bengio. "Generative Adversarial Nets". *Advances in Neural Information Processing Systems*. Ed. by Z. Ghahramani, M. Welling, C. Cortes, N. Lawrence, and K.Q. Weinberger. Vol. 27. Curran Associates, Inc., 2014. URL: `https://proceedings.neurips.cc/paper_files/paper/2014/file/5ca3e9b122f61f8f06494c97b1afccf3-Paper.pdf`.

[103] Pegah Salehi, Abdolah Chalechale, and Maryam Taghizadeh. *Generative Adversarial Networks (GANs): An Overview of Theoretical Model, Evaluation Metrics, and Recent Developments*. 2020. arXiv: `2005.13178 [cs.CV]`. URL: `https://arxiv.org/abs/2005.13178`.

[104] Mehdi Mirza and Simon Osindero. *Conditional Generative Adversarial Nets*. 2014. arXiv: `1411.1784 [cs.LG]`. URL: `https://arxiv.org/abs/1411.1784`.

[105] Phillip Isola, Jun-Yan Zhu, Tinghui Zhou, and Alexei A. Efros. *Image-to-Image Translation with Conditional Adversarial Networks*. 2018. arXiv: `1611.07004 [cs.CV]`. URL: `https://arxiv.org/abs/1611.07004`.

[106] Mihaela Cosinschi, Amanda T. Preda, C.-A. Pantis-Simut, N. Filipoiu, I. Ghitiu, M. A. Dulea, L. Ion, A. Manolescu, and G. A. Nemnes. "Collective dynamics of Ca atoms encapsulated in C60 endohedral fullerenes". *Phys. Chem. Chem. Phys.* 26 (33 2024), 22090–22098. DOI: `10.1039/D4CP01048E`. URL: `http://dx.doi.org/10.1039/D4CP01048E`.

[107] Kun-Bin Cai, Hsiu-Ying Huang, Meng-Lin Hsieh, Po-Wen Chen, Shou-En Chiang, Sheng Hsiung Chang, Ji-Lin Shen, Wei-Ren Liu, and Chi-Tsu Yuan. "Two-dimensional self-assembly of boric acid-functionalized graphene quantum dots: Tunable and superior optical properties for efficient eco-friendly luminescent solar concentrators". *ACS nano* 16.3 (2022), 3994–4003.

[108] Xiaobing Yan, Yifei Pei, Huawei Chen, Jianhui Zhao, Zhenyu Zhou, Hong Wang, Lei Zhang, Jingjuan Wang, Xiaoyan Li, Cuiya Qin, et al. "Self-assembled networked PbS distribution quantum dots for resistive switching and artificial synapse performance boost of memristors". *Advanced materials* 31.7 (2019), 1805284.

[109] Lucas Cuadra and José Carlos Nieto-Borge. "Modeling quantum dot systems as random geometric graphs with probability amplitude-based weighted links". *Nanomaterials* 11.2 (2021), 375.

[110] George Alexandru Nemnes, Tudor Luca Mitran, Amanda Teodora Preda, Iulia Ghiu, Mihai Marciu, and Andrei Manolescu. "Investigation of bi-particle states in gate-array-controlled quantum-dot systems aided by machine learning techniques". *Physica Scripta* 97 (2022), 055813. DOI: `10.1088/1402-4896/ac5ff6`. URL: `https://dx.doi.org/10.1088/1402-4896/ac5ff6`.

[111] Surajit Basak and Andrzej Ptok. "Shiba states in systems with density of states singularities". *Physical Review B* 105.9 (Mar. 2022). DOI: `10.1103/physrevb.105.094204`.

[112] Wei Jiang, Huaqing Huang, and Feng Liu. "A Lieb-like lattice in a covalent-organic framework and its Stoner ferromagnetism". *Nature Communications* 10.1 (2019), 2207. DOI: `10.1038/s41467-019-10094-3`. URL: `https://doi.org/10.1038/s41467-019-10094-3`.

[113] Mengzhu Shi, Fanghang Yu, Ye Yang, Fanbao Meng, Bin Lei, Yang Luo, Zhe Sun, Junfeng He, Rui Wang, Zhicheng Jiang, Zhengtai Liu, Dawei Shen, Tao Wu, Zhenyu Wang, Ziji Xiang, Jianjun Ying, and Xianhui Chen. "A new class of bilayer kagome lattice compounds with Dirac nodal lines and pressure-induced superconductivity". *Nature Communications* 13.1 (2022), 2773. DOI: `10.1038/s41467-022-30442-0`. URL: `https://doi.org/10.1038/s41467-022-30442-0`.

[114] Linghao Yan and Peter Liljeroth. “Engineered electronic states in atomically precise artificial lattices and graphene nanoribbons”. *Advances in Physics: X* 4.1 (2019), 1651672. DOI: 10.1080/23746149.2019.1651672. eprint: https://doi.org/10.1080/23746149.2019.1651672. URL: https://doi.org/10.1080/23746149.2019.1651672.

[115] Wei Jiang, Shunhong Zhang, Zhengfei Wang, Feng Liu, and Tony Low. “Topological Band Engineering of Lieb Lattice in Phthalocyanine-Based Metal–Organic Frameworks”. *Nano Letters* 20.3 (2020). PMID: 32078326, 1959–1966. DOI: 10.1021/acs.nanolett.9b05242. eprint: https://doi.org/10.1021/acs.nanolett.9b05242. URL: https://doi.org/10.1021/acs.nanolett.9b05242.

[116] Robert Drost, Teemu Ojanen, Ari Harju, and Peter Liljeroth. “Topological states in engineered atomic lattices”. *Nature Physics* 13.7 (2017), 668–671. DOI: 10.1038/nphys4080. URL: https://doi.org/10.1038/nphys4080.

[117] Amanda Teodora Preda, Calin-Andrei Pantis-Simut, Mihai Marciu, Dragos-Victor Anghel, Alaa Allosh, Lucian Ion, Andrei Manolescu, and George Alexandru Nemnes. “Design of Nanoscale Quantum Interconnects Aided by Conditional Generative Adversarial Networks”. *Applied Sciences* 14.3 (2024). ISSN: 2076-3417. URL: https://www.mdpi.com/2076-3417/14/3/1111.

[118] Dennis V Christensen, Regina Dittmann, Bernabe Linares-Barranco, Abu Sebastian, Manuel Le Gallo, Andrea Redaelli, Stefan Slesazeck, Thomas Mikolajick, Sabina Spiga, Stephan Menzel, Ilia Valov, Gianluca Milano, Carlo Ricciardi, Shi-Jun Liang, Feng Miao, Mario Lanza, Tyler J Quill, Scott T Keene, Alberto Salleo, Julie Grollier, Danijela Marković, Alice Mizrahi, Peng Yao, J Joshua Yang, Giacomo Indiveri, John Paul Strachan, Suman Datta, Elisa Vianello, Alexandre Valentian, Johannes Feldmann, Xuan Li, Wolfram H P Pernice, Harish Bhaskaran, Steve Furber, Emre Neftci, Franz Scherr, Wolfgang Maass, Srikanth Ramaswamy, Jonathan Tapson, Priyadarshini Panda, Youngeun Kim, Gouhei Tanaka, Simon Thorpe, Chiara Bartolozzi, Thomas A Cleland, Christoph Posch, ShihChii Liu, Gabriella Panuccio, Mufti Mahmud, Arnab Neelim Mazumder, Morteza Hosseini, Tinoosh Mohsenin, Elisa Donati, Silvia Tolu, Roberto Galeazzi, Martin Ejsing Christensen, Sune Holm, Daniele Ielmini, and N Pryds. “2022 roadmap on neuromorphic computing and engineering”. *Neuromorphic Computing and Engineering* 2.2 (May 2022), 022501. DOI: 10.1088/2634-4386/ac4a83. URL: https://dx.doi.org/10.1088/2634-4386/ac4a83.

[119] Ulrich Wulf, Amanda Teodora Preda, and George Alexandru Nemnes. “Transport in a Two-Channel Nanotransistor Device with Lateral Resonant Tunneling”. *Micromachines* 15.10 (2024). ISSN: 2072-666X. DOI: 10.3390/mi15101270. URL: https://www.mdpi.com/2072-666X/15/10/1270.

[120] Gordon Moore. “Cramming more components onto integrated circuits (1965)”. *Electronics* 38 (1965), 114–117.

[121] M. Waldrop. “The chips are down for Moore’s law”. *Nature News* 530 (Feb. 2016), 144. DOI: 10.1038/530144a.

[122] Deji Akinwande, Cedric Huyghebaert, Ching-Hua Wang, Martha I. Serna, Stijn Goossens, Lain-Jong Li, H. -S. Philip Wong, and Frank H. L. Koppens. “Graphene and two-dimensional materials for silicon technology”. *Nature* 573.7775 (2019), 507–518. DOI: 10.1038/s41586-019-1573-9. URL: https://doi.org/10.1038/s41586-019-1573-9.

[123] Jibesh K. Saha, Nitish Chakma, and Mehedhi Hasan. "Impact of channel length, gate insulator thickness, gate insulator material, and temperature on the performance of nanoscale FETs". *Journal of Computational Electronics* 17.4 (2018), 1521–1527. DOI: `10.1007/s10825-018-1235-4`. URL: `https://doi.org/10.1007/s10825-018-1235-4`.

[124] Ulrich Wulf, Marcus Krahlisch, and Hans Richter. "Scaling properties of ballistic nano-transistors". *Nanoscale Research Letters* 6 (2011), 1–8.

[125] Pedram Razavi, Giorgos Fagas, Isabelle Ferain, Ran Yu, Samaresh Das, and Jean-Pierre Colinge. "Influence of channel material properties on performance of nanowire transistors". *Journal of Applied Physics* 111.12 (June 2012), 124509. ISSN: 0021-8979. DOI: `10.1063/1.4729777`. eprint: `https://pubs.aip.org/aip/jap/article-pdf/doi/10.1063/1.4729777/13368211/124509\_1\_online.pdf`. URL: `https://doi.org/10.1063/1.4729777`.

[126] Ulrich Wulf. "A One-Dimensional Effective Model for Nanotransistors in Landauer–Büttiker Formalism". *Micromachines* 11.4 (2020). ISSN: 2072-666X. DOI: `10.3390/mi11040359`. URL: `https://www.mdpi.com/2072-666X/11/4/359`.

[127] George Nemnes, U. Wulf, and Paul Racec. "Nano-transistors in the Landauer–Büttiker formalism". *Journal of Applied Physics* 96 (July 2004), 596–604. DOI: `10.1063/1.1748858`.

[128] Ulrich Wulf, Jan Kučera, Hans Richter, Manfred Horstmann, Maciej Wiatr, and Jan Höntschel. "Channel Engineering for Nanotransistors in a Semiempirical Quantum Transport Model". *Mathematics* 5.4 (2017). ISSN: 2227-7390. DOI: `10.3390/math5040068`. URL: `https://www.mdpi.com/2227-7390/5/4/68`.

[129] M. Anantram and Alexei Svizhenko. "Multidimensional Modeling of Nanotransistors". *Electron Devices, IEEE Transactions on* 54 (Oct. 2007), 2100–2115. DOI: `10.1109/TED.2007.902857`.

[130] Frank Stern. "Self-Consistent Results for n-Type Si Inversion Layers". *Phys. Rev. B* 5 (12 June 1972), 4891–4899. DOI: `10.1103/PhysRevB.5.4891`. URL: `https://link.aps.org/doi/10.1103/PhysRevB.5.4891`.

[131] Tsuneya Ando, Alan B. Fowler, and Frank Stern. "Electronic properties of two-dimensional systems". *Rev. Mod. Phys.* 54 (2 Apr. 1982), 437–672. DOI: `10.1103/RevModPhys.54.437`. URL: `https://link.aps.org/doi/10.1103/RevModPhys.54.437`.

[132] Junyan Zhu, Jiang Cao, Chen Song, Bo Li, and Zhengsheng Han. "Numerical investigation on the convergence of self-consistent Schrödinger-Poisson equations in semiconductor device transport simulation". *Nanotechnology* 35.31 (2024), 315001. DOI: `10.1088/1361-6528/ad4558`. URL: `https://dx.doi.org/10.1088/1361-6528/ad4558`.

[133] Devin Verreck, Anne S. Verhulst, Maarten L. Van de Put, Bart Sorée, Wim Magnus, Nadine Collaert, Anda Mocuta, and Guido Groeseneken. "Self-consistent procedure including envelope function normalization for full-zone Schrödinger-Poisson problems with transmitting boundary conditions". *Journal of Applied Physics* 124.20 (Nov. 2018), 204501. ISSN: 0021-8979. DOI: `10.1063/1.5047087`. eprint: `https://pubs.aip.org/aip/jap/article-pdf/doi/10.1063/1.5047087/13806085/204501\_1\_online.pdf`. URL: `https://doi.org/10.1063/1.5047087`.

[134] George Nemnes, Lucian Ion, and Stefan Antohe. "Self-consistent potentials and linear regime conductance of cylindrical nanowire transistors in the R-matrix formalism". *Journal of Applied Physics* 106 (Jan. 2010), 113714–113714. DOI: 10.1063/1.3269704.

[135] Rachana Venugopal, Zhibin Ren, and M.s Lundstrom. "Simulating quantum transport in nanoscale MOSFETs: Ballistic hole transport, subband engineering and boundary conditions". *Nanotechnology, IEEE Transactions on* 2 (Oct. 2003), 135–143. DOI: 10.1109/TNANO.2003.817229.

[136] Anisur Rahman, Jing Guo, S. Datta, and M.s Lundstrom. "Theory of ballistic nanotransistors". *Electron Devices, IEEE Transactions on* 50 (Oct. 2003), 1853–1864. DOI: 10.1109/TED.2003.815366.

[137] Amanda Teodora Preda, Iulia Ghiu, Lucian Ion, Ulrich Wulf, Andrei Manolescu, and George Alexandru Nemnes. "Implementation of a multi-terminal quantum sorter in solid state systems". *Scientific Reports* 15.1 (2025), 23738. DOI: 10.1038/s41598-025-05860-x. URL: https://doi.org/10.1038/s41598-025-05860-x.

[138] Timothy P Spiller. "Quantum information technology". *Materials Today* 6.1 (2003), 30–36. ISSN: 1369-7021. DOI: https://doi.org/10.1016/S1369-7021(03)00130-5. URL: https://www.sciencedirect.com/science/article/pii/S1369702103001305.

[139] Masahito Hayashi, Satoshi Ishizaka, Akinori Kawachi, Gen Kimura, and Tomohiro Ogawa. *Introduction to Quantum Information Science*. Springer Berlin, Heidelberg, 2014. DOI: https://doi.org/10.1007/978-3-662-43502-1.

[140] Malvika Garikapati, Santosh Kumar, He Zhang, Yong Meng Sua, and Yu-Ping Huang. "Programmable Spatiotemporal Quantum Parametric Mode Sorter". *Phys. Rev. Appl.* 19 (4 Apr. 2023), 044070. DOI: 10.1103/PhysRevApplied.19.044070. URL: https://link.aps.org/doi/10.1103/PhysRevApplied.19.044070.

[141] Jonathan Leach, Miles J. Padgett, Stephen M. Barnett, Sonja Franke-Arnold, and Johannes Courtial. "Measuring the Orbital Angular Momentum of a Single Photon". *Phys. Rev. Lett.* 88 (25 2002), 257901. DOI: 10.1103/PhysRevLett.88.257901. URL: https://link.aps.org/doi/10.1103/PhysRevLett.88.257901.

[142] Gregorius C. G. Berkhout, Martin P. J. Lavery, Johannes Courtial, Marco W. Beijersbergen, and Miles J. Padgett. "Efficient Sorting of Orbital Angular Momentum States of Light". *Phys. Rev. Lett.* 105 (15 2010), 153601. DOI: 10.1103/PhysRevLett.105.153601. URL: https://link.aps.org/doi/10.1103/PhysRevLett.105.153601.

[143] Martin P. J. Lavery, David J. Robertson, Gregorius C. G. Berkhout, Gordon D. Love, Miles J. Padgett, and Johannes Courtial. "Refractive elements for the measurement of the orbital angular momentum of a single photon". *Opt. Express* 20.3 (Jan. 2012), 2110–2115. DOI: 10.1364/OE.20.002110. URL: https://opg.optica.org/oe/abstract.cfm?URI=oe-20-3-2110.

[144] Mohammad Mirhosseini, Mehul Malik, Zhimin Shi, and Robert W. Boyd. "Efficient separation of the orbital angular momentum eigenstates of light". *Nature Communications* 4.1 (2013), 2781. URL: https://doi.org/10.1038/ncomms3781.

[145] Sebastian A. Schulz, Taras Machula, Ebrahim Karimi, and Robert W. Boyd. "Integrated multi vector vortex beam generator". *Opt. Express* 21.13 (2013), 16130–16141. DOI: `10.1364/OE.21.016130`. URL: `https://opg.optica.org/oe/abstract.cfm?URI=oe-21-13-16130`.

[146] Fang-Xiang Wang, Wei Chen, Zhen-Qiang Yin, Shuang Wang, Guang-Can Guo, and Zheng-Fu Han. "Scalable orbital-angular-momentum sorting without destroying photon states". *Phys. Rev. A* 94 (3 2016), 033847. DOI: `10.1103/PhysRevA.94.033847`. URL: `https://link.aps.org/doi/10.1103/PhysRevA.94.033847`.

[147] Hugo Larocque, Jérémie Gagnon-Bischoff, Dominic Mortimer, Yingwen Zhang, Frédéric Bouchard, Jeremy Upham, Vincenzo Grillo, Robert W. Boyd, and Ebrahim Karimi. "Generalized optical angular momentum sorter and its application to high-dimensional quantum cryptography". *Opt. Express* 25.17 (2017), 19832–19843. DOI: `10.1364/OE.25.019832`. URL: `https://opg.optica.org/oe/abstract.cfm?URI=oe-25-17-19832`.

[148] Jonathan Leach, Johannes Courtial, Kenneth Skeldon, Stephen M. Barnett, Sonja Franke-Arnold, and Miles J. Padgett. "Interferometric Methods to Measure Orbital and Spin, or the Total Angular Momentum of a Single Photon". *Phys. Rev. Lett.* 92 (1 2004), 013601. DOI: `10.1103/PhysRevLett.92.013601`. URL: `https://link.aps.org/doi/10.1103/PhysRevLett.92.013601`.

[149] Yiyu Zhou, Mohammad Mirhosseini, Dongzhi Fu, Jiapeng Zhao, Seyed Mohammad Hashemi Rafsanjani, Alan E. Willner, and Robert W. Boyd. "Sorting Photons by Radial Quantum Number". *Phys. Rev. Lett.* 119 (26 Dec. 2017), 263602. DOI: `10.1103/PhysRevLett.119.263602`. URL: `https://link.aps.org/doi/10.1103/PhysRevLett.119.263602`.

[150] Xuemei Gu, Mario Krenn, Manuel Erhard, and Anton Zeilinger. "Gouy Phase Radial Mode Sorter for Light: Concepts and Experiments". *Phys. Rev. Lett.* 120 (10 2018), 103601. DOI: `10.1103/PhysRevLett.120.103601`. URL: `https://link.aps.org/doi/10.1103/PhysRevLett.120.103601`.

[151] Yiyu Zhou, Jing Yang, Jeremy D. Hassett, Seyed Mohammad Hashemi Rafsanjani, Mohammad Mirhosseini, A. Nick Vamivakas, Andrew N. Jordan, Zhimin Shi, and Robert W. Boyd. "Quantum-limited estimation of the axial separation of two incoherent point sources". *Optica* 6.5 (2019), 534–541. DOI: `10.1364/OPTICA.6.000534`. URL: `https://opg.optica.org/optica/abstract.cfm?URI=optica-6-5-534`.

[152] Yiyu Zhou, Mohammad Mirhosseini, Stone Oliver, Jiapeng Zhao, Seyed Mohammad Hashemi Rafsanjani, Martin P. J. Lavery, Alan E. Willner, and Robert W. Boyd. "Using all transverse degrees of freedom in quantum communications based on a generic mode sorter". *Opt. Express* 27.7 (Apr. 2019), 10383–10394. DOI: `10.1364/OE.27.010383`. URL: `https://opg.optica.org/oe/abstract.cfm?URI=oe-27-7-10383`.

[153] Enno Krauss, Gary Razinskas, Dominik Köck, Swen Grossmann, and Bert Hecht. "Reversible Mapping and Sorting the Spin of Photons on the Nanoscale: A Spin-Optical Nanodevice". *Nano Letters* 19.5 (May 2019), 3364–3369. DOI: `10.1021/acs.nanolett.9b01162`. URL: `https://doi.org/10.1021/acs.nanolett.9b01162`.

[154] Robert Fickler, Frédéric Bouchard, Enno Giese, Vincenzo Grillo, Gerd Leuchs, and Ebrahim Karimi. "Full-field mode sorter using two optimized phase transformations for high-dimensional quantum cryptography". *Journal of Optics* 22.2 (2020), 024001. DOI: `10.1088/2040-8986/ab6303`. URL: `https://dx.doi.org/10.1088/2040-8986/ab6303`.

[155] Hugo Defienne and Daniele Faccio. "Arbitrary spatial mode sorting in a multimode fiber". *Phys. Rev. A* 101 (6 2020), 063830. DOI: `10.1103/PhysRevA.101.063830`. URL: `https://link.aps.org/doi/10.1103/PhysRevA.101.063830`.

[156] Kfir Sulimany and Yaron Bromberg. "All-fiber source and sorter for multimode correlated photons". *npj Quantum Information* 8.1 (2022), 4. DOI: `10.1038/s41534-021-00515-x`. URL: `https://doi.org/10.1038/s41534-021-00515-x`.

[157] Radu Ionicioiu. "Sorting quantum systems efficiently". *Scientific Reports* 6.1 (2016), 25356. DOI: `10.1038/srep25356`. URL: `https://doi.org/10.1038/srep25356`.

[158] Iulia Ghiu. "Simultaneous sorting many quDits using different input ports". *Quantum Information Processing* 18.9 (2019), 285. DOI: `10.1007/s11128-019-2395-2`. URL: `https://doi.org/10.1007/s11128-019-2395-2`.

[159] Iulia Ghiu. "Determining the output port from the distance". *Romanian Reports in Physics* 72 (2020), 115.

[160] Arnab Pal, Shuo Zhang, Tanmay Chavan, Kunjesh Agashiwala, Chao-Hui Yeh, Wei Cao, and Kaustav Banerjee. "Quantum-Engineered Devices Based on 2D Materials for Next-Generation Information Processing and Storage". *Advanced Materials* 35.27 (2023), 2109894. DOI: `https://doi.org/10.1002/adma.202109894`. eprint: `https://onlinelibrary.wiley.com/doi/pdf/10.1002/adma.202109894`. URL: `https://onlinelibrary.wiley.com/doi/abs/10.1002/adma.202109894`.

[161] Benjamin J McMorran, Tyler R Harvey, and Martin P J Lavery. "Efficient sorting of free electron orbital angular momentum". *New Journal of Physics* 19.2 (Feb. 2017), 023053. DOI: `10.1088/1367-2630/aa5f6f`. URL: `https://dx.doi.org/10.1088/1367-2630/aa5f6f`.

[162] Branislav K. Nikolic and Satofumi Souma. "Decoherence of transported spin in multichannel spin-orbit-coupled spintronic devices: Scattering approach to spin-density matrix from the ballistic to the localized regime". *Phys. Rev. B* 71 (19 2005), 195328. DOI: `10.1103/PhysRevB.71.195328`. URL: `https://link.aps.org/doi/10.1103/PhysRevB.71.195328`.

[163] P. St ředa and P. Šeba. "Antisymmetric Spin Filtering in One-Dimensional Electron Systems with Uniform Spin-Orbit Coupling". *Phys. Rev. Lett.* 90 (25 June 2003), 256601. DOI: `10.1103/PhysRevLett.90.256601`. URL: `https://link.aps.org/doi/10.1103/PhysRevLett.90.256601`.

[164] Matthew J Gilbert. "Topological electronics". *Communications Physics* 4.1 (2021), 70.

[165] Minggang Zeng and Gengchiau Liang. "Spin filtering and spin separating effects in U-shaped topological insulator devices". *Journal of Applied Physics* 112.7 (Oct. 2012), 073707. ISSN: 0021-8979. DOI: `10.1063/1.4757411`. eprint: `https://pubs.aip.org/aip/jap/article-pdf/doi/10.1063/1.4757411/15095423/073707\_1\_online.pdf`. URL: `https://doi.org/10.1063/1.4757411`.

List of Figures

List of Tables

List of Abbreviations

2D	Two-dimensional
3D	Three-dimensional
2DEG	Two-dimensional electron gas
AIMD	*Ab initio* molecular dynamics
ANN	Artificial Neural Networks
BHZ	Bernevig-Hughes-Zhang
CNN	Convolutional Neural Networks
DFT	Density functional theory
ED	Exact Diagonalization
GAN	Generative Adversarial Networks
cGAN	Conditional Generative Adversarial Networks
HF	Hartree-Fock
HK	Hoheberg-Kohn
KS	Kohn-Sham
LB	Landauer-Buttiker
ML	Machine Learning
NEGF	Nonequilibrium Green's functions formalism
NN	Nearest Neighbors
NNN	Next Nearest Neighbors
QD	Quantum Dot
QHE	Quantum Hall Effect
QI	Quantum Interconnect
STM	Scanning Tunneling Microscope
SQHE	Spin Quantum Hall Effect
TB	Tight binding
TCM	Tunneling Current Map
TI	Topological Insulator
WFM	Wavefunction matching

Research activity

Published articles

1. A. T. Preda and I. Ghiu and L. Ion and U. Wulf and A. Manolescu and G. A. Nemnes . "Implementation of a multi-terminal quantum sorter in solid state systems". *Scientific Reports* 15, 23738 (2025). `https://www.nature.com/articles/s41598-025-05860-x`. **AIS: 1.029 IF: 3.9**

2. A. T. Preda and C. A. Pantis-Simut and M. Marciu and D. V. Anghel and A Allosh and L. Ion and A. Manolescu and G. A. Nemnes. "Design of Nanoscale Quantum Interconnects Aided by Conditional Generative Adversarial Networks". *Applied Sciences* 14, 1111 (2024). `https://www.mdpi.com/2076-3417/14/3/1111`. **AIS: 0.428 IF: 2.5**

3. U. Wulf and A. T. Preda and G. A. Nemnes. "Transport in a Two-Channel Nanotransistor Device with Lateral Resonant Tunneling". *Micromachines* 15, 1270 (2024). `https://www.mdpi.com/2072-666X/15/10/1270`. **AIS:0.490 IF:3.0**

4. D.V. Anghel, A. T. Preda, G. A. Nemnes. "The R-matrix formalism for two-particle scattering problems". *Physics Letters A* 425 , 127865 (2022). DOI: `https://doi.org/10.1016/j.physleta.2021.127865`. **AIS:0.469 IF: 2.6**

5. G. A. Nemnes and T. L. Mitran and A. T. Preda and I. Ghiu and M. Marciu and A. Manolescu. "Investigation of bi-particle states in gate-array-controlled quantum-dot systems aided by machine learning techniques". *Physica Scripta* 055813, 055813 (2022). DOI: `https://dx.doi.org/10.1088/1402-4896/ac5ff6`. **AIS:0.465 IF: 2.9**

6. C. A. Pantis-Simut and A. T. Preda and L. Ion and A. Manolescu and G. A. Nemnes. "Mapping confinement potentials and charge densities of interacting quantum systems using conditional generative adversarial networks". *Machine Learning: Science and Technology* 4, 025023 (2023) `https://dx.doi.org/10.1088/2632-2153/acd6d8` **AIS: 2.148 IF: 6.8**

7. C. A. Pantis-Simut and A. T. Preda and N. Filipoiu and A. Allosh, and G. A. Nemnes. "Electric-Field Control in Phosphorene-Based Heterostructures". *Nanomaterials* 12, 3650(2022) `https://www.mdpi.com/2079-4991/12/20/3650`. **AIS:0.712 IF: 5.3**

8. M. Cosinschi and A. T. Preda and C. A. Pantis-Simut and N. Filipoiu and I. Ghitiu, and M. Dulea, and L. Ion and A. Manolescu and G. A. Nemnes. "Collective dynamics of Ca atoms encapsulated in C60 endohedral fullerenes". *Phys. Chem. Chem. Phys.* 26, 22090-22098 (2024). `http://dx.doi.org/10.1039/D4CP01048E`. **AIS: 0.624 IF: 2.9**

Total AIS: **6.365**